Fall 2021

Experimental characterization and crystal plasticity modeling of mechanical properties and microstructure evolution of additively manufactured Inconel 718 superalloy

Saeede Ghorbanpour
University of New Hampshire, Durham, Saeede.Ghorbanpour@unh.edu

Experimental characterization and crystal plasticity modeling of mechanical properties and microstructure evolution of additively manufactured Inconel 718 superalloy

By

Saeede Ghorbanpour

BS in Mechanical Engineering, Isfahan University of Technology, 2009

MS in Mechanical Engineering, K. N. Toosi University of Technology, 2013

DISSERTATION

Submitted to the University of New Hampshire

in Partial Fulfillment of

the Requirements for the Degree of

Doctor of Philosophy

In

Mechanical Engineering

September 2021

DISSERTATION COMMITTEE PAGE

This dissertation has been examined and approved in partial fulfilment of the requirements for the degree of Doctor of Philosophy in Mechanical Engineering by:

Marko Knezevic, Associate Professor (Mechanical Engineering), Advisor

Vera Popovich, Associate Professor (Department of Materials Science and Engineering, TU Delft), Co-advisor

Todd Gross, Professor (Mechanical Engineering)

James Krzanowski, Professor (Mechanical Engineering)

Igor Tsukrov, Professor (Mechanical Engineering)

On 06.09.2021

DEDICATION

I dedicate my dissertation to my husband, Vahid, whom his love and support was always given to me.

I also would like to express my sincere gratitude to my parents, Sima and Akbar, and my sisters, Sara, Zizi, and Zari.

ACKNOWLEDGEMENTS

I would like to thank my advisor Professor Marko Knezevic for his continuous support during my PhD program. I am grateful to him for all the knowledge and experience I earned working in his group.

I would like to thank Dr. Vera Popovich for her mentorship and providing me the opportunity of the visiting research position at TU Delft in the last year of my PhD.

I would like to thank Professor Todd Gross, Professor James Krzanowski, Professor Igor Tsukrov, and Professor Yansis Korkolis for their classes in the college of engineering and physical science, discussing and answering my questions, helping me to understand experimental procedures, and providing me feedback on my research.

I would like to thank Dr. Tsuyoshi Furushima at The University of Tokyo for hosting me as a visiting research scholar.

I would like to thank Nancy Cherim for helping me with the electron microscopy facilities and Scott Campbell for squeezing my many sample machining processes in his busy schedule.

I would like to thank the UNH College of Engineering and Physical Science, the UNH Graduate School, The Mechanical, Maritime and Materials Engineering (3ME) department at TU Delft, and the Institute of Industrial Science at The University of Tokyo.

I would like to thank all my friends at UNH, colleagues in S211 and S212 in mechanical engineering department at UNH, and colleagues in 3ME at TUD.

Table of Contents

Abstract

Experimental characterization and crystal plasticity modeling of mechanical properties and microstructure evolution of additively manufactured Inconel 718 superalloy

By

Saeede Ghorbanpour

University of New Hampshire, September 2021

In this thesis, the mechanical behavior of the additively manufactured (AM) IN718 nickel-based superalloy and their correlations with the evolution of microstructure are studied comprehensively. The effects of manufacturing parameters, build orientations, and post processing procedures, i.e. standard heat treatment and hot isostatic pressing (HIP), on various mechanical properties including monotonic compression and tension strength, low cyclic fatigue performance, high cyclic fatigue behaviour, and fatigue crack growth behavior are investigated. Due to the high temperature applications of the IN718 alloy, elevated temperature properties are examined as well. Electron Backscattered Diffraction (EBSD) technique is employed to measure the initial and deformed textures. In addition, an elasto-plastic self-consistent polycrystal plasticity model is developed to interpret the deformation behavior of the alloy in room temperature and high temperatures. The model incorporates the contributions of solid solution, precipitates shearing, and grain size and shape effects into the initial slip resistance. For activating the slip systems, the non-Schmid effects and backstress are implemented in the model. The crystal plasticity model is capable of simulating the monotonic and large-strain load reversal cycles of the material with pole figure difference (PFD) values no more than 0.2.

Chapter 1: A crystal plasticity model incorporating the effects of precipitates in superalloys: Application to tensile, compressive, and cyclic deformation of Inconel 718

This chapter was published as “A crystal plasticity model incorporating the effects of precipitates in superalloys: Application to tensile, compressive, and cyclic deformation of Inconel 718” in the International Journal of Plasticity, 99 (2017): 162-185. The Authors of this paper are Saeede Ghorbanpour, Milovan Zecevic, Anil Kumar, Mohammad Jahedi, Jonathan Bicknell, Luke Jorgensen, Irene J Beyerlein, and Marko Knezevic. My contribution to this chapter was performing all mechanical testing, performing initial and final texture measurements. In addition, I developed the crystal plasticity model by modifying the initial slip resistance calculations, introducing the mean free path, latent hardening matrix, non-schmid effect, and backstress effects to the model. I performed all the simulations and generated all the simulation results.

A crystal plasticity model incorporating the effects of precipitates in superalloys: Application to tensile, compressive, and cyclic deformation of Inconel 718

Saeede Ghorbanpour[a], Milovan Zecevic[a], Anil Kumar[b], Mohammad Jahedi[a], Jonathan Bicknell[c], Luke Jorgensen[c], Irene J. Beyerlein[d], and Marko Knezevic[a,]

[a] Department of Mechanical Engineering, University of New Hampshire, Durham, NH 03824, USA.

[b] Theoretical Division, Los Alamos National Laboratory, Los Alamos, NM 87545, USA.

[c] Turbocam Energy Solutions, Turbocam International, Dover, NH 03820, USA.

[d] Mechanical Engineering Department, Materials Department, University of California at Santa Barbara, Santa Barbara, CA 93106, USA.

Abstract

An elasto-plastic polycrystal plasticity model is developed and applied to an Inconel 718 (IN718) superalloy that was produced by additive manufacturing (AM). The model takes into account the contributions of solid solution, precipitates shearing, and grain size and shape effects into the initial slip resistance. Non-Schmid effects and backstress are also included in the crystal plasticity model for activating slip. The hardening law for the critical resolved shear stress is based on the evolution of dislocation density. Using the same set of material and physical parameters, the model is compared against a suite of compression, tension, and large-strain cyclic mechanical test data applied in different AM build directions. It is demonstrated that the model is capable of predicting the particularities of both monotonic and cyclic deformation to large strains of the alloy, including decreasing hardening rate during monotonic loading, the non-linear unloading upon the load reversal, the Bauschinger effect, the hardening rate change during loading in the reverse direction as well as plastic anisotropy and the concomitant microstructure evolution. It is anticipated that the general model developed here can be applied to other multiphase alloys containing precipitates.

1. Introduction

Inconel 718 (IN718) is a Ni-based superalloy exhibiting a range of excellent properties including high yield strength, toughness, and corrosion resistance enabling the components made of it to operate under extreme mechanical and thermal conditions (Francis et al., 2014; Kuo et al., 2009; Mei et al., 2015; Rao et al., 2003; Slama and Abdellaoui, 2000). It is extensively used for various applications in turbine engines, jet engines, power generation plants, heat treatment equipment, etc. (Davis, 1997; Herderick, 2015; Knezevic et al., 2012b). Some of these parts can take on complex shapes. Achieving the shapes needed often requires machining. The costs can be expensive since these materials are very hard and can quickly wear machining tools. An alternative technique to make the required shapes of IN718 is additive manufacturing.

Modeling the deformation behavior of IN718, made by any manufacturing process, is challenging due to its complex microstructure featuring γ' and γ" precipitates within a γ matrix (Antolovich, 2015; Rao et al., 2003; Xiao et al., 2005). The chemical composition of the γ' precipitate is $Ni_3(Al,Ti)$. This γ' precipitate is usually spherical in shape with a diameter of 20-30 nm when the material is heat treated according to AMS 5663, where the atoms are arranged in a $L1_2$ structure (Paulonis et al., 1969; Worthem et al., 1990). The lattice parameter a for the γ' compound face-centered cubic (FCC) crystal structure is 0.3605 nm (Wlodek and Field, 1994). The alloy retains its strength at up to 650 °C primarily due to metastable γ". The chemical composition of the γ" precipitate is Ni_3Nb. These precipitates are disk shaped, wherein the atoms are arranged in a $D0_{22}$ structure (Paulonis et al., 1969; Worthem et al., 1990). The diameter of the disks is 20-30 nm, while their thickness is 5-6 nm, when the material is heat treated according to AMS 5663 (Kalh et al.; Worthem et al., 1990; Xiao et al., 2005; Xie et al., 2005b). The values of lattice parameters a and c for the γ" body-centered tetragonal (BCT) compound are 0.3624 nm and 0.7406 nm, respectively (Brown and Muzyka, 1987; Hinojos et al., 2016; Paulonis et al., 1969). Additionally, the alloy typically contains a small, less than one weight

percent, fraction of coherent δ precipitates (Wang and Li, 2004). The composition of the δ phase is also Ni_3Nb but the structure is orthorhombic with the following lattice constants a = 0.5114, b = 0.4244 nm, and c = 0.4538 nm (Dehmas et al., 2011; Fang et al., 1992). The metastable γ" decomposes into the stable Ni_3Nb δ phase at very long aging times, which could be met in service.

The plastic deformation response, including flow stress, hardening rate, tension-compression asymmetry and temperature dependence of Ni-based superalloys depends on the precipitate volume fraction and morphologies. Plasticity of the γ matrix is primarily carried by twelve octahedral $\{111\}\langle 1\bar{1}0\rangle$ glide systems, although activity of the six cubic $\{001\}\langle 110\rangle$ glide systems has also been reported (Ding et al., 2004; Haddou et al., 2004; Österle et al., 2000). Generally, the γ' and γ" precipitates are the primary strengtheners. Dislocations gliding on octahedral planes shear the γ' and γ" precipitates, since they are very small, nanoparticles, much smaller than the critical radius above which a dislocation would instead loop around the particle. When a dislocation shears through an ordered γ′ or γ" precipitate, it leaves an anti-phase boundary (APB) behind, which increases the energy of the crystal (Gleiter and Hornbogen, 1968; Huther and Reppich, 1978; Maciejewski et al., 2013). The APB values can affect the slip system selection. The APB energy for the cubic planes tends to be lower than that for the octahedral planes (Umakoshi et al., 1984) and hence, screw dislocations would tend to cross slip onto the $\{001\}$ planes. In contrast to γ′ or γ" strengtheners, the δ precipitates are known to deteriorate mechanical properties, unless they appear as spherical δ precipitates at grain boundaries, in which case they can prevent grain boundary sliding and improve the material's creep behavior (Davis, 1997; Ghosh et al., 2008).

Ni-based superalloys containing a large fraction of γ' are known to exhibit a pronounced tension-compression (T-C) asymmetry (Copley and Kear, 1967a, b; Keshavarz and Ghosh, 2015). [001] γ' single crystals show a higher yield stress in tension than in compression and the [011] γ' single crystals show a higher yield stress in compression than in tension. It has been proposed that the origin of the T-C asymmetry is, in part, due to the non-planar core structure of the screw dislocations and

hence influenced by the Non-Schmid (NS) effects on the glide of screw dislocations on the {111} planes. According to the Schmid law, dislocation glide activates when the stress tensor projected onto the glide plane in its glide direction reaches a value of slip resistance (Schmid and Boas, 1950). According to the NS law, dislocation glide results not only from the resolved shear stress along the direction of slip (Schmid law) but also from shear stresses resolved along directions orthogonal to the slip direction as well as the three normal stress components (Dao and Asaro, 1993). NS effects have been observed for every γ' crystal orientation tested in the literature, thus far, with exception of the [111] orientation, where the cubic slip has the highest Schmid factor and found to dominate even at room temperature (Lall et al., 1979). Complex deformation characteristics of Ni-based superalloys are also attributed to the formation of Kear-Wilsdorf (KW) locks, which accompany the shearing large γ′ and γ" precipitates by dislocation glide (Hirsch, 2003; Veyssieìre and Saada, 1996). The KW locks are pinned segments of dislocations that are created when they cross slip from octahedral planes in the γ matrix to cubic planes within γ' and γ" and then transitions back onto octahedral planes. It has been found that the frequency of KW locks as well as the activity of cubic slip increases with temperature (Paidar et al., 1984). With more cross-slip activity with increasing temperature, KW lock formation is promoted, resulting in more obstacles for mobile dislocations and enhanced hardening.

Linking these mechanisms to mechanical behavior is possible with microstructure based constitutive laws. For superalloys, many of these modeling efforts have used polycrystalline plasticity schemes such as finite element and self-consistent (Francis et al., 2014; Keshavarz and Ghosh, 2015; Shenoy et al., 2008). Further, to account for both contributions from elasticity and plasticity, the particular elasto-plastic self-consistent (EPSC) mean-field homogenization (Neil et al., 2010; Turner and Tomé, 1994) is appropriate. In EPSC, a polycrystal is treated as a collection of single crystals each having a specific orientation, a volume fraction, and an ellipsoidal shape. Each ellipsoidal representative grain orientation is treated as an elasto-plastic inclusion in the homogeneous equivalent medium (HEM), which would have average properties of the polycrystal. A self-consistent scheme is used to relate the

deformation of the polycrystal to the deformation of grain. Recently, EPSC has been used to model Ni-based superalloys (Francis et al., 2014). The model with a phenomenological Voce-type hardening successfully interpreted the elastic lattice strain data gained from a neutron diffraction experiment concluding that the γ and γ′ deform jointly in the fine γ′ microstructure, but not in the medium and coarse γ′. However, no effort was made to incorporate the shearing of precipitates effect into hardening nor backstress and non-Schmid effects were considered. Later, another version of EPSC was developed for predicting the behavior of metals under cyclic deformation (Zecevic et al., 2016). The model incorporated an updated hardening law that explicitly evolves a set of dislocation densities. The hardening law connected inter-granular and slip system backstresses to the annihilation and reverse glide of certain populations of dislocations, enabling the prediction of non-linear unloading, the Bauschinger effect upon reloading in the reverse direction, and the hardening rate under further reversal strains. The model, however, was not used for modeling of materials requiring the consideration of precipitates and their effects on dislocation motion and backstress generation.

The objective of this article is to present an advancement of the EPSC model to account for the effects of precipitates, in particular the APB formation due to precipitate shearing and backstress. The model, called P-EPSC, is applied to an IN718 Ni-based superalloy that has been fabricated using the direct metal laser sintering process (DMLS), which is an additive manufacturing (AM) process. The KW locks are unlikely to form in IN718 due to the size of the precipitates but the model is sufficiently flexible to incorporate the effect through the latent hardening matrix, which is considered by the model. Previously reported room temperature tension and compression tests are used to calibrate and validate the model (Smith et al., 2016). Additionally, we performed, also at room temperature, experimental large strain load reversal tests and carry out the analogous simulations with the model to establish a baskstress and reversible dislocation glide parameters. We show that the model predicts the dependence of the mechanical behavior for samples built in different directions, an anisotropy stemming primarily from the texture and grain structure elongated in the build direction. The

measurements and calculations suggest that as the pre-strain increases, the backstresses increase causing the non-linearity of unloading to increase. It is also found that the intra- and inter-granular stresses govern the Bauschinger effect while reversible dislocation motion plays a major role in hardening during reverse loading. Although we only investigate room temperature deformation in this work, the formulation can be extended to elevated temperatures. The microstructure, constituents, and behavior of AM IN718 are similar to those of wrought IN718 as well as other Ni-based superalloys, and therefore, the microstructure-sensitive model developed here can be generalized to a broad range of alloys.

2. Material

2.1 Additive manufacturing

The samples of IN718 have been fabricated using the direct metal laser sintering process (DMLS) as defined in ASTM F2792-12a (2012b). The powder for use in the EOS M280 DMLS machine were produced by gas atomization and the final particle sizes had an average diameter of 35μm, and a range of <1μm to 80μm. The chemical composition of the powder was (wt%) 55.5 Ni, 18.2 Cr, 5.5 Nb, 3.3 Mo, 1.0 Co, 0.35 Si, 0.35 Mn, 0.3 Cu, 1.15 Ti, 0.3 Al, 0.08 C, 0.015 P, 0.015S, 0.006 B, and balance Fe, meeting the chemical composition of the IN718 standard. The material was printed in the form of bars and rods, which were subsequently machines into the samples for testing. The samples were finally heat treated according to AMS 5663. This heat treatment results in an optimized structure which contains a high fraction of γ' and γ" phases and a lower fraction of δ phase (Kuo et al., 2009; Wang and Li, 2004). The volume fraction of γ' and γ" phases in the material studied here will be presented later in Table 4.

2.2 Microstructure

Samples before and after deformation were prepared for EBSD by sectioning along and perpendicular to the loading direction. Automated grinding and polishing procedures were used to prepare the sections for characterization. These grinding methods employed a series of SiC grinding papers ranging from 120 grit to 1200 grit. The samples were then polished on a cloth using steps of 6 μm and 0.25 μm diamond polishing compound. At this stage, the samples have been etched for 10-15 s. The solution for etching contained 25 mL deionized water, 20 mL hydrochloric acid (HCl), and 5 milliliter hydrogen peroxide (30%) (H_2O_2). Final polish was done by 0.02 μm colloidal silica suspension.

The automated electron backscattered diffraction (EBSD) data collection was performed using the Pegasus system (Octane Plus SDD detector and Hikari High Speed Camera) attached to a Tescan Lyra (Ga) field emission scanning electron microscope (SEM) at a voltage of 20 kV. The EBSD scans ran over sufficiently large areas to obtain representative texture measurement, at a working distance of 9 mm and spot size of 56.0 nm, with a 1 μm step size.

Figure 1a shows an EBSD orientation map to depict the initial grain structure of the alloy. The microstructure exhibits columnar grains with average major axis a = 65.93 μm and minor axis b = 13.16 μm resulting with a ratio of approximately 5. The average grain size in the material is approximately 45 μm. The directional columnar grain structure is a consequence of the heat flow direction during solidification of DMLS molten pool, which was roughly perpendicular to the surface of substrate or the pre-deposited layers.

To obtain information about the initial crystallographic texture in the material, multiple EBSD scans were collected over an area of several square millimeters. Figure 1b shows the corresponding pole figures. The measurement finds that the samples possessed a moderately intense <001> texture component along the build direction (BD), with multiples of random distribution intensity approaching 3.

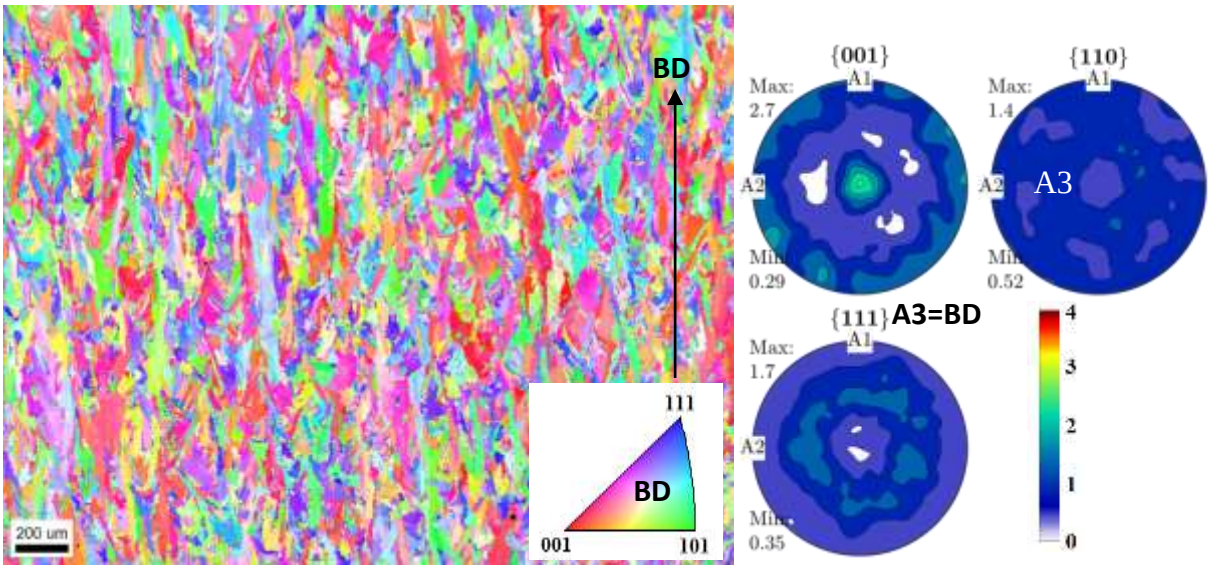

Figure 1. Inverse pole figure (IPF) map showing microstructure in IN718 made by DMLS after heat treatment. The colors in the maps indicate the orientation of the built direction (aligned with the axis of vertically built samples) with respect to the crystal reference frame according to the IPF triangle. On the right are pole figures showing the corresponding texture. (For interpretation of the references to colour in this figure legend, the reader is referred to the web version of this article.)

2.3 Mechanical testing

For calibration and verification of the model, we characterize the plastic anisotropy, T-C asymmetry, and the cyclic, tension-compression response to large strains for the IN718 alloy. The material was tested in tension using flat dog-bone samples and in compression using cylinders deposited in three orientations with respect to BD (figure 2a): vertical (V), diagonal at 45° (D), and horizontal (H) in earlier studies (Gribbin et al., 2016; Smith et al., 2016). The tensile test samples were machined using a CNC machine according to the ASTM E8 (2015) standard with a gauge section of 25 mm in length and cross-sectional geometry of 6 × 3 mm. The compression test samples were machined as right cylinders 6 mm in diameter and 8 mm in height. Note that machining reduces the surface roughness created by AM. The average roughness was measured to be approximately 0.9 μm finish.

The specimens for load reversal tests to large strains were designed according to the ASTM E606 (2012a) standard. We only modified the grip section in order to fit into the existing flat hydraulic grips. The gage section remained 14 mm long and 6.35 mm in diameter according to the standard.

Samples were prepared in two orientations with respect to the BD: D and H (figure 2b). These samples were also machined to the average roughness of surfaces of approximately 0.9 μm finish. After machining all specimens were heat treated per AMS 5663.

Cyclic loading at room temperature was carried out on an MTS Landmark 370 tension/compression servohydraulic-testing machine with a controller and Flextest software. In this machine, samples were clamped with hydraulic grips. The nominal strain rate of the tests was 10^{-3} s^{-1}. During the tests, actuator load and displacement and average strain over a 25 mm gage length, acquired with an MTS 623.12E-24 extensometer, were recorded.

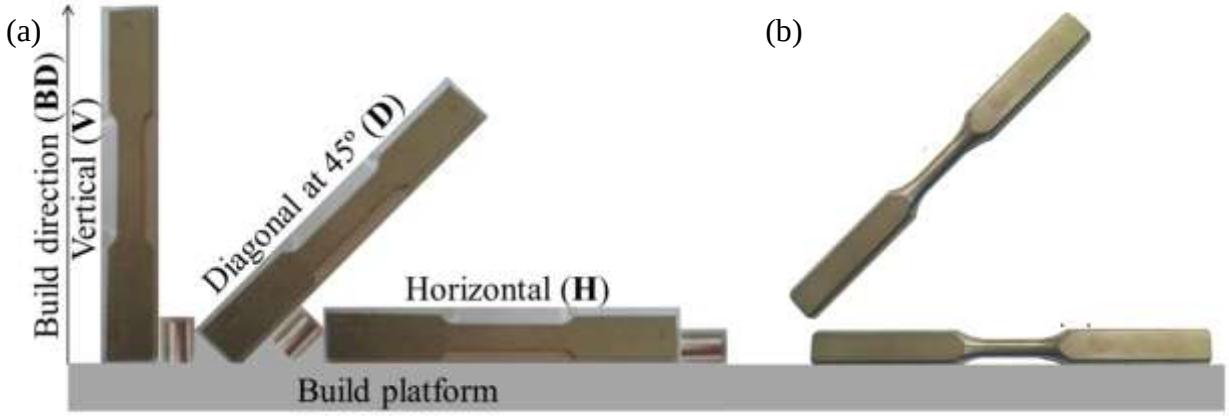

Figure 2. Orientation of ASTM E8 tensile bars and compression samples with respect to the BD. (b) Orientation of ASTM E606 samples used for cyclic loading with respect to the BD. The loading direction (LD) is coincident with the sample orientation in both (a) and (b).

2.4 Stress-strain response

To test for tension-compression asymmetry in flow behavior, the samples were tested separately in compression and in tension. Due to the moderate texture and elongated grain structure along the BD, both tension and compression tests were repeated for the V, D, and H samples to assess anisotropy. Figure 3 presents the measured compressive and tensile true stress–true strain responses of DMLS heat-treated material for the three builds. Multiple samples (at least five samples) were tested for every direction and the results were repeatable to less than 3% difference. We observe that all curves

exhibit a classical decreasing hardening rate throughout, a signature of the slip-dominated plastic deformation. Samples in all build directions exhibited significant T-C asymmetry. The T-C asymmetry did not depend on build direction; the tensile flow stresses are lower than the compression flow stresses in all cases. Table 1 shows yield stress for all six monotonic tests. In both tension and compression, the flow stress is found to depend on the loading direction with respect to the build direction. The material built in the H and D directions exhibited similar flow stresses and were higher than those tested in the V direction.

Table 1. Yield stress [MPa] (0.2% offset) in tension and compression as a function of build direction.

	Vertical	Diagonal	Horizontal
Tension	1215	1305	1290
Compression	1255	1370	1345

Next, the material was tested under large strain cyclic deformation. The samples were first pulled in tension to a given strain level and then unloaded and reloaded in compression until the total strain was zero. Finally, they were reloaded in tension to failure. Figure 4 shows the true stress–true strain curves for the H samples, when the samples are first loaded in tension to strains of either (a) 0.02 or (b) 0.03. Upon unloading, the material exhibits an initial linear portion and a subsequent non-linear portion. The extent of the macroscopically non-linear portion increases with the level of plastic pre-strain. When the material becomes compressed, it yields at a lower value than yield in the tensile pre-strain. After yielding, the hardening rate rapidly increases. The lower yield in reverse loading followed by a rapid hardening rate is characteristic of the Bauschinger effect for many materials (Bauschinger, 1886). The lower yield in the reversal compression path than forward tension path can be attributed to the BE rather than the T-C asymmetry, since as we have seen in figure 3, when tested separately compression would have a higher yield stress than tension.

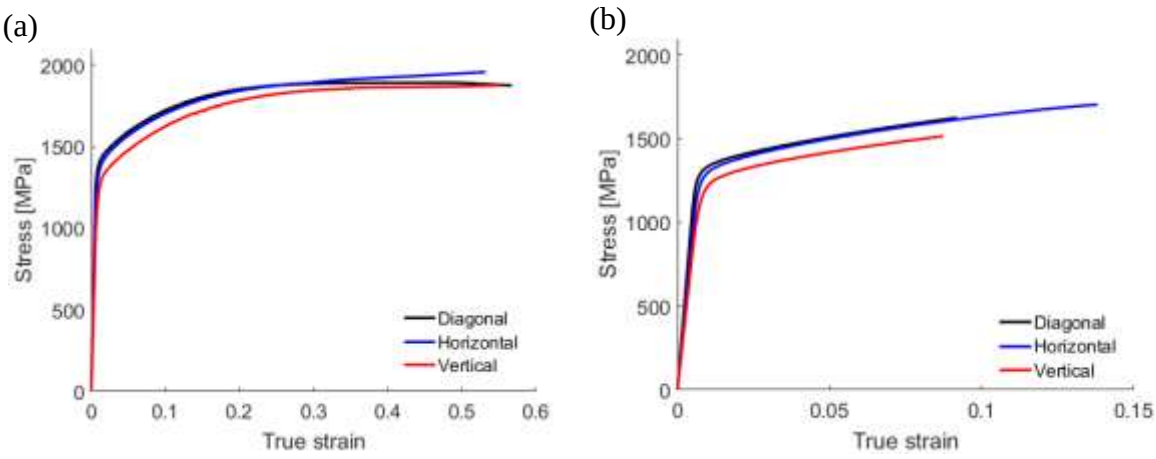

Figure 3. True stress-true strain response of IN718 samples as a function of built direction in (a) compression and (b) tension.

Figure 4c compares the forward-reverse responses for 0.01, 0.02, 0.03, and 0.04 tensile pre-strain. The BE became more pronounced with higher pre-strain. The corresponding normalized strain hardening behavior is shown in figure 4d. The difference between tension vs. compression is clearly evident, where tension is much steeper than compression. Also, the slope is a strong function of pre-strain level. The normalization factor is the shear modulus, μ, taken to be 80GPa (Fukuhara and Sanpei, 1993). The two curves start from the value corresponding to the ratio between Young's modulus and the shear modulus, E/μ (Jahedi et al., 2017; Knezevic et al., 2010). Due to non-linear unloading, the compressive curves are always below E/μ at zero macroscopic stress. The same is true for the tensile reloading curves.

Figure 4e shows that for every forward strain level, the flow stress in reversal (compression) remained below that reached in the forward straining (tension), a behavior referred to as permanent softening. This type of permanent softening after strain reversal was first observed in (Hasegawa et al., 1975) for a polycrystalline Al alloy during tension and compression. This softening was attributed to the annihilation of dislocations (recovery effects) after the reversal of the slip directions during loading in the reverse direction.

A few load reversal tests were repeated for the D samples. Figure 5 shows that the behavior is similar to the H sample response when first tension tested to 0.02. The BE is slightly smaller in the sense that the difference in yield stress between the forward and reverse load paths is smaller for the D sample than the H sample.

3. Crystal plasticity model

A polycrystal model, called P-EPSC, is developed here in order to provide a microstructure-based constitutive law for IN718, one that can give insight into the microstructural origin of the observed deformation behavior: tension-compression asymmetry, anisotropy with respect to build direction, non-linear unloading, the BE, and the change in strain hardening rate during strain reversals. The model is based on a polycrystalline EPSC formulation originally developed in (Turner and Tomé, 1994) and later extensions (Lentz et al., 2015a; Lentz et al., 2015b; Neil et al., 2010; Zecevic et al., 2017; Zecevic and Knezevic, 2017; Zecevic et al., 2015). Here we adopt a recently presented version of the EPSC model for cyclic loading (Zecevic and Knezevic, 2015), which integrates a hardening law based on evolution of dislocation density and slip system backstresses and further extend it to materials containing precipitates, such as IN718. In this new development, the effect of intermetallic APB is treated as well as the backstresses are due to not only grain-to-grain interactions within a single-phase, as before, but also from the precipitates. Note that the modeling approach does not explicitly model the precipitates but accounts for them in a homogenized way. This is a reasonable assumption since their size is orders of magnitude smaller than the grain size and their shape and distributions are not highly oriented. The modeling framework is described in the next section.

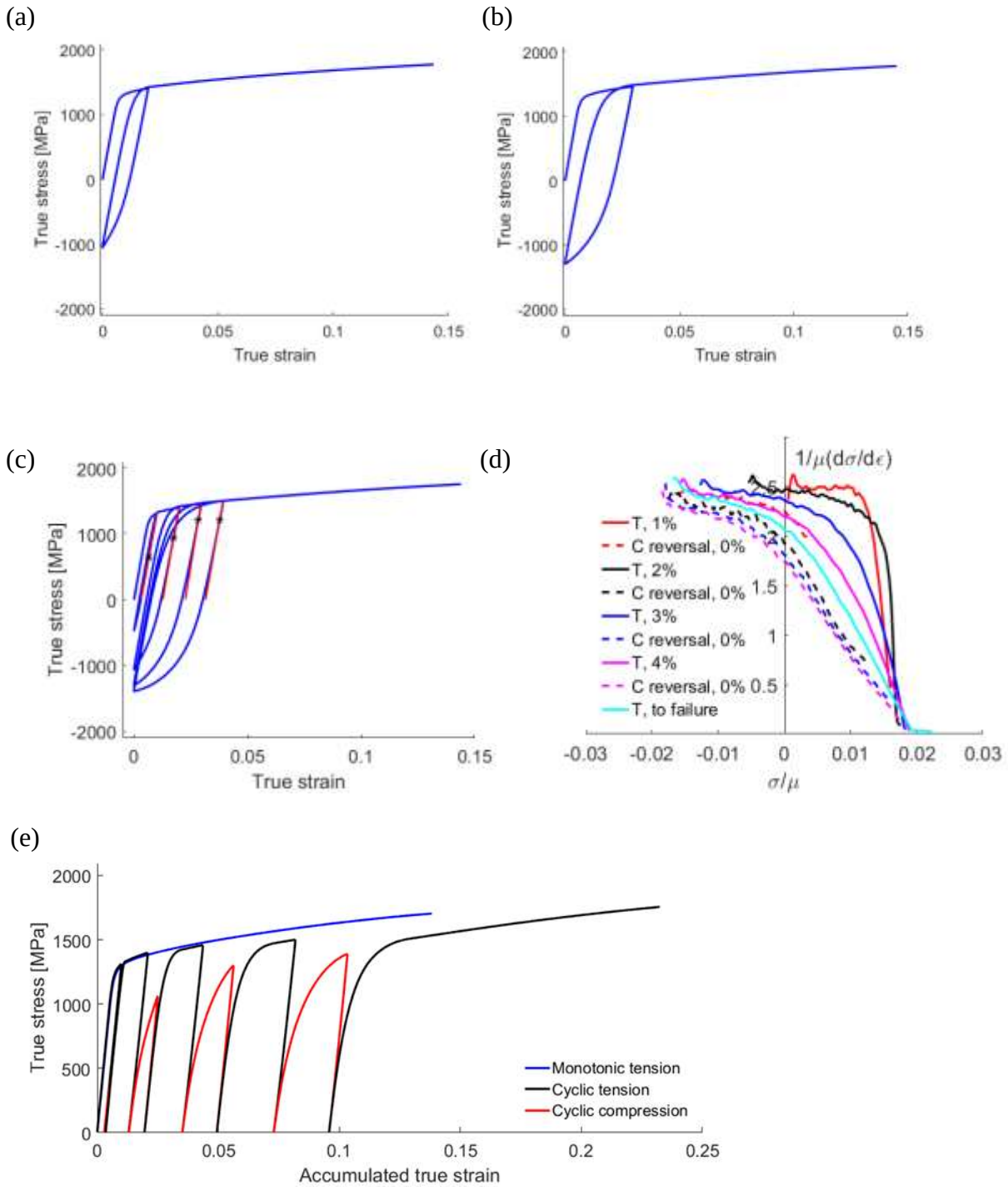

Figure 4. True stress-true strain response of IN718 samples built horizontally under single tension-compression cycle pre-strained in tension to (a) 0.02 and (b) 0.03 and then pulled to failure, and multiple tension-compression cycles pre-strained in tension to (c) 0.01, 0.02, 0.03, and 0.04 and then pulled to failure. Macro-yield points in compression at approximately 0.005 offset are indicated. (d) Strain hardening rates corresponding to (c). (e) True stress-true strain curve shown in (c) as a function of accumulated true strain showing drops in yield stress upon load reversal and permanent softening during subsequent straining.

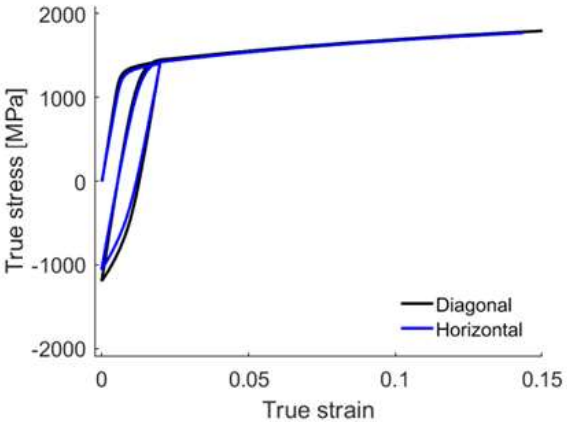

Figure 5. Comparison of true stress-true strain response of IN718 samples built horizontally and at 45° under single tension-compression cycle pre-strained in tension to a strain of 0.02 and then pulled to failure.

In EPSC, a polycrystal is represented by a set of grains with each having an orientation, shape, and a volume fraction. Each grain is treated as an elasto-plastic inclusion embedded in a homogeneous effective medium (HEM). Individual grains do not interact explicitly with each other but only with HEM (Lipinski and Berveiller, 1989).The elementary inclusion problem is solved using a Green's function approach. Enforcing the macro-homogeneity condition of self-consistency between the macroscopic stress and grain average stresses allows for calculation of the elasto-plastic properties of the effective medium. The HEM response corresponds to that of the polycrystal and is to be compared with that of the tested sample."

In the description below, we use "·" to represent a contracted or dot product and "⊗" for uncontracted or tensor product.

The macroscopic Jaumann stress rate and strain rate are linked through the following linear relationship:

$$\hat{\boldsymbol{\sigma}} = \mathbf{L}\dot{\boldsymbol{\varepsilon}}, \qquad (1)$$

where $\mathbf{L}$ is the instantaneous elasto-plastic stiffness tensor of the polycrystal, which at the outset is unknown and must be solved iteratively through the standard self-consistent procedure (Turner and Tomé, 1994) until equilibrium and strain compatibility are satisfied (Eshelby, 1957). The strain rate in the individual crystals is related to the macroscopic strain rate via

$$\dot{\boldsymbol{\varepsilon}}^{c} = \mathbf{A}^{c}\dot{\boldsymbol{\varepsilon}}, \tag{2}$$

where $\mathbf{A}^{c} = \left(\mathbf{L}^{c} + \mathbf{L}^{c^{*}}\right)^{-1}\left(\mathbf{L}^{c^{*}} + \mathbf{L}\right)$ is the localization tensor for elasto-plastic ellipsoidal inclusion, $\mathbf{L}^{c}$ is the instantaneous single crystal, c, elasto-plastic stiffness tensor, and $\mathbf{L}^{c^{*}} = \mathbf{L}\left(\mathbf{S}^{c^{-1}} - \mathbf{I}\right)$ is the effective stiffness tensor. The latter relates the stress and total strain rate in a grain to the stress and total strain rate in the macroscopic medium through an interaction equation, given by $(\hat{\boldsymbol{\sigma}}^{c} - \hat{\boldsymbol{\sigma}}) = -\mathbf{L}^{c^{*}}(\dot{\boldsymbol{\varepsilon}}^{c} - \dot{\boldsymbol{\varepsilon}})$, and it contains the $\mathbf{S}^{c}$, which is the symmetric Eshelby tensor and $\mathbf{I}$ is the fourth rank identity matrix.

Next the condition that the polycrystal stress and strain rate is equal to the volume average of the stress and strain rate in grains is enforced:

$$\hat{\boldsymbol{\sigma}} = \langle\hat{\boldsymbol{\sigma}}^{c}\rangle, \tag{3}$$

and

$$\dot{\boldsymbol{\varepsilon}} = \langle\dot{\boldsymbol{\varepsilon}}^{c}\rangle, \tag{4}$$

which provides an expression for L:

$$\mathbf{L} = \langle\mathbf{L}^{c}\mathbf{A}^{c}\rangle\langle\mathbf{A}^{c}\rangle^{-1}. \tag{5}$$

Last, to calculate the macroscopic Cauchy stress, we recall the relationship between the Cauchy stress rate and Jaumann rate given by $\dot{\boldsymbol{\sigma}} = \hat{\boldsymbol{\sigma}} + \langle\mathbf{W}^{c}\boldsymbol{\sigma}^{c}\rangle - \langle\boldsymbol{\sigma}^{c}\mathbf{W}^{c}\rangle = \mathbf{L}\dot{\boldsymbol{\varepsilon}} + \langle\mathbf{W}^{c}\boldsymbol{\sigma}^{c}\rangle - \langle\boldsymbol{\sigma}^{c}\mathbf{W}^{c}\rangle$, where $\mathbf{W}^{c}$ is the elastic spin of crystal, *c*. The above relationship is integrated explicitly over time, i.e., $\boldsymbol{\sigma}_{n+1} =$

$\boldsymbol{\sigma}_n + \mathbf{L}_n\dot{\boldsymbol{\varepsilon}}_n\Delta t + \langle \mathbf{W}_n^c\boldsymbol{\sigma}_n^c\rangle\Delta t - \langle \boldsymbol{\sigma}_n^c\mathbf{W}_n^c\rangle\Delta t$. With the remaining field variables, such as the elastic spin and strain rate updated at the current increment n, the macroscopic stress can be updated for the next increment n + 1.

The constitutive relationship at the single crystal level between the Jaumann stress rate, $\hat{\boldsymbol{\sigma}}^c$, and the strain rate, $\dot{\boldsymbol{\varepsilon}}^c$, is:

$$\hat{\boldsymbol{\sigma}}^c = \mathbf{C}^c(\dot{\boldsymbol{\varepsilon}}^c - \sum_s \mathbf{m}^{c,s}\dot{\gamma}^{c,s}) - \boldsymbol{\sigma}^c tr(\dot{\boldsymbol{\varepsilon}}^c), \quad (6)$$

where $\mathbf{C}^c$ is the single crystal elastic stiffness tensor and $\sum_s \mathbf{m}^{c,s}\dot{\gamma}^{c,s}$ is the plastic strain rate, which is defined as the sum of shear strain rates, $\dot{\gamma}^{c,s}$, from each slip system, s. The tensor $\mathbf{m}^{c,s} = 0.5(\mathbf{b}^{c,s} \otimes \mathbf{n}^{c,s} + \mathbf{n}^{c,s} \otimes \mathbf{b}^{c,s})$ is the symmetric part of the Schmid tensor for slip system s, and $\mathbf{b}^{c,s}$ and $\mathbf{n}^{c,s}$ are respectively the orthonormal unit vectors representing the slip direction and slip plane normal. To account for changes in orientation due to texture evolution, the elastic stiffness is calculated at the beginning of each deformation increment. The invariant single crystal elastic constants are provided in the next section.

The present formulation incorporates the non-Schmid driving force, where five non-glide stress components: the two shear stresses $\mathbf{t}^{c,s}\otimes\mathbf{b}^{c,s}$ and $\mathbf{t}\otimes\mathbf{n}^{c,s}$, acting normal to the Burgers vector and the three normal stresses $\mathbf{n}^{c,s}\otimes\mathbf{n}^{c,s}$, $\mathbf{t}^{c,s}\otimes\mathbf{t}^{c,s}$, and $\mathbf{b}^{c,s}\otimes\mathbf{b}^{c,s}$, are contained. To include their effects, a non-Schmid tensor $\mathbf{m}_{ns}^s$ has been defined (Dao and Asaro, 1993; Knezevic et al., 2014a; Lim et al., 2013; Savage et al., 2017), as:

$$\mathbf{m}_{ns}^{c,s} = c_1(\mathbf{t}^{c,s}\otimes\mathbf{b}^{c,s}) + c_2(\mathbf{t}^{c,s}\otimes\mathbf{n}^{c,s}) + c_3(\mathbf{n}^{c,s}\otimes\mathbf{n}^{c,s}) + c_4(\mathbf{t}^{c,s}\otimes\mathbf{t}^{c,s}) - (c_3 + c_4)(\mathbf{b}^{c,s}\otimes\mathbf{b}^{c,s}), \quad (7)$$

where the ci are weighting coefficients. Under incompressible flow, only four of these coefficients ci, are independent. The driving force for slip then becomes modified to be:

$$\mathbf{m}^{c,s} \cdot \boldsymbol{\sigma}^c + \mathbf{m}_{ns}^{c,s} \cdot \boldsymbol{\sigma}^c = \mathbf{m}_{tot}^{c,s} \cdot \boldsymbol{\sigma}^c, \tag{8}$$

where $\mathbf{m}_{tot}^{c,s} = \mathbf{m}^{c,s} + \mathbf{m}_{ns}^{c,s}$. If we include that a backstress, $\tau_{bs}^{c,s}$, must be overcome in order for a slip system to activate, then two conditions must be satisfied: first $\mathbf{m}_{tot}^{c,s} \cdot \boldsymbol{\sigma}^c - \tau_{bs}^{c,s} = \tau_c^{c,s}$ and second $\mathbf{m}_{tot}^{c,s} \cdot \hat{\boldsymbol{\sigma}}^c - \dot{\tau}_{bs}^{c,s} = \dot{\tau}_c^{c,s}$, which requires that the stress must remain on the single crystal yield surface. Since these two conditions do not allow for negative shear, each slip system is split into two, having the same plane normal but opposite sense of shearing.

The relationship between the rates of slip resistance, $\dot{\tau}_c^{c,s}$, and the backstress, $\dot{\tau}_{bs}^{c,s}$, are given by the following relations (Zecevic and Knezevic, 2015):

$$\dot{\tau}_c^{c,s} = \sum_{s'} h^{ss'} \dot{\gamma}^{c,s'}, \tag{9a}$$

$$\dot{\tau}_{bs}^{c,s} = \sum_{s'} h_{bs}^{ss'} \dot{\gamma}^{c,s'}, \tag{9b}$$

where $h^{ss'}$ and $h_{bs}^{ss'}$ are the hardening and backstress matrices, respectively. Expressions for $h^{ss'}$ and $h_{bs}^{ss'}$ follow the derivation given in (Zecevic and Knezevic, 2015) and are provided in appendix A.

To get the expression for shear rates, relations (6), (9a) and (9b) are used in condition $\mathbf{m}_{tot}^{c,s} \cdot \hat{\boldsymbol{\sigma}}^c - \dot{\tau}_{bs}^{c,s} = \dot{\tau}_c^{c,s}$:

$$\mathbf{m}_{tot}^{c,s} \cdot \left(\mathbf{C}^c \left(\dot{\boldsymbol{\varepsilon}}^c - \sum_{s'} \mathbf{m}^{c,s'} \dot{\gamma}^{c,s'} \right) - \boldsymbol{\sigma}^c tr(\dot{\boldsymbol{\varepsilon}}^c) \right) = \sum_{s'} h^{ss'} \dot{\gamma}^{c,s'} + \sum_{s'} h_{bs}^{ss'} \dot{\gamma}^{c,s'}. \tag{10}$$

Equation (10) represents a set of scalar linear equations for shear rates, $\dot{\gamma}^{c,s'}$. Performing some algebraic manipulations allows expressing shear rates on active slip systems in terms of strain rate in crystal:

$$\dot{\gamma}^{c,s} = \left(\sum_{s'} \left(X^{ss'} \right)^{-1} \mathbf{m}_{tot}^{c,s'} \left(\mathbf{C}^c - \boldsymbol{\sigma}^c \otimes \mathbf{i} \right) \right) \cdot \dot{\boldsymbol{\varepsilon}}^c \tag{11}$$

where

$$X^{ss'} = h^{ss'} + h_{bs}^{ss'} + \mathbf{C}^c \cdot \mathbf{m}_{tot}^{c,s} \otimes \mathbf{m}^{c,s'}. \tag{12}$$

Finally, we obtain the modulus $\mathbf{L}^c$ consistent with changed loading conditions including non-schmid tensor, which relates the Jaumann rate for a crystal and the strain rate via

$$\widehat{\boldsymbol{\sigma}}^c = \mathbf{L}^c \dot{\boldsymbol{\varepsilon}}^c, \tag{13}$$

as

$$\mathbf{L}^c = \mathbf{C}^c - \mathbf{C}^c \sum_s \mathbf{m}^{c,s} \otimes \left(\sum_{s'} \left(X^{ss'} \right)^{-1} \mathbf{m}_{tot}^{c,s'} \left(\mathbf{C}^c - \boldsymbol{\sigma}^c \otimes \mathbf{i} \right) \right) - \boldsymbol{\sigma}^c \otimes \mathbf{i}, \tag{14}$$

Last, the lattice rotation rate tensor, $\mathbf{W}^c$, is defined as:

$$\mathbf{W}^c = \mathbf{W}^{app} + \mathbf{\Pi}^c - \mathbf{W}^{p,c} \tag{15}$$

where $\mathbf{W}^{app}$ is the applied rotation rate and $\mathbf{W}^{p,c}$ the plastic rotation rate. The plastic rotation rate is calculated from the shearing rates as:

$$\mathbf{W}^{p,c} = \sum_s \mathbf{q}^{c,s} \dot{\gamma}^{c,s} \tag{16}$$

where $\mathbf{q}^{c,s} = 0.5(\mathbf{b}^{c,s} \otimes \mathbf{n}^{c,s} - \mathbf{n}^{c,s} \otimes \mathbf{b}^{c,s})$ is the skew part of the dyadic product of the unit Burgers direction and the slip plane normal. The tensor $\mathbf{\Pi}^c$ arises from the antisymmetric part of the Eshelby tensor (Lebensohn and Tomé, 1993).

3.1 Initial slip resistance

The initial slip resistance is given by the following equation

$$\tau_0^s = \tau_{0,ss}^{\alpha} + \tau_{0,HP}^{s} + \tau_{0,shear}^{\alpha}, \tag{17}$$

where $\tau_{0,ss}^{\alpha}$ represents the contribution due to the solid solution strengthening, $\tau_{0,HP}^{s}$ is the Hall-Petch-like term, and $\tau_{0,shear}^{\alpha}$ is the contribution caused by dislocation shearing of the precipitates.

The theory for multi-component solid-solution hardening is based on a model proposed by Gypen and Deruyttere (Gypen and Deruyttere, 1977), which assumes a superposition of strengthening of

individual solutes that individually have differing potencies. The theory has widely been used for Ni-based superalloys (Kozar et al., 2009; Maciejewski et al., 2013). Because solute spacing is proportional to the square root of the concentration, the resultant strengthening is given by

$$\tau_{0,ss}^{\alpha} = \frac{1}{M}\sum \frac{d\sigma}{d\sqrt{g_i}}\sqrt{g_i} \quad (18)$$

where M is the Taylor factor, g is the atomic fraction, and $\frac{d\sigma}{d\sqrt{g_i}}$ is the strengthening coefficient of the solute elements in IN718, which are taken from (Roth et al., 1997). The strengthening coefficient reflects the strengthening potency of each alloying element and represents the strain induced in the lattice. For both cubic and octahedral slip systems the value of $\tau_{0,ss}^{\alpha}$ was estimated to be 263.2 MPa.

The Hall-Petch-like term follows the equation (Beyerlein and Tomé, 2008)

$$\tau_{0,HP}^{s} = \frac{H^{\alpha}\mu_{\mathrm{IN718}}^{\alpha}\sqrt{b^{\alpha}}}{\sqrt{d_{mfp}^{s}}}, \quad (19)$$

where H^{α}, b^{α}, d_{mfp}^{s}, and $\mu_{\mathrm{IN718}}^{\alpha}$ are the Hall-Petch coefficient per slip mode, the Burgers vector for the <110> dislocations ($b^{\alpha} = 2.492\ 10^{-10}\ m$), the mean free path for a given slip system s, and the shear modulus of the alloy, respectively. The shear modulus on the slip system is obtained using the single crystal stiffness tensor, as explained later. The effect of grain size strengthening of IN718 has been studied (Zhao et al., 2016). The study reported a Hall-Petch coefficient of 1260 MPa$\sqrt{\mu m}$ for a macroscopic Hall-Petch law at room temperature, which considers only an average grain size. In contrast, Eq. (19) used here considers a dislocation mean free path, d_{mfp}^{s}. Figure 6 shows schematically the advantage of using d_{mfp}^{s} instead of using average grain size for microstructures exhibiting elongated grain morphology, such as those in DMLS IN718 studied here. Given the average values of major a and minor b axis for ellipsoid representing an average shape of initial grain structure, d_{mfp}^{s} can be estimated using

$$d^s_{mfp} = \frac{2}{\sqrt{\left(\frac{\hat{b}^s_x}{a}\right)^2 + \left(\frac{\hat{b}^s_y}{b}\right)^2 + \left(\frac{\hat{b}^s_z}{c}\right)^2}}. \quad (20)$$

Note that b = c for the average grain shape shown in figure 6 and $\hat{b}^s_x, \hat{b}^s_y, \hat{b}^s_z$ are components of a unit vector in the Burgers direction expressed in a frame of the ellipsoid. Equation (20) finds the longest possible distance in the Burgers direction given the ellipsoid. It is worth mentioning that unlike the conventional macroscopic law, Eq. (19) accounts for local crystallography as it considers the slip-system shear modulus and the length of Burgers vector per slip mode. As a reference, the Hall-Petch contribution using 1260 MPa$\sqrt{\mu m}$ is 61.4 MPa calculated using an average grain size of d = 45 μm, i.e., $\frac{1260}{M\sqrt{d}}$, where M is the Taylor factor approximately taken to be 3. The value calculated using Eq. (19) using $H^\alpha = 0.31$ for both cubic and octahedral slip varies but the average over many grains is 67.9 MPa, which is in reasonable agreement with the macroscopic value.

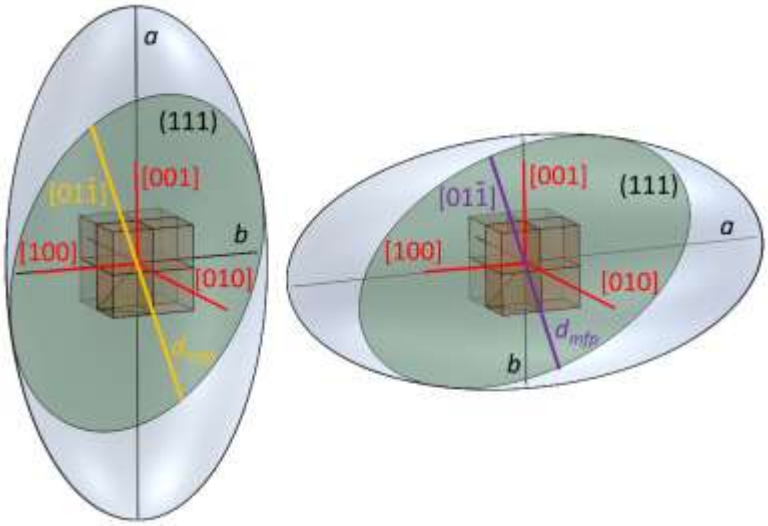

Figure 6. Schematic showing mean free path of a dislocation on (111) plane in $[01\bar{1}]$ direction for a crystal embedded in an ellipsoid oriented with its major axis *a* vertically and in an ellipsoid oriented with its major axis *a* horizontally. These two correspond to grain shape in V and H samples, respectively. The loading axis to activate the defined slip system is vertical in both.

As mentioned earlier, the model considers the moving dislocations to shear the precipitates as opposed to moving around them. In this model, one contribution to the resistance to precipitate shearing is included in the initial slip resistance following (Courtney, 1990; Maciejewski et al., 2013):

$$\tau_{0,shear}^{\alpha} = 0.7\mu_{\gamma'}\left(\frac{\mathrm{APB}_{\gamma'}^{\alpha}}{\mu_{\gamma'}^{\alpha} b_{\gamma'}^{\alpha}}\right)^{\frac{3}{2}}\left(\frac{f_{\gamma'}\bar{r}_{\gamma'}}{b_{\gamma'}^{\alpha}}\right)^{\frac{1}{2}} + 0.7\mu_{\gamma''}\left(\frac{\mathrm{APB}_{\gamma''}^{\alpha}}{\mu_{\gamma''}^{\alpha} b_{\gamma''}^{\alpha}}\right)^{\frac{3}{2}}\left(\frac{f_{\gamma''}\bar{r}_{\gamma''}}{b_{\gamma''}^{\alpha}}\right)^{\frac{1}{2}}, \qquad (21)$$

where f is the volume fraction of the precipitate and $\bar{r}$ is the average radius of the precipitates, γ' and γ". Note that most of the variable in Eq. (21) differ for the octahedral slip and cubic slip modes. The values are provided in next section.

3.2 Anti-phase boundary (APB) energy for slip modes in IN718

In light of the model for slip resistance presented above, it can be appreciated that the APB energies of different slip modes would affect slip activity under deformation. However, to date, APB energies among reported studies vary widely and particularly for γ" precipitates are not as readily available for all the slip modes. Beauchamp et al. (Beauchamp et al., 1987) calculated the value of APB energy of γ' for both cubic and octahedral planes 90 $\frac{mJ}{m^2}$ and 111 $\frac{mJ}{m^2}$, respectively. They performed atomic simulations modifying the potentials which have been introduced by (Paidar et al., 1982; Yamaguchi et al., 1982). Their calculated values were close to those which Douin et al. (Douin et al., 1986) measured employing the weak-beam electron microscopy. Ardell et al. (Ardell and Huang, 1988) performed theoretical analysis to calculate the APB energy of γ' on the {111} planes and reported the value of 161±24 $\frac{mJ}{m^2}$. They used the relationship between the APB energy and the critical diameter of particles in which the shearing to looping transition occurs, <d>max, for their analysis. The value of APB energy for γ' of 140 $\frac{mJ}{m^2}$ has been chosen by (Heilmaier et al., 2001; Maciejewski et al., 2013). Nemoto et al. (Nemoto et al., 1991) estimated 180 $\frac{mJ}{m^2}$ for the APB energy by calculating the leading

and trailing dislocations force balance. Glazer et al. (Glazer and Morris, 1987) calculated the APB energy of γ' precipitates by modifying the CRSS solution of Hanson-Mirris (Hanson and Jr., 1975) which was for a random array of point obstacles. Their solution resulted in a relationship between the APB energy and the minimum looped precipitate diameter and they predicted a value of 102±35 $\frac{mJ}{m^2}$. Kozar et al. (Kozar et al., 2009) used 200 $\frac{mJ}{m^2}$ as the APB energy for tertiary γ' in the IN100, which has approximately the same size as the γ' precipitate in IN718. Due to difficulty in determining the exact value from the literature, they also tried 150 $\frac{mJ}{m^2}$. This is similar to the value of 164 $\frac{mJ}{m^2}$ for the APB energy of γ' used by Wang et al. (Wang et al., 2006) for use in their constitutive model for IN100 alloy at 650 °C. Smallman et al. (Alankar et al.; Beauchamp et al., 1987; Douin et al., 1986; Smallman and Bishop, 1999) performed electron microscopy measurements to investigate the effect of Al fraction on the APB energy varying the aluminum from 23.5% to 26.5%. Increasing the Al content decreased the APB energy from 183±12 $\frac{mJ}{m^2}$ to 175±12 $\frac{mJ}{m^2}$ on the octahedral planes while the changes were from 157±8 $\frac{mJ}{m^2}$ to 113±10 $\frac{mJ}{m^2}$ for the cubic planes. However, another value of 12 $\frac{mJ}{m^2}$ has also been reported in the other literature (Oblak et al., 1974) calculated based on the average fault energy in a region and the associated volume fraction of γ' and γ". Yu et al. (Yu et al., 1994) measured the APB energy of both cubic and octahedral planes in Ni_3Al as a function of temperature and some elements concentrations based on the dislocation pairs separation. They claimed that the APB energy of the octahedral planes is not dependent to the composition or temperature significantly and they reported 170±14 $\frac{mJ}{m^2}$ in the room temperature. The APB energy value for the cubic planes at room temperature was 124±10 $\frac{mJ}{m^2}$. To calculate the APBE of Ni_3Al, Voter et al. (Voter and Chen, 1987) employed the embedded atom method and calculated the values of 83 $\frac{mJ}{m^2}$ and 142 $\frac{mJ}{m^2}$ for cubic and octahedral planes respectively which they claimed is in a good agreement with the measured values of 140±14 $\frac{mJ}{m^2}$ and 180±30 $\frac{mJ}{m^2}$ by Veyssiere et al. (Veyssiere et al., 1985). A similar calculation method was

employed by Foiles et al. (Foiles and Daw, 2011) and the results were 28 $\frac{mJ}{m^2}$ and 96 $\frac{mJ}{m^2}$ for the cubic and octahedral planes respectively. Yoo et al. (Yoo et al., 1994) calculated the values of 140 $\frac{mJ}{m^2}$ and 175 $\frac{mJ}{m^2}$ for the antiphase boundary energy of cubic and octahedral planes at 0 K. Manga et al. (Manga et al., 2015) calculated the APB energy of γ' employing the first-principles calculations and the effects of the APB energy on the Helmholtz free energy and the total Gibbs free energy. In their calculations the APB energy of (111) planes was not dependent to the temperature and changed from 178 $\frac{mJ}{m^2}$ to 183 $\frac{mJ}{m^2}$ when temperature varied from 100 K to 1000 K. However, the cubic planes APB energy was dependent to the temperature and for the same change in the temperature, APB energy dropped from 73 $\frac{mJ}{m^2}$ to just 11 $\frac{mJ}{m^2}$. Unlike the wide ranges of measured and calculated APB energy values for γ', few studies investigated APB energies for γ". We only found 95±17 $\frac{mJ}{m^2}$, which was calculated based on the precipitations kinetics and interfacial energy between the precipitates and the matrix and 296 $\frac{mJ}{m^2}$ considering the average fault energy and make it proportional to the volume fraction of precipitates for an area have been reported (Devaux et al., 2008; Oblak et al., 1974). A table that summarizes values based on a literature of the literature is given in appendix B.

3.3 First-principles calculations of APB energy for slip modes in IN718

Due to the variance in the reports for APB energies and the approaches, the values of the APB energy for the two slip modes within the two γ' and γ" precipitates were calculated using density functional theory (DFT). These values were then used in the initial slip resistance equations described in the previous section. The DFT calculations employed the generalized gradient approximation (GGA) for the exchange correlation functional with the Perdew-Becke-Ernzerhof (PBE) parametrization (Perdew et al., 1996) as implemented in the Vienna Ab initio Simulation Package (VASP) code (Kresse and

Furthmüller, 1996; Kresse and Hafner, 1994). The interaction between the valence electrons and ionic cores is treated using the Projector-Augmented Wave (PAW) potentials (Blöchl, 1994; Kresse and Joubert, 1999). The number of valence electrons in the PAW potentials is 10 for Ni, 3 for Al, 4 for Ti and 13 for Nb. We used a plane wave energy cutoff of 400 eV and optimized the atomic structure until the force on each atom is smaller than 0.01 eV/˚A. For the calculations of the lattice constants of the cubic primitive unit cell, we used a 19 × 19 × 19 Γ-centered Monkhorst Pack (Pack and Monkhorst, 1977) k-point to integrate the Brillouin Zone. The resulting values of lattice constants and elastic constants are given in Table 2. The comparison of energies of different compounds in the $L1_2$ or $D0_{22}$ crystal structures shows that the stable crystal structure for Ni_3Al, Ni_3Ti, and $Ni_3Al_{0.5}Ti_{0.5}$ compounds is $L1_2$ and the stable crystal structure for Ni_3Nb is $D0_{22}$.

Table 2. The calculated lattice constants (in Å) and single crystal elastic constants (in GPa) for different compounds in IN718 in their ground state structure. The Zener ratio is defined as $\left(\frac{2C_{44}}{C_{11}-C_{12}}\right)$ for both the cubic and tetragonal structures (Meyers and Chawla, 1998). The measure single crystal elastic constants for IN718 have been reported to be: $C_{11} = 242.2$ GPa, $C_{12} = 138.9$ GPa, and $C_{44} = 104.2$ GPa (Haldipur, 2006), which are used in our homogenized calculations. The average between Ni_3Al and Ni_3Ti was used in calculations for γ'.

Compounds	a, b, c	C_{11}	C_{12}	C_{44}	C_{33}	C_{13}	C_{66}	Zener ratio
Ni (FCC)	3.508,3.508, 3.508	272.1	169.0	131.0				2.541
Ni_3Al ($L1_2$)	3.562, 3.562, 3.562	243.0	154.8	132.3				3.000
Ni_3Ti ($L1_2$)	3.605, 3.605, 3.605	285.0	151.2	107.4				1.602
$Ni_3Al_{0.5}Ti_{0.5}$ ($L1_2$)	3.593, 3.593, 7.110	273.0	148.0	134.2	264.4	154.5	128.6	2.147
Ni_3Nb ($D0_{22}$)	3.635, 3.635, 7.483	290.6	187.0	114.2	30.9.6	160.7	119.2	2.205

For the APB energy for the Ni-based compound on (100) glide plane, we take a periodic supercell consisting of 48 atoms for both the $L1_2$ and $D0_{22}$ structures, whereas for the (111) glide plane we take

a supercell consisting of 144 atoms for $L1_2$ structure and 72 atoms for $D0_{22}$ structure (see figure 7). Each supercell consists of a 15 Å thick vacuum layer along the direction normal to slip plane.

To calculate the APB for different slip systems, we shift the upper half of the crystal with respect to the lower half of the crystal along the glide direction as shown in figure 7. For Ni based compounds in $L1_2$ and $D0_{22}$ structures, the normalized displacement of 1 along [110] corresponds to the APB structure (figure 8). We minimize the energy of the system by allowing additional relaxation along the x and y directions as described in (Kumar et al., 2017).

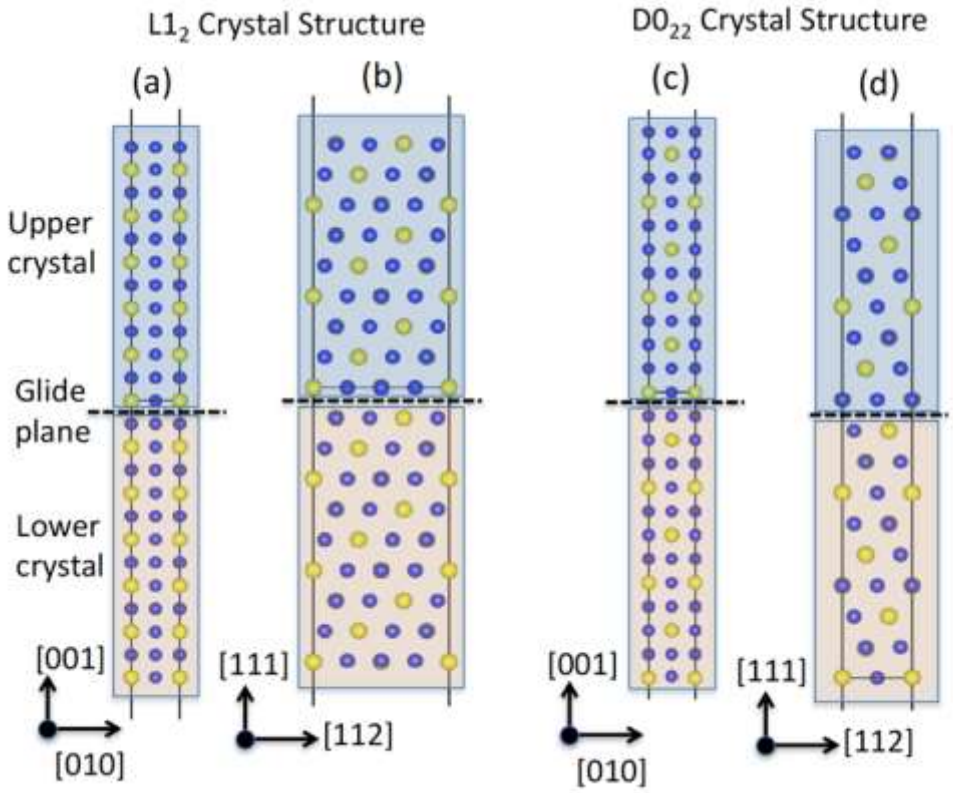

Figure 7. Periodic models used to calculate APB energy for cubic (100) <110>, and octahedral (111) <110> & (111) <112> slip systems in Ni_3Al and Ni_3Ti in the $L1_2$ crystal structure (a) and (b); Ni_3Nb in the $D0_{22}$ crystal structure (c) and (d). The supercell in (a) and (c) contains 48 atoms, and supercell in (b) and (d) contains 144 and 72 atoms respectively. Ni atoms are shown in blue and Al and Nb atoms are shown in yellow.

The DFT calculations APB energies and values of complex stacking fault for these compounds on (100) and (111) plane are summarized in Table 3. Interestingly, the DFT calculations find that the APB configuration on (100) plane for Ni_3Ti is more stable than the perfect $L1_2$ structure (corresponding to x=0), leading to a negative APB energy. In other words, the APB structure is more favorable than the bulk reference state use. Last, we point out that one interesting result from these calculations is that Ti lowers the APB energy for cubic slip, implying that more Ti could promote cubic slip.

Table 3. The anti-phase boundary (APB) energies (in mJ/m^2) for (100) and (111) glide planes and the complex stacking fault (CSF) energy corresponding to fault energy at 0.33 displacement along (112) direction on (111) plane in the Ni based compounds. To calculate the APB energies, we fully relax all the atoms in the APB configuration, however, to calculate the CSF energy we do not relax atom along the glide directions.

Compounds	APB Energy at (100) plane	APB Energy at (111) pane	CSF Energy at (111) plane
Ni (FCC)	-	-	123.65
Ni_3Al ($L1_2$)	130.74	188.74	243.4
Ni_3Ti ($L1_2$)	-133.67	245.13	461.72
$Ni_3Al_{0.5}Ti_{0.5}$ ($L1_2$)	448.85	400.86	540.70
Ni_3Nb ($D0_{22}$)	329.93	378.13	-38.54

One of the parameters that directly uses these results is $\tau^{\alpha}_{0,shear}$. The values that result from the DFT calculations is given in Table 4 along with shear modulus, Burgers vector, and volume fraction and size of precipitates. The latter two are taken as averages from measurements reported in the following literature (Brown and Muzyka, 1987; Kalh et al.; Liu et al., 2002; Wang and Li, 2004; Worthem et al., 1990; Xiao et al., 2008; Xie et al., 2005a). Note that the APB energy values for octahedral slip in γ' were appropriately weighted for Al and Ti. The $\tau^{\alpha}_{0,shear}$ values are 302.6 MPa and 177.7 MPa for octahedral and cubic slip respectively. Although $\tau^{\alpha}_{0,shear}$for cubic slip is lower than that for octahedral

based on the APB values, the total initial resistance for cubic slip is much higher than octahedral slip if the cubic slip dislocations are hard to move with a high Peierls barrier and/or drag coefficient. In order to eliminate the activity of cubic slip in IN718, the total initial slip resistance for cubic slip was approximately 1700 MPa. The increase is justified by an additional Peierls barrier contribution to the initial slip resistance, which requires further investigation and data at elevated temperatures.

3.4 Hardening

In this section, we present a description of hardening on individual slip systems in IN718. We use the Greek superscript α to denote slip modes and let superscripts *s*, *s'* span over the individual slip systems belonging to a mode α. The sense of slip that is positive *s*+ and negative *s*- directions are arbitrarily chosen.

Table 4. Calculated, geometric, and microstructure parameters used for calculation of $\tau_{0,shear}^{\alpha}$, Eq. (21), for octahedral, 1, and cubic, 2, slip systems.

	APB^1 $[\frac{mJ}{m^2}]$	APB^2 $[\frac{mJ}{m^2}]$	μ^1 [GPa]	μ^2 [GPa]	b^α [nm] $\frac{a}{2}\langle 110\rangle$	f [%]	$\bar{r}$ [nm]
γ'	207	130.7	78.2	115.6	0.254912	3.9	12.5
γ''	378.1	329.9	72.6	114.2	0.256255	10	5.85

First, the evolution of slip resistance from its initial value is defined as (Ardeljan et al., 2014; Ardeljan et al., 2016; Ardeljan et al., 2015; Jahedi et al., 2015; Knezevic et al., 2012a; Knezevic et al., 2015; Knezevic et al., 2016):

$$\tau_c^s = \tau_0^\alpha + \tau_{forest}^s + \tau_{debris}^\alpha, \qquad (22)$$

where τ_{forest}^s is a forest term for the statistically stored dislocations and τ_{debris}^α is a debris term for dislocations stored as debris from incomplete recovery reactions. The former evolves with stored forest dislocations according to a Taylor-type relation, which includes the latent hardening term (Kitayama et al., 2013):

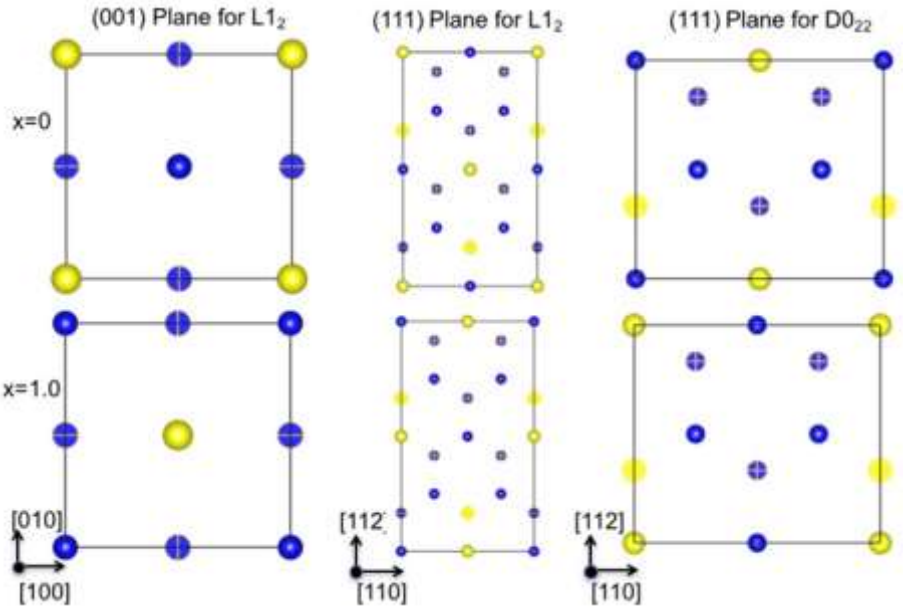

Figure 8. Top view of the atomic structure of one layer from upper crystal and one layer from the lower crystal near the glide plane corresponding to normalized displacement x=0 (upper panels) and x=1.0 (lower panes). The atoms in the lower layer are shown by + symbol.

$$\tau_{forest}^{s} = b^{\alpha}\chi\mu_{\mathrm{IN718}}^{\alpha}\sqrt{\sum_{s'} L^{ss'}\rho_{tot}^{s'}}, \qquad (23)$$

where $\chi = 0.9$ is a dislocation interaction constant, ρ_{tot}^{s} is the total forest dislocation density for sth slip system ($s \in \alpha$) and $L^{ss'}$ is a latent hardening interaction matrix. The slip system shear modulus is calculated using $\mu_{\mathrm{IN718}}^{\alpha} = m_{ij}^{\alpha}C_{ijkl}m_{kl}^{\alpha}$, where m_{ij}^{α} is a Schmid tensor of an arbitrary slip system belonging to mode α and C_{ijkl} is the single crystal stiffness tensor. Since all slip systems within one mode are crystallographically equivalent, shear modulus is the same for all slip systems within one mode. $\mu_{\mathrm{IN718}}^{\alpha}$ is calculated based on the IN718 single crystal constants: μ_{IN718}^{1} = 69.3 GPa and μ_{IN718}^{2} = 118 GPa.

The formation of KW locks has been linked to the anomalous yield stress dependence on temperature (a higher yield stress at elevated than at room temperature). Two scenarios for the cross-slip process involved in the formation of KW locks have been discussed in the literature, one involving

superpartial dislocations and another involving Shockley partial (Keshavarz and Ghosh, 2015). In the former case, a leading superpartial cross slips from the {111} onto a {001} plane for some distance and then cross slips back onto a {111} plane. It moves onto the {111} plane until the trailing superpartial meets the cross-slipped {001} plane. At this point motion on the {111} plane stops forming the KW lock. In the latter case, the superpartials would additionally dissociate and split into two Shockley partials creating a complex stacking fault gliding in the <112> direction and then cross slips onto the {001}. In order for the individual Shockley partials to cross slip they must constrict before cross slipping on the {001} plane. Hence cubic slip activation is promoted when the sense of loading permits the Shockley partials to constrict for cross slip. If the sense of loading is reversed, the Shockley partials expand, hindering cross slip and, thus, formation of KW locks. The resolved shear stress needed to constrict the Shockley partials for the cross slip is asymmetric and hence can potentially explain the T-C asymmetry.

Latent hardening is a way of modeling dislocation interactions as well as representing the effect of KW locks on cross slip propensity, promoting cross slip in one direction (and hence leading to more cubic slip) but not the other (hence leading to less cubic slip). However, dislocation mechanisms in the IN718 alloy are not expected to form KW locks like in other Ni-based superalloys because of small size of the precipitate. Thus, the latent hardening will only be modeled for octahedral slip dislocation interactions. The octahedral-to-cubic interaction coefficients will not be characterized because of no activity of cubic slip at room temperature. Future research involving high temperature data and will characterize these. It would be expected that a cubic-to-octahedral coefficient will harden octahedral slip more in compression than in tension to promote cubic slip activity in compression, which would result in higher flow stress in compression than in tension.

The latter term is related to the dislocation debris via an extended Taylor-type relation (Madec et al., 2003):

$$\tau^{\alpha}_{debris} = k_{deb}\mu^{\alpha}_{\mathrm{IN718}} b^{\alpha}\sqrt{\rho_{deb}}\, log\left(\frac{1}{b^{\alpha}\sqrt{\rho_{deb}}}\right), \quad (24)$$

where $k_{deb} = 0.086$ is a material independent constant that recovers the Taylor law i.e., Eq. (23) for low values of dislocation density and ρ_{deb} is the density of dislocations stored as debris.

Hardening of slip systems is based on the thermodynamics of dislocation storage, stored either as forest dislocations or debris. Here, we adapt the evolution laws presented in (Zecevic and Knezevic, 2015) to simulate hardening during strain path changes of IN718. The model introduces a reversible dislocation density that is accumulated in forward loading and represents the fraction of dislocations available to move in reverse loading. Recall that each slip system is split into a s^+ and s^- system sharing the same slip plane but opposing directions. In this case, the total dislocation density on each slip system is written as the following sum:

$$\rho^{s}_{tot} = \rho^{s}_{for} + \rho^{s^+}_{rev} + \rho^{s^-}_{rev}, \quad (25)$$

where ρ^{s}_{for} is the forward dislocation density common to both directions s+ and s- follows the following law (Kocks and Mecking, 1981):

$$\frac{\partial \rho^{s}_{for}}{\partial \gamma^{s}} = (1-p)k^{\alpha}_{1}\sqrt{\rho^{s}_{tot}} - k^{\alpha}_{2}(\dot{\varepsilon}, T)\rho^{s}_{for}, \quad (26)$$

where k^{α}_{1} is a coefficient accounting for the rate of generation of statistically stored dislocations, k^{α}_{2} is a rate-sensitive coefficient for dynamic recovery (Beyerlein and Tomé, 2008), and p is a reversibility parameter having value between 0 and 1.

The $\rho^{s^+}_{rev}$ and $\rho^{s^-}_{rev}$ are the reversible dislocation densities respectively associated with the s+ and s- directions. They depend on the previous strain history and shearing direction. The p parameter divides the increment in total stored dislocation density into a forward ($(1-p)k^{\alpha}_{1}\sqrt{\rho^{s}_{tot}}\, d\gamma^{s}$) and a reversible ($pk^{\alpha}_{1}\sqrt{\rho^{s}_{tot}}\, d\gamma^{s}$). The evolution of ρ^{s}_{for} is independent of the direction of shear strain per

slip system. The remaining increment in total dislocation density ($pk_1^\alpha\sqrt{\rho_{tot}^s}\,d\gamma^s$) is stored as reversible dislocation density depending on shear direction on slip system, that is,

(If $d\gamma^{s^+} > 0$)

$$\frac{\partial \rho_{rev}^{s^+}}{\partial \gamma^s} = pk_1^\alpha\sqrt{\rho_{tot}^s} - k_2^\alpha(\dot{\varepsilon},T)\rho_{rev}^{s^+}, \tag{27}$$

$$\frac{\partial \rho_{rev}^{s^-}}{\partial \gamma^s} = -k_1^\alpha\sqrt{\rho_{tot}^s}\left(\frac{\rho_{rev}^{s^-}}{\rho_0^s}\right)^m, \tag{28}$$

where the parameter m controls the rate of dislocation recombination and here is set to 0.5 (Wen et al.). The density ρ_0^s is the total dislocation density at the moment the shear on the sth slip system is reversed (Kitayama et al., 2013).

If $d\gamma^{s-} > 0$, the increments in $\rho_{rev}^{s^-}$ and $\rho_{rev}^{s^+}$ evolve in analogous manner to that presented in Eqs. (27) and (28), respectively. The initial conditions for the presented dislocation density evolution laws are: $\rho_{for}^s(\gamma^s = 0) = \rho_{initial}^s$, $\rho_{rev}^{s^+}(\gamma^s = 0) = 0$ and $\rho_{rev}^{s^-}(\gamma^s = 0) = 0$. The initial dislocation density was set to 1.5 10^{12}.

The coefficient k_2^α is calculated using:

$$\frac{k_2^\alpha}{k_1^\alpha} = \frac{\chi b^\alpha}{g^\alpha}\left(1 - \frac{k_B T}{D^\alpha (b^\alpha)^3} ln\left(\frac{\dot{\varepsilon}}{\dot{\varepsilon}_0}\right)\right), \tag{29}$$

where k_B, $\dot{\varepsilon}_0$, g^α and D^α are the Boltzmann constant, a reference strain rate of value 10^7 s^{-1}, an effective activation enthalpy and a drag stress, respectively. Finally, $d\rho_{deb}$ is coupled to the rate of recovery of all active dislocations via:

$$d\rho_{deb} = \sum_s q^\alpha b^\alpha\sqrt{\rho_{deb}}k_2^\alpha(\dot{\varepsilon},T)\rho_{tot}^s d\gamma^s, \tag{30}$$

where q^α is a coefficient that extracts a fraction of α-type dislocations that are not annihilated but become debris. The sum is over both the cubic and octahedral slip systems.

3.5 Evolution of backstress during forward loading

Backstresses are involved in activating slip, via the following condition: $\mathbf{m}_{tot}^{c,s} \cdot \boldsymbol{\sigma}^c - \tau_{bs}^s = \tau_c^s$. Clearly, satisfying this condition is controlled in part by the evolution of the backstresses. During deformation, the backstress on individual slip system will evolve as a function of shear strain on that slip system. We will adopt backstress evolution laws similar to (Beyerlein and Tomé, 2007; Zecevic and Knezevic, 2015), but slightly corrected for use of backstress law for multiple load reversals. In the case of shearing in s+ direction, $d\gamma^{s^+} > 0$, with $\tau_{bs}^{s^+} \geq 0$, the evolution law is:

$$\tau_{bs}^{s^+} = \tau_{bs}^{sat}\left(1 - \exp\left(-\nu\gamma^{s^+}\right)\right), \tag{31}$$

$$\tau_{bs}^{s^-} = -A\tau_{bs}^{s^+}, \tag{32}$$

where backstresses $\tau_{bs}^{s^+}$ and $\tau_{bs}^{s^-}$ act in the two opposite directions, τ_{bs}^{sat} is the saturation value, A and ν are fit parameters and γ^{s^+} is the accumulated shear strain on the sth slip system. The parameter A introduces an asymmetry in the law and takes into account "micro-backstresses" due to pileups (Sritharan and Chandel, 1997). $\tau_{bs}^{s^+}$ acts against the resolved shear stress on s+, i.e. $\mathbf{m}^{s^+} \cdot \boldsymbol{\sigma}^c - \tau_{bs}^{s^+} = \tau_c^s$, while $\tau_{bs}^{s^-}$ acts with the resolved shear stress on the slip system s- according to: $\mathbf{m}^{s^-} \cdot \boldsymbol{\sigma}^c - \tau_{bs}^{s^-} = \tau_c^s$. In this way, the micro plasticity processes responsible for non-linear unloading and the BE are captured.

When the material is reloaded in the opposite direction, slip systems activated during the forward path, s+, unload and activate in the opposite direction, s-. The backstress evolves after each reversal, $d\gamma^{s^-} > 0$, according to:

$$\tau_{bs}^{s^-} = -(A+1)\tau_{bs}^{sat}\, exp\left(-\frac{\gamma^{s^-}}{\gamma_b}\right) + \tau_{bs}^{sat}, \tau_{bs}^{s^+} = -\frac{1}{A}\tau_{bs}^{s^-}\ if\ \ \tau_{bs}^{s^-} < 0, \tag{33}$$

$$\tau_{bs}^{s^-} = \tau_{bs}^{sat}(1 - exp(-\nu\gamma^{s^-})), \tau_{bs}^{s^+} = -A\tau_{bs}^{s^-}\ if\ \ \tau_{bs}^{s^-} > 0 \tag{34}$$

where γ_b is a fit parameter. Prior models (Beyerlein and Tomé, 2007; Zecevic and Knezevic, 2015) used similar relationships.

4. Results and discussion

4.1 Monotonic tension and compression to large strains

We first characterize the modeling parameters associated with the hardening law presented in the previous section. The initial texture used in the simulation is the measured texture given in figure 1 and the grain shape aspect ratio is set to 5 representing the measured columnar grain structure. Deformation simulations are carried out in uniaxial compression or tension in one of three directions: H, V, and D. The prescribed strain rate was $10^{-3}\ s^{-1}$, corresponding to the laboratory test and the temperature was set to room temperature.

Using values for the material parameter within appropriate bounds, the values were changed and simulations repeated until calculation agreed with measurement in yield stress, flow stress, and hardening rate. Part of the characterization involves the DD-based hardening law. The single set of DD model parameters is given in table 5. Different slip dislocations have different atomic core structures and they in principle should have their own k_1^{α}, activation barrier for de-pinning g^{α}, and drag stress D^{α}. Therefore, these parameters should be characterized for each slip mode and verified using a large suite of data, including stress–strain responses in multiple load directions, different temperatures, and changes in temperature and strain path. To simplify characterization due to lack of high-temperature data, we consider only octahedral slip. As presented, multiple stress–strain measurements and texture data are used for calibration and validation. However, the parameters are valid only for room temperature deformation of IN718. Thus, we should keep in mind that the parameters for IN718 reported here will require extension in the future high-temperature studies Even so, it is possible to estimate the hardening parameters for IN718 from one stress–strain curve since individual parameters introduced in our model are responsible for different portions of the curve. For

example, τ_0^α is mainly responsible for the yield stress, k_1^α mainly governs the initial slope of the stress–strain curve, while g^α and D^α control the response at higher strain levels.

Table 5. Hardening parameters for the evolution of τ_{forest}^s and τ_{debris}^α. The parameters for cubic slip are arbitrarily set.

	k_1^α [$\frac{1}{m}$]	D^α [MPa]	g^α	q^α	H^α	c_1	c_2
{111}	3.2e+8	520	0.04	16	0.31	0.045	0.97
{001}	2.8e+8	600	0.04	16	0.31	0	0

In addition, we needed to characterize the latent hardening matrix used in Eq. (23), which is:

$$L^{ss\prime} = \begin{bmatrix} \mathbf{A} & \blacksquare \\ \blacksquare & \blacksquare \end{bmatrix}, \qquad (35)$$

where A is the interaction matrix (defined in appendix C) for octahedral slip systems for the FCC metals (Franciosi and Zaoui, 1982). We used values calculated for FCC metals by Hoc et al. (Hoc et al., 2004) and Devincre et al. (Devincre et al., 2006) employing dislocation dynamic simulations. The values are given in table 6. It should be mentioned that a_0, a_1, a_2, a_3, a_4, and a_5 correspond to the self-interaction, coplanar interaction, Hirth, collinear, Glissile, and Lomer interaction coefficients, respectively. Anisotropic hardening of γ/ γ' superalloy single crystals has been studied in (Estevez et al., 1997; Hoinard et al., 1995). It was found that hardening anisotropy at 650°C is comparable to one of the most anisotropic pure FCC metals, mainly because of the hardening asymmetry on the octahedral slip systems. Because cubic slip is not active at room temperature, cubic-octahedral, cubic-to-cubic, and octahedral-to-cubic interactions have not been characterized. The non characterized entrees in Eq. (35) are indicated by ■.

Table 6. Latent hardening interaction matrix constants.

a_0	a_1	a_2	a_3	a_4	a_5
0.068	0.068	0.0454	0.625	0.137	0.122

Last, in the characterization step, we also sought values for some of the NS coefficients. Although non-zero c_3 and c_4 NS coefficients could lead to a T-C asymmetry, we did not have a physical basis or a reasonable range of values. However, it is known that the non glide stresses that shrink or expand the super-partials on the $\{111\}$ plane are controlled by the c1 and c2 NS coefficients (Steinmann et al., 1998). Here, these coefficients were characterized to be $c_1 = 0.045$ and $c_2 = 0.97$. The values are presented in table 5. The high value of c_2 is in agreement with the recent finding that the separation between Shokley partials in FCC metals should only be dependent on $\mathbf{t} \otimes \mathbf{n}$ NS resolved shear stress term (Baudouin et al., 2013). It should be noted that the characterization here applies only to octahedral slip systems and not cubic slip, since cubic slip was inactive for most of the deformation process. Figure 9 compares the model curves using the above set of parameters with the measurement for each build direction. As shown, the model captures well the tension-compression asymmetry and hardening rate in each case.

As a validation of the model, we calculate the texture evolution corresponding to each test. figure 10 shows the texture evolution using stereographic pole figures after compression in the V, D, and H. After deformation, the samples have formed the <011> fiber texture as expected in compression of FCC metals. Note that the initial texture from the AM processing was a <001> fiber aligned with the BD. The differences among the deformation directions are not substantial because of the large straining in compression. A direct comparison is made using pole figures in figure 11. As shown the model captures well the main components to first order. To quantify the degree of agreement between measured (figure 10) and predicted (figure 11) textures, we calculate the pole figure difference (PFD), which is given by (Knezevic and Bhattacharyya, 2017; Knezevic et al., 2014b; Knezevic and Landry, 2015):

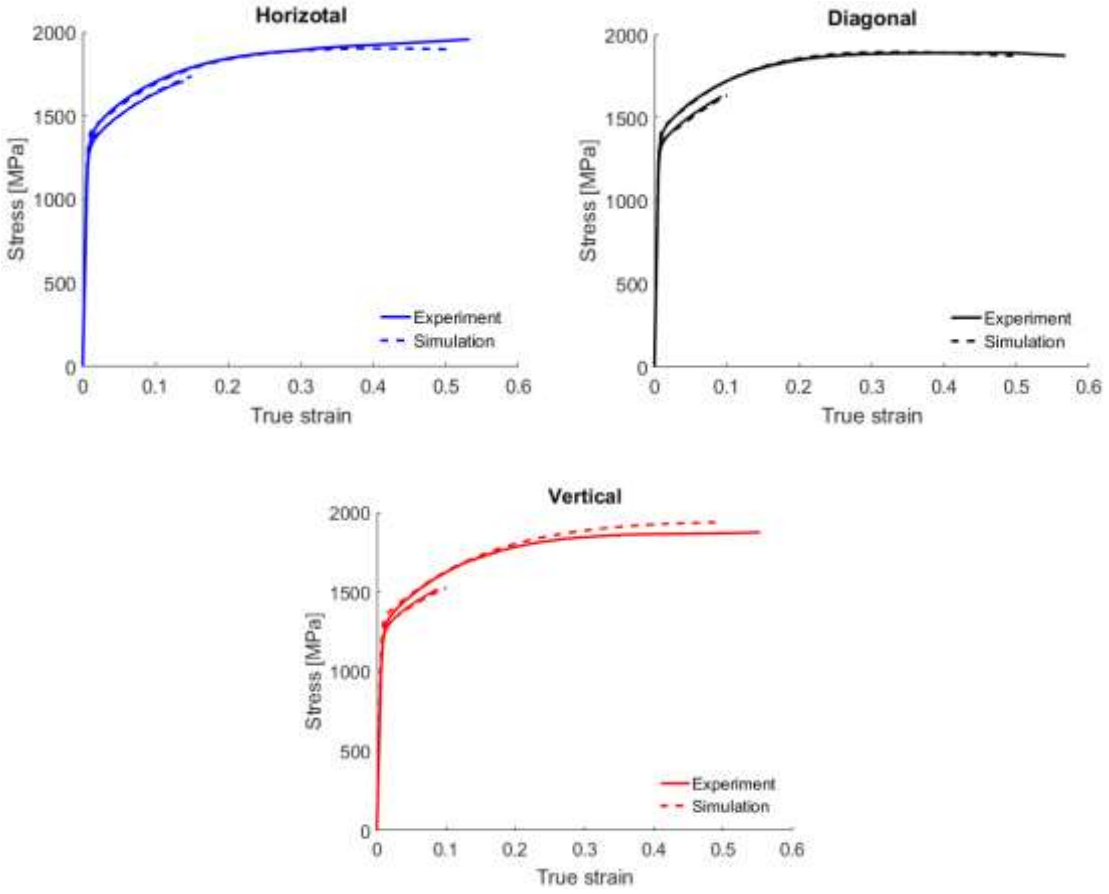

Figure 9. Comparison of measured and predicted true stress–true strain responses in tension and compression of IN718 as a function of build direction as indicated in the figure. The measured data is from figure 3.

$$\mathrm{PFD}^{hkl} = \frac{\int_{\phi=0}^{2\pi}\int_{\theta=0}^{\pi/2}\left|I_{(\phi,\theta)}^{measured} - I_{(\phi,\theta)}^{predicted}\right|\sin\theta d\theta d\phi}{\int_{\phi=0}^{2\pi}\int_{\theta=0}^{\pi/2}\left|I_{(\phi,\theta)}^{measured} + I_{(\phi,\theta)}^{predicted}\right|\sin\theta d\theta d\phi}. \qquad (36)$$

where ϕ and θ are the longitude and latitude positions in a given $\{hkl\}$ pole figure, while $I_{(\phi,\theta)}^{measured}$ and $I_{(\phi,\theta)}^{predicted}$ are intensities at those position in the pole figure. A value of PFD = 0 corresponds to a perfect match and PFD = 1 corresponds to a maximum misorientation between two textures. Two textures with a PFD < 0.2 are considered to be well matched. The calculated values averaged over three poles are 0.1905, 0.1806, and 0.1991 for V, D, and H pole figures, respectively. As mentioned

above, the contributions of the cubic slip modes to tension and compression were none and, thus, the relative activity plots of deformation modes are not presented.

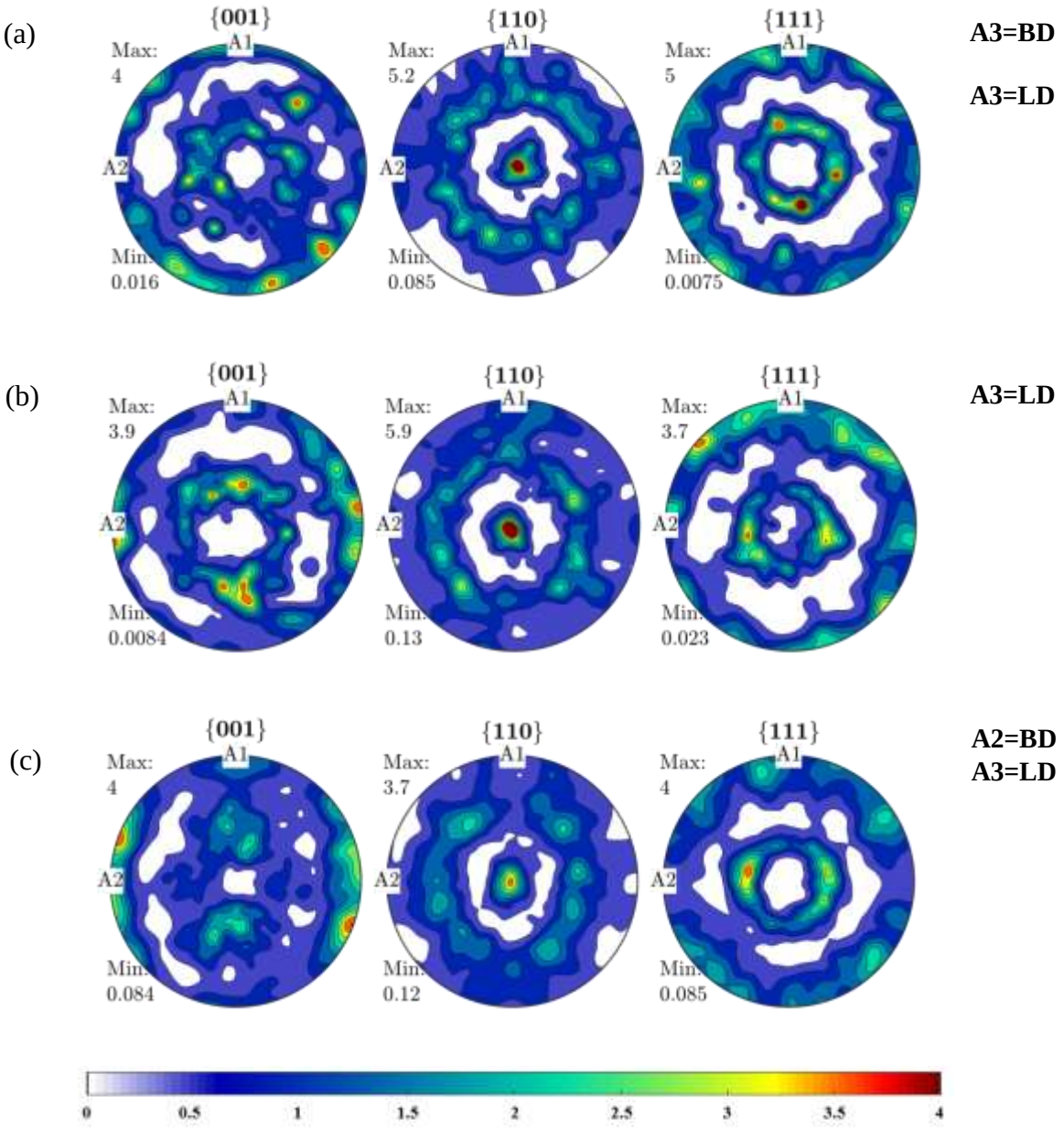

Figure 10. Pole figures showing the measured texture in the compressed DMLS IN718 samples along (a) vertical (V) direction to a strain of 0.55, (b) diagonally at 45° direction to a strain of 0.57, and (c) horizontal (H) direction to a strain of 0.53. The compression direction is in the center of the pole figures.

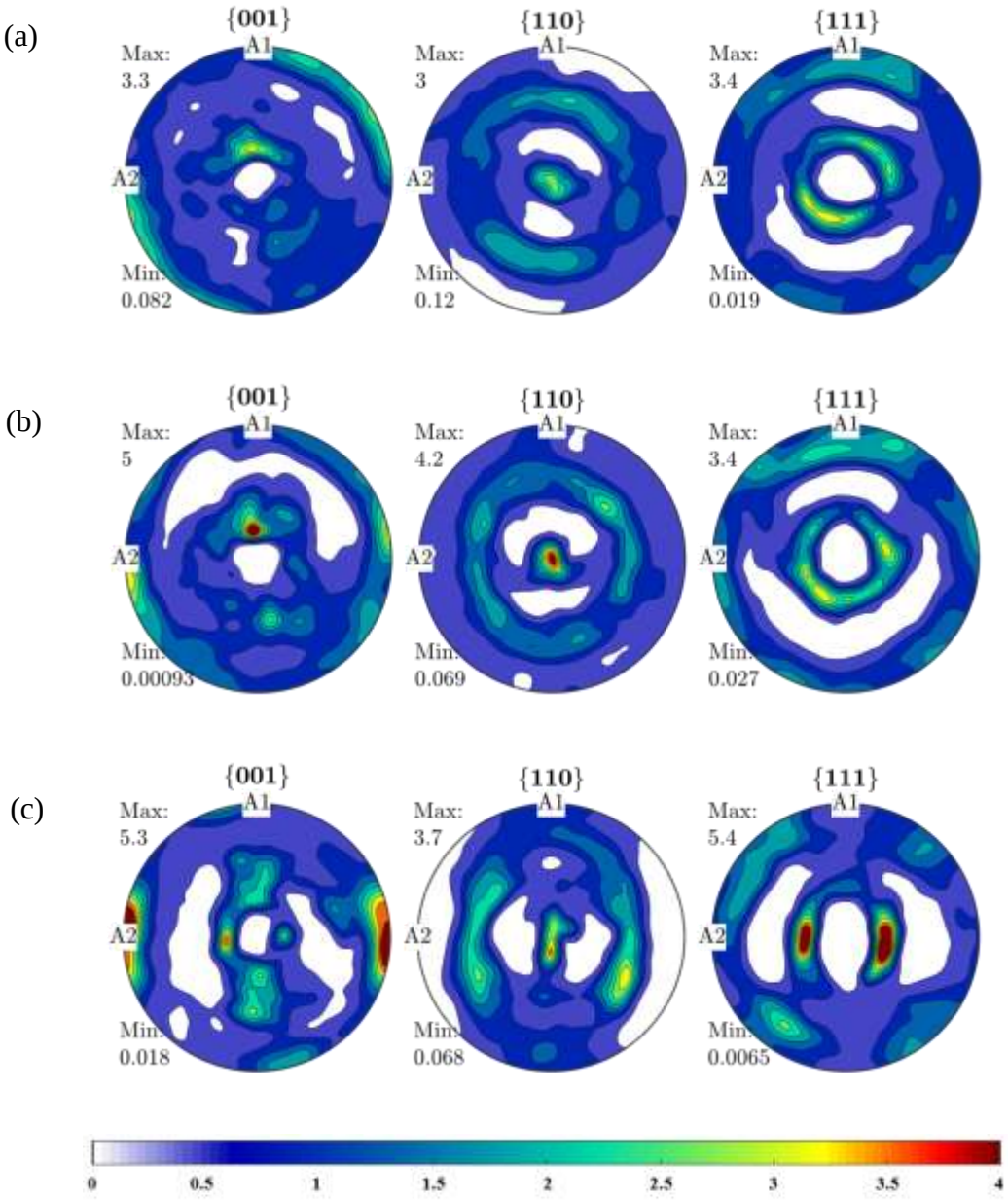

Figure 11. Pole figures showing the simulated texture corresponding to those measured shown in figure 10.

4.2 Large strain cyclic tension and compression

For large strain cyclic deformation i.e., forward-reversal loading, the backstress term needs a calibration. The cyclic curve in Fig. 4b was used to identify the backstress parameters, which are presented in table 7. The backstress parameters control the level of nonlinear unloading, the BE, and hardening in the reverse direction. Note that tables 5 and 7 contain ten model parameters, which were adjusted to fit the IN718 data.

Table 7. Constitutive parameters for backstress evolution.

τ_{bs}^{sat} [MPa]	v	γ_b	A
100	600.0	0.01	6.5

Without further adjusting the model, we simulate the remaining large strain forward and reversal loading cases from Figs. 3 and 4. Figure 12 compares the model and measurement for the D and H cases after a tension pre-strain of 0.02 to 0.04. Clearly the agreement in non-linear unloading, flow stress, hardening rate, and BE are good. Notably, the model captures the increase BE with larger pre-strains, the lower yield in reverse loading, the higher hardening rate after yield. We find that the backstresses are primarily responsible for the increases in the non-linear unloading with the amount of pre-strain. Both the backstresses and inter-granular stresses were responsible for the BE, however. Last, reversible dislocation motion activity governed the hardening rates during reverse loading.

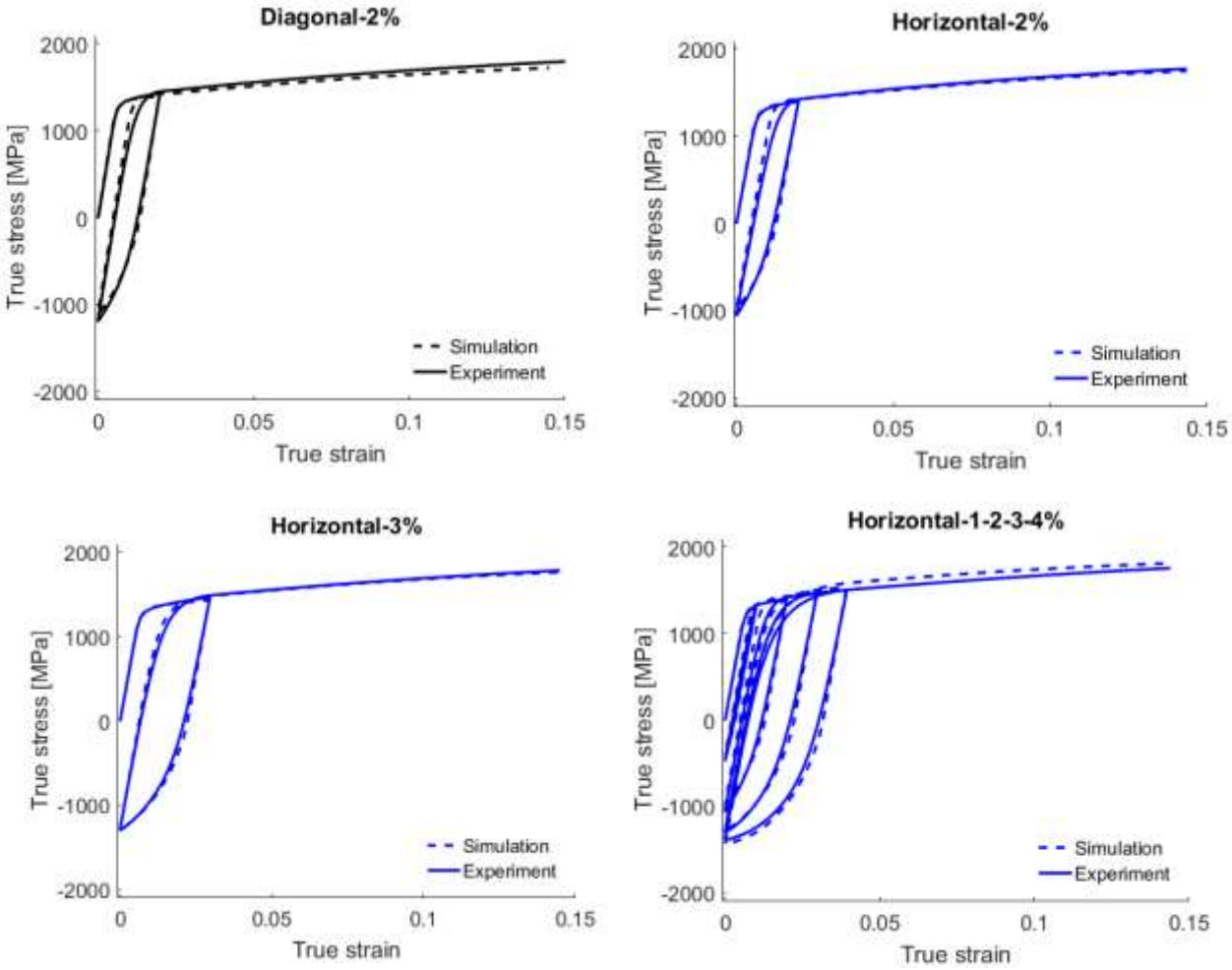

Figure 12. Comparison of measured and predicted true stress–true strain responses during cyclic tension-compression of IN718. The measured data is from figures 4 and 5.

5. Conclusions

In this work, we present an experimental and modeling study of the room temperature deformation behavior of a Ni-based superalloy IN718 fabricated by an additive manufacturing technique called DMLS. The DMLS IN718 alloy shows plastic anisotropy with respect to the build direction and tension-compression asymmetry behavior. Upon the change in strain path from tension to compression, the material exhibits non-linear unloading, a BE, and an increasing reduction in yield stress during reverse loading as the strain for forward loading is increased. To gain the insights into the microstructural origins of this behavior, we advance an EPSC model, called P-EPSC, to account for the effects of nanoscale precipitates on the plastic deformation response of this Ni-based

superalloy. The effects are encased within an updated hardening law for both octahedral $\{111\}\langle 1\bar{1}0\rangle$ slip and cubic slip $\{001\}\langle 110\rangle$ that accounts for the APB energy for these two slip modes in two compositions of precipitates. In order to use consistent values of the APB energy from one source, we used density functional theory to calculate the APB energies for these modes. Coupled with the inherited models for backstress and reversible dislocations, and latent hardening, we demonstrate that the new P-EPSC model, with the precipitate sensitive slip resistance, non-Schmid effects, and the grain shape sensitive dislocation mean-free-path, is capable of predicting the constitutive response in monotonic loading, the tension-compression asymmetry, and the non-linearities during unloading, the BE, and permanent softening associated with cyclic loading. The latter cyclic responses are also successfully predicted as a function of loading directions and level of pre-strain. The model calculations suggest that as the pre-strain increases, the backstresses increase causing the non-linearity during the unloading step to increase. It is also suggested that the backstresses and inter-granular stresses govern the Bauschinger effect while reversible dislocation motion plays a major role in hardening during reverse loading. As many of these features in the behavior of IN718 are similar to other Ni-based superalloys, the present modeling framework is expected to be useful for a wider set of materials such as superalloys and other cubic metals.

Acknowledgments

This work was supported by Turbocam Energy Solutions and the New Hampshire Innovation Research Center under grants No. 13R217 and 13R265. The samples of IN718 for this project were printed, machined, and heat treated at Turbocam. I.J.B. acknowledges financial support from the National Science Foundation (NSF CMMI-1541918). The authors acknowledge Mr. Sean Gribbin for help with cyclic testing and Professor Igor Tsukrov for several discussions.

Appendix A

The hardening matrix is:

$$h^{ss'} = \frac{\partial \tau_c^s}{\partial \gamma^{s'}} = \frac{\partial \tau_0^\alpha}{\partial \gamma^{s'}} + \frac{\partial \tau_{forest}^s}{\partial \gamma^{s'}} + \frac{\partial \tau_{debris}^\alpha}{\partial \gamma^{s'}}, \quad \text{(A1)}$$

with:

$$\frac{\partial \tau_0^\alpha}{\partial \gamma^{s\prime}} = 0, \quad \text{(A2)}$$

$$\frac{\partial \tau_{forest}^s}{\partial \gamma^{s\prime}} = \frac{\partial \tau_{forest}^s}{\partial \rho_{tot}^{s'}} \frac{\partial \rho_{tot}^{s'}}{\partial \gamma^{s\prime}} = b^\alpha \chi \mu_{\mathrm{IN718}}^\alpha \frac{1}{2\sqrt{\sum_{s'} L^{ss'} \rho_{tot}^{s'}}} L^{ss'} \left(\frac{\partial \rho_{for}^{s'}}{\partial \gamma^{s'}} + \frac{\partial \rho_{rev}^{s'^+}}{\partial \gamma^{s'}} + \frac{\partial \rho_{rev}^{s'^-}}{\partial \gamma^{s'}} \right), \quad \text{(A3)}$$

$$\frac{\partial \tau_{debris}^\alpha}{\partial \gamma^{s\prime}} = \frac{\partial \tau_{debris}^\alpha}{\partial \rho_{deb}} \frac{\partial \rho_{deb}}{\partial \gamma^{s\prime}} = -k_{deb} \mu_{\mathrm{IN718}}^\alpha b^\alpha \left(log\left(b^\alpha \sqrt{\rho_{deb}} \right) + 1 \right) \frac{1}{2\sqrt{\rho_{deb}}} \frac{\partial \rho_{deb}}{\partial \gamma^{s\prime}}. \quad \text{(A4)}$$

The backstress hardening matrix, in the case of shearing in the s+ direction, $d\gamma^{s^+} > 0$, with $\tau_{bs}^{s^+} \geq 0$ is:

$$h_{bs}^{s^+ s^+} = \frac{\partial \tau_{bs}^{s^+}}{\partial \gamma^{s^+}} = \tau_{bs}^{sat} \nu \exp\left(-\nu \gamma^{s^+}\right), \quad \text{(A5)}$$

$$h_{bs}^{s^- s^+} = \frac{\partial \tau_{bs}^{s^-}}{\partial \gamma^{s^+}} = -A h_{bs}^{s^+ s^+}, \quad \text{(A6)}$$

The backstress hardening matrix after reversal (i.e. $d\gamma^{s^-} > 0$) in the case $\tau_{bs}^{s^-} < 0$ is:

$$h_{bs}^{s^- s^-} = \frac{\partial \tau_{bs}^{s^-}}{\partial \gamma^{s^-}} = \frac{(A+1)\tau_{bs}^{sat}}{\gamma_b} exp\left(-\frac{\gamma^{s^-}}{\gamma_b}\right), \quad \text{(A7)}$$

$$h_{bs}^{s^+ s^-} = \frac{\partial \tau_{bs}^{s^+}}{\partial \gamma^{s^-}} = \frac{1}{A} h_{bs}^{s^- s^-}, \quad \text{(A8)}$$

while if $\tau_{bs}^{s^-} \geq 0$ the hardening matrix is then defined as:

$$h_{bs}^{s^- s^-} = \frac{\partial \tau_{bs}^{s^-}}{\partial \gamma^{s^-}} = \tau_{bs}^{sat} \nu \exp(-\nu \gamma^{s^-}), \quad \text{(A9)}$$

$$h_{bs}^{s^+ s^-} = \frac{\partial \tau_{bs}^{s^+}}{\partial \gamma^{s^-}} = -A h_{bs}^{s^- s^-}. \quad \text{(A10)}$$

Appendix B

Summary of APB values for γ' and γ'', including the method used to obtain the values, and the source.

$\gamma'_{(111)}\left[\frac{mJ}{m^2}\right]$	$\gamma'_{(001)}\left[\frac{mJ}{m^2}\right]$	$\gamma''_{(111)}\left[\frac{mJ}{m^2}\right]$	Method	References
111	90		Calculations- modified potentials.	(Beauchamp et al., 1987)
111±15	90±5		Measurement- weak-beam electron microscopy.	(Douin et al., 1986)
161±24			Measurement- relationship between the APB energy and <d>max.	(Ardell and Huang, 1988)
140			Chosen as appropriate.	(Heilmaier et al., 2001)
180 (at 923 K)			Calculations- force balance between the trailing and leading dislocations.	(Nemoto et al., 1991)
102±35			Calculations- modifying a relationship between the APB energy and the minimum looped precipitate diameter.	(Glazer and Morris, 1987)
200			Chosen as appropriate.	(Kozar et al., 2009)
164			Chosen as appropriate.	(Wang et al., 2006)
183±12-175±12	157±8-113±10		Measurement- electron microscopy.	(Smallman and Bishop, 1999)
12		296	Calculations- average fault energy and volume fractions of the precipitates.	(Oblak et al., 1974)

170±14	124±10		Calculations- precipitations kinetics and interfacial energy between the precipitates and the matrix.	(Yu et al., 1994)
142	83		Calculations- embedded atom method.	(Voter and Chen, 1987)
180±30	140±14		Measurement – not described.	(Veyssiere et al., 1985)
96	28		Calculations- embedded atom method.	(Foiles and Daw, 2011)
175 (0 K)	140		Calculations- not described.	(Yoo et al., 1994)
178 (at 100 K) -183 (at 1000 K)	73-11		Calculations- the Helmholtz free energy and the total Gibbs free energy.	(Manga et al., 2015)
		95±17 at (973 K)	Calculations- average fault energy and volume fractions of the precipitates.	(Devaux et al., 2008)

Appendix C

The interaction matrix for FCC metals, where A_2, A_3, A_6, B_2, B_4, B_5, C_1, C_3, C_5, D_1, D_4, and D_6 are the slip systems with A, B, C, and D representing the $(\bar{1}11)$, (111), $(\bar{1}\bar{1}1)$, and $(1\bar{1}1)$ slip planes and 1 to 6 representing [011], $[0\bar{1}1]$, [101], $[\bar{1}01]$, $[\bar{1}10]$, and [110] slip directions (Franciosi and Zaoui, 1982).

	A_2	A_3	A_6	B_2	B_4	B_5	C_1	C_3	C_5	D_1	D_4	D_6
A_2	a_0	a_1	a_1	a_3	a_4	a_4	a_2	a_4	a_5	a_2	a_5	a_4
A_3		a_0	a_1	a_4	a_2	a_5	a_4	a_3	a_4	a_5	a_2	a_4
A_6			a_0	a_4	a_5	a_2	a_5	a_4	a_2	a_4	a_4	a_3
B_2				a_0	a_1	a_1	a_2	a_5	a_4	a_2	a_4	a_5
B_4					a_0	a_1	a_5	a_2	a_4	a_4	a_3	a_4
B_5						a_0	a_4	a_4	a_3	a_5	a_4	a_2
C_1							a_0	a_1	a_1	a_3	a_4	a_4
C_3								a_0	a_1	a_4	a_2	a_5
C_5									a_0	a_4	a_5	a_2

D_1										a_0	a_1	a_1
D_4											a_0	a_1
D_6												a_0

References

2001. CRC Materials Science and Engineering Handook, 2001 ed. CRC Press LLC, Boca Raton.

2012a. ASTM E606/E606M-12, Standard Test Method for Strain-Controlled Fatigue Testing. ASTM International, West Conshohocken, PA.

2012b. F2792 12a, Standard Terminology for Additive Manufacturing Technologies. ASTM International, West Conshohocken, PA.

2015. ASTM E8/E8M-15a, Standard Test Methods for Tension Testing of Metallic Materials. ASTM International, West Conshohocken, PA.

Alankar, A., Field, D.P., Raabe, D., 2014. Plastic anisotropy of electro-deposited pure α-iron with sharp crystallographic <111>// texture in normal direction: Analysis by an explicitly dislocation-based crystal plasticity model. Int. J. Plast. 52, 18-32.

Antolovich, S.D., 2015. Microstructural aspects of fatigue in Ni-base superalloys. Philosophical Transactions of the Royal Society of London A: Mathematical, Physical and Engineering Sciences 373, 20140128.

Ardeljan, M., Beyerlein, I.J., Knezevic, M., 2014. A dislocation density based crystal plasticity finite element model: Application to a two-phase polycrystalline HCP/BCC composites. J. Mech. Phys. Solids 66, 16-31.

Ardeljan, M., Beyerlein, I.J., McWilliams, B.A., Knezevic, M., 2016. Strain rate and temperature sensitive multi-level crystal plasticity model for large plastic deformation behavior: Application to AZ31 magnesium alloy. Int. J. Plast. 83, 90-109.

Ardeljan, M., Knezevic, M., Nizolek, T., Beyerlein, I.J., Mara, N.A., Pollock, T.M., 2015. A study of microstructure-driven strain localizations in two-phase polycrystalline HCP/BCC composites using a multi-scale model. Int. J. Plast. 74, 35-57.

Ardell, A.J., Huang, J.C., 1988. Antiphase boundary energies and the transition from shearing to looping in alloys strengthened by ordered precipitates. Philosophical Magazine Letters 58, 189-197.

Baudouin, J.-B., Monnet, G., Perez, M., Domain, C., Nomoto, A., 2013. Effect of the applied stress and the friction stress on the dislocation dissociation in face centered cubic metals. Materials Letters 97, 93-96.

Bauschinger, J., 1886. Über die Veränderung der Elasticitätsgrenze und Festigkeit des Eisen und Stahls durch Strecken und Quetschen, durch Erwarmen und Abkühlen und durch oftmal wiederholte Beanspruchung. Mitteilungen aus dem mechanisch-technischen Laboratorium der k. polytechnischen Schule, 1877-1836.

Beauchamp, P., Douin, J., Veyssière, P., 1987. Dependence of the antiphase boundary energy upon orientation in the $L1_2$ structure. Philosophical Magazine A 55, 565-581.

Beyerlein, I.J., Tomé, C.N., 2007. Modeling transients in the mechanical response of copper due to strain path changes. Int. J. Plast. 23, 640-664.

Beyerlein, I.J., Tomé, C.N., 2008. A dislocation-based constitutive law for pure Zr including temperature effects. Int. J. Plast. 24, 867-895.

Blöchl, P.E., 1994. Projector augmented-wave method. Physical Review B 50, 17953.

Brown, E.E., Muzyka, D.R., 1987. chapter 6, Nickel-Iron Alloys, in: Sims, C.T., Stoloff, N.S., Hagel, W.C. (Eds.), Superalloys II, pp. 165-188.

Copley, S., Kear, B., 1967a. A dynamic theory of coherent precipitation hardening with application to nickel-base alloys(Coherent precipitation hardening theory treats yielding in nickel base alloy

containing coherent stress-free ordered particles as dynamic process). AIME, TRANSACTIONS 239, 984-992.

Copley, S., Kear, B., 1967b. Temperature and orientation dependence of the flow stress in off-stoichiometric Ni sub 3 Al/gamma' phase/(Strength characteristics of single crystals of nickel aluminide/gamma phase/, discussing temperature and orientation dependence of work hardening). AIME, TRANSACTIONS 239, 977-984.

Courtney, T.H., 1990. Strengthening of Crystalline Materials, Mechanical Behavior of Materials.

Dao, M., Asaro, R.J., 1993. Non-Schmid effects and localized plastic flow in intermetallic alloys. Mater. Sci. Eng. A 170, 143-160.

Davis, J.R., 1997. ASM specialty handbook: heat-resistant materials. ASM International.

Dehmas, M., Lacaze, J., Niang, A., Viguier, B., 2011. TEM study of high-temperature precipitation of delta phase in Inconel 718 alloy. Advances in materials science and engineering 2011, 1-9.

Devaux, A., Nazé, L., Molins, R., Pineau, A., Organista, A., Guédou, J.Y., Uginet, J.F., Héritier, P., 2008. Gamma double prime precipitation kinetic in Alloy 718. Materials Science and Engineering: A 486, 117-122.

Devincre, B., Kubin, L., Hoc, T., 2006. Physical analyses of crystal plasticity by DD simulations. Scr. Mater. 54, 741-746.

Ding, Z., Liu, Y., Yin, Z., Yang, Z., Cheng, X., 2004. Study of elastoplastic constitutive model for single crystal nickel-based superalloy. Hangkong Dongli Xuebao/Journal of Aerospace Power 19, 755-761.

Douin, J., Veyssière, P., Beauchamp, P., 1986. Dislocation line stability in Ni_3AI. Philosophical Magazine A 54, 375-393.

Eshelby, J.D., 1957. The determination of the elastic field of an ellipsoidal inclusion, and related problems. Proc R. Soc. Lond. A 241, 376-396.

Estevez, R., Hoinard, G., Franciosi, P., 1997. Hardening anisotropy of γγ′ superalloy single crystals—II. Numberical analysis of heterogeneity effects. Acta. Mater. 45, 1567-1584.

Fang, T., Kennedy, S., Quan, L., Hicks, T., 1992. The structure and paramagnetism of Ni_3Nb. Journal of Physics: Condensed Matter 4, 2405.

Foiles, S.M., Daw, M.S., 2011. Application of the embedded atom method to Ni_3Al. Journal of Materials Research 2, 5-15.

Franciosi, P., Zaoui, A., 1982. Multislip in f.c.c. crystals a theoretical approach compared with experimental data. Acta Metallurgica 30, 1627-1637.

Francis, E.M., Grant, B.M.B., Fonseca, J.Q.d., Phillips, P.J., Mills, M.J., Daymond, M.R., Preuss, M., 2014. High-temperature deformation mechanisms in a polycrystalline nickel-base superalloy studied by neutron diffraction and electron microscopy. Acta. Mater. 74, 18-29.

Fukuhara, M., Sanpei, A., 1993. Elastic moduli and internal frictions of Inconel 718 and Ti-6Al-4V as a function of temperature. Journal of Materials Science Letters 12, 1122-1124.

Ghosh, S., Yadav, S., Das, G., 2008. Study of standard heat treatment on mechanical properties of Inconel 718 using ball indentation technique. Materials Letters 62, 2619-2622.

Glazer, J., Morris, J.W., 1987. Strengthening contributions of strong ordered precipitates. Philosophical Magazine A 56, 507-515.

Gleiter, H., Hornbogen, E., 1968. Precipitation hardening by coherent particles. Materials Science and Engineering 2, 285-302.

Gribbin, S., Bicknell, J., Jorgensen, L., Tsukrov, I., Knezevic, M., 2016. Low cycle fatigue behavior of direct metal laser sintered Inconel alloy 718. Int. J. Fatigue 93, Part 1, 156-167.

Gypen, L.A., Deruyttere, A., 1977. Multi-component solid solution hardening. J. Mater. Sci. 12, 1028-1033.

Haddou, H., Risbet, M., Marichal, G., Feaugas, X., 2004. The effects of grain size on the cyclic deformation behaviour of polycrystalline nickel. Mater. Sci. Eng. A 379, 102-111.

Haldipur, P., 2006. Material characterization of nickel-based super alloys through ultrasonic inspection, Materials Science and Engineering Iowa State University, Ames, Iowa

Hanson, K., Jr., J.W.M., 1975. Limiting configuration in dislocation glide through a random array of point obstacles. Journal of Applied Physics 46, 983-990.

Hasegawa, T., Yakou, T., Karashima, S., 1975. Deformation behaviour and dislocation structures upon stress reversal in polycrystalline aluminium. Materials Science and Engineering 20, 267-276.

Heilmaier, M., Leetz, U., Reppich, B., 2001. Order strengthening in the cast nickel-based superalloy IN 100 at room temperature. Materials Science and Engineering: A 319–321, 375-378.

Herderick, E., 2015. Progress in Additive Manufacturing. JOM 67, 580-581.

Hinojos, A., Mireles, J., Reichardt, A., Frigola, P., Hosemann, P., Murr, L.E., Wicker, R.B., 2016. Joining of Inconel 718 and 316 Stainless Steel using electron beam melting additive manufacturing technology. Materials & Design 94, 17-27.

Hirsch, P.B., 2003. Kear-Wilsdorf locks and the formation of antiphase-boundary tubes in L1 2 alloys. Philosophical Magazine 83, 1007-1032.

Hoc, T., Devincre, B., Kubin, L.P., 2004. Deformation stage I of FCC crystals: constitutive modelling, in: Gundlach, C., Haldrup, K., Hansen, N., Huang, X., Jensen, D.J., Leffers, T., Li, Z.J., Nielsen, S.F., Pantleon, W., Wert, J.A., Winther, G. (Eds.), Proceedings of the 25th Riso International Symposium on Materials Science: Evolution of Deformation Microstructures in 3D, Riso National Laboratory, Roskilde, Denmark.

Hoinard, G., Estevez, R., Franciosi, P., 1995. Hardening anisotropy of γ/γ′ superalloy single crystals—I. Experimental estimates at 650°C from a homogeneous analysis. Acta Metall. Mater. 43, 1593-1607.

Huther, W., Reppich, B., 1978. Interaction of Dislocations with Coherent, Stree-Free Ordered Particles. Zeitschrift Fur Metallkunde 69, 628-634.

Jahedi, M., Ardeljan, M., Beyerlein, I.J., Paydar, M.H., Knezevic, M., 2015. Enhancement of orientation gradients during simple shear deformation by application of simple compression. J. Appl. Phys. 117, 214309.

Jahedi, M., McWilliams, B.A., Moy, P., Knezevic, M., 2017. Deformation twinning in rolled WE43-T5 rare earth magnesium alloy: Influence on strain hardening and texture evolution. Acta. Mater. 131, 221-232.

Kalh, S., Rao, K.B.S., Halford, G.R., McGaw, M.A., DEFORMATION AND DAMAGE MECHANISMS IN INCONEL 718 SUPERALLOY.

Keshavarz, S., Ghosh, S., 2015. A crystal plasticity finite element model for flow stress anomalies in Ni_3Al single crystals. Philosophical Magazine 95, 2639-2660.

Kitayama, K., Tomé, C.N., Rauch, E.F., Gracio, J.J., Barlat, F., 2013. A crystallographic dislocation model for describing hardening of polycrystals during strain path changes. Application to low carbon steels. International Journal of Plasticity in press.

Knezevic, M., Beyerlein, I.J., Lovato, M.L., Tomé, C.N., Richards, A.W., McCabe, R.J., 2014a. A strain-rate and temperature dependent constitutive model for BCC metals incorporating non-Schmid effects: Application to tantalum–tungsten alloys. Int. J. Plast. 62, 93-104.

Knezevic, M., Bhattacharyya, A., 2017. Characterization of microstructure in Nb rods processed by rolling: Effect of grooved rolling die geometry on texture uniformity. International Journal of Refractory Metals and Hard Materials 66, 44-51.

Knezevic, M., Capolungo, L., Tomé, C.N., Lebensohn, R.A., Alexander, D.J., Mihaila, B., McCabe, R.J., 2012a. Anisotropic stress-strain response and microstructure evolution of textured a-uranium. Acta. Mater. 60, 702-715.

Knezevic, M., Chun, B.K., Oh, J.Y., Wu, W.T., Ress Iii, R.A., Glavicic, M.G., Srivatsa, S., 2012b. Modeling machining distortion using the finite element method: Application to engine disk, pp. 40-46.

Knezevic, M., Jahedi, M., Korkolis, Y.P., Beyerlein, I.J., 2014b. Material-based design of the extrusion of bimetallic tubes. Comput. Mater. Sci. 95, 63-73.

Knezevic, M., Landry, N.W., 2015. Procedures for reducing large datasets of crystal orientations using generalized spherical harmonics. Mechanics of Materials 88, 73-86.

Knezevic, M., Levinson, A., Harris, R., Mishra, R.K., Doherty, R.D., Kalidindi, S.R., 2010. Deformation twinning in AZ31: Influence on strain hardening and texture evolution. Acta. Mater. 58, 6230-6242.

Knezevic, M., Zecevic, M., Beyerlein, I.J., Bingert, J.F., McCabe, R.J., 2015. Strain rate and temperature effects on the selection of primary and secondary slip and twinning systems in HCP Zr. Acta. Mater. 88, 55-73.

Knezevic, M., Zecevic, M., Beyerlein, I.J., Lebensohn, R.A., 2016. A numerical procedure enabling accurate descriptions of strain rate-sensitive flow of polycrystals within crystal visco-plasticity theory. Computer Methods in Applied Mechanics and Engineering 308, 468-482.

Kocks, U.F., Mecking, H., 1981. Kinetics of Flow and Strain-Hardening. Acta Metall. 29, 1865-1875.

Kozar, R.W., Suzuki, A., Milligan, W.W., Schirra, J.J., Savage, M.F., Pollock, T.M., 2009. Strengthening Mechanisms in Polycrystalline Multimodal Nickel-Base Superalloys. Metall. Mater. Trans. A 40, 1588-1603.

Kresse, G., Furthmüller, J., 1996. Efficient iterative schemes for ab initio total-energy calculations using a plane-wave basis set. Physical Review B 54, 11169.

Kresse, G., Hafner, J., 1994. Ab initio molecular-dynamics simulation of the liquid-metal–amorphous-semiconductor transition in germanium. Physical Review B 49, 14251.

Kresse, G., Joubert, D., 1999. From ultrasoft pseudopotentials to the projector augmented-wave method. Physical Review B 59, 1758.

Kumar, A., Morrow, B.M., McCabe, R.J., Beyerlein, I.J., 2017. An atomic-scale modeling and experimental study of dislocations in Mg. Mater. Sci. Eng. A 695, 270-278.

Kuo, C.M., Yang, Y.T., Bor, H.Y., Wei, C.N., Tai, C.C., 2009. Aging effects on the microstructure and creep behavior of Inconel 718 superalloy. Materials Science and Engineering: A 510–511, 289-294.

Lall, C., Chin, S., Pope, D., 1979. The orientation and temperature dependence of the yield stress of Ni_3 (Al, Nb) single crystals. MTA 10, 1323-1332.

Lebensohn, R.A., Tomé, C.N., 1993. A self-consistent anisotropic approach for the simulation of plastic deformation and texture development of polycrystals: Application to zirconium alloys. Acta Metall. Mater. 41, 2611-2624.

Lentz, M., Klaus, M., Beyerlein, I.J., Zecevic, M., Reimers, W., Knezevic, M., 2015a. In situ X-ray diffraction and crystal plasticity modeling of the deformation behavior of extruded Mg–Li–(Al) alloys: An uncommon tension–compression asymmetry. Acta. Mater. 86, 254-268.

Lentz, M., Klaus, M., Wagner, M., Fahrenson, C., Beyerlein, I.J., Zecevic, M., Reimers, W., Knezevic, M., 2015b. Effect of age hardening on the deformation behavior of an Mg–Y–Nd alloy: In-situ X-ray diffraction and crystal plasticity modeling. Mater. Sci. Eng. A 628, 396-409.

Lim, H., Weinberger, C.R., Battaile, C.C., Buchheit, T.E., 2013. Application of generalized non-Schmid yield law to low-temperature plasticity in bcc transition metals. Modelling and Simulation in Materials Science and Engineering 21, 045015.

Lipinski, P., Berveiller, M., 1989. Elastoplasticity of micro-inhomogeneous metals at large strains. Int. J. Plast. 5, 149-172.

Liu, L., Tanaka, K., Hirose, A., Kobayashi, K.F., 2002. Effects of precipitation phases on the hydrogen embrittlement sensitivity of Inconel 718. Science and Technology of Advanced Materials 3, 335-344.

Maciejewski, K., Jouiad, M., Ghonem, H., 2013. Dislocation/precipitate interactions in IN100 at 650 °C. Materials Science and Engineering: A 582, 47-54.

Madec, R., Devincre, B., Kubin, L., Hoc, T., Rodney, D., 2003. The role of collinear interaction in dislocation-induced hardening. Science 301, 1879-1882.

Manga, V.R., Shang, S.-L., Wang, W.Y., Wang, Y., Liang, J., Crespi, V.H., Liu, Z.-K., 2015. Anomalous phonon stiffening associated with the (1 1 1) antiphase boundary in $L1_2$ Ni_3Al. Acta Materialia 82, 287-294.

Mei, Y., Liu, Y., Liu, C., Li, C., Yu, L., Guo, Q., Li, H., 2015. Effects of cold rolling on the precipitation kinetics and the morphology evolution of intermediate phases in Inconel 718 alloy. Journal of Alloys and Compounds 649, 949-960.

Meyers, M.A., Chawla, K.K., 1998. Mechanical Behavior of Materials. Prentice Hall, Upper Saddle River, New Jersey.

Neil, C.J., Wollmershauser, J.A., Clausen, B., Tomé, C.N., Agnew, S.R., 2010. Modeling lattice strain evolution at finite strains and experimental verification for copper and stainless steel using in situ neutron diffraction. Int. J. Plast. 26, 1772-1791.

Nemoto, M., Tian, W.H., Sano, T., 1991. Coherent precipitation strengthening by /in $L1_2$-ordered phases. J. Phys. III 1, 1099-1117.

Oblak, J.M., Paulonis, D.F., Duvall, D.S., 1974. Coherency strengthening in Ni base alloys hardened by DO22 γ′ precipitates. Metallurgical Transactions 5, 143.

Österle, W., Bettge, D., Fedelich, B., Klingelhöffer, H., 2000. Modelling the orientation and direction dependence of the critical resolved shear stress of nickel-base superalloy single crystals. Acta. Mater. 48, 689-700.

Pack, J.D., Monkhorst, H.J., 1977. " Special points for Brillouin-zone integrations"—a reply. Physical Review B 16, 1748.

Paidar, V., Pope, D.P., Vitek, V., 1984. A theory of the anomalous yield behavior in $L1_2$ ordered alloys. Acta Metall. 32, 435-448.

Paidar, V., Yamaguchi, M., Pope, D.P., Vitek, V., 1982. Dissociation and core structure of 〈110〉 screw dislocations in $L1_2$ ordered alloys II. Effects of an applied shear stress. Philosophical Magazine A 45, 883-894.

Paulonis, D.F., Oblak, J.M., Duvall, D.S., 1969. PRECIPITATION IN NICKEL-BASE ALLOY 718. ASM (Amer. Soc. Metals), Trans. Quart., 62: 611-22(Sept. 1969). Medium: X.

Perdew, J.P., Burke, K., Ernzerhof, M., 1996. Generalized gradient approximation made simple. Physical review letters 77, 3865.

Rao, G.A., Kumar, M., Srinivas, M., Sarma, D., 2003. Effect of standard heat treatment on the microstructure and mechanical properties of hot isostatically pressed superalloy inconel 718. Mater. Sci. Eng. A 355, 114-125.

Roth, H.A., Davis, C.L., Thomson, R.C., 1997. Modeling solid solution strengthening in nickel alloys. Metallurgical and Materials Transactions A 28, 1329-1335.

Savage, D.J., Beyerlein, I.J., Knezevic, M., 2017. Coupled texture and non-Schmid effects on yield surfaces of body-centered cubic polycrystals predicted by a crystal plasticity finite element approach. International Journal of Solids and Structures 109, 22-32.

Schmid, E., Boas, W., 1950. Plasticity of crystals with special reference to metals. English translation F.A. Hughes, London

Shenoy, M., Tjiptowidjojo, Y., McDowell, D., 2008. Microstructure-sensitive modeling of polycrystalline IN 100. Int. J. Plast. 24, 1694-1730.

Slama, C., Abdellaoui, M., 2000. Structural characterization of the aged Inconel 718. Journal of Alloys and Compounds 306, 277-284.

Smallman, R.E., Bishop, R.J., 1999. Chapter 9 - Modern alloy developments, Modern Physical Metallurgy and Materials Engineering (Sixth Edition). Butterworth-Heinemann, Oxford, pp. 297-319.

Smith, D.H., Bicknell, J., Jorgensen, L., Patterson, B.M., Cordes, N.L., Tsukrov, I., Knezevic, M., 2016. Microstructure and mechanical behavior of direct metal laser sintered Inconel alloy 718. Mater. Charact. 113, 1-9.

Sritharan, T., Chandel, R.S., 1997. Phenomena in interrupted tensile tests of heat treated aluminium alloy 6061. Acta. Mater. 45, 3155-3161.

Steinmann, P., Kuhl, E., Stein, E., 1998. Aspects of non-associated single crystal plasticity: influence of non-Schmid effects and localization analysis. International journal of solids and structures 35, 4437-4456.

Turner, P.A., Tomé, C.N., 1994. A study of residual stresses in Zircaloy-2 with rod texture. Acta Metall. Mater. 42, 4143-4153.

Umakoshi, Y., Pope, D.P., Vitek, V., 1984. The asymmetry of the flow stress in $Ni_3(Al,Ta)$ single crystals. Acta Metallurgica 32, 449-456.

Veyssieìre, P., Saada, G., 1996. Dislocations in Solids, Vol. 10, edited by FRN Nabarro and MS Duesbery. Amsterdam: Elsevier, p. 253.

Veyssiere, P., Douin, J., Beauchamp, P., 1985. On the presence of super lattice intrinsic stacking faults in plastically deformed Ni_3Al. Philosophical Magazine A 51, 469-483.

Voter, A.F., Chen, S.P., 1987. Accurate interatomic potentials for Ni, Al and Ni_3Al. Theoretical Division, Los Alamos National Laboratory, Los Alamos, NM 87545 82, 175-177.

Wang, A.-J., Kumar, R.S., Shenoy, M.M., McDowell, D., 2006. Microstructure-based multiscale constitutive modeling of γ—γ′ nickel-base superalloys. International Journal for Multiscale Computational Engineering 4, 663-692.

Wang, C., Li, R., 2004. Effect of double aging treatment on structure in Inconel 718 alloy. J. Mater. Sci. 39, 2593-2595.

Wen, W., Borodachenkova, M., Tomé, C.N., Vincze, G., Rauch, E.F., Barlat, F., Grácio, J.J., 2014. Mechanical behavior of Mg subjected to strain path changes: Experiments and modeling. Int. J. Plast.

Wlodek, S.T., Field, R.D., 1994. The effect of long time exposure on alloy 718. Superalloys 718, 625, 706 and Various Derivatives, 659-670.

Worthem, D.W., Robertson, I.M., Leckie, F.A., Socie, D.F., Altstetter, C.J., 1990. Inhomogeneous deformation in INCONEL 718 during monotonic and cyclic loadings. Metallurgical Transactions A 21, 3215-3220.

Xiao, L., Chen, D.L., Chaturvedi, M.C., 2005. Shearing of γ″ precipitates and formation of planar slip bands in Inconel 718 during cyclic deformation. Scripta Materialia 52, 603-607.

Xiao, L., Chen, D.L., Chaturvedi, M.C., 2008. Cyclic deformation mechanisms of precipitation-hardened Inconel 718 superalloy. Materials Science and Engineering: A 483–484, 369-372.

Xie, X., Dong, J., Wang, G., You, W., 2005a. The effect of Nb, Ti, Al on precipitation and strengthening behavior of 718 type superalloys, in: Loria, E.A. (Ed.), Superalloys 718, 625, 706 and Derivatives 2005, TMS (The Minerals, Metals & Materials Society), pp. 287-298.

Xie, X., Dong, J., Wang, G., You, W., Du, J., Zhao, C., Wang, Z., Loria, E., 2005b. The effect of Nb, Ti, Al on precipitation and strengthening behavior of 718 type superalloys. Superalloys 718, 625-706.

Yamaguchi, M., Paidar, V., Pope, D.P., Vitek, V., 1982. Dissociation and core structure of 〈110〉 screw dislocations in $L1_2$ ordered alloys I. Core structure in an unstressed crystal. Philosophical Magazine A 45, 867-882.

Yoo, M.H., Fu, C.L., Horton, J.A., 1994. Crack-tip dislocations and fracture behavior in Ni_3Al and Ni_3Si. Materials Science and Engineering: A 176, 431-437.

Yu, H.F., Jones, I.P., Smallman, R.E., 1994. The effects of temperature, composition and strain rate on the deformation microstructure of Ni_3Al. Philosophical Magazine A 70, 951-967.

Zecevic, M., Beyerlein, I.J., Knezevic, M., 2017. Coupling elasto-plastic self-consistent crystal plasticity and implicit finite elements: Applications to compression, cyclic tension-compression, and bending to large strains. Int. J. Plast. 93, 187-211.

Zecevic, M., Knezevic, M., 2015. A dislocation density based elasto-plastic self-consistent model for the prediction of cyclic deformation: Application to Al6022-T4. Int. J. Plast. 72, 200-217.

Zecevic, M., Knezevic, M., 2017. Modeling of Sheet Metal Forming Based on Implicit Embedding of the Elasto-Plastic Self-Consistent Formulation in Shell Elements: Application to Cup Drawing of AA6022-T4. JOM 69, 922-929.

Zecevic, M., Knezevic, M., Beyerlein, I.J., Tomé, C.N., 2015. An elasto-plastic self-consistent model with hardening based on dislocation density, twinning and de-twinning: Application to strain path changes in HCP metals. Mater. Sci. Eng. A 638, 262-274.

Zecevic, M., Korkolis, Y.P., Kuwabara, T., Knezevic, M., 2016. Dual-phase steel sheets under cyclic tension–compression to large strains: Experiments and crystal plasticity modeling. J. Mech. Phys. Solids 96, 65-87.

Zhao, R., Han, J.Q., Liu, B.B., Wan, M., 2016. Interaction of forming temperature and grain size effect in micro/meso-scale plastic deformation of nickel-base superalloy. Materials & Design 94, 195-206.

Chapter 2: Experimental characterization and crystal plasticity modeling of anisotropy, tension-compression asymmetry, and texture evolution of additively manufactured Inconel 718 at room and elevated temperatures

This chapter was published as “Experimental characterization and crystal plasticity modeling of anisotropy, tension-compression asymmetry, and texture evolution of additively manufactured Inconel 718 at room and elevated temperatures” in the International Journal of Plasticity, 125 (2020): 63-79. The Authors of this paper are Saeede Ghorbanpour, Md Ershadul Alam, Nicholas C Ferreri, Anil Kumar, Brandon A McWilliams, Sven C Vogel, Jonathan Bicknell, Irene J Beyerlein, Marko Knezevic. My contribution to this chapter was developing the crystal plasticity model, performing the simulations, and generating all the crystal plasticity simulation results.

Experimental characterization and crystal plasticity modeling of anisotropy, tension-compression asymmetry, and texture evolution of additively manufactured Inconel 718 at room and elevated temperatures

Abstract

In this work, strength and microstructural evolution of superalloy Inconel 718 (IN718) are characterized as a function of the initial microstructure created via direct metal laser melting (DMLM) additive manufacturing (AM) technology along with subsequent hot isostatic pressing (HIP) and heat treatments as well as wrought processing. Stress-strain curves are measured in tension and compression from room temperature to 550 °C and crystallographic texture is characterized using neutron diffraction. Furthermore, a recently developed crystal plasticity model incorporating the effects of precipitates is extended to interpret the temperature dependent deformation behavior of the alloy. The model accounts for solid solution, precipitate shearing, and grain size and shape contributions to initial slip resistance, which evolves with a dislocation density-based hardening law considering latent hardening, while non-Schmid effects are taken into account in the activation stress. Part of the experimental data is used for calibration of the model, while the rest is used for experimental validation of the model. It is shown that the model is capable of modeling the data with accuracy. Based on the comparison of the data and model predictions, it is inferred that the grain structure and texture give rise to plastic anisotropy of the alloy, while its tension-compression asymmetry results from non-Schmid effects and latent hardening.

1. Introduction

Inconel 718 (IN718) superalloy is well known for its high strength, toughness, and corrosion resistance and is widely used for a number of components operating under mechanical and thermal extremes (Barrett et al., 2018; Francis et al., 2014; Knezevic et al., 2012b; Knezevic and

Ghorbanpour, 2018; Kuo et al., 2009; Mei et al., 2015; Rao et al., 2003; Slama and Abdellaoui, 2000). Yet the parts for such applications are of complicated shape, requiring careful machining. Due to the high strength and hardness of alloy 718, the cutting tools wear relatively quickly translating into a high cost of machining. Additive manufacturing (AM) is a technology that can print complex shapes from powders, minimizing the need for machining. AM of the alloy and its behavior have recently been extensively studied (Amato et al., 2012; Gribbin et al., 2016).

The alloy has a relatively complex microstructure, featuring several precipitates and carbides in a γ matrix (Antolovich, 2015; Rao et al., 2003; Xiao et al., 2005). These are summarized in Table 1. These precipitates govern the behavior of the alloy. Their volume fraction and distribution depend on processing. For example, the content of δ precipitates was found to be significantly larger in AM IN718 (Gribbin et al., 2019) than wrought processing. Octahedral $\{111\}\langle 1\bar{1}0\rangle$ slip systems accommodate plastic deformation of γ matrix. Additionally, the activity of the six cubic {001}〈110〉 glide systems has been reported at the high temperatures associated with wrought processing of the alloy (Ding et al., 2004; Haddou et al., 2004; Österle et al., 2000; Semiatin et al., 2004).

Table 1. Phases in alloy IN718.

	Phase	Crystal structure	Space group	Composition	Lattice Parameters (Å)			References
					a	b	c	
Solid solution matrix	γ	Cubic	Fm-3m	Co,Cr,Ni,Fe - Based	3.59	-	-	(Murr et al., 2011) (Amato et al., 2012) (Murr et al., 2012)

Intermetallic	γ'	Cubic	Pm-3m	$Ni_3(Ti,Al,Nb)$	3.58	-	-	(Mukherji et al., 2003)
	γ"	Tetragonal	I4/mmm	Ni_3Nb	3.62	-	7.41	(Murr et al., 2011) (Amato et al., 2012) (Murr et al., 2012)
	δ	Orthorhombic	Pmmn	Ni_3Nb	4.55	4.25	5.11	(Amato et al., 2012)
Topographically close-packed (intermetallic)	η	Hexagonal	P63/mmc	$Ni_3(Ti,Al)$	5.10	-	8.30	(Evans et al., 2004)
	Laves	Hexagonal	P63/mmc	$(Ni,Cr,Fe)_2(Nb,Ti)$	4.83	-	7.88	(Manikandan et al., 2015)
Carbide	MC	Cubic	Fm-3m	(Nb,Ti)(C,N)	4.46	-	-	(Mostafa et al., 2017)
	$M_{23}C_6$	Cubic	Fm-3m	$(Cr,Fe)_{23}C_6$	10.60	-	-	(Evans et al., 2004)

The strengthening results from the γ′ and γ" precipitates, which are shearable by dislocations. After the dislocations cut through them, an anti-phase boundary (APB) in the precipitate is left behind. APB can further contribute to strengthening by increasing the energy of the crystal (Gleiter and Hornbogen,

1968; Huther and Reppich, 1978; Maciejewski et al., 2013). Therefore, knowledge of the values of APB energy would benefit an understanding of precipitate strengthening. For instance, the APB energy for the cubic planes was found to be lower than that for the octahedral planes (Umakoshi et al., 1984), which provided an explanation for why screw dislocations would tend to cross slip onto the {001} planes. The calculated values for APB energies for γ′ and γ" precipitates have been presented in our earlier study (Ghorbanpour et al., 2017). In contrast to γ′ or γ" strengtheners, the APB for δ precipitates has not been studied in the past, likely because of size of these precipitates. However, δ precipitates in AM alloy IN718 vary in size substantially and a fraction of them could be sheared (Gribbin et al., 2019), and thus quantification of their APB energy is warranted.

The stress-strain response of the alloy shows a pronounced tension-compression (T-C) asymmetry (Copley and Kear, 1967a, b; Keshavarz and Ghosh, 2015). These have been attributed to the complex microstructural features and the non-Schmid effects at the slip level (Bhattacharyya et al., 2015; Dao and Asaro, 1993; Knezevic and Bhattacharyya, 2017; Schmid and Boas, 1950). Relationships between microstructure, mechanisms, and mechanical behavior have been studied using microstructure-based constitutive laws (Francis et al., 2014; Keshavarz and Ghosh, 2015; Shenoy et al., 2008). These works have focused on room temperature behavior. Considerably less attention has been dedicated to modeling of high temperature plastic behavior. The anisotropic response of γ/γ' superalloy single crystals at 650 °C was examined in (Estevez et al., 1997; Hoinard et al., 1995). The hardening anisotropy was comparable to that of most anisotropic pure face-centered cubic (FCC) metals, likely because the hardening asymmetry on the octahedral slip systems is similar.

In this work, we study the stress-strain behavior of IN718 that has been additively manufactured at elevated temperatures of 450 °C and 550 °C, corresponding to typical service temperatures for this alloy. This work extends the elasto-plastic self-consistent (EPSC) mean-field homogenization, originally developed in (Barrett and Knezevic, 2019; Neil et al., 2010; Turner and Tomé, 1994; Zecevic et al., 2017; Zecevic and Knezevic, 2017, 2019) and recently advanced to P-EPSC for

IN718 (Ghorbanpour et al., 2017), to model temperature dependent behavior of IN718. The model incorporates latent hardening, a temperature-dependent initial slip resistance and a temperature-dependent hardening law that explicitly evolves a set of dislocation densities. The initial slip resistance accounts for the effects of grain shape and size and the formation of APB in precipitates as mobile dislocations shearing through them.

The model is calibrated and validated on the comprehensive set of data on IN718 that has been created by AM. We demonstrate its capability to replicate both the texture evolution and stress-strain response to large strains across a broad range of temperatures and the dependence of the mechanical behavior built in different directions. The model suggests that the anisotropy stems primarily from the texture and elongated grain structure oriented along the build direction, while asymmetry is due to non-Schmid activation and latent hardening.

2. Material and experiments

2.1 Additive manufacturing

The compression/tension specimens have been fabricated using direct metal laser melting (DMLM) in the EOS M280 machine. The powder produced by gas atomization had an average diameter of 35 μm, and a range of < 1 μm to 80 μm. The chemical composition is given in Table 2, meeting the chemical composition of the IN718 standard. Details pertaining to DMLM are given in (Gribbin et al., 2016). The material was printed in the form of bars and rods, which were subsequently machined into the samples for testing. Three categories of the DMLM IN718 samples are prepared for testing in tension and compression to evaluate the effect of their associate microstructures on strength. The three categories are different orientations with respect to the build direction (BD) and will be labeled as: H-horizontal, D-diagonal at 45°, and V-vertical. Hot isostatic pressing (HIP) treatment was done for a set of samples at 1163 °C for 4 h under 100 MPa. Finally, samples of wrought IN718 were machined from a shaped forging with sample loading direction perpendicular to the axial direction. The samples of

every material category were heat treated (HT) after machining according to AMS 5663. The AMS 5663 HT is a solution treatment at 954 °C for 1 h, fan cooling in argon to below 120 °C, and double aging. The double aging involves holding samples at 718 °C for 8 h, followed by furnace cooling at a rate of 50 °C/h to 621 °C, holding at 621 °C for 8 h, and finally air cooling to room temperature.

Table 2. Alloy IN718 composition in wt%.

Ni	Cr	Nb	Mo	Ti	Mn	Si	Cu	Al	C	S	P	B	Fe
55.5	18.2	5.5	3.3	1.15	0.35	0.35	0.3	0.3	0.08	0.015	0.015	0.006	Bal

2.2 Texture and microstructure

Electron backscattered diffraction (EBSD) characterization of grain structure in the three material categories have been presented in (Gribbin et al., 2019). In the present paper, the bulk texture in the samples before and after deformation was measured using neutron diffraction.

2.3 Mechanical testing

Room temperature (RT) tensile data is taken from (Gribbin et al., 2016; Smith et al., 2016), while room temperature compression data for DMLM materials is taken from (Smith et al., 2016). Room temperature compression testing of the DMLM + HIP and wrought samples is performed here for the first time. Consistent with the procedure presented in (Ghorbanpour et al., 2019a, b; Jahedi et al., 2017; Knezevic et al., 2010; Smith et al., 2016), these tests are performed on an Instron Model # 1350 servohydraulic testing machine with DAX software and controller. The machine was equipped with a customized compression fixture consisting of two cylindrical compression dies aligned vertically along the axis of the actuator. Compliance of the testing setup was measured by compressing the dies without a specimen to correct the raw data before computing the true stress–true strain curves. The

samples were compressed to a true strain of approximately 0.5 (i.e. the tests are interrupted before sample fracturing). Three samples are tested per category.

Tensile testing at two different test temperatures (450 °C and 550 °C) was carried out on subsized, flat and dog-bone shaped specimens with a nominal gage section of 12.7x3.0x1.2 mm. First, the gage section of these DMLM IN718 specimens was machined down, by the electrical discharge machining (EDM), to half of their original length to reduce the force required to break the specimens, and to facilitate high temperature friction gripping without slippage. All the machined specimens were polished up to 1500 grit SiC paper to remove surface oxidation (if any) and damage caused by the EDM. They were then cleaned in ultrasonic vibrator using water. An MTS 810 servo-hydraulic universal testing machine (capacity: 250 kN) equipped with a clamshell furnace (MTS 657.02, capacity 1600 °C) was used to conduct the tests in the air at 450 °C and 550 °C, with ±1 °C accuracy. The specimens were heated to the target temperature at load-control mode and held for 30 min before shifting to displacement control for testing at a displacement rate of 0.75 mm/min, or a strain rate $\approx 10^{-3}$/s. A high temperature extensometer (MTS 632.53E-11, range: ±20% of 25.4 mm), with ceramic arms extending into the furnace, was used to measure the specimen displacement. The load and displacement of the actuator were also recorded for verification. The samples were deformed to failure. Tensile properties were determined according to the ASTM test standard E8M-13 (2013).

Simple compression tests were conducted on cylindrical IN718 specimens, EDMed down to 4 mm diameter from their original 6 mm diameter in order to reduce the load required to deform the specimens at high temperature. However, to maintain consistency with the room temperature test (Smith et al., 2016), the length to diameter ratio was kept 1.2. Both surfaces of the specimens are polished using 1500 grit SiC paper.

All compression tests were performed on the same MTS 810 machine, and using the same furnace and extensometer as the high-temperature tensile tests. However, the machine was equipped with a

customized compression fixture consisting of two cylindrical compression dies aligned vertically along the axis of the actuator. The compression dies are made of Inconel with smooth, flat surfaces. Tungsten carbide (WC) bearing blocks (5 mm thick, 20 mm diameter), also flat-surfaced, were used at both sides of the dies to protect the face of the Inconel dies and to help transmit the axial load. Boron nitride spray-II was used to minimize the effects of contact friction between the faces of the specimen and the upper and lower compression dies and blocks. All the dies and the blocks were aligned before tests and found parallel to the loading axis after tests.

The samples were compressed to a true strain of approximately −0.25 to −0.4. The maximum strain is determined by the maximum compressive load that the WC can bear (25 kN–30 kN) before shattering at that temperature. The tests were performed at a strain rate of 10^{-3}/s in the air at 550 °C. Three samples were deformed per category to ensure the reputability and accuracy of the measured data. Compression test loads and displacements were measured in accordance with the ASTM E209, 2018, ASTM E9-09, 2018.

3. Experimental results

This section presents results of mechanical testing and texture characterization for alloy IN718.

3.1 Texture and microstructure

The initial grain structure in all samples (DMLM, DMLM + HIP, and wrought) were characterized previously in (Gribbin et al., 2019). It was found that the DMLM material exhibits a strongly elongated grain structure along the deposition direction (average major and minor axis of 130 μm and 25 μm, respectively), while the aspect ratio is significantly reduced in the DMLM + HIP material but grains are much coarser (average major and minor axis of 280 μm and 80 μm, respectively). Incoherent annealing twins are introduced in the microstructure by HIP treatment. Wrought material exhibits an equiaxed grain structure of approximately 105 μm and a large fraction of the coherent twin boundaries. Porosity content was also studied in the earlier work (Smith et al., 2016). The content of

porosity in the DMLM material was found to be approximately 0.18% with 0% in DMLM + HIP and wrought.

It was found that the δ precipitates in the DMLM material were intragranular with some present along the grain boundaries (GBs) (Gribbin et al., 2019). In contrast, the δ precipitates in the DMLM + HIP and wrought materials were primarily along the GBs. The high fraction of intragranular δ precipitates in the DMLM sample was attributed to heterogeneity in the solidification microstructure that occurred during the DMLM process, whereas localized inter-dendritic regions can have relatively high concentrations of Nb and Ni (Lass et al., 2017). GB δ precipitates in DMLM + HIP and wrought samples were much larger than those in the DMLM. The DMLM + HIP and wrought samples also contain carbides. Existence of δ precipitates of variable size in the DMLM material suggests that both shearing and looping hardening mechanisms will be activated during their interaction with mobile dislocations. Due to their size in IN718 both γ" and γ′ are shearable. In addition to shearing of γ" and γ', the shearing contribution from the δ phase is also considered but the contribution is very small. Importantly, we have been able to fit the initial slip resistance without considering any looping, which suggests that looping has a minimal effect in alloy IN718. The content of δ precipitates was 7.9% in DMLM, while only 0.7% in DMLM + HIP and 0.8% in wrought (Ferreri et al., 2019).

Crystallographic texture has also been characterized using EBSD (Smith et al., 2016). However, the micro technique is not well suited to do so, especially for coarse grained materials. In the present work, the textures have been characterized using neutron diffraction (figure 1). As shown, a moderately strong <100> fiber along the deposition direction is found for DMLM. As a result of the preferential grain structure and texture, the mechanical response will vary among the V, D, and H samples. Texture in the DMLM + HIP material is even weaker, which is a consequence of static recrystallization and grain growth. Texture in the wrought material is a consequence of the ring rolling process. Weak to moderately strong textures in the samples will likely have a secondary effect on the plastic behavior of these materials.

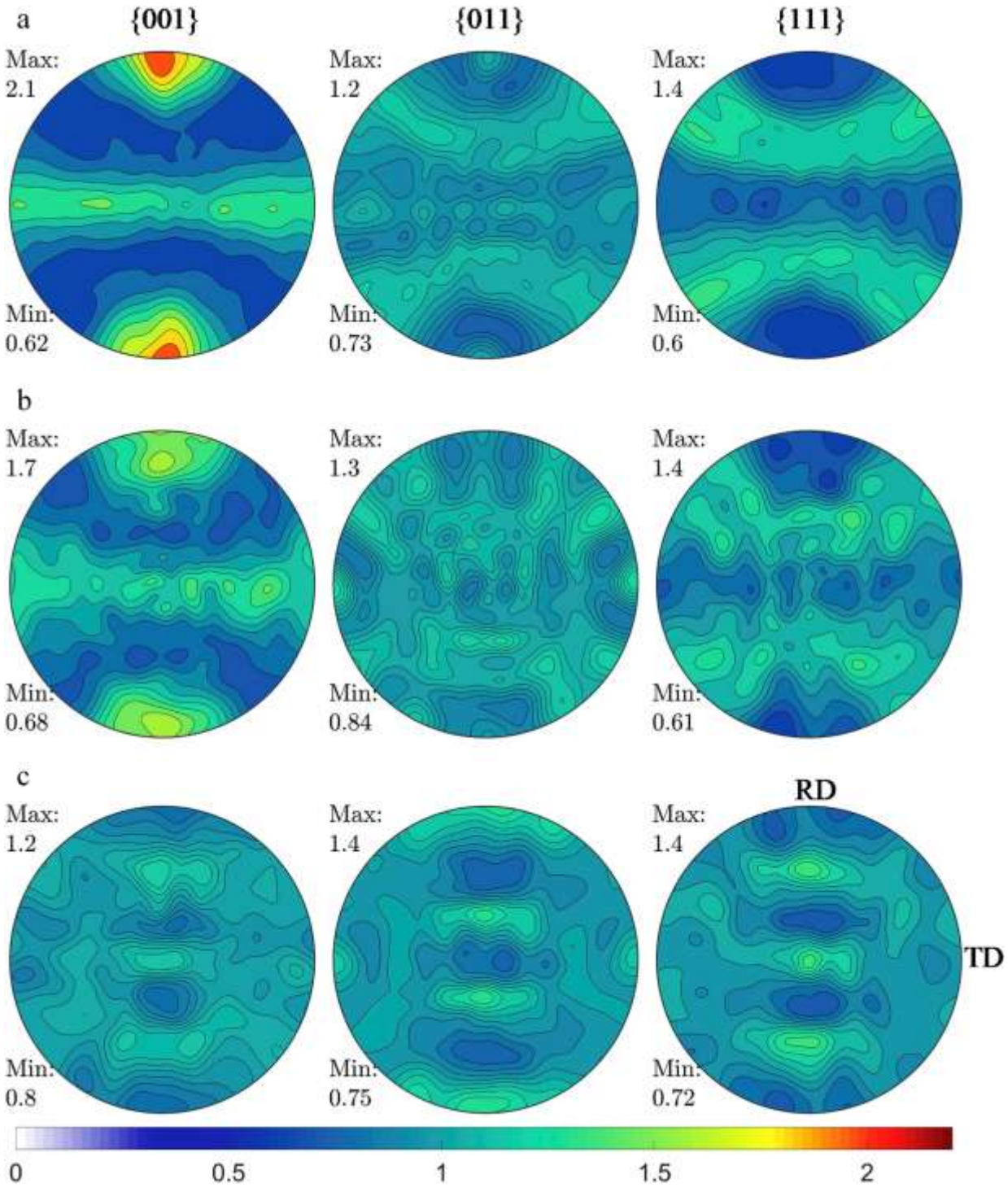

Figure 1. Stereographic pole figures as measured using the neutron diffraction technique showing the initial crystallographic texture in the samples of IN718: (a) DMLM, (b) DMLM + HIP, and (c) wrought. BD is vertical for (a) and (b).

3.2 Stress-strain response

Figure 2 shows the measured true stress-true strain data at room temperature and two elevated temperatures 450 °C and 550 °C. The DMLM samples are stronger in tension and compression than DMLM + HIP and wrought materials. However, wrought and DMLM + HIP samples show more elongation to fracture. Initial microstructures of the samples govern such behavior. The DMLM material contains some porosity limiting its elongation to fracture. The DMLM material exhibits much smaller grains than wrought and DMLM + HIP, making it stronger, as explained below. The difference in the behavior between the DMLM V, H, and D samples is driven by the grain morphology and texture. As explained earlier, the HIP treatment changes the structure to a coarse-grained one and randomizes the texture. The treatment also dissolves the precipitates, including the δ precipitates, and rebuilds them in different amounts. These δ precipitates are not dissolved during the subsequent heat treatment per AMS 5663. Thus, the material is comparatively softer and more ductile than the DMLM material without HIPing. The wrought material also has a coarser grain structure making it weaker than the DMLM material. Among the room temperature tests on the DMLM material, the V sample shows relatively lower strength than the H and D counterparts, both in tension and compression (figure 2). This trend also persists at high temperatures, although the difference in strengths among the V, H, and D samples has slightly reduced. Since presented in the form of true stress-true strain, the provided elevated temperature tensile data is up to the maximum load point, meaning that the softening portion of the curves is not shown. The 0.2% yield strength (YS) slightly decreases with increasing temperature from RT to 550 °C, but are still comparable (especially for DMLM D and H) to the room temperature HIPed and wrought alloy (Table 3). However, DMLM samples in all three build directions exhibited some T-C asymmetry, which will be shown using modeling results.

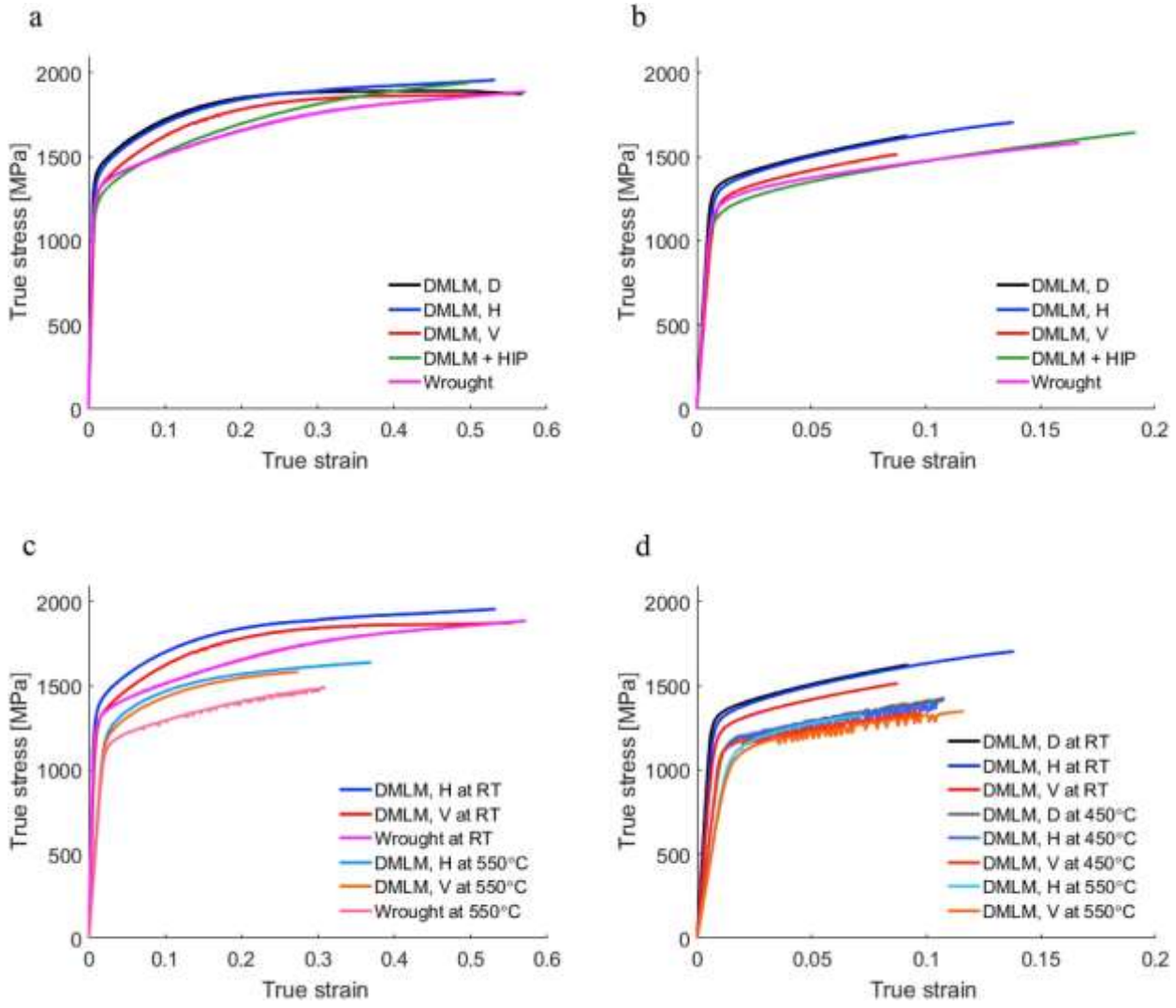

Figure 2. Simple tension and compression responses of IN718 as a function of sample orientation and temperature measured under 0.001/s strain rate: (a) compression: DMLM along D, H, and V, DMLM + HIP, and wrought at RT, (b) tension: DMLM along D, H, and V, DMLM + HIP, and wrought at RT, (c) compression: DMLM along V and H, and wrought at RT, DMLM along V and H, and wrought at 550 °C, (d) tension: DMLM along V, D, and H at RT, DMLM along V, D, and H at 450 °C, DMLM along V, and H at 550 °C. The samples tested in tension went to fracture, while those tested in compression were interrupted before fracture.

Some of the high temperature stress-strain curves for tensile test shown in figure 2 reveal dynamic strain aging (DSA) or serration, which is common in some metals, including Ni-based alloys that generally occurs during plastic deformation within a specific temperature range and strain rate (Beese et al., 2018; Cai et al., 2017; Hayes and Hayes, 1982; Maj et al., 2014; Mannan, 1993). In our case, type-C serration was seen of tested specimens for all three DMLM samples at 450 °C, and only for

DMLM-V sample at 550 °C in tension, although their spacing and stress-amplitude vary (see figure 2). A critical strain is also required to initiate the serrated response, which is ~0.02 at 450 °C for all three DMLD specimens, ~0.035 for DMDL-V at 550 °C. It is widely accepted that the DSA occurs due to the interaction between diffusing solute atoms and mobile dislocations that are blocked by these solute atoms and strengthen materials.

Table 3. Yield stress estimates at 0.2% offset strain in tension and compression (expressed in [MPa]). The values are average of 2 or 3 tests.

	DMLM, V	DMLM, D	DMLM, H	DMLM+HIP	Wrought
Tension at RT	1215	1305	1290	1105	1170
Compression at RT	1255	1370	1345	1125	1205
Tension at 450 ℃	1110	1130	1125	-	-
Tension at 550 ℃	1015	-	1045	-	-
Compression at 550 ℃	1135	-	1160	-	1100

When the stress reaches a critical value, these mobile dislocations are released and thereby a lower stress is needed for deformation, resulting serration in the stress-strain curve (Beese et al., 2018; Cai et al., 2017; Maj et al., 2014). We note that the compression test at 550 °C for all three DMLM specimens did not show such a serrated response or DSA. On the contrary, the IN718-wrought (forged) sample exhibited serration at the same temperature in compression. This finding is consistent with (Beese et al., 2018), who observed DSA for conventionally processed Inconel 625, whereas an absence of DSA for the AM-processed counterpart during compression at 600 °C. The presence of coarser precipitates, especially carbides, at grain boundaries is the main reasons for serration of

wrought IN718 (Beese et al., 2018; Mannan, 1993; Weaver and Hale, 2001). The DMLM processed IN718 does not contain coarser carbide and delta phases at grain boundaries but much more dispersed intra-granular delta phases (Gribbin et al., 2019). The dislocation arrest theory (proposed by (Sleeswyk, 1958)) and supported by many subsequent works (Beese et al., 2018; Hayes and Hayes, 1984)) assumes that solute atmospheres (carbon atoms) form on forest dislocations. At room/low temperature, solute atoms are immobile within the lattice, however, they become mobile along with dislocations at higher temperature. As mobile dislocations glide under applied loading, they encounter obstacles like immobile forest dislocation surrounded by solute ambience. The obstacles could temporarily or permanently arrest mobile dislocations. If temporarily, during the waiting time, solute atoms drain from forest dislocations to mobile dislocations via pipe diffusion. This accumulation of solute atoms in mobile dislocations further strengthens the obstacles that raise the critical stress needed to overcome these obstacles. When the applied flow stress exceeds the critical stress, these mobile dislocations quickly move to the next obstacles (with increased strain and relaxed stress). The process repeats leading to the serration. For DMLM processed IN718, these mobile dislocations are obstructed by the finely distributed precipitates at the grain interior whit high dispersion hardening effect. The precipitates can react with carbon and act as sinks for solute atoms; therefore, draining carbon from the mobile dislocation rather than forming obstacles. However, for wrought IN718, the large carbides and delta phases are coarsely distributed, mostly along the grain boundaries, so, the probability for arresting mobile dislocations is low because of low dispersion hardening effect. This allows mobile dislocations to move freely until arrest at the forest dislocations, and dislocation pipe diffusion mechanism dominates during waiting time, resulting in serration during deformation. Details of the dislocation arrest theory can be found in (Beese et al., 2018; Hayes and Hayes, 1984; Sleeswyk, 1958). Grain size and texture also play their role on DSA behavior (Beese et al., 2018; Mannan, 1993). It is also well established that the negative strain rate sensitivity of the flow stress is correlated with DSA phenomena (Beese et al., 2018; Hayes and Hayes, 1984; Mannan, 1993).

4. Modeling framework

The recently developed P-EPSC (Ghorbanpour et al., 2017) is advanced here into a temperature dependent constitutive law for IN718, by applying it to model the behavior of the alloy across a temperature range from room to 550 °C. The model integrates a dislocation density-based hardening law. While precipitates are not modeled explicitly because of their size, the model takes into account the effect of the APB formation in γ', γ'', and δ precipitates into the slip resistance. Finally, the model considers latent hardening and non-Schmid activation stresses. In our description, we use "·" to denote a dot product and "⊗" to denote a tensor product.

The EPSC model represents a polycrystal as an aggregate of grains with a distinct crystallographic orientation and volume fraction. Each grain is modeled as an elasto-plastic ellipsoid inclusion in a homogeneous medium. The constitutive response of the polycrystalline aggregate is assumed to follow a linear relationship given by:

$$\widehat{\boldsymbol{\sigma}} = \mathbf{L}\dot{\boldsymbol{\varepsilon}}, \tag{1}$$

where $\mathbf{L}$ is the instantaneous elasto-plastic stiffness tensor of the polycrystal, $\widehat{\boldsymbol{\sigma}}$ is the macroscopic Jaumann stress rate, and $\dot{\boldsymbol{\varepsilon}}$ the strain rate. The self-consistent scheme solves for $\mathbf{L}$ iteratively (Turner and Tomé, 1994) until equilibrium and strain compatibility are satisfied (Eshelby, 1957). The polycrystalline $\dot{\boldsymbol{\varepsilon}}$ is related to the strain rate of the individual crystals $\dot{\boldsymbol{\varepsilon}}^c$ according to

$$\dot{\boldsymbol{\varepsilon}}^c = \mathbf{A}^c\dot{\boldsymbol{\varepsilon}}, \tag{2}$$

where $\mathbf{A}^c = \left(\mathbf{L}^c + \mathbf{L}^{c^*}\right)^{-1}\left(\mathbf{L}^{c^*} + \mathbf{L}\right)$ is the localization tensor for the ellipsoidal inclusion c, $\mathbf{L}^c$ is its instantaneous elasto-plastic stiffness tensor and $\mathbf{L}^{c^*} = \mathbf{L}\left(\mathbf{S}^{c^{-1}} - \mathbf{I}\right)$ is its effective stiffness tensor. Note that the latter contains the symmetric Eshelby tensor $\mathbf{S}^c$. $\mathbf{I}$ is the fourth rank identity matrix. The tensor $\mathbf{L}^{c^*}$ relates the grain stress and total strain rate to the polycrystalline (i.e., homogeneous medium) stress and total strain rate through an interaction equation, given by

$$(\widehat{\boldsymbol{\sigma}}^{\boldsymbol{c}} - \widehat{\boldsymbol{\sigma}}) = -\mathbf{L}^{c^*}(\dot{\boldsymbol{\varepsilon}}^{c} - \dot{\boldsymbol{\varepsilon}}),$$

In the self-consistent scheme, the polycrystal stress and strain rate are enforced to be equal to the volume average of the stress and strain rate in all grains:

$$\widehat{\boldsymbol{\sigma}} = \langle \widehat{\boldsymbol{\sigma}}^{c} \rangle, \tag{3}$$

and

$$\dot{\boldsymbol{\varepsilon}} = \langle \dot{\boldsymbol{\varepsilon}}^{c} \rangle, \tag{4}$$

The above conditions lead to the following expression for L:

$$\mathbf{L} = \langle \mathbf{L}^{c}\mathbf{A}^{c} \rangle \langle \mathbf{A}^{c} \rangle^{-\mathbf{1}}. \tag{5}$$

Finally, the macroscopic stress is updated using the following relationship between the Cauchy stress rate and Jaumann rate

$$\dot{\boldsymbol{\sigma}} = \widehat{\boldsymbol{\sigma}} + \langle \mathbf{W}^{\mathbf{c}}\boldsymbol{\sigma}^{\mathbf{c}} \rangle - \langle \boldsymbol{\sigma}^{\mathbf{c}}\mathbf{W}^{\mathbf{c}} \rangle = \mathbf{L}\dot{\boldsymbol{\varepsilon}} + \langle \mathbf{W}^{\mathbf{c}}\boldsymbol{\sigma}^{\mathbf{c}} \rangle - \langle \boldsymbol{\sigma}^{\mathbf{c}}\mathbf{W}^{\mathbf{c}} \rangle,$$

where $\mathbf{W}^{\mathbf{c}}$ is elastic spin of crystal c. The macroscopic Cauchy stress is solved by explicit time integration, i.e., $\boldsymbol{\sigma}_{n+1} = \boldsymbol{\sigma}_n + \mathbf{L}_n\dot{\boldsymbol{\varepsilon}}_n\Delta t + \langle \mathbf{W}_n^c\boldsymbol{\sigma}_n^c \rangle \Delta t - \langle \boldsymbol{\sigma}_n^c\mathbf{W}_n^c \rangle \Delta t$.

For an individual grain, the constitutive relationship is:

$$\widehat{\boldsymbol{\sigma}}^{c} = \mathbf{C}^{c}(\dot{\boldsymbol{\varepsilon}}^{c} - \textstyle\sum_{\mathrm{s}} \mathbf{m}^{c,s}\dot{\gamma}^{c,s}) - \boldsymbol{\sigma}^{c} tr(\dot{\boldsymbol{\varepsilon}}^{c}), \tag{6}$$

where the grain Jaumann stress rate is $\widehat{\boldsymbol{\sigma}}^{c}$, the grain strain rate is $\dot{\boldsymbol{\varepsilon}}^{c}$, the grain stiffness tensor is $\mathbf{C}^{c}$ and the grain plastic strain rate is $\sum_{\mathrm{s}} \mathbf{m}^{c,s}\dot{\gamma}^{c,s}$. The latter is given by the sum of the product of the shear strain rates, $\dot{\gamma}^{c,s}$, from each slip system, s, and the tensor $\mathbf{m}^{c,s} = 0.5(\mathbf{b}^{c,s} \otimes \mathbf{n}^{c,s} + \mathbf{n}^{c,s} \otimes \mathbf{b}^{c,s})$, which is the symmetric part of the Schmid tensor for slip system s. The Schmid tensor is calculated as the tensor product of $\mathbf{b}^{c,s}$ and $\mathbf{n}^{c,s}$, the orthonormal unit vectors representing the slip direction and

slip plane normal, respectively. Since the grain orientation can change during deformation, the elastic stiffness and Schmid tensors are updated at the beginning of each deformation increment.

Due to the core structure of dislocations in Ni-based superalloys, non-Schmid effects can be important. Non-Schmid effects are included in the crystal level constitutive law via the introduction of a non-Schmid tensor $\mathbf{m}_{ns}^{c,s}$. To define $\mathbf{m}_{ns}^{c,s}$, we consider five non-glide stress components: the two shear stresses $\mathbf{t}^{c,s}\otimes\mathbf{b}^{c,s}$ and $\mathbf{t}^{c,s}\otimes\mathbf{n}^{c,s}$, acting normal to the Burgers vector and the three normal stresses $\mathbf{n}^{c,s}\otimes\mathbf{n}^{c,s}$, $\mathbf{t}^{c,s}\otimes\mathbf{t}^{c,s}$, and $\mathbf{b}^{c,s}\otimes\mathbf{b}^{c,s}$. These components are related to the non-Schmid tensor via (Dao and Asaro, 1993; Knezevic et al., 2014a; Lim et al., 2013; Savage et al., 2017):

$$\mathbf{m}_{ns}^{c,s} = c_1(\mathbf{t}^{c,s}\otimes\mathbf{b}^{c,s}) + c_2(\mathbf{t}^{c,s}\otimes\mathbf{n}^{c,s}) + c_3(\mathbf{n}^{c,s}\otimes\mathbf{n}^{c,s}) + c_4(\mathbf{t}^{c,s}\otimes\mathbf{t}^{c,s}) - (c_3 + c_4)(\mathbf{b}^{c,s}\otimes\mathbf{b}^{c,s}), \tag{7}$$

The non-Schmid tensor is added to the Schmid tensor to give the total Schmid tensor where $\mathbf{m}_{tot}^{c,s} = \mathbf{m}^{c,s} + \mathbf{m}_{ns}^{c,s}$ to provide the stress used to activated slip:

$$\mathbf{m}^{c,s}\cdot\boldsymbol{\sigma}^{c} + \mathbf{m}_{ns}^{c,s}\cdot\boldsymbol{\sigma}^{c} = \mathbf{m}_{tot}^{c,s}\cdot\boldsymbol{\sigma}^{c}, \tag{8}$$

In Eq. (7), ci is the weighting coefficient for the non-Schmid effect i. Only four coefficients are needed since only four are independent under incompressible flow.

The relationship between the evolution of slip resistance, $\dot{\tau}_c^{c,s}$, and the rates of slip on other slip systems is given by (Zecevic and Knezevic, 2015; Zecevic and Knezevic, 2018a):

$$\dot{\tau}_c^{c,s} = \sum_{s'} h^{ss'}\,\dot{\gamma}^{c,s'}, \tag{9}$$

where $h^{ss'}$ is the hardening matrix. Expressions for $h^{ss'}$ are given in (Zecevic and Knezevic, 2015).

Combining relations (6) and (9) with $\mathbf{m}_{tot}^{c,s}\cdot\hat{\boldsymbol{\sigma}}^{c} = \dot{\tau}_c^{c,s}$ gives a set of linear equations for the shear rates:

$$\mathbf{m}_{tot}^{c,s}\cdot\left(\mathbf{C}^{c}\left(\dot{\boldsymbol{\varepsilon}}^{c} - \sum_{s'}\mathbf{m}^{c,s'}\dot{\gamma}^{c,s'}\right) - \boldsymbol{\sigma}^{c}tr(\dot{\boldsymbol{\varepsilon}}^{c})\right) = \sum_{s'} h^{ss'}\,\dot{\gamma}^{c,s'}. \tag{10}$$

These shear rates are related to the strain rate in crystal following

$$\dot{\gamma}^{c,s} = \left(\sum_{s'} \left(X^{ss'} \right)^{-1} \mathbf{m}_{tot}^{c,s'} \left(\mathbf{C}^c - \boldsymbol{\sigma}^c \otimes \mathbf{i} \right) \right) \cdot \dot{\boldsymbol{\varepsilon}}^c, \tag{11}$$

where

$$X^{ss'} = h^{ss'} + + \mathbf{C}^c \cdot \mathbf{m}_{tot}^{c,s} \otimes \mathbf{m}^{c,s'}. \tag{12}$$

Given the above, the modulus $\mathbf{L}^c$ that relates the grain strain rate and Jaumann rate according to

$$\hat{\boldsymbol{\sigma}}^c = \mathbf{L}^c \dot{\boldsymbol{\varepsilon}}^c, \tag{13}$$

can be calculated

$$\mathbf{L}^c = \mathbf{C}^c - \mathbf{C}^c \sum_s \mathbf{m}^{c,s} \otimes \left(\sum_{s'} \left(X^{ss'} \right)^{-1} \mathbf{m}_{tot}^{c,s'} \left(\mathbf{C}^c - \boldsymbol{\sigma}^c \otimes \mathbf{i} \right) \right) - \boldsymbol{\sigma}^c \otimes \mathbf{i}, \tag{14}$$

Finally, to update the texture, we calculate the lattice rotation rate tensor, $\mathbf{W}^c$, according to

$$\mathbf{W}^c = \mathbf{W}^{app} + \mathbf{\Pi}^c - \mathbf{W}^{p,c}, \tag{15}$$

where $\mathbf{W}^{app}$ is the applied rotation rate, $\mathbf{\Pi}^c$ is the antisymmetric part of the Eshelby tensor (Lebensohn and Tomé, 1993), and $\mathbf{W}^{p,c}$ is the plastic rotation rate. The latter is related to the slip system slip rates according to:

$$\mathbf{W}^{p,c} = \sum_s \mathbf{q}^{c,s} \dot{\gamma}^{c,s}, \tag{16}$$

where $\mathbf{q}^{c,s} = 0.5(\mathbf{b}^{c,s} \otimes \mathbf{n}^{c,s} - \mathbf{n}^{c,s} \otimes \mathbf{b}^{c,s})$.

4.1 First-principles calculations of APB energy for the delta phase in IN718

In prior work, the values of the APB energy within the two γ′ and γ" precipitates were calculated using density functional theory (DFT) (Ghorbanpour et al., 2017). In this work, we additionally calculate the APB energy for the δ phase. The APB energy values are used in the initial slip resistance equations described in the previous section.

To calculate the generalizes stacking fault energy (GSFE) in the delta phase of Ni_3Nb, we performed DFT calculations using the Vienna Ab initio Simulation Package (VASP) code (Kresse and Furthmüller, 1996; Kresse and Hafner, 1994). For exchange correlation functional in DFT, we used generalized gradient approximation (GGA) with the Perdew-Becke-Ernzerhof (PBE) parametrization (Perdew et al., 1996) and Projector-Augmented Wave (PAW) pseudopotentials for the interaction between valence electrons and ionic cores (Blöchl, 1994; Kresse and Joubert, 1999). The numbers of valence electrons are 10 and 13 for the Ni and Nb pseudopotentials, respectively. For the calculations of the lattice constants of the cubic primitive unit cell, we used a 19 × 19 × 19 Γ-centered Monkhorst Pack k-point to integrate the Brillouin Zone. We used a plane wave energy cutoff of 400 eV, and optimized the atomic structure until the force on each atom is smaller than 0.01 eV/Å.

The crystal structure of the delta phase is orthorhombic. The calculated lattice constants for the orthorhombic structure (space group #59) are given in Table 1. To calculate the GSFE curves on (100) plane in Ni_3Nb, we take a periodic supercell consisting of 64 atoms (48 Ni and 16 Nb atoms) as shown in figure 3a. Supercell consists of a 15 A thick vacuum layer along the direction normal to slip plane. As shown in figure 3a, there are two interlayer distances (0.72 Å and 1.44 Å) along normal to (100) plane. figure 3b and c shows the calculated GSFE curves for the interlayer 2 (separation 1.44 Å) and interlayer 1 (separation 0.72 Å) along three directions respectively. The calculated antiphase boundary (APB) energy on the (100) plane is 65 mJ/m^2.

4.2 Initial resistance to slip

Initial slip resistance is expressed as

$$\tau_0^S = \tau_{0,ss} + \tau_{0,HP}^S + \tau_{0,shear}. \quad (17)$$

The contributing terms to the slip resistance are the solid solution strengthening, the Hall-Petch-like barrier effect, and precipitates shearing effect.

The first term is given by

$$\tau_{0,ss} = \frac{1}{M}\sum \frac{d\sigma}{d\sqrt{g_i}}\sqrt{g_i} \quad (18)$$

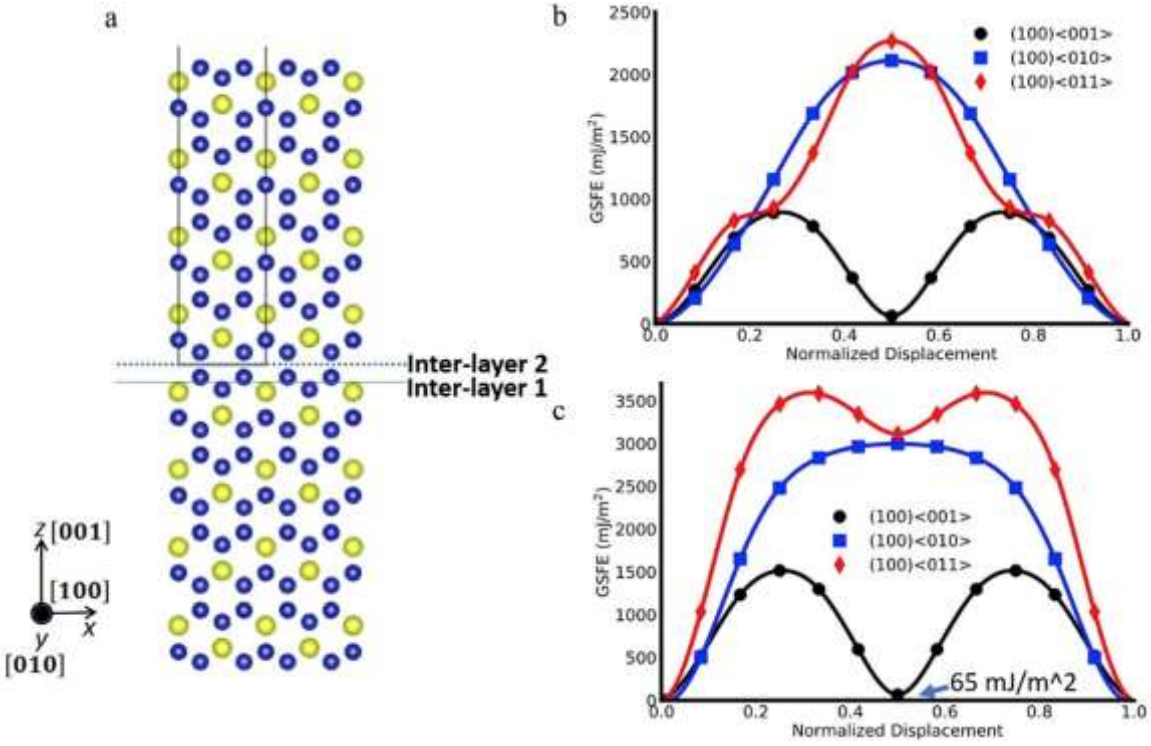

Figure 3. Generalizes stacking fault energy (GSFE) curves along three directions on (100) plane for Ni_3Nb in the δ phase. Nb atoms are shown in yellow and Ni atoms are shown in blue. (For interpretation of the references to colour in this figure legend, the reader is referred to the Web version of this article.)

where M is the Taylor factor, g is the atomic fraction, and $\frac{d\sigma}{d\sqrt{g_i}}$ is the strengthening coefficient of the solute elements in IN718, which are taken from (Roth et al., 1997). Using these values in Eq. (18) along with M for the measured texture, the solid solution strengthening contribution is 263.2 MPa.

The second term is

$$\tau^{S}_{0,HP} = \frac{H\,\mu_{\mathrm{IN718}}\sqrt{b}}{\sqrt{d^{S}_{mfp}}}, \quad (19)$$

with

$$d_{mfp}^{s} = \frac{2}{\sqrt{\left(\frac{\hat{b}_x^s}{a}\right)^2 + \left(\frac{\hat{b}_y^s}{b}\right)^2 + \left(\frac{\hat{b}_z^s}{c}\right)^2}} \quad (20)$$

where H, b, d_{mfp}^{s}, and μ_{IN718} are the Hall-Petch coefficient per slip mode, the Burgers vector for the <110> dislocations ($b = 2.492\ 10^{-10}\ m$), the mean free path for a given slip system s, and the shear modulus of the alloy, respectively. Component, $\hat{b}_x^s, \hat{b}_y^s, \hat{b}_z^s$, represent a unit vector in the Burgers direction expressed in a frame of the ellipsoid of size a, b, and c. The value calculated using Eq. (19) averaged over many grains is 67.9 MPa.

The remaining term is (Courtney, 1990; Maciejewski et al., 2013)

$$\tau_{0,shear} = 0.7\mu_{\gamma'}\left(\frac{\mathrm{APB}_{\gamma'}}{\mu_{\gamma'}b_{\gamma'}}\right)^{\frac{3}{2}}\left(\frac{f_{\gamma'}\bar{r}_{\gamma'}}{b_{\gamma'}}\right)^{\frac{1}{2}} + 0.7\mu_{\gamma''}\left(\frac{\mathrm{APB}_{\gamma''}}{\mu_{\gamma''}b_{\gamma''}}\right)^{\frac{3}{2}}\left(\frac{f_{\gamma''}\bar{r}_{\gamma''}}{b_{\gamma''}}\right)^{\frac{1}{2}} + 0.7\mu_{\gamma''}\left(\frac{\mathrm{APB}_{\delta}}{\mu_{\delta}b_{\delta}}\right)^{\frac{3}{2}}\left(\frac{f_{\delta}\bar{r}_{\delta}}{b_{\delta}}\right)^{\frac{1}{2}}, \quad (21)$$

where f is the volume fraction of the precipitate and $\bar{r}$ is the average radius of the precipitates. APB values for γ' and γ" have been provided in (Ghorbanpour et al., 2017). In this work, we provide the value for δ based on the DFT calculations. As noted above, not all δ precipitates are shearable. Only a small fraction of 1 % is assumed shearable. Table 4 presents the input values for Eq. (21). The estimated value is 267.2 MPa.

Table 4. Data used for the calculation of $\tau_{0,shear}$ using Eq. (21).

	APB $[\frac{mJ}{m^2}]$	μ [GPa]	b [nm] $\frac{a}{2}\langle 110\rangle$	f [%]	$\bar{r}$ [nm]
γ'	207	78.2	0.254912	13.2	12.5
γ''	378	72.6	0.256255	2.9	5.85
δ	65	84.3	0.3217	1	10

The initial slip resistance depends on temperature and the values calculated above use input that are applicable to RT. Note, the RT value was obtained with no calibration constants. With measured

material response at elevated temperatures, we have the opportunity to characterize this temperature dependence in initial slip resistance. In doing so, we assume that the net value of the resistance considering all contributions will decrease with increases in temperature from room temperature. Individually, the first term in the equation for the initial slip resistance represents the resistance from lattice friction and it is assumed that the increase in lattice vibrations with increase in temperature results in a reduction in this value as a result of weaker atomic bond strength at high temperatures. The second term decrease as well since it aids slip transfer across the grain boundaries. The third term also depends on the temperature through the temperature dependence of APB energy and the shear modulus, which decrease with increases in temperature (Li et al., 2019). In summary, we do not calculate the temperature-dependent APB energy and the shear modulus but establish the temperature-dependent initial slip resistance by fitting the mechanical data.

4.3 Evolution of slip resistance

In this model, we allow for the slip resistance on individual slip systems to evolve with strain, temperature, and strain rate. The slip resistance is defined as (Ardeljan et al., 2014, 2015, 2016, 2017; Ardeljan and Knezevic, 2018; Jahedi et al., 2015; Knezevic et al., 2012a, 2013, 2015b, 2016):

$$\tau_c^s = \tau_0 + \tau_{forest}^s + \tau_{debris}, \tag{22}$$

where τ_{forest}^s is the resistance from the forest of dislocations and τ_{debris} is the resistance from residual dislocation debris from incomplete recovery reactions. The τ_{forest}^s evolves according to (Kitayama et al., 2013):

$$\tau_{forest}^s = b\chi\mu_{\text{IN718}}\sqrt{\sum_{s'} L^{ss'}\rho_{tot}^{s'}}, \tag{23}$$

where $\chi = 0.9$ is a dislocation interaction constant, $\mu_{\text{IN718}}^{\alpha}$ is the shear modulus in the slip system coordinate system, ρ_{tot}^s is the accumulated forest dislocation density for s$^{\text{th}}$ slip system and $L^{ss'}$ is a

latent hardening interaction matrix.

The τ_{debris} is related to the density of dislocations stored as debris ρ_{deb} using the extended Taylor law (Madec et al., 2003):

$$\tau_{debris}^{\alpha} = k_{deb}\mu_{\mathrm{IN718}}\, b\sqrt{\rho_{deb}}log\left(\frac{1}{b\sqrt{\rho_{deb}}}\right), \quad (24)$$

where $k_{deb} = 0.086$ is a material independent constant that recovers the Taylor law i.e., Eq. (24) for low values of dislocation density.

The rate of stored dislocation density with strain is governed by a competition between the rate of trapping and the rate of recovery.

$$\frac{\partial \rho_{for}^{s}}{\partial \gamma^{s}} = k_1\sqrt{\rho_{for}^{s} + \rho_{rev}^{s}} - k_2(\dot{\varepsilon}, T)\rho_{for}^{s}, \quad (25)$$

The rate coefficient of trapping k_1 is assumed to be insensitive to temperature and strain rate. However, the rate coefficient of recovery k_2 is calculated using:

$$\frac{k_2}{k_1} = \frac{\chi b}{g}\left(1 - \frac{k_B T}{D(b)^3} ln\left(\frac{\dot{\varepsilon}}{\dot{\varepsilon}_0}\right)\right), \quad (26)$$

where k_B, $\dot{\varepsilon}_0$, g and D are the Boltzmann constant, a reference strain rate of value 10^7 s^{-1}, an effective activation enthalpy and a drag stress, respectively. The drag stress is assumed to be a function of temperature following (Risse et al., 2017). Finally, the increment in debris density $d\rho_{deb}$ depends on the rate of recovery via:

$$d\rho_{deb} = \sum_s qb\sqrt{\rho_{deb}}k_2(\dot{\varepsilon}, T)\rho_{tot}^{s} d\gamma^{s}, \quad (27)$$

where q is a coefficient that scales with the fraction of α-type dislocations that are transformed into debris.

4.4 Model setup

Hardening parameters pertaining to the temperature dependent hardening law are identified using part of the mechanical data. These are presented in Table 5. To the authors' knowledge, the high temperature single crystal moduli of this material are not publicly available. The measured single crystal elastic constants for IN718 of C_{11}=242.2GPa, C_{12}=138.9GPa, and C_{44}=104.2GPa (Haldipur, 2006) have been used in the room temperature calculations and softened to match the experimentally measured elastic slope for elevated temperature data. The measured elastic slopes at elevated temperatures are softer than expected for the alloy (Fukuhara and Sanpei, 1993), since the data is presented as measured i.e. without attempting to correct the slopes.

Table 5. Hardening law constants calibrated as functions of temperature in [K]. T_{ref} is room temperature, 298 K.

$\tau_0(T)$ [MPa]	$D(T)$ [MPa]	g	k_1 $[m^{-1}]$	q	H
637.9-37.9*exp((T-T_{ref})/261.1)	468.2+4.4*exp(-T/150.9)	0.04	3.2e+8	4.0	0.31

The initial texture used in the simulation is reconstructed from the neutron diffraction pole figure measurements and is represented using 5000 crystal orientations using procedures from (Barrett et al., 2019; Eghtesad et al., 2018; Knezevic and Landry, 2015). Figure 4 shows pole figures of the initial texture for simulations with respect to the loading direction (LD). The grain shape aspect ratio is set to 5, consistent with the measured grain structure. The simulations are performed in simple compression and tension in three directions relative to the BD: H, V, and D. Consistent with experiments, the imposed strain rate was 10^{-3} s^{-1}.

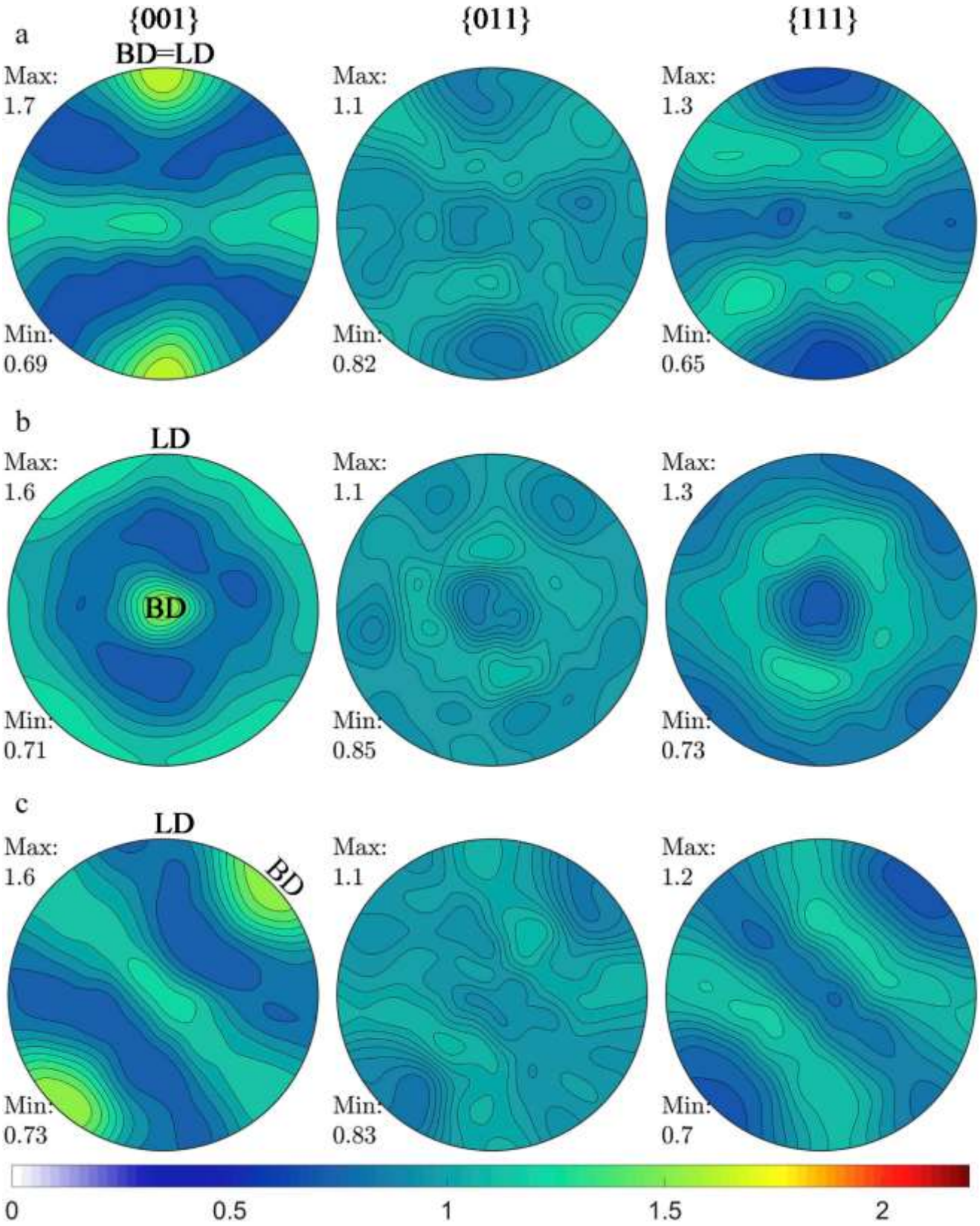

Figure 4. Stereographic pole figures visualizing texture in the DMLM samples with respect to the loading direction (LD). The texture was constructed from the neutron diffraction measurements (figure 1a) and represented with 5000 orientations, which are used in the crystal plasticity modeling.

In this model, we make available only the octahedral $\langle 111 \rangle \langle 1\bar{1}0 \rangle$ slip mode, since it is the main deformation mode in the service conditions from room temperature to 550 °C. It has been reported experimentally that cubic slip activates at much higher temperatures than considered in this work and therefore, we make available the same octahedral slip systems at all temperatures (Ding et al., 2004; Haddou et al., 2004; Österle et al., 2000; Semiatin et al., 2004).

The final part of developing the model is to characterize the material parameters associated with the hardening model. In earlier work, these parameters were defined for room temperature deformation (Ghorbanpour et al., 2017). Here we identify any temperature dependencies in these parameters by applying the model to a range of temperature, from room to high-temperature deformation of the alloy IN718.

The latent hardening interaction matrix used in Eq. (23) is based on notation in (Franciosi and Zaoui, 1982) with the values from (Devincre et al., 2006; Hoc et al., 2004), which were obtained using dislocation dynamic simulations. The values are $a_0 = 0.068$, $a_1 = 0.068$, $a_2 = 0.0454$, $a_3 = 0.625$, $a_4 = 0.137$, and $a_5 = 0.122$ and correspond to the self-interaction, coplanar interaction, Hirth, collinear, Glissile, and Lomer interaction coefficients, respectively. The matrix is explicitly defined in (Ghorbanpour et al., 2017).

5. Modeling results and discussion

Figure 5 compares measured and simulated data. As shown, the model achieves agreement in the yield stress, flow stress, and hardening rate for all cases and temperatures. In particular, the calculated response has the same T-C asymmetry, anisotropy, and hardening rate as the measurement. More importantly, changes in these features with an increase in temperature agree with the measured responses.

Figure 6 and figure 7 compare the measured and calculated texture after deformation. Earlier works (Knezevic et al., 2014a, 2014b) have shown no appreciable difference in texture evolution between

RT and elevated temperature in materials deforming by the same slip modes at RT and elevated temperatures. Thus, the texture was measured only for the deformed samples experiencing the largest amount of strain to evaluate texture evolution. From the measurements, we observe that for all three samples, H, V, and D, a strong <011> fiber texture formed along the loading direction, which is common for FCC metals. The model achieves an excellent agreement with the measurements.

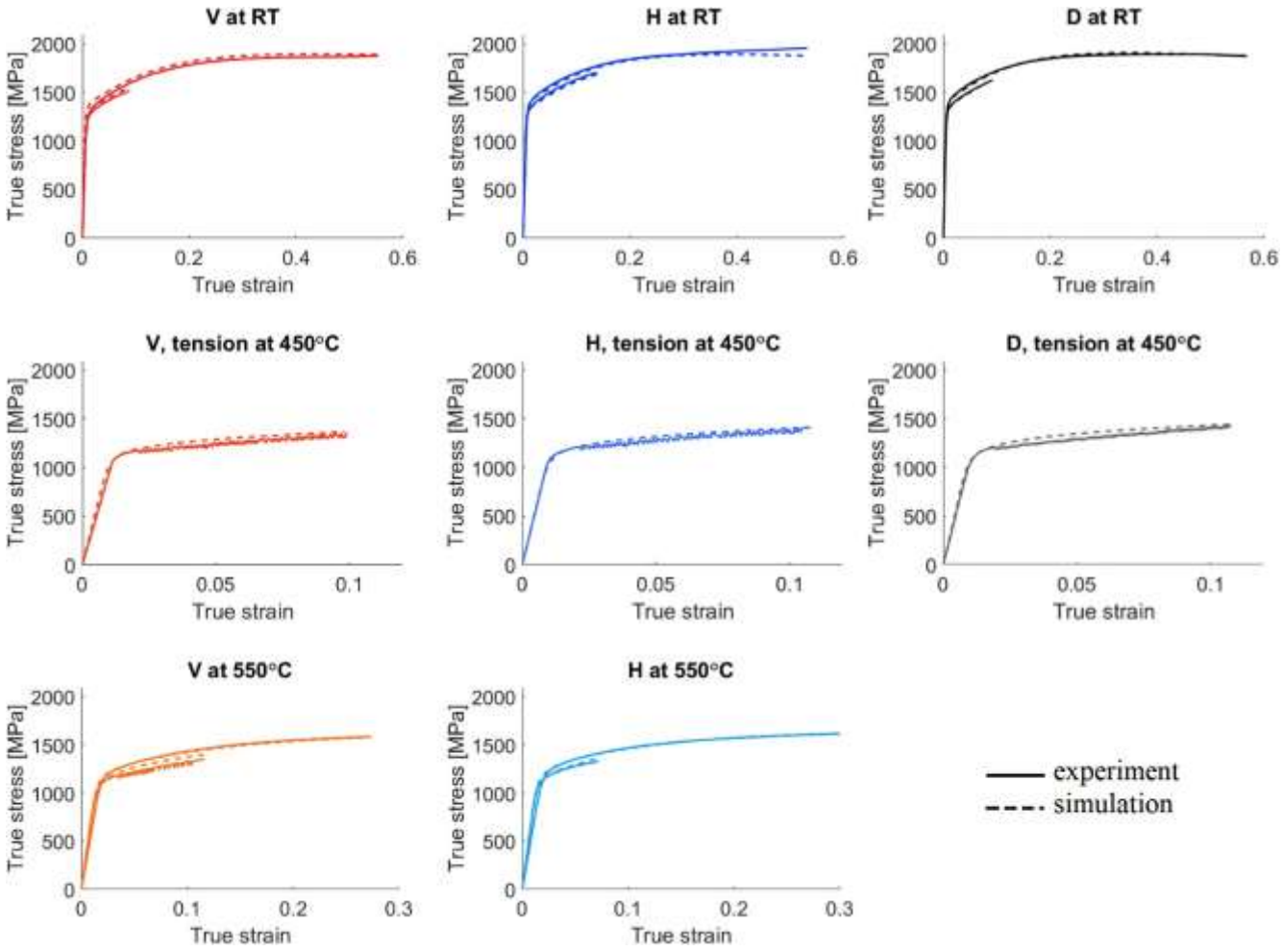

Figure 5. Comparison of measured and predicted true stress–true strain responses in tension (the shorter curve per plot) and compression (the longer curve per plot) for alloy IN718 as a function of temperature and build direction as indicated in the figure. The measured data is from figure 2. Length of the x-axis is different for every row.

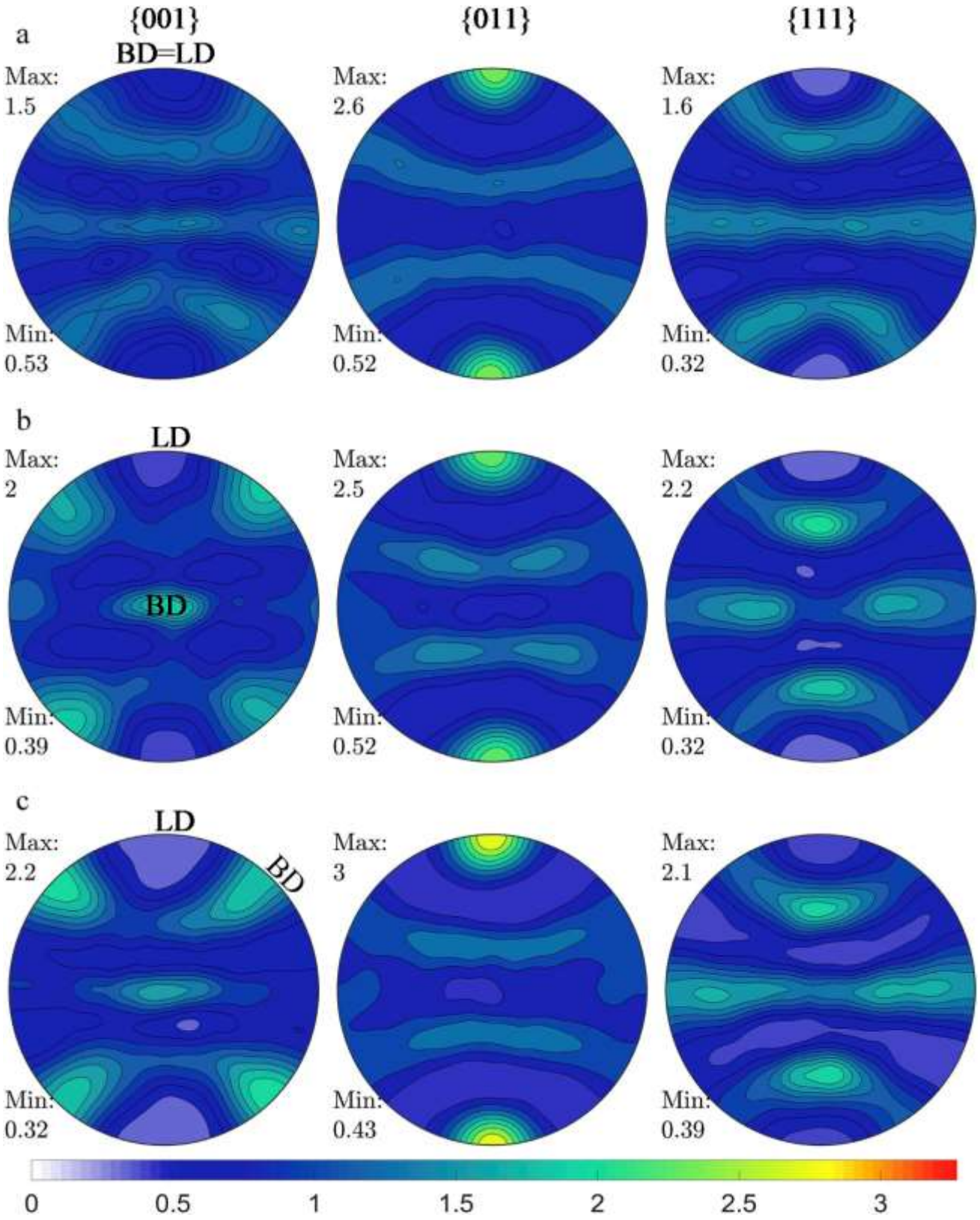

Figure 6. Stereographic pole figures measured using the neutron diffraction technique showing texture after simple compression for: (a) V, (b) H, and (c) D samples of alloy IN718. The strain values are 0.55, 0.53, and 0.57 respectively. LD is the loading direction, which is vertical. BD is the build direction, which varies.

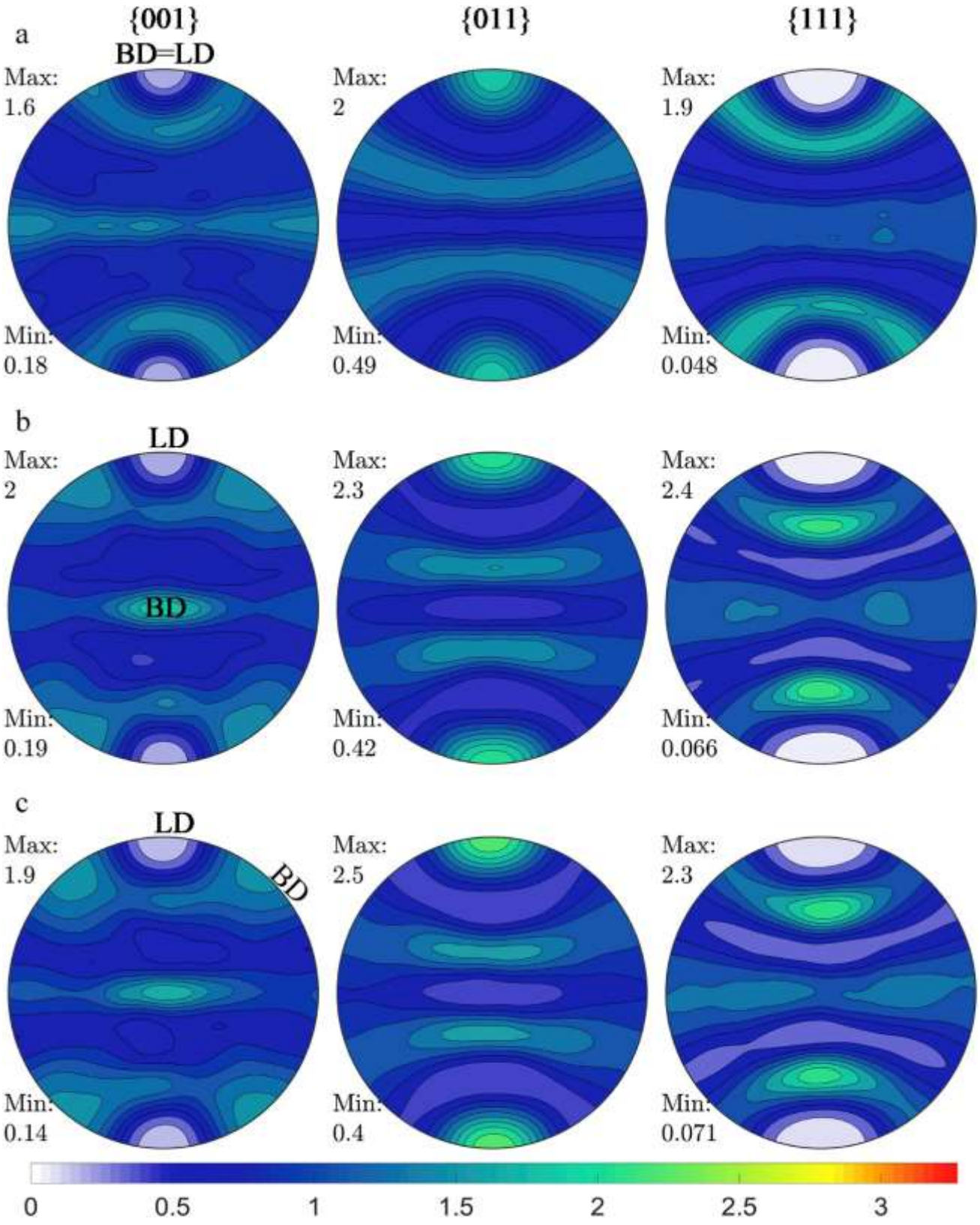

Figure 7. Pole figures showing simulated textures corresponding to those given in figure 6. The corresponding initial texture relative to LD for each simulation case is given in figure 4.

With a single set of parameters, the model was able to predict the stress-strain response in three build directions, both tension and compression and for three temperatures (for cases when data is available). The analysis finds that not all slip hardening-related parameters are dependent on temperature. It is suggested that the observed decrease in the yield and flow stress with increase in temperature can be understood by a decrease in the initial slip resistance. Table 5 contains the empirical relationships for τ_0(T) and D(T) used in the calculations shown in figure 5. The remaining parameters governing statistical trapping of dislocations, activation enthalpy for recovery processes, and latent hardening parameters could remain temperature independent.

At both RT and 550 C, the alloy exhibits a T-C asymmetry in yield stress, where the yield stress in compression is consistently higher than that in tension. The two components of the model responsible for the T-C asymmetry in the calculated response are the latent hardening parameters and non-Schmid coefficients with the latter having a dominant effect. Three coefficients, c_2, c_3, and c_4, can lead to a T-C asymmetry (Savage et al., 2017). In this work, we elected to vary only c_1 and c_2 NS coefficients since these coefficients have been associated with separation between the super-partials and Shockley partial separation (Baudouin et al., 2013; Steinmann et al., 1998). Interestingly, the model suggests that $c1 = 0.045$ is very small in magnitude and insensitive to temperature, whereas the c_2 is much larger in magnitude. Furthermore, c_2 is found to decrease with temperature from 0.97 at RT to 0.75 at 450 °C to 0.3 at 550 °C, indicating that temperature reduces the effect of the t⊗n non-Schmid resolved shear stress term and hence the evolution of T-C asymmetry. Similar findings have been reported for tantalum in (Zecevic and Knezevic, 2018b).

6. Conclusions

In this work, we studied the mechanical response of alloy IN718 as a function of the initial microstructure created by DMLM, subsequent HIP, and wrought manufacturing. The high temperature stress-strain responses for the alloy in the three DMLM and wrought conditions are provided for the

first time. Serrated response is seen for all three DMLM samples tested in tension at 450 °C, and only for DMLM-V sample tested in tension at 550 °C, with variable spacing and stress-amplitude. A critical strain required to initiate the serrated response is ~0.02 at 450 °C, while ~0.035 for DMDL-V at 550 °C. Furthermore, serration is observed for wrought samples tested in compression at 550 °C but interestingly not for the DMLM samples tested at the same temperature in compression. The modeling is carried out only for the DMLM materials in function of the deposition direction and temperature. An elasto-plastic crystal plasticity model is extended to predict the temperature-dependent deformation of DMLM alloy IN718. The model predicts hardening and texture evolution for several test directions across a range of temperatures. The model suggests that anisotropy stems from grain structure, while tension/compression asymmetry predominantly from non-Schmid activation and some from latent hardening.

Acknowledgments

This research was sponsored by the U.S. Army Research Laboratory and was accomplished under Cooperative agreement no. W911NF-15-2-0084. I. J. B and M.E.A. acknowledge financial support from the National Science Foundation (NSF CMMI-1728224). A. K. and I. J. B. acknowledge support from the Center for Scientific Computing from the CNSI, MRL: an NSF MRSEC (DMR-1121053).

References

2013. ASTM E8 / E8M-13, Standard Test Methods for Tension Testing of Metallic Materials. ASTM International, West Conshohocken, PA.

2018a. ASTM E9-09, Standard Test Methods of Compression Testing of Metallic Materials at Room Temperature. ASTM International, West Conshohocken, PA.

2018b. ASTM E209, Standard Practice for Compression Tests of Metallic Materials at Elevated Temperatures with Conventional or Rapid Heating Rates and Strain Rates. ASTM International, West Conshohocken, PA.

Amato, K., Gaytan, S., Murr, L., Martinez, E., Shindo, P., Hernandez, J., Collins, S., Medina, F., 2012. Microstructures and mechanical behavior of Inconel 718 fabricated by selective laser melting. Acta. Mater. 60, 2229-2239.

Antolovich, S.D., 2015. Microstructural aspects of fatigue in Ni-base superalloys. Philosophical Transactions of the Royal Society of London A: Mathematical, Physical and Engineering Sciences 373, 20140128.

Ardeljan, M., Beyerlein, I.J., Knezevic, M., 2014. A dislocation density based crystal plasticity finite element model: Application to a two-phase polycrystalline HCP/BCC composites. J. Mech. Phys. Solids 66, 16-31.

Ardeljan, M., Beyerlein, I.J., McWilliams, B.A., Knezevic, M., 2016. Strain rate and temperature sensitive multi-level crystal plasticity model for large plastic deformation behavior: Application to AZ31 magnesium alloy. Int. J. Plast. 83, 90-109.

Ardeljan, M., Knezevic, M., Nizolek, T., Beyerlein, I.J., Mara, N.A., Pollock, T.M., 2015. A study of microstructure-driven strain localizations in two-phase polycrystalline HCP/BCC composites using a multi-scale model. Int. J. Plast. 74, 35-57.

Baudouin, J.-B., Monnet, G., Perez, M., Domain, C., Nomoto, A., 2013. Effect of the applied stress and the friction stress on the dislocation dissociation in face centered cubic metals. Materials Letters 97, 93-96.

Beese, A.M., Wang, Z., Stoica, A.D., Ma, D., 2018. Absence of dynamic strain aging in an additively manufactured nickel-base superalloy. Nature communications 9, 2083.

Blöchl, P.E., 1994. Projector augmented-wave method. Physical Review B 50, 17953.

Cai, Y., Tian, C., Zhang, G., Han, G., Yang, S., Fu, S., Cui, C., Zhang, Q., 2017. Influence of γ′ precipitates on the critical strain and localized deformation of serrated flow in Ni-based superalloys. J. Alloys Compd. 690, 707-715.

Copley, S., Kear, B., 1967a. A dynamic theory of coherent precipitation hardening with application to nickel-base alloys(Coherent precipitation hardening theory treats yielding in nickel base alloy containing coherent stress-free ordered particles as dynamic process). AIME, TRANSACTIONS 239, 984-992.

Copley, S., Kear, B., 1967b. Temperature and orientation dependence of the flow stress in off-stoichiometric Ni sub 3 Al/gamma' phase/(Strength characteristics of single crystals of nickel aluminide/gamma phase/, discussing temperature and orientation dependence of work hardening). AIME, TRANSACTIONS 239, 977-984.

Courtney, T.H., 1990. Strengthening of Crystalline Materials, Mechanical Behavior of Materials.

Dao, M., Asaro, R.J., 1993. Non-Schmid effects and localized plastic flow in intermetallic alloys. Mater. Sci. Eng. A 170, 143-160.

Devincre, B., Kubin, L., Hoc, T., 2006. Physical analyses of crystal plasticity by DD simulations. Scr. Mater. 54, 741-746.

Ding, Z., Liu, Y., Yin, Z., Yang, Z., Cheng, X., 2004. Study of elastoplastic constitutive model for single crystal nickel-based superalloy. Hangkong Dongli Xuebao/Journal of Aerospace Power 19, 755-761.

Eshelby, J.D., 1957. The determination of the elastic field of an ellipsoidal inclusion, and related problems. Proc R. Soc. Lond. A 241, 376-396.

Estevez, R., Hoinard, G., Franciosi, P., 1997. Hardening anisotropy of γγ′ superalloy single crystals—II. Numberical analysis of heterogeneity effects. Acta. Mater. 45, 1567-1584.

Evans, N., Maziasz, P., Swindeman, R., Smith, G., 2004. Microstructure and phase stability in INCONEL alloy 740 during creep. Scr. Mater. 51, 503-507.

Ferreri, N.C., Savage, D.J., Vogel, S.C., Knezevic, M., 2019. Unusual phase content in additively manufactured Inconel 718 as revealed by neutron diffraction identification procedures. Acta. Mater.

Franciosi, P., Zaoui, A., 1982. Multislip in f.c.c. crystals a theoretical approach compared with experimental data. Acta Metallurgica 30, 1627-1637.

Francis, E.M., Grant, B.M.B., Fonseca, J.Q.d., Phillips, P.J., Mills, M.J., Daymond, M.R., Preuss, M., 2014. High-temperature deformation mechanisms in a polycrystalline nickel-base superalloy studied by neutron diffraction and electron microscopy. Acta. Mater. 74, 18-29.

Fukuhara, M., Sanpei, A., 1993. Elastic moduli and internal frictions of Inconel 718 and Ti-6Al-4V as a function of temperature. J Mater Sci Lett 12, 1122-1124.

Ghorbanpour, S., Zecevic, M., Kumar, A., Jahedi, M., Bicknell, J., Jorgensen, L., Beyerlein, I.J., Knezevic, M., 2017. A crystal plasticity model incorporating the effects of precipitates in superalloys: Application to tensile, compressive, and cyclic deformation of Inconel 718. Int. J. Plast. 99, 162-185.

Gleiter, H., Hornbogen, E., 1968. Precipitation hardening by coherent particles. Materials Science and Engineering 2, 285-302.

Gribbin, S., Bicknell, J., Jorgensen, L., Tsukrov, I., Knezevic, M., 2016. Low cycle fatigue behavior of direct metal laser sintered Inconel alloy 718. Int. J. Fatigue 93, Part 1, 156-167.

Gribbin, S., Ghorbanpour, S., Ferreri, N.C., Bicknell, J., Tsukrov, I., Knezevic, M., 2019. Role of grain structure, grain boundaries, crystallographic texture, precipitates, and porosity on fatigue behavior of Inconel 718 at room and elevated temperatures. Mater. Charact. 149, 184-197.

Haddou, H., Risbet, M., Marichal, G., Feaugas, X., 2004. The effects of grain size on the cyclic deformation behaviour of polycrystalline nickel. Mater. Sci. Eng. A 379, 102-111.

Haldipur, P., 2006. Material characterization of nickel-based super alloys through ultrasonic inspection, Materials Science and Engineering Iowa State University, Ames, Iowa

Hayes, R.W., Hayes, W.C., 1982. On the mechanism of delayed discontinuous plastic flow in an age-hardened nickel alloy. Acta Metall. 30, 1295-1301.

Hoc, T., Devincre, B., Kubin, L.P., 2004. Deformation stage I of FCC crystals: constitutive modelling, in: Gundlach, C., Haldrup, K., Hansen, N., Huang, X., Jensen, D.J., Leffers, T., Li, Z.J., Nielsen, S.F., Pantleon, W., Wert, J.A., Winther, G. (Eds.), Proceedings of the 25th Riso International Symposium on Materials Science: Evolution of Deformation Microstructures in 3D, Riso National Laboratory, Roskilde, Denmark.

Hoinard, G., Estevez, R., Franciosi, P., 1995. Hardening anisotropy of γ/γ′ superalloy single crystals—I. Experimental estimates at 650°C from a homogeneous analysis. Acta Metall. Mater. 43, 1593-1607.

Huther, W., Reppich, B., 1978. Interaction of Dislocations with Coherent, Stree-Free Ordered Particles. Zeitschrift Fur Metallkunde 69, 628-634.

Jahedi, M., Ardeljan, M., Beyerlein, I.J., Paydar, M.H., Knezevic, M., 2015. Enhancement of orientation gradients during simple shear deformation by application of simple compression. J. Appl. Phys. 117, 214309.

Keshavarz, S., Ghosh, S., 2015. A crystal plasticity finite element model for flow stress anomalies in Ni_3Al single crystals. Philosophical Magazine 95, 2639-2660.

Kitayama, K., Tomé, C.N., Rauch, E.F., Gracio, J.J., Barlat, F., 2013. A crystallographic dislocation model for describing hardening of polycrystals during strain path changes. Application to low carbon steels. International Journal of Plasticity in press.

Knezevic, M., Beyerlein, I.J., Lovato, M.L., Tomé, C.N., Richards, A.W., McCabe, R.J., 2014a. A strain-rate and temperature dependent constitutive model for BCC metals incorporating non-Schmid effects: Application to tantalum–tungsten alloys. Int. J. Plast. 62, 93-104.

Knezevic, M., Capolungo, L., Tomé, C.N., Lebensohn, R.A., Alexander, D.J., Mihaila, B., McCabe, R.J., 2012. Anisotropic stress-strain response and microstructure evolution of textured a-uranium. Acta. Mater. 60, 702-715.

Knezevic, M., Carpenter, J.S., Lovato, M.L., McCabe, R.J., 2014b. Deformation behavior of the cobalt-based superalloy Haynes 25: Experimental characterization and crystal plasticity modeling. Acta. Mater. 63, 162-168.

Knezevic, M., Zecevic, M., Beyerlein, I.J., Bingert, J.F., McCabe, R.J., 2015. Strain rate and temperature effects on the selection of primary and secondary slip and twinning systems in HCP Zr. Acta. Mater. 88, 55-73.

Knezevic, M., Zecevic, M., Beyerlein, I.J., Lebensohn, R.A., 2016. A numerical procedure enabling accurate descriptions of strain rate-sensitive flow of polycrystals within crystal visco-plasticity theory. Computer Methods in Applied Mechanics and Engineering 308, 468-482.

Kresse, G., Furthmüller, J., 1996. Efficient iterative schemes for ab initio total-energy calculations using a plane-wave basis set. Physical Review B 54, 11169.

Kresse, G., Hafner, J., 1994. Ab initio molecular-dynamics simulation of the liquid-metal–amorphous-semiconductor transition in germanium. Physical Review B 49, 14251.

Kresse, G., Joubert, D., 1999. From ultrasoft pseudopotentials to the projector augmented-wave method. Physical Review B 59, 1758.

Kuo, C.M., Yang, Y.T., Bor, H.Y., Wei, C.N., Tai, C.C., 2009. Aging effects on the microstructure and creep behavior of Inconel 718 superalloy. Materials Science and Engineering: A 510–511, 289-294.

Lass, E.A., Stoudt, M.R., Williams, M.E., Katz, M.B., Levine, L.E., Phan, T.Q., Gnaeupel-Herold, T.H., Ng, D.S., 2017. Formation of the Ni_3Nb δ-Phase in Stress-Relieved Inconel 625 Produced via Laser Powder-Bed Fusion Additive Manufacturing. Metall. Mater. Trans. A 48, 5547-5558.

Lebensohn, R.A., Tomé, C.N., 1993. A self-consistent anisotropic approach for the simulation of plastic deformation and texture development of polycrystals: Application to zirconium alloys. Acta Metall. Mater. 41, 2611-2624.

Lim, H., Weinberger, C.R., Battaile, C.C., Buchheit, T.E., 2013. Application of generalized non-Schmid yield law to low-temperature plasticity in bcc transition metals. Modelling and Simulation in Materials Science and Engineering 21, 045015.

Maciejewski, K., Jouiad, M., Ghonem, H., 2013. Dislocation/precipitate interactions in IN100 at 650 °C. Materials Science and Engineering: A 582, 47-54.

Madec, R., Devincre, B., Kubin, L., Hoc, T., Rodney, D., 2003. The role of collinear interaction in dislocation-induced hardening. Science 301, 1879-1882.

Maj, P., Zdunek, J., Gizynski, M., Mizera, J., Kurzydlowski, K.J., 2014. Statistical analysis of the Portevin–Le Chatelier effect in Inconel 718 at high temperature. Mater. Sci. Eng. A 619, 158-164.

Manikandan, S., Sivakumar, D., Rao, K.P., Kamaraj, M., 2015. Laves phase in alloy 718 fusion zone—microscopic and calorimetric studies. Mater. Charact. 100, 192-206.

Mannan, S., 1993. Role of dynamic strain ageing in low cycle fatigue. Bulletin of Materials Science 16, 561-582.

Mei, Y., Liu, Y., Liu, C., Li, C., Yu, L., Guo, Q., Li, H., 2015. Effects of cold rolling on the precipitation kinetics and the morphology evolution of intermediate phases in Inconel 718 alloy. Journal of Alloys and Compounds 649, 949-960.

Mostafa, A., Picazo Rubio, I., Brailovski, V., Jahazi, M., Medraj, M., 2017. Structure, Texture and Phases in 3D Printed IN718 Alloy Subjected to Homogenization and HIP Treatments. Metals 7, 196.

Mukherji, D., Gilles, R., Barbier, B., Del Genovese, D., Hasse, B., Strunz, P., Wroblewski, T., Fuess, H., Rösler, J., 2003. Lattice misfit measurement in Inconel 706 containing coherent γ′ and γ ″precipitates. Scr. Mater. 48, 333-339.

Murr, L.E., Martinez, E., Amato, K.N., Gaytan, S.M., Hernandez, J., Ramirez, D.A., Shindo, P.W., Medina, F., Wicker, R.B., 2012. Fabrication of metal and alloy components by additive manufacturing: examples of 3D materials science. Journal of Materials Research and Technology 1, 42-54.

Murr, L.E., Martinez, E., Gaytan, S., Ramirez, D., Machado, B., Shindo, P., Martinez, J., Medina, F., Wooten, J., Ciscel, D., 2011. Microstructural architecture, microstructures, and mechanical properties for a nickel-base superalloy fabricated by electron beam melting. Metall. Mater. Trans. A 42, 3491-3508.

Neil, C.J., Wollmershauser, J.A., Clausen, B., Tomé, C.N., Agnew, S.R., 2010. Modeling lattice strain evolution at finite strains and experimental verification for copper and stainless steel using in situ neutron diffraction. Int. J. Plast. 26, 1772-1791.

Österle, W., Bettge, D., Fedelich, B., Klingelhöffer, H., 2000. Modelling the orientation and direction dependence of the critical resolved shear stress of nickel-base superalloy single crystals. Acta. Mater. 48, 689-700.

Perdew, J.P., Burke, K., Ernzerhof, M., 1996. Generalized gradient approximation made simple. Physical review letters 77, 3865.

Rao, G.A., Kumar, M., Srinivas, M., Sarma, D., 2003. Effect of standard heat treatment on the microstructure and mechanical properties of hot isostatically pressed superalloy inconel 718. Mater. Sci. Eng. A 355, 114-125.

Risse, M., Lentz, M., Fahrenson, C., Reimers, W., Knezevic, M., Beyerlein, I.J., 2017. Elevated Temperature Effects on the Plastic Anisotropy of an Extruded Mg-4 Wt Pct Li Alloy: Experiments and Polycrystal Modeling. Metall. Mater. Trans. A 48, 446-458.

Roth, H.A., Davis, C.L., Thomson, R.C., 1997. Modeling solid solution strengthening in nickel alloys. Metallurgical and Materials Transactions A 28, 1329-1335.

Savage, D.J., Beyerlein, I.J., Knezevic, M., 2017. Coupled texture and non-Schmid effects on yield surfaces of body-centered cubic polycrystals predicted by a crystal plasticity finite element approach. International Journal of Solids and Structures 109, 22-32.

Schmid, E., Boas, W., 1950. Plasticity of crystals with special reference to metals. English translation F.A. Hughes, London

Semiatin, S., Fagin, P., Glavicic, M., Raabe, D., 2004. Deformation behavior of Waspaloy at hot-working temperatures. Scr. Mater. 50, 625-629.

Shenoy, M., Tjiptowidjojo, Y., McDowell, D., 2008. Microstructure-sensitive modeling of polycrystalline IN 100. Int. J. Plast. 24, 1694-1730.

Slama, C., Abdellaoui, M., 2000. Structural characterization of the aged Inconel 718. Journal of Alloys and Compounds 306, 277-284.

Smith, D.H., Bicknell, J., Jorgensen, L., Patterson, B.M., Cordes, N.L., Tsukrov, I., Knezevic, M., 2016. Microstructure and mechanical behavior of direct metal laser sintered Inconel alloy 718. Mater. Charact. 113, 1-9.

Steinmann, P., Kuhl, E., Stein, E., 1998. Aspects of non-associated single crystal plasticity: influence of non-Schmid effects and localization analysis. International journal of solids and structures 35, 4437-4456.

Turner, P.A., Tomé, C.N., 1994. A study of residual stresses in Zircaloy-2 with rod texture. Acta Metall. Mater. 42, 4143-4153.

Umakoshi, Y., Pope, D.P., Vitek, V., 1984. The asymmetry of the flow stress in Ni_3(Al,Ta) single crystals. Acta Metallurgica 32, 449-456.

Xiao, L., Chen, D.L., Chaturvedi, M.C., 2005. Shearing of γ″ precipitates and formation of planar slip bands in Inconel 718 during cyclic deformation. Scripta Materialia 52, 603-607.

Zecevic, M., Beyerlein, I.J., Knezevic, M., 2017. Coupling elasto-plastic self-consistent crystal plasticity and implicit finite elements: Applications to compression, cyclic tension-compression, and bending to large strains. Int. J. Plast. 93, 187-211.

Zecevic, M., Knezevic, M., 2015. A dislocation density based elasto-plastic self-consistent model for the prediction of cyclic deformation: Application to Al6022-T4. Int. J. Plast. 72, 200-217.

Zecevic, M., Knezevic, M., 2017. Modeling of Sheet Metal Forming Based on Implicit Embedding of the Elasto-Plastic Self-Consistent Formulation in Shell Elements: Application to Cup Drawing of AA6022-T4. JOM 69, 922-929.

Zecevic, M., Knezevic, M., 2018a. Latent hardening within the elasto-plastic self-consistent polycrystal homogenization to enable the prediction of anisotropy of AA6022-T4 sheets. Int. J. Plast. 105, 141-163.

Zecevic, M., Knezevic, M., 2018b. A new visco-plastic self-consistent formulation implicit in dislocation-based hardening within implicit finite elements: Application to high strain rate and impact deformation of tantalum. Computer Methods in Applied Mechanics and Engineering 341, 888-916.

Chapter 3: Effect of microstructure induced anisotropy on fatigue behaviour of functionally graded Inconel 718 fabricated by additive manufacturing

This manuscript is submitted to the Materials Characterizations entitled “Effect of microstructure induced anisotropy on fatigue behaviour of functionally graded Inconel 718 fabricated by additive manufacturing”. The authors of the paper are Saeede Ghorbanpour, Saswat Sahu, Kaustubh Deshmukh, Evgenii Borisov, Ton Riemslag, Elise Reinton, Virginia Bertolo, Quanxin Jiang, Anatolii Popovich, Aleksey Shamshurin, Marko Knezevic, and Vera Popovich. My contribution to this chapter was analysing the data from the mechanical tests, performing and analysing all microstructural analysis and writing the manuscript.

Effect of microstructure induced anisotropy on fatigue behaviour of functionally graded Inconel 718 fabricated by additive manufacturing

Saeede Ghorbanpour[a] , Saswat Sahu[a], Kaustubh Deshmukh[a], Evgenii Borisov[b], Ton Riemslag[a], Elise Reinton[a], Virginia Bertolo[a], Quanxin Jiang[a], Anatolii Popovich[b], Aleksey Shamshurin[b], Marko Knezevic[c], Vera Popovich[a,b]

a. Department of Materials Science and Engineering, Delft University of Technology, The Netherlands

b. Peter the Great Saint-Petersburg Polytechnic University, Saint Petersburg, Russia

c. Department of Mechanical Engineering, University of New Hampshire, Durham, NH 03824, USA

Abstract

In this paper, the effect of microstructural anisotropy on the fatigue crack growth behaviour of the functionally graded Inconel 718 fabricated through laser powder bed fusion (L-PBF) is investigated. Different manufacturing parameters, including low and high laser powers, were used to produce a variety of non-graded (NG) and functionally graded (G) specimens in two build directions, vertical and horizontal. In addition, a group of heat treated wrought samples was tested as a reference. It was observed that the different manufacturing parameters result in various grain size, crystallographic textures, precipitates and Laves phases, porosity, and un-melted particles. Three-point bending fatigue tests were conducted to measure the threshold stress intensity factor (ΔK_{th}) and fatigue crack growth rate (FCGR),da/dN. Only the lower laser power L-BPF Inconel material was found to have comparable to the wrought heat treated material fatigue crack growth behaviour. Furthermore, a new approach of automatically controlling ΔK as a function of the crack length was employed for graded

specimens to investigate the crack growth rate as a function of local microstructure. The FCGR value of the vertical L-PBF samples, in which the crack direction was perpendicular to the build direction, remained constant. In contrast, the da/dN value of the horizontal samples with the crack direction parallel to the build direction increased constantly with the increase of the crack length. This behaviour is in good agreement with the hardness profile of the graded materials. Melt pool boundaries, graded interface boundaries, and grain orientations close to <001> were found to deflect the crack path. Additionally, it was found that L-PBF material is more affected (at a low stress ratio of R=0.1) by the roughness-induced crack closure than the wrought counterparts. This study has successfully demonstrated the feasibility of using an additive manufacturing process to fabricate functionally graded materials featuring tailorable fatigue response of the local microstructures.

1. Introduction

Inconel 718 (IN718), due to its outstanding combination of superior strength, creep and wear resistance, corrosion and oxidation, even at cryogenic and elevated temperatures (up to 650 °C), is widely used in various applications in petrochemical, aeronautics, energy, and aerospace industries [1-5]. IN718 is a precipitation hardened Nickel-base superalloy with main strengthening precipitates γ' (Ni_3Al) with an $L1_2$ lattice structure and γ" (Ni_3Nb) with a DO_{22} structure [1, 6-8]. γ' precipitates are spherical shape with diameters ranging between 10 and 40 nm, while γ" precipitates are disk shaped with diameters of 20-30 nm and thickness of 5-6 nm [2, 9-12]. The weight percentages of γ' and γ" can vary around 3-8% and 8-18%, respectively, based on the manufacturing methods and post processing history [13, 14]. In addition to the strengthening precipitates, undesired phases such as hexagonal Laves $(Ni,Fe,Cr)_2(Nb,Mo,Ti)$ and MC carbides could be present in the alloy [7, 15].

IN718 also exhibits high low cycle fatigue (LCF) strength and high temperature fatigue crack growth resistance [1, 16]. Some research [1, 17-22] was performed on the short and long crack initiation and growth behaviour of conventionally manufactured IN718. Short crack initiation and growth of a

solution treated forged IN718 were studied at 600 ˚C [17]. Due to mismatch strains between the oxidized particles and the matrix, crack initiation sites with sub-surface primary carbides (Nb, Ti) C oxidation were developed. Short crack growth rates (before reaching a couple of hundred microns) were found to be constant across a wide range of crack lengths. However, they transitioned to rapid and accelerating growth while the crack length increased to several hundred microns [17]. Room temperature fatigue crack growth was found to be transgranular with different crack growth mechanisms such as pure shearing on slip planes or formation of microcracks and subsequent linking [18]. The high temperature fatigue crack growth rate (FCGR) was studied in [1, 19-21] and it was found that the FCGR increases with temperature. However, the high temperature fatigue behaviour of IN718 is not the scope of the current study. In addition to the test temperature, the microstructure can play an important role in the fatigue crack growth behaviour. Coarsening the grain size from 22 µm to 91 µm was found to reduce the near threshold crack growth rates while increases the threshold stress intensity factor [22].

Additive manufacturing (AM) has been considered a replacement manufacturing technique for conventional methods due to the near net shape (NNS) production capability, which is desirable for complicated geometries. Altering the manufacturing parameters can influence the microstructure and grain size and thus affect the mechanical properties of the final products. Different scanning strategies, namely cross snake (CS) and cross snake 10 (CS10), in the selective electron beam melting method results in columnar and equiaxed grains with significantly different sizes [23]. The AM process has been previously used to tailor the microstructure and develop site-specific and user-defined functional properties[24]. As reported in [24-26] the microstructure is affected by various AM methods and different manufacturing parameters, resulting in cube or Goss textures. Laser powder bed fusion (L-PBF) which is a common AM method employs a laser beam to melt powders layer by layer and build the final geometry defined by a computer aided design (CAD) model [24, 27, 28].

Since the AM methods became more widely used, more research has been focusing on the mechanical properties including the fatigue behaviour. Long crack propagation of L-PBF IN718 was formulated in the threshold and Paris regions in [28]. It was found that L-PBF IN718 is less resistant to the long crack growth in the near threshold region due to the effect of the residual stress, finer microstructure, and low content of boron [28]. Similarly, a higher crack growth rate compared to the wrought material was reported in the L-PBF IN718 with columnar grains and an average grain size of 100 μm on the building direction cross section [29]. In situ fatigue testing at 25˚C and 650˚C revealed that the fatigue short crack growth rates are much higher in the build direction (BD) due to the small misorientation of adjacent grains and the lower strength compared with the other orientations [30].

Functionally graded materials (FGM)s refer to a class of advanced materials with different compositions or microstructures along with the geometry, which results in different properties [31-33]. The transition of the microstructure, composition, and morphology can be used to grade the materials and functional properties [31]. FGM parts can be made from one material, single-material FGM, or different materials known as multi-material FGM. While the former can be used to achieve superior and functional properties, the latter can also be a means of joining dissimilar metals. In our earlier works, it was successfully demonstrated that the microstructure of IN718 can be graded by manipulation of L-PBF process parameters. It was shown [24, 34, 35] that Vickers hardness, tensile strength, and creep of the functionally graded IN718 can be tailored to achieve location-specific properties. However, the fatigue crack growth behaviour of the functionally graded IN718 material has not been investigated yet. Furthermore, the experimental approach to investigate the fatigue crack growth behaviour in functionally graded materials, which could account for dissimilar microstructures and interface behaviour has not been reported to date.

The objective of the current research is to study the effect of the grain size, texture, and graded interface on the fatigue crack growth behaviour of a functionally graded L-PBF IN718. Graded samples with different build orientations were manufactured employing the L-PBF technique.

Additionally, a set of non-graded samples with a variety of grain sizes, textures and build directions were manufactured and studied. In addition, heat treated wrought samples (based on AMS 5663 [36]) were tested and the corresponding data were used as a reference. Interactions of fatigue crack path with various microstructural features and graded interface are studied in detail. Furthermore, a novel fatigue crack growth setup and approach are developed to account for the graded interface behaviour.

2. Materials and methods

2.1 Materials

The IN718 samples were manufactured using the powder produced by the gas atomization of the hot melt with a chemical composition of (wt%) 51.45 Ni, 19.38 Cr, 18.49 Fe, 5.3 Nb, 3.4 Mo, 1.04 Ti, 0.72 Al, 0.1 Co, and 0.12 Mn. The particle diameters of the powder ranged between d_{10}=20 µm and d_{90}=64 µm. Samples for this study were manufactured using the L-PBF technique with an SLM 280^{HL} facility (SLM Solutions Group AG, Germany). Two different laser power values of 250 W and 950 W with a wavelength of 1070 nm were employed to build the fatigue specimens. To optimise the manufacturing parameters, the linear energy density (LED), E_l, which is the ratio of the laser power to the laser scanning speed was adjusted and is defined by equation (1). The volume energy density (VED), E_v, is another parameter which accounts for the combined effect of laser power and speed in addition to the hatch distance and layer thickness [37]. E_v is described by equation (2). The L-PBF parameters were optimized in a way that the volume energy density remained about the same for both laser powers.

$$E_l = \frac{P}{v} \tag{1}$$

$$E_v = \frac{P}{v.h.t} \tag{2}$$

Where *P* is the laser power, *v* is the laser scanning speed, *t* is the layer thickness, and *h* is the hatch distance. Note that *t* and *h* are in mm.

The laser beams for 250 W and 950 W laser powers were 80 µm diameter with Gaussian distribution and 100 µm diameter with flat top distributions respectively. It is known that large and homogenous beams are beneficial for suppressing the spatters and powder bed degradation and allowing the production of denser parts [38]. In addition, the hatch distances of the low and high laser power categories were different which can influence the final textures of the AM parts [39]. Table 1 summarizes the process parameters which were optimized and used in this study to produce different parts.

Table 1. L-PBF process parameters used in this study.

Build direction	*P* [W]	*V* [mm/s]	*h* [mm]	*t* [mm]	Beam diameter [µm]	Beam distribution	E_l [J/mm]	E_v [J/mm^3]
H	250	700	0.12	0.05	80	Gaussian	0.36	59.5
H	950	320	0.5	0.1	100	Flat top	2.97	59.4
V	950	320	0.5	0.1	100	Flat top	2.97	59.4

Two categories of specimens denoted as Non-graded (NG) and Graded (G) samples were manufactured (see Figure 1). One constant laser power was employed during the whole manufacturing process in the former group while there was a transition of the laser power from 250W to 950W in the latter one. Another parameter which was altered during the manufacturing process was the building direction with respect to the sample axis or the crack direction (CD). All fatigue samples were designed in a way that the anticipated crack path was located aligned with the sample's vertical symmetry axis. The samples were denoted as vertical (V) when the build direction and CD were perpendicular, and horizontal (H) when those two directions were parallel. Graded samples and higher laser power of NG specimens, i.e. 950 W, were designed and built in two V and H orientations, while

the NG 250 W samples were manufactured only in the H direction. Figure 2 depicts a schematic of the manufactured samples showing their orientation concerning the build direction and sample axes.

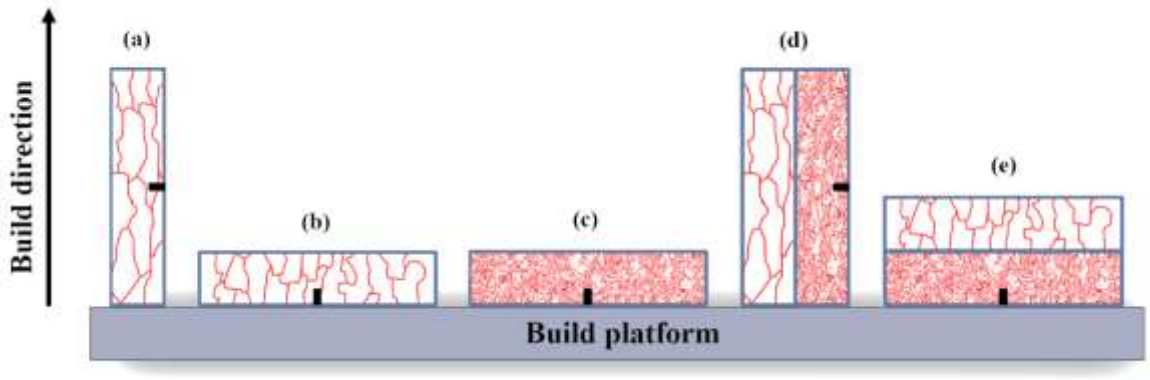

Figure 1. Schematics of the graded and non-graded specimens showing the sample orientations with respect to the BD. Note that the crack direction (CD) is always aligned with the sample symmetry axes. (a) NG-V-950W, (b) NG-H-950W, (c) NG-H-250W, (d) G-V, and (e) G-H. Note that the dimensions are schematic and not up to the actual scale.

Rectangular single-edge-notched samples were manufactured based on the ASTM E399 [40] specifications, as shown in figure 2. The final dimensions of the samples were achieved after milling. The notch with a total depth of 0.5 mm and a radius of 0.2 mm was machined using the electrical discharge machining (EDM) technique. A crack of length 1.5 mm was produced by fatigue pre-cracking in all samples according to the requirements in ASTM E399 [40].

2.2 Microstructural characterization

Optical and scanning electron microscopy (SEM) observations were performed to study the grain morphology and size, melt pools, different structures caused by various manufacturing parameters, precipitates, and carbides. Prior to the observations, samples' surfaces were prepared by grinding (180 to 2000 European grit size), polishing down to 1 µm, and etching for 3 seconds in a Glyceregia etchant solution of 5 ml HNO_3, 10 ml Glycerol, and 15 ml HCl. Leica DMLM optical microscope equipped with analySIS 5.0 by Olympus soft Imaging Solutions GmbH, Keyence VHX-5000, and JEOL JSM IT-100 SEM with JEOL InTouchScope software were used. Besides, fracture surface

analyses by SEM were performed on the graded samples, which were intentionally overloaded in constant ΔK tests.

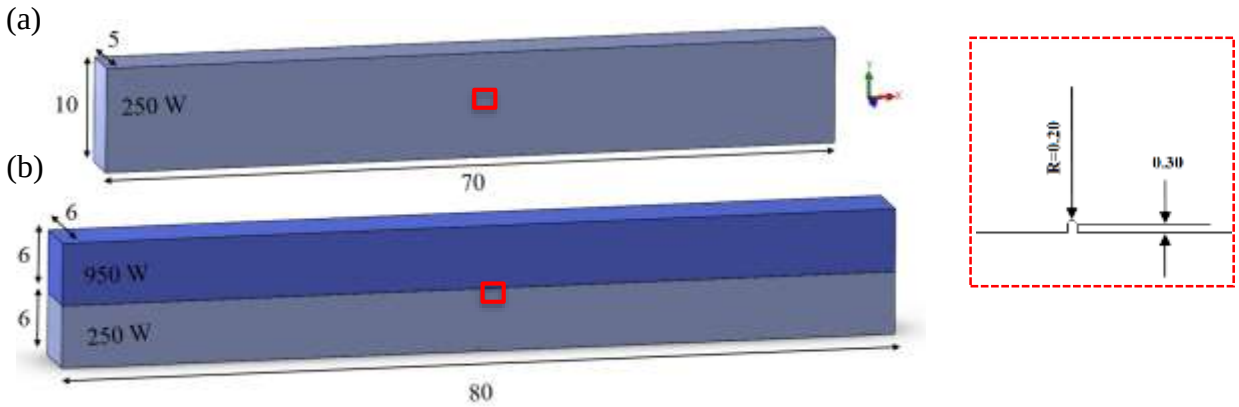

Figure 2. The geometry of the single edge notched samples used in this study (a) non-graded and (b) graded fatigue test specimens. As provided in the text, the dimensions are slightly different for G and NG samples. The notch specifications are provided in the insert. All dimensions are in mm.

To identify the present phases, X-ray diffraction (XRD) analyses were performed on the wrought and non-graded samples. Prior to the XRD measurements, samples were polished for 10 minutes by colloidal silica. A Bruker D8 advanced diffractometer with a Co Kα radiation (wavelength of 1.78897 Å) equipped with Bruker software Diffrac. EVA vs 5.0 was used to collect the XRD patterns. The 2θ range of scan was set between 20 and 140 degrees with a scanning step size of 0.035 degrees. The X-ray beam was collimated to a spot size of 0.5 mm in diameter. The applied voltage and current were 45 kV and 35 mA respectively, which resulted in a penetration depth of 6 µm.

Crystallographic maps of the wrought and additively manufactured parts were collected using the electron backscattered diffraction (EBSD) technique to study the texture and reveal the microstructure at the surface along the fatigue crack path. Sample preparation was done similar to the microscopy sample preparation. However, an additional polishing step with 0.25 µm colloidal silica slurry followed by ultrasonic bath cleaning with isopropanol was done. EBSD data collection was performed using an SEM Mira 3 Tescan equipped with channel 5- HKL software. The accelerating voltage was

set to 20 kV. To study the crack growth path and reveal the microstructure of the materials, the step sizes of 1 µm and 0.8-1.2 µm were used for imaging around the crack and on large areas far from the cracks respectively. To post process the acquired data, TSL-OIM analysis software version 8 was used. The number of collected data points in the IPF maps used for microstructural analyses, varied from 2,797,299 points, in the scans with larger step size, to 6,842,364 points in the scan with the smallest step size. At least 96.57 percent of the collected points were indexed, and the lowest average confidence index (CI) of the measured data was 0.35. Grains were classified in relation to the neighboring groups as groupings of more than 10 pixels with crystallographic misorientation of larger than 5 degrees [41]. To plot the pole figures, a generalized spherical harmonic expansion smoothing with series rank (L) of 16, a Gaussian half-width of 5 degrees, and a triclinic symmetry was used.

Vickers hardness measurements were done on different AM and wrought samples using a Struers DuraScan G5 testing machine at a load of 1000 gf (HV1) and the holding time of 10 s. Hardness measurements of the NG and wrought samples were repeated 10 times to assure the reliability and consistency of the tests. For G specimens Vickers hardness measurements were performed in intervals of 0.3 mm along the entire width in multiple locations to understand the effect of the microstructure gradient on the surface hardness. Prior to the measurements, all samples surfaces were prepared as provided in the ASTM E92 [42].

2.3 Fatigue crack propagation

2.3.1 Fatigue testing

Three-point bending fatigue tests were performed using a servo hydraulic MTS machine with a loading capacity of 25 kN equipped with the MTS MultiPurpose TestWare and Flextest electronic control unit. Specifically, for this work, a novel fatigue test setup, as shown in figure 3, capable of investigating the fatigue crack growth of graded materials in an accurate and reproducible manner,

was developed. Three-point bending tests were conducted employing fatigue test configurations and stress intensity solutions as described in ASTM E399 [40]. An S690 steel platform with two fixed rollers was made and mounted to the lower grip of the MTS machine. Reference marks, with 0.5 mm intervals, were fabricated on the surface of the samples from the edge of the notch up to 7 mm. For visual crack calibration and to monitor the symmetry of the crack propagation, Limess digital image correlation (DIC) 5 megapixel cameras on two sides of the samples were used, and the average optically-measured crack lengths were periodically compared. Direct current potential drop (DCPD) equipment from Howden brand with a typical crack length measurement resolution of about 0.05 mm, was used to determine the dependence between the actual crack length and the measured voltage in two places across the samples. A polymer clamp system (PMMA) was designed to facilitate stable connections of the DCPD probes as well as to ensure the proper alignment of the samples on the platform. To minimize the errors and increase the accuracy, prior to the tests equipment and setups were tuned and calibrated.

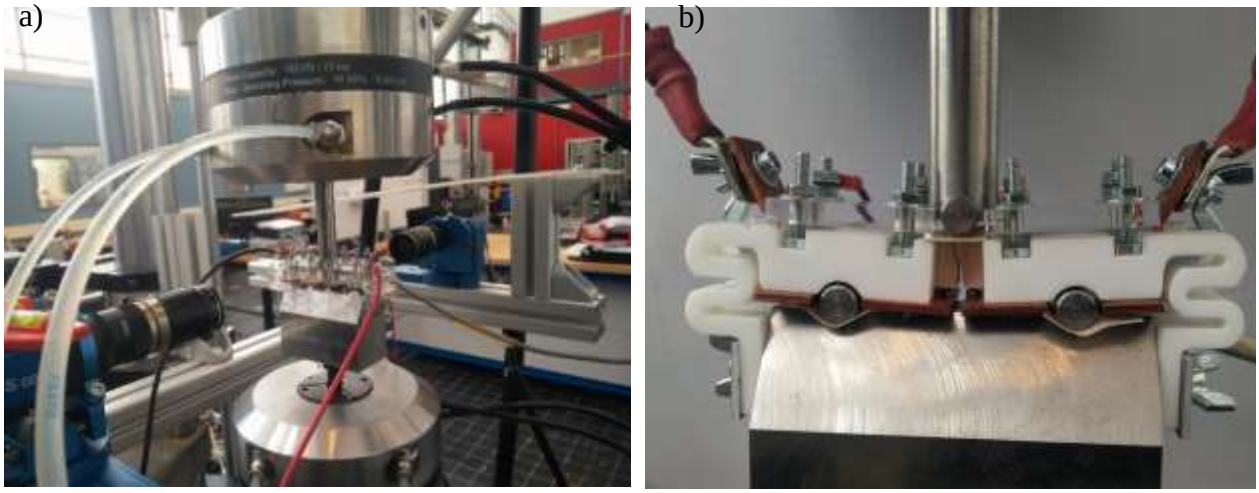

Figure 3. The novel fatigue test setup designed for this study to facilitate accurate testing of the graded samples. (a) shows an overall view of the three-point bending test setup and equipment and (b) depicts the sample, DCPD connections, and loading fixture.

Fatigue crack propagation testing was done through the following procedures:

Constant K_{max} tests were done to determine the threshold stress intensity range (ΔK_{th}). The ΔK_{th} tests were conducted at a frequency of 30 Hz and an initial load ratio of R=0.1 (where $R=K_{min}/K_{max}$), which then was increased to R=0.6 and R=0.7 for the wrought and L-PBF materials, respectively. The K_{max} was calculated according to equation (3) to facilitate an appropriate ΔK to grow a crack. The value of K_{min} was adjusted using equation (4).

$$K_{\max} = \frac{\Delta K}{1-R} \tag{3}$$

$$K_{\min} = K_0 \exp\left(C\left(a - a_0\right)\right) \tag{4}$$

Where K_0 is the value of the initial K_{min}, C is the stress intensity gradient which was chosen to be -0.4 mm-1, a_0 is the initial crack length measured optically, and a is the instantaneous crack length measured by DCPD and validated by periodical optical and DIC observations.

K_{min} was calculated and adjusted at intervals of 0.1 mm. The adjustment process was carried out until the crack did not grow by 0.1 mm in 100000 cycles, which indicates a crack growth rate of 10-6 mm/cycle or less. The final reading of ΔK was considered as the ΔK_{th} value.

Constant load amplitude tests (Paris regime) were performed to formulate the crack growth rate as a function of stress intensity range (ΔK). The crack growth rate tests were done at a frequency of 50 Hz and based on the condition provided by ASTM-E647 [43].

The graded samples were examined under constant stress intensity range (constant ΔK) condition to evaluate the effect of the FGM microstructure on the crack growth rate behaviour. Since at a given ΔK level the FCGR is a constant value for a particular microstructure, maintaining a constant ΔK should reveal the effect of the functionally graded structure on the FCGR. It should be pointed out that the

standard K solutions for determining the load levels as a function of f(a/W) are for homogenous materials hence do not apply to the functionally graded parts and require adaptation.

It should be mentioned that for the constant Kmax and constant ΔK tests, the loads were adjusted automatically during crack growth, to match the desired stress intensity range for the crack length measured by the DCDP system.

2.3.2 Modelling

In order to obtain accurate customized K solutions for constant ΔK tests of graded materials, an elastic FEM model within ABAQUS software was developed. In this model, each graded specimen is represented by two halves, i.e. 250 W and 950 W, with an interface plane perpendicular to the crack. Figure 4(a) shows the model used in the current study. The half-span of the specimen is modeled under 2D plane strain condition, where the global X axis is the transversal direction and the global Y axis is the direction of deflection. Crack is modeled at the symmetry plane of the specimen. The crack length is varied from 1.5 mm to 7.5 mm in order to study the change of the stress intensity factor during the crack growth. At the symmetry plane, displacement along X axis is constrained at the non-cracked edge, while free boundary condition is applied to the crack. The applied load is modeled with a point load along the negative Y direction at the top edge and the support is modeled as a point pined constraint at the bottom edge. Due to the symmetry, the total load applied to the FEM is 5 kN, as the test load at the mid-span of the specimen is 10 kN. The Young's moduli of the 250 W and 950 W parts are obtained from the compliance measurements of the fatigue tests of the non-graded specimens. The Poisson's ratio is set to be 0.3. The interface based on a previous research [24] has a total thickness of 1 mm and is divided into 5 layers of 0.2 mm height, with a linearly changing Young's modulus assigned to each layer. Small mesh elements of 0.02 mm are used near the crack tip, while elements of 0.5 mm are used outside the crack-influenced area. In total 185 CPE6M (6-node modified quadratic plane strain element, with hourglass control) and 4456 CPE8R (8-node biquadratic

plane strain element with reduced integration) elements are used. J integral is calculated at the fifth contour from the crack tip. The fifth contour involves a circular area with a radius of 0.08 mm, shown in Figure 4(b). K solution is then obtained from the J integral according to equation (5).

$$K = \sqrt{J \times \frac{E}{1-\nu^2}} \tag{5}$$

Where E is the Young's modulus at the crack tip, J is the integral value and ν is the Poisson's ratio.

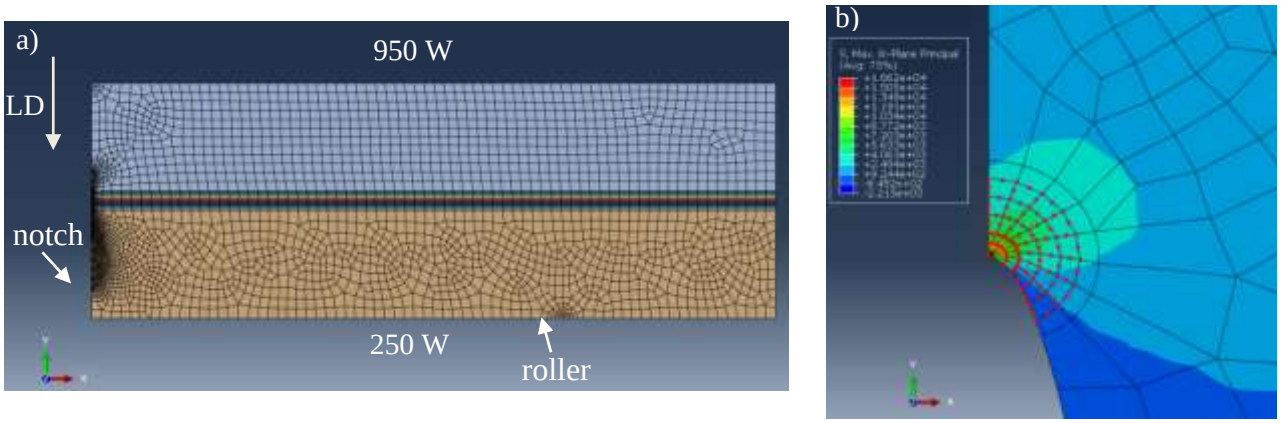

Figure 4. a) The model used for the FEM analysis of the graded materials. Since the sample is symmetric about the axis containing the notch, half of it is modelled. The loading direction (LD) and the location of one of the rollers are determined in the figure. The notch is on the left edge where the mesh has more elements. The mid-height region which has different colours represents the five layers of the interface in the model. b) Nodes involved in the fifth contour to calculate the J integral.

The goal of conducting the constant K tests was to determine the effect of the graded microstructure on the crack growth rate. For a particular microstructure, at a given level of ΔK, the crack growth rate is expected to be constant. To maintain the constant ΔK criterion the load level should be modified based on accurate solutions of K. The standard K solutions are only applicable to materials with a constant Young's modulus (E). However, graded samples are intentionally manufactured with various microstructures, hence different material properties (including E) are expected. Therefore, prior to the FEM modelling, the values of E for the non-graded materials were estimated from the load-line-

compliance [44]. The load line displacement (δ_{total}) of the fatigue test and the load line displacement in the absence of the crack, $\delta_{no\text{-}crack}$, are given by equations (6) and (7) respectively.

$$\delta_{total} = \delta_{crack} + \delta_{no-crack} \tag{6}$$

$$\delta_{no-crack} = \frac{P.S^3}{4.E.B.W^3} \tag{7}$$

Where P is the applied load, S is the span length, E is the Young's modulus at the crack tip, B is the height of the sample, and W is the width of the specimen. The additional displacement due to the presence of a crack, δ_{crack} is given by equation (8).

$$\delta_{crack} = \frac{3.P.S^2\left(1-\nu^2\right)}{2.E.B.W^2} f\left(\frac{a}{W}\right) \tag{8}$$

Where ν is the Poisson's ratio and $f(a/W)$ is a dimensionless geometry factor defined by equation (9).

$$f\left(\frac{a}{W}\right) = \left(\frac{\frac{a}{W}}{1-\frac{a}{w}}\right)^2 \left\{5.58 - 19.57\left(\frac{a}{W}\right) + 36.82\left(\frac{a}{W}\right)^2 - 34.94\left(\frac{a}{W}\right)^3 + 12.77\left(\frac{a}{W}\right)^4\right\} \tag{9}$$

Measurements of displacement and load during the fatigue tests were applied to the equation (6)-(9) to estimate the Young's modulus for each microstructure of AP IN718. The calculated values of Young's moduli from non-graded specimens, given in table 2, which are in good agreement with values in [24], were applied to the FEM-model to calculate the modified K solutions.

Table 2. Young's modulus of non-graded L-PBF IN718 superalloy obtained from three-point bending tests.

Laser power [W]	Specimen direction	Measured Young's modulus [GPa]
950	V	139 ± 36
950	H	136 ± 10
250	H	186 ± 15

3. Results and discussions

3.1 Microstructural Characterization

Figure 5 shows the light optical microscopy images of the longitudinal cross sections of the IN718 samples processed using 250 W and 950 W laser powers. Figure 5 (a) depicts the 250 W material with finer melt pools, while figures 5 (b) and 5 (c) show the 950 W material with irregular and larger melt pool contours. Moreover, higher magnification optical micrographs in figures 5 (d) and 5 (e) are provided for a better comparison. The differences in the size and shape of the melt pools arise from the different process parameters used in this study. Higher laser power is capable of penetrating deeper and melting the previously solidified layers, and as a result, larger melt pools can be generated. The other parameter that affected the melt pools' size was the laser scanning speed which was 320 mm/s and 700 mm/s for the higher and lower laser powers. The lower laser scanning speed was found to result in wider and deeper melt pools and vice versa due to the changes in the melt pool penetration depth [45, 46]. Considering the effect of the laser power and laser scanning speed simultaneously, lower LED values results in deeper and narrower beads, with an average of 133 µm depth and 108 µm width of the beads, while the higher LED values make shallower and wider beads, with average values of 62 µm depth and 116 µm width of the beads. Similar behaviour is reported in a previous research [47].

Optical micrographs of the longitudinal cross sections of the interfaces in the graded samples are provided in figure 6. The deposition of each layer in the vertical (V) sample shown in figure 6(a) contains a transition at the interface from 250 W to 950 W. The melt pools out of the interface region show the characteristics of the NG samples corresponding to each laser power, as discussed before. The interface is distinguished by the finer melt pools in the centre, and keyhole-induced porosities, unmelted particles, and deeper melt pools in the edges which can be a result of overlapped melt pools.

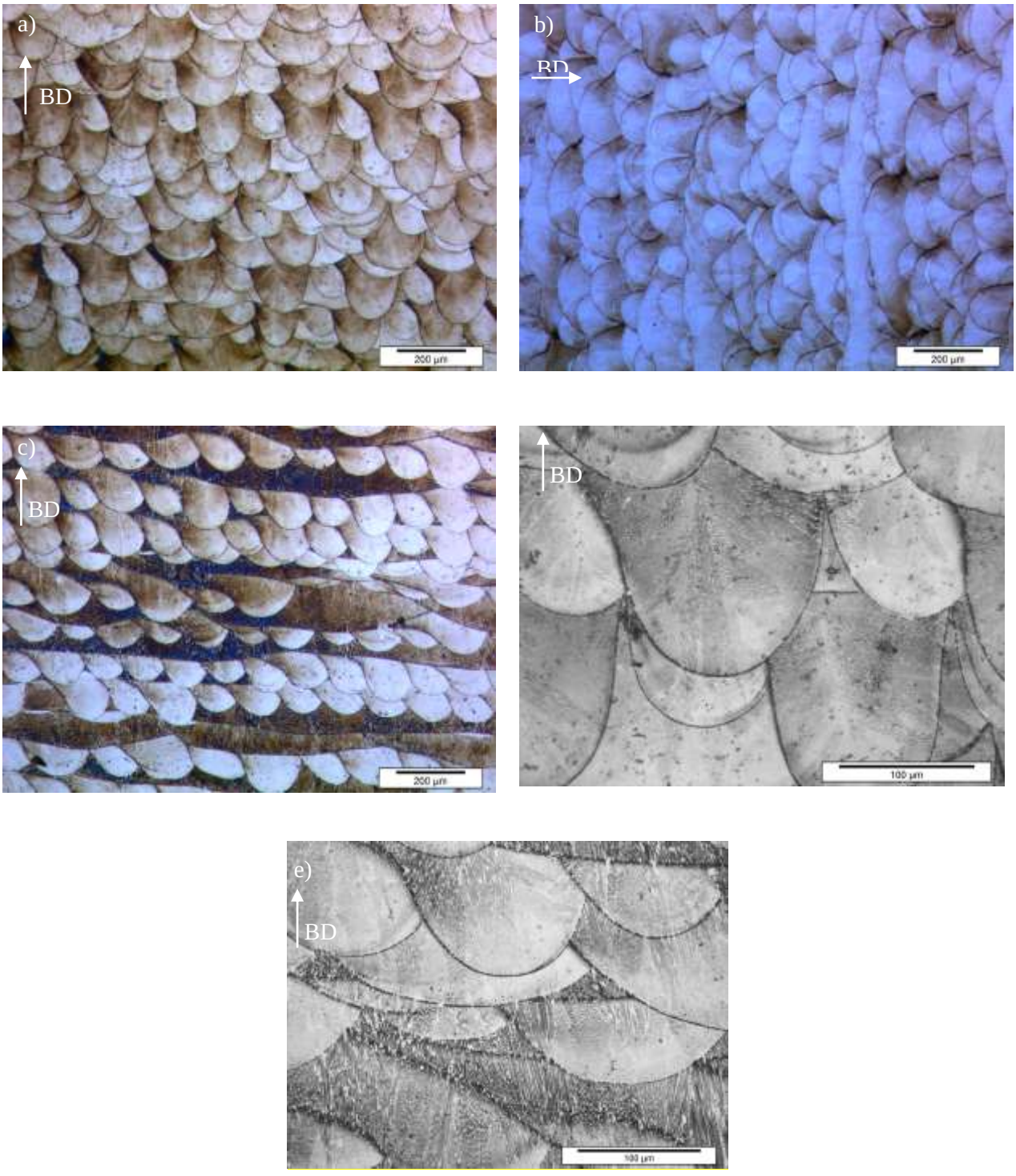

Figure 5. Optical micrographs of longitudinal cross sections of the as-printed samples (a) 250 W-H, (b) 950 W-V, and (c) 950 W-H showing the melt pools. Higher magnification optical micrographs of (a) and (c) are provided in (d) and (e) respectively.

In addition, the time window associated with the change of the depositing parameters which takes place in each pass can influence the interface microstructure. The transition in the horizontal (H)

graded sample was smoother since each layer was deposited using one laser power, namely 250 W in the bottom of the micrograph and 950 W in the top layers, as shown in figure 6(b). Melt pools in the lower and upper parts are thus similar to those discussed earlier in the NG 250 W and 950 W laser power samples. Figure 6(c) which is also obtained on an H sample is taken by a non-digital microscope and shows the characteristic dendritic growth and epitaxial microstructure.

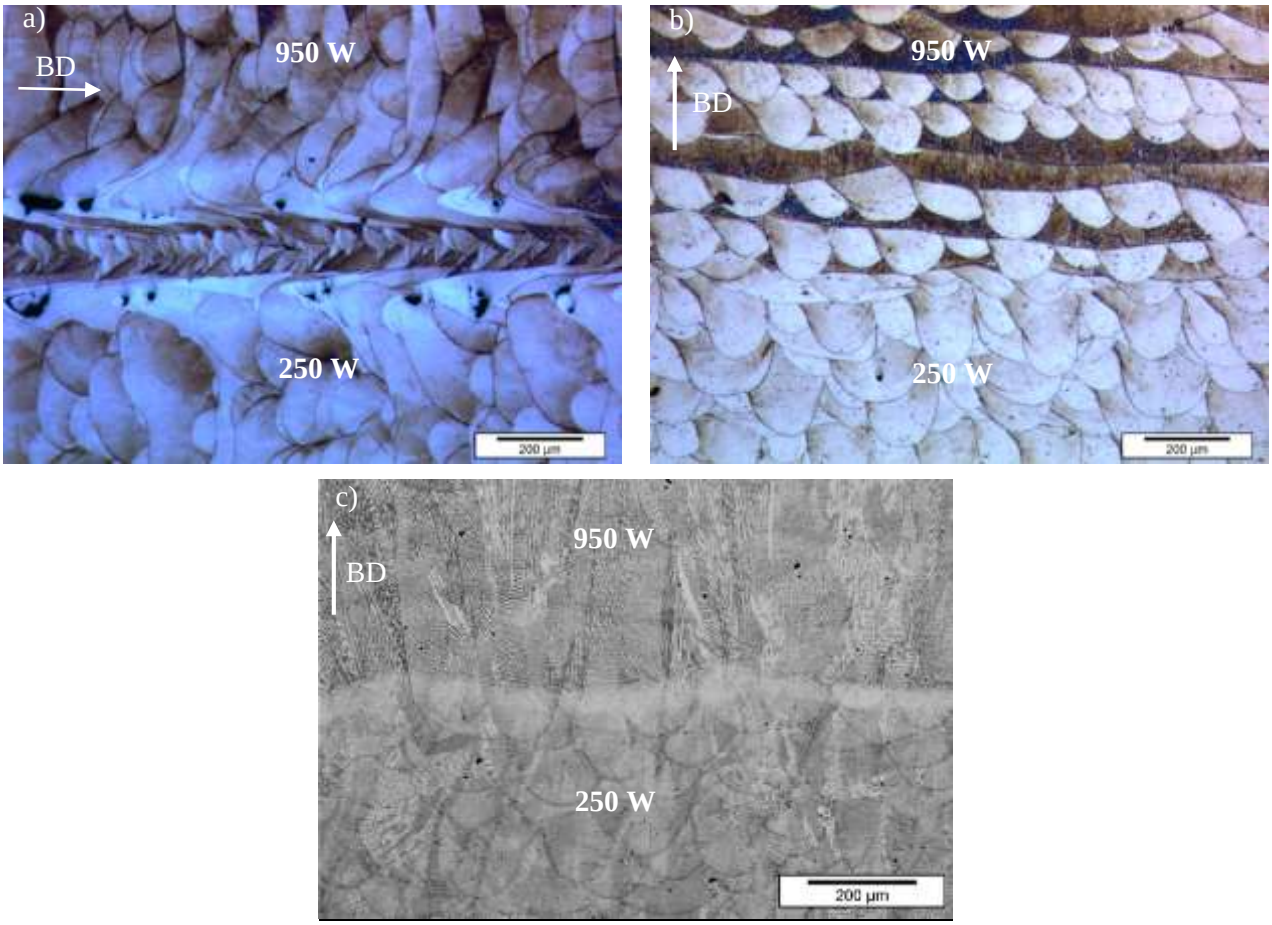

Figure 6. Optical micrographs of the interface area in the graded AP samples in (a) V, (b), and (c) H orientations. The laser power used for each side of the interface along with the build directions are provided in the figures. It should be noted that figure c is taken by a different microscope to highlight the epitaxial columnar dendrites and interface transition.

Figure 7 shows the SEM micrographs of the as-processed (AP) L-PBF specimens in the sections parallel to the build direction (BD) along with a micrograph of the wrought sample. As can be seen in all L-PBF categories, grains are extended along the BD. The layer thickness of the 250 W and 950 W laser power samples were 50 µm and 100 µm, respectively. In the micrographs, the larger axis of the

grains in all categories exceeds the layer thickness, which is an indication of melting the previously solidified layers and a strong trend of the epitaxial grain growth from one layer to another [24]. In the higher magnification micrographs, fine dendritic segregations are captured along the build direction. The presence of such dendritic structures has been reported in the AM IN718 alloy in the earlier research and is attributed to the very high solidification cooling rates [48, 49]. Similar to the grains, dendritic structures showed the epitaxial growth between the layers in all three studied categories.

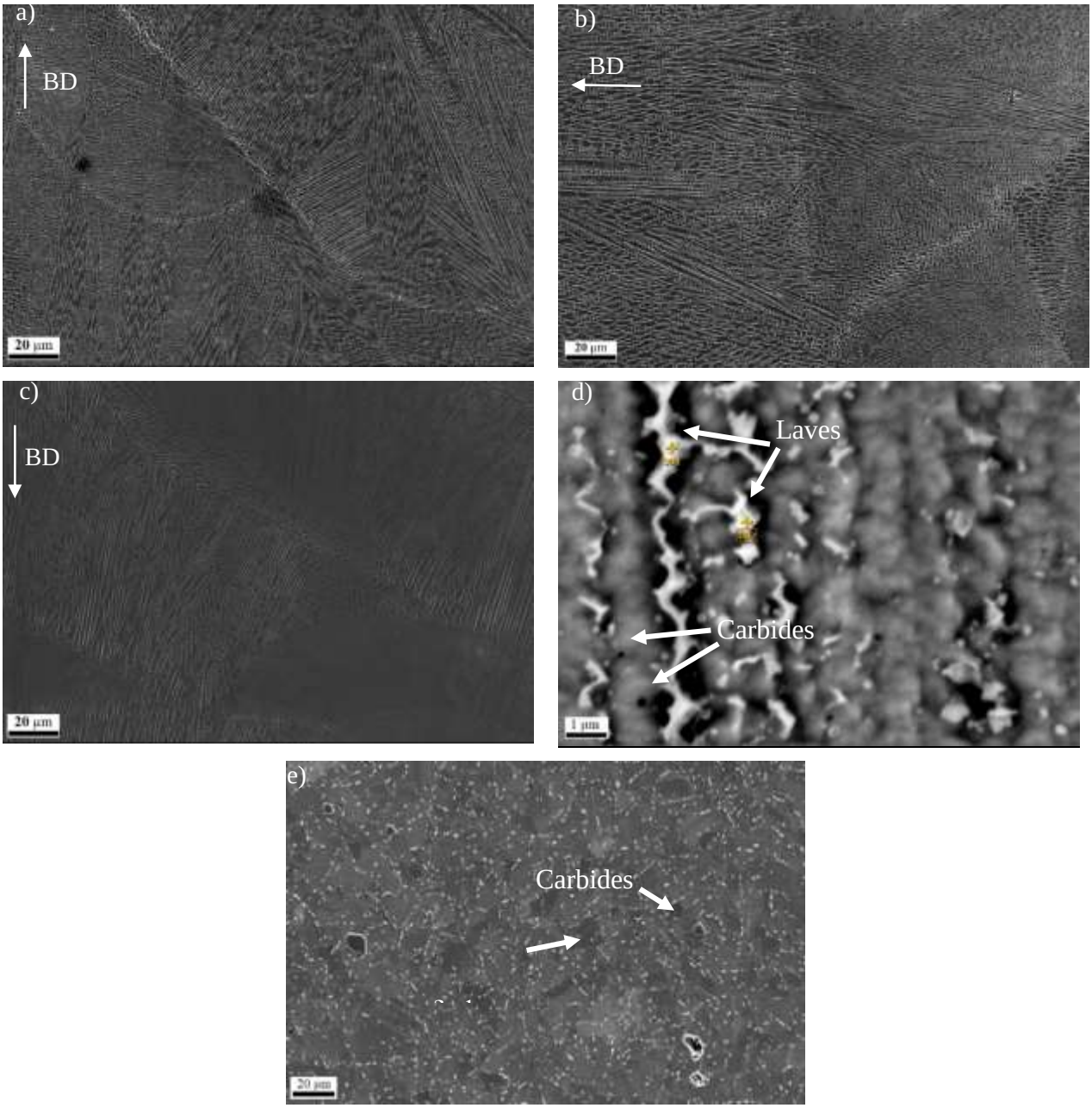

Figure 7. SEM micrographs of the AP specimens manufactured in different conditions (a) 250 W, (b) 950 W-V, (c) 950 W-H, and (d) a high magnification BEC micrograph of the sample shown in (c). The micrograph in (e) shows an SEM image of the heat treated wrought sample where the precipitates are found mostly around the grain boundaries.

To better reveal the existing larger phases such as Laves phase and carbides, the backscattered electron composition (BEC) technique was used, and imaging was performed in higher magnification. As can be seen in figure 7(d), carbides and inter-dendritic Laves phases are present in the AP material, which could affect the fatigue properties. The composition of these phases acquired by Energy Dispersive X-Ray Spectroscopy (EDS) is given in table 3. In the micrograph of the wrought material shown in figure 7(e), needle shape and globular δ phases are captured close to the grain boundaries. The SEM micrographs do not reveal the fine strengthening precipitates due to their nanometer-size dimensions. Since the SEM micrographs shown in figure 7 are performed in such a magnification that a number of melt pools were captured, the precipitates in orders of microns could be detected. Moreover, the strengthening precipitates of the AM IN718 estimated to have their sizes ranging between 10 nm and 50 nm [50]. Therefore, compared with SEM, transmission electron microscopy (TEM) is a more suitable method for detecting them. It should be noted that the Laves phases, which form during the solidification in the AM process, are not present in the wrought material.

Table 3. EDS analyses of the Laves phase and carbides in the 950 W-H material.

	Ti	Cr	Mo	Fe	Ni	Nb	C
Laves	2.63	18.58	4.48	16.57	38.19	19.55	-
Carbides	7.10	0.63	-	0.57	1.37	50.19	40.15

To identify all existing phases, XRD analyses on all groups of materials were performed and the results are summarized in figure 8. The precipitate peaks in the L-PBF samples are minor, and the precipitate concentration based on the previous study [24] does not exceed 2 wt.%, which is not high enough to have a strong effect on the mechanical properties. In both laser powers materials, Laves

phases are present, which are detrimental to the mechanical properties and can be altered by heat treatment and post processing procedures [7]. In all materials, the γ peaks were found at 2θ of 51, 59, and 89 degrees. The γ peaks at 2θ equal to 51 and 59 degrees in the 950 W- H material are not identical and the first peak is significantly shorter than the other, which suggests an anisotropy in the texture. However, the γ peaks of the 250 W and 950 W- V materials are similar, which indicates more uniform textures. The γ', γ", and δ phases peaks only were observed in the wrought materials.

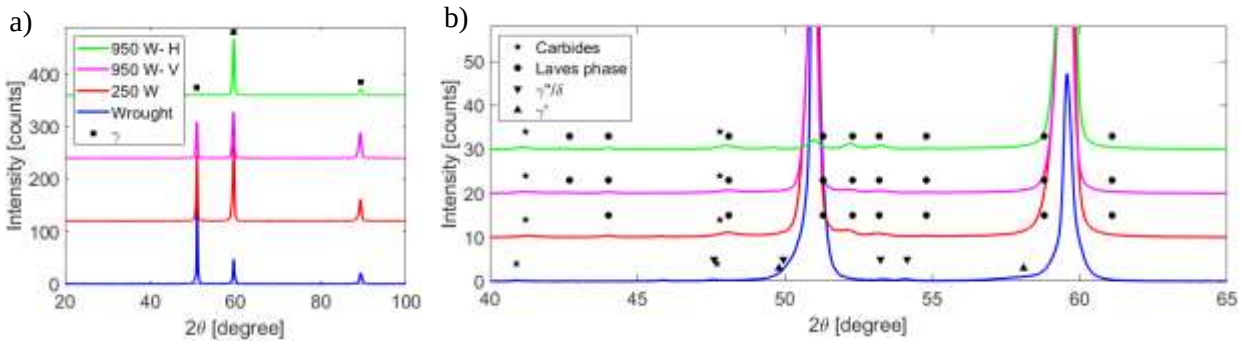

Figure 8. XRD spectra showing different phases in the AP material manufactured using different laser powers and the wrought material. Sub-figure (b) shows a zoomed-in view with identified phases.

The average values of the Vickers hardness in all non-graded L-PBF categories as well as the wrought material are summarized in table 4. The average hardness values of the AM parts are relatively close to each other, with the 250 W sample category about 9% and 18% higher than the 950 W- H and 950 W- V groups. This higher hardness of the 250 W samples can be attributed to its finer grains and higher yield strength [24], which is explained by the Hall-Petch relationship. Among the two groups of 950 W laser power, the average hardness of the horizontal orientation specimens is about 11% higher than the vertical direction samples, which cannot be explained by the grain size effect. The morphology and content of the brittle Laves phases which form in the interdendritic regions [50, 51] can also influence the hardness. Coarsened Laves phases with lower volume fraction result in a higher hardness compared with a higher volume fraction of fine dendrites and particles of Laves phases [50]. The Vickers hardness of the wrought material is 25% higher than that of the 250 W group. As next it will be explored in more depth, the wrought material has significantly finer grains compared with the

L-PBF parts. This can result in higher yield strength and hardness. In addition, the presence of the strengthening precipitates formed during the heat treatment affects the hardness. Therefore, the higher hardness values of the wrought material arise from the combined effect of the grain size and strengthening precipitates.

Figure 9 shows the hardness profile measured along the width of the graded samples. The measurements were done on multiple locations for both samples which are shown on the schematics provided in the insert of figure 9. In the V samples, the average hardness value of the material closer to the build platform, denoted as V-1, found to be a constant value of about 340 HV with some fluctuations of around 5% present due to the inhomogeneity in the microstructure [50]. Similarly, the measurements on the side further from the build platform, V-2, which correspond to the final layers of deposition, showed a constant value of about 320 HV. While the average hardness values of the V sample remain approximately constant in one layer (or close layers) of deposited material, it depends on the measurement location with respect to the build platform. The average hardness of the V sample in the parts close to the notch, i.e. near the centre of the specimen, and layers closer to the build platform were approximately constant and higher than the final deposited layers. This behaviour can be attributed to the higher number of thermal cycles which the initial and middle layers experience compared with the final deposited materials. The hardness measurements of the horizontal sample along the width, however, showed a different trend. The measurements were repeated at different distances with respect to the notch position. In all measurements independent of the measurement location, the average hardness value of the 250 W side, which is closer to the build platform, is about 360 HV. Going through the interface, there is no significant change of the hardness and it fluctuates between 344 HV and 358 HV. On the 950 W side, the hardness decreases to an average value of 340 HV. For a better comparison, these hardness values along with the average Vickers hardness of the non-graded and wrought material are provided in table 4. The higher values of hardness in the layers closer to the build platform and the middle parts of the samples compared with the final deposited

layers is related to the different fractions and morphology of the Laves phases which form during the last steps of solidifications. The initially deposited layers experience a larger number of thermal cycles which result in the diffusion of Nb into the matrix and decreases the Laves phase fraction [50, 51].

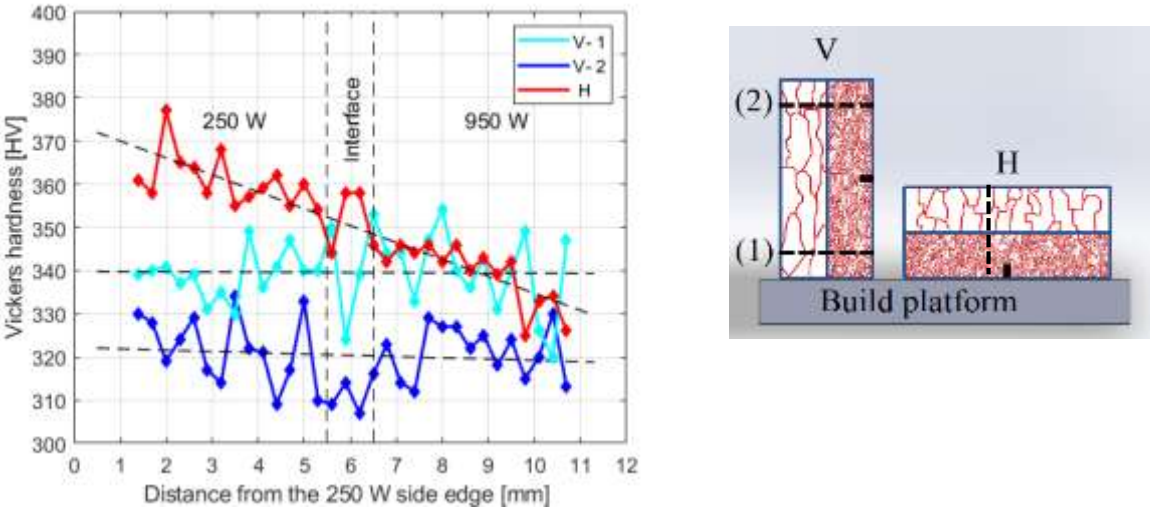

Figure 9. Hardness profiles of AP graded samples. The measurements are done through the samples' height starting from the 250 W side. The measurements of the vertical sample are plotted for two locations: V-1 which is closer to the build platform, and V-2 which is closer to the final deposited layers. The hardness measurements were performed multiple times along with the dashed lines which are determined in the schematics provided in the insert.

Table 4. Average Vickers hardness measured for different sample groups.

Sample group	Not Graded					
Hardness [HV1]	H 250W	H 950W	V 950W	Wrought		
	373 ± 11	341 ± 9	303 ± 10	486 ± 9		
	Graded					
	H 250W side	H 950W side	V 250W side	V 950W side	H interface	V interface
	361 ± 6	340 ± 7	339 ± 5	340 ± 9	351 ± 7	341 ± 13

Moving towards the final deposited layers, the material experiences fewer thermal cycles, and more Laves phase can be present, which results in a lower hardness value. The observed different behaviour in two categories of graded samples is thus a consequence of the different processing orientations. In addition, the different hardness behaviour of the V and H samples can be related to their different textures, since strong textures are known to cause anisotropy in hardness[52]. As will be discussed in the next part, horizontal samples have a strong <001> texture compared with the vertical samples. It is apparent that altering the processing parameters combined by the build direction influences the local mechanical properties. As will be shown later the observed hardness profiles for graded samples correlates well with the fatigue crack growth profiles.

To further study the effects of the manufacturing parameters on the microstructure, EBSD analyses on the planes parallel to the build directions were performed on all NG samples in addition to the heat treated wrought sample. Figures 10 (a-d) show the Inverse Pole Figure (IPF) maps and pole figures from the EBSD analyses on the NG and wrought samples. Studied herein, L-PBF samples were found to exhibit columnar grain structures in the deposition direction. However, the grain elongations varied with the manufacturing parameters. The aspect ratio and average major axis length of the 250 W and 950 W- V are close to each other. But the 950 W- H material has significantly larger grains with a lower aspect ratio. The grains in the wrought material, are equiaxed and their size is in order of magnitude smaller than the grains in the L-PBF materials. Table 5 gives a summary of the minor and major axes lengths as well as the values of the grain aspect ratios of the NG and wrought samples. Columnar grain structures originate from the dendritic and epitaxial growth, which is affected by the heat flow during the L-PBF process [24, 53]. Due to the constraints imposed by the solidified parts and layers on the side and bottom, the heat flow in the molten parts is known to be perpendicular to the deposit direction and from the top to bottom [47, 53]. Grains form parallel or nearly parallel to the heat flow [54]. The heat flow of different scan passes is expected to be similar and uniform in the inner parts, far enough from the sides and edges of the samples, while the heat flow of the parts closer

to the edges can vary due to the effects of the free surfaces. The grain sizes can thus be influenced by this variation in the heat flow when the samples are built in different directions. It is noted that if a specific direction of an FCC crystal matches the heat flow direction of the melt pool, that particular direction will grow faster and become dominant [47]. The IPF map of the 250 W sample shows a combination of all crystallographic directions. The <001> direction is, however, dominant in the higher laser power IPF maps. In the 950 W- H sample, the faster growth of grains aligned with the <001> direction blocked the slower growing grains with other orientations.

Figure 10 depicts the $\{001\}$, $\{110\}$, and $\{111\}$ stereographic pole figures with triclinic symmetry for NG and wrought samples. The pole figures are constructed from the measured EBSD data using an orientation distribution function. The as processed AM IN718 microstructure is expected to show either cubic texture ($\{001\}\langle 100\rangle$) or Goss texture ($\{110\}\langle 001\rangle$) [55]. Figure 10(a) gives the crystallographic texture of the 250 W sample, which shows a weak Goss texture component. Similar texture components were observed to form in the as-built AM Inconel 625 alloy [56, 57]. Pole figures of the higher laser power samples are given in figures 10 (b) and 10 (c). As can be seen, both 950 W-V and 950 W-H materials have strong cube textures. The largest maximum value of the multiples of a random distribution (m.r.d.) is observed in the 950 W-H material, which shows the strongest texture. The wrought sample has a weak random texture. The formation of the Goss and cube textures in different samples in this study can be attributed to the orientations of the dendritic solidifications driven by the heat flow which is controlled by the AM parameters. In addition to the various texture components, texture intensity can alter the mechanical properties in different sample categories, and thus anisotropic performance is expected.

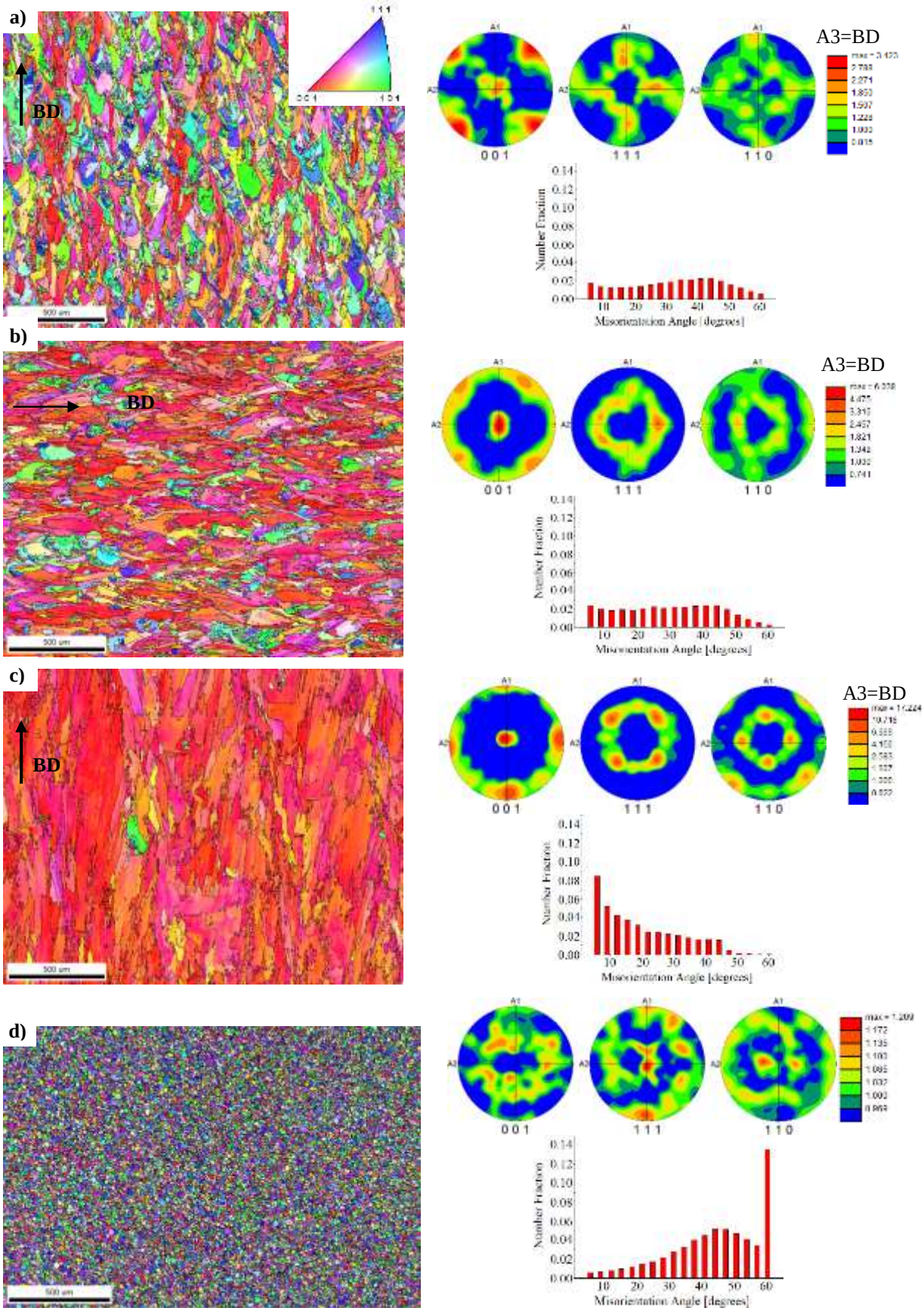
a)
BD
111
001
101
A3=BD
001
111
110
Number Fraction
Misorientation Angle [degrees]
b)
BD
A3=BD
001
111
110
Number Fraction
Misorientation Angle [degrees]
c)
BD
A3=BD
001
111
110
Number Fraction
Misorientation Angle [degrees]
d)
001
111
110
Number Fraction
Misorientation Angle [degrees]

Figure10. Inverse pole figure maps, pole figures, and misorientation angle plots obtained from the EBSD data of L-PBF materials (a) 250W, (b) 950 W- V, (c) 950 W- H, along with (d) wrought material. Note that grain boundaries with angles less than 5 degrees are not included in the misorientation plots. Textures of the L-PBF samples are rotated in a way that the build direction (BD) is parallel to the A3 (out of plane) direction. Intensities of the pole figures are plotted in multiples of a random distribution.

Table 5. Average grain major and minor axis, aspect ratio, and grain shape of the NG IN718 as well as the wrought material.

Manufacturing condition		Major axis [µm]	Minor axis [µm]	Aspect ratio	Grain shape/Preferred texture
L-PBF	250 W	135.6	28.9	0.27	Elongated in BD / No
	950 W - V	147.7	27.3	0.25	Elongated in BD / <001>
	950 W - H	518.4	79.9	0.18	Elongated in BD / <001>
Wrought		17.5	9.6	0.55	Equiaxed / No

From the misorientation angle plots of the non-graded and wrought materials in figure 10, it can be seen that the distribution of misorientation angles in the 250 W sample and 950 W- V specimen with finer grains are similar and more uniform, while in the horizontal samples (figure 10 (c)), the low angle grain boundaries (LAGB)s, i.e. misorientation angles less than 15 degrees [58], are dominant. The difference in the fraction of LAGBs could affect the fracture behavior of these categories. High fractions of LAGBs in AM nickel-based superalloys were observed in other studies [59, 60]. However, in the wrought material the presence of the annealing twin boundaries, which are defined at 60 degrees, is relatively high with a number fraction of about 0.14. Twin boundaries can increase the strength and ductility of the material by introducing more grain boundaries [61], while having detrimental effects on the fatigue performance by acting as crack nucleation sites [53, 62]. The number fraction of annealing twins in the AM materials is negligible, while they are significantly present in the wrought material.

This study confirms that L-PBF parameters can be effectively used to produce and design materials with different grain size, grain shapes and orientations, textures, and grain boundary (GB) character distributions and phases. The effect of these microstructural parameters on the fatigue crack growth behaviour will further be investigated.

3.2 Fatigue crack propagation

3.2.1 FEM model

The stress intensity factors have been calculated for twenty-one different crack lengths between 1.5 mm and 7.5 mm. The values of stress intensity factors were calculated from the FEM and normalized by the stress intensity factors calculated from the empirical formula given by equation (10) according to ISO 12135 [63].

$$f\left(\frac{a}{w}\right)=\frac{3\left(\frac{a}{w}\right)^{0.5}\left[1.99-\left(\frac{a}{w}\right)\left(1-\frac{a}{w}\right)\left(2.15-\frac{3.93a}{w}+\frac{2.7a^{2}}{w^{2}}\right)\right]}{2\left(1+\frac{2a}{w}\right)\left(1-\frac{a}{w}\right)^{1.5}} \quad (10)$$

Where a is the initial crack length, and W is the width of the specimens. The normalized values are plotted against the crack length, a, in figure 11. The normalized K values from the standard formula is a constant value at 1. It can be observed that the stress intensity factors of both categories of graded specimens are greater than the values calculated by the standard formula, which is due to the existence of the interface layer. The trends in both groups of G samples are very similar, with the normalized K values slightly higher for the H samples. Both curves show the most significant deviation from the standard when the crack tip is about to enter the interface. After the crack propagates across the interface, the influence of the interface vanishes. The values of the stress intensity factors reach the standard values rapidly after passing the interface.

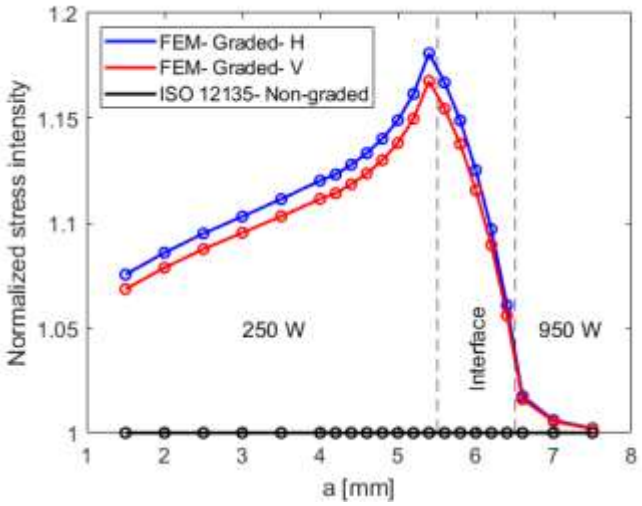

Figure 11. Plot represents the normalized values of K versus the crack length over the width obtained from the FEM model compared with the values provided by ISO 12135 which applies to the NG materials.

3.2.2 Fatigue behavior of Non-graded material

This section discusses the results of the two types of fatigue crack growth parameters, namely the stress intensity range threshold for fatigue crack growth (ΔK_{th}) and the Paris law crack growth behaviour. To establish the crack propagation behaviour of different microstructures, constant K_{max} tests were performed on various non-graded materials. Also, as a reference, the wrought material was tested. Table 6 gives a summary of obtained ΔK_{th} with respect to the manufacturing conditions and sample directions. In the L-PBF material categories, samples produced with 250 W laser power had the highest ΔK_{th} closely followed by the 950 W- V samples. The 950 W- H material showed the lowest amount of ΔK_{th} among the AM parts. The wrought material had a significantly higher ΔK_{th}. This behaviour can be attributed to the different microstructures in the materials. As was discussed in the previous section, the 250 W material has finer grains compared with the 950 W categories. Finer grains or more grain boundaries can introduce differently oriented less favorable slip systems, which increases the resistance to short crack growth [64]. Similarly, vertical samples with finer grains have a higher threshold stress intensity range compared with the horizontal samples with coarser grains. In addition to the smaller grains, 950 W- V samples have columnar grains oriented perpendicular to the crack direction resulting in more grain boundaries in front of the crack growth path. It should also be noted that ΔK_{th} of all produced herein L-PBF samples is twice higher than values reported for AM IN718 with the same orientations [60]. The wrought samples however showed the highest value of the threshold stress intensity range due to the equiaxed fine grains with a large number of grain boundaries in the crack path. Additionally, the presence of the strengthening precipitates formed during the heat treatment process can increase the threshold stress intensity range. In a previous research [65], ΔK_{th} of a heat treated forged IN718 (for R=0.1) with grain size of 40-60 µm, was reported to be 10.2 MPa$\sqrt{m}$. This is consistent with the effect of the grain size on the ΔK_{th} and the value which was obtained in the current study.

Table 6. FCG threshold (ΔK_{th}) values measured in constant K_{max} tests for samples with different processing conditions.

Manufacturing condition		Sample direction	ΔK_{th} [MPa$\sqrt{m}$]	R
L-PBF	950 W	V	7.0 ± 0.3	0.7
	950 W	H	6.0 ± 0.2	0.7
	250 W	H	7.2 ± 0.3	0.7
Wrought		-	13.1 ± 0.9	0.6

Figure 12 shows variations of fatigue crack growth rate against the stress intensity factor range, ΔK, describing the long crack behaviour of the various studied herein AM and wrought materials. The measured data of the L-PBF specimens showed some fluctuations, which are attributed to their heterogeneous microstructure and the residual stresses imposed during the manufacturing process [60]. It should be noted that the linear fits of the experimental data for crack growth rates of 5E-7 and higher are plotted. The fitting curves are based on the power law given by equation (11).

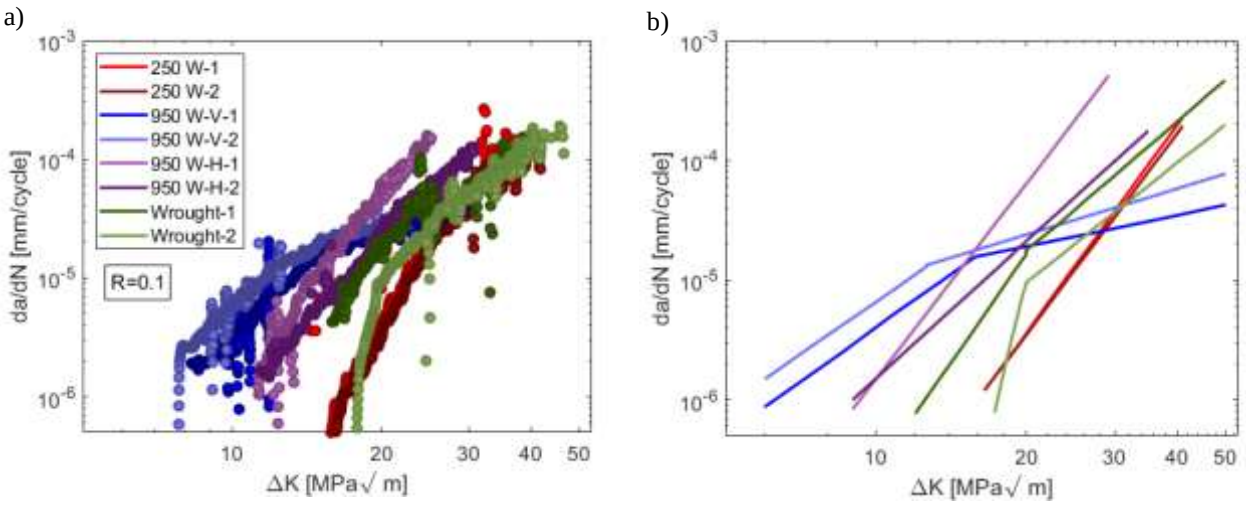

Figure 12. (a) Measured data and (b) Paris law fits of NG L-PBF samples with different microstructures as well as the wrought samples as references. Two data sets per category are provided. The legend in (a) applies to both figures.

$$\frac{da}{dN} = C(\Delta K)^m \tag{11}$$

Where *C* is the Paris constant and *m* is the Paris exponent. Paris constants along with the R-squared values of the fits in figure 12 are summarized in table 7.

ΔK_{th} values obtained from the curves in figure 12 for 250 W, H-950 W, and wrought categories are higher than those provided in table 6, which were tested at a higher R ratio. It is known that at a low stress ratio of 0.1 the crack closure phenomenon affects the threshold stress intensity range [28, 65, 66]. A similar dependency of the ΔK_{th} to the stress ratio of an additively manufactured [67] and wrought [68] nickel based superalloy was reported. However, the threshold stress intensity ranges of the V-950 W L-PBF samples did not show a significant difference when R changed. In this work, a strong dependency between roughness-induced crack closure and R ratio was found for H-950W and H-250W L-PBF materials. Hence, threshold values reported in Table 6 can be considered as true representative values not affected by the crack closure.

As it can be seen in figure 12, the fatigue crack growth rate versus ΔK in 250 W and 950 W- V categories show a single fitting curve, while in the other groups, the behaviour changes around an FCGR of 1E-5. Such lower plateaus were also observed in constant K_{max} tests at R=0.1 in wrought Inconel 718, which was attributed to the accumulation of fretting debris that caused darkening of the fatigue surfaces [66, 68]. It is known that the larger values of the Paris exponent are indications of finer fatigue striations [60]. The wrought material and the 250 W with finer grains have higher Paris exponent values in the Paris relationship. It can be seen that for lower values of ΔK, the 250 W category has the lowest FCGR values which indicates its better fatigue performance in comparison with other specimens. For larger ΔKs in the Paris region, 950 W- V specimens show the lowest FCGR. It can be related to the larger number of grain boundaries mostly oriented perpendicular to the crack path.

Table 7. A summary of Paris law constants for NG and wrought samples tested at R=0.1. The ΔK_{th} values are calculated by extrapolations of the Paris curves.

Manufacturing condition		BD	ΔK_{th} [MPa$\sqrt{m}$]	Paris exponent (m_1)	Paris exponent (m_2)	Paris constant (c_1)	Paris constant (c_2)	R_1^2	R_2^2
L-PBF	950 W	V	6 ± 0.5	3.0 ± 0.1	1.1 ± 0.2	(6.0 ± 2.3) E-9	(9.4 ± 4.3) E-7	0.946	-
		H	9.2 ± 0.2	4.6 ± 0.8	-	(1.2 ± 1.1) E-10	-	0.972	0.978
	250 W	H	16.5 ± 0.1	5.7 ± 0.1	-	(1.6 ± 0.5) E-13	-	0.936	0.984
Wrought		-	15.1 ± 2.4	11.3 ± 5.7	6.1 ± 0.1	(4.5 ± 4.5) E-13	(3.5 ± 1.1) E-10	0.960	0.815

3.2.3 Fatigue behaviour of graded material

The previous part focused on the fatigue behaviour of the non-graded specimens. However, one of the main interests of this study was to investigate the fatigue behaviour of the graded parts. In order to study the fatigue crack growth of the graded samples, constant ΔK tests were performed on both graded material categories. To maintain the constant ΔK condition, particularly near and across the interface area, the customized K solutions based on the J-integral values around the crack tip were used. The fatigue crack growth rate versus crack length, a, of constant ΔK experiments for both categories of graded materials are provided in figure 13. In both vertical and horizontal orientations, the FCGR increases as the crack propagates into the interface. This behaviour can be associated with the microstructural features of the interface area. The crack growth rate of the graded vertical 250W→950 W-V sample tested at 22.5 MPa$\sqrt{m}$ is relatively constant, with the variation of the $\frac{da}{dN}$ around 3E-5- 6E-5 mm/cycle in both sides of the interface. This behaviour is related to the build direction of the sample. The crack path in the V specimens grows within a layer of deposited material, which went through the same or a close number of thermal cycles. This implies that the distributions of the probable strengthening precipitates, carbides, and detrimental Laves phases are uniform along

the crack path. A similar trend was observed in the Vickers hardness profile of the vertical samples, shown in Figure 9. The crack growth rate of the vertically graded sample in the 250 W region is higher than that in the 250 W non-graded, which is about 6E-6 mm/cycle. Similarly, the FCGR of the 950 W region of the graded sample is also higher than the non-graded 950 W specimen, which is about 1E-5 mm/cycle. The differences in the $\frac{da}{dN}$ values arise from the differences in the residual stresses developed in the materials during the manufacturing process. Compressive residual stresses act as extrinsic closure factors which can lead to crack closure and hindrance of the crack growth [65]. Table 8 gives the measured residual stresses on the non-graded samples. It also should be noted that the lowest fatigue crack growth rate of the graded vertical sample, 2E-5 mm/cycle, was observed inside the interface.

The fatigue crack growth rate of the horizontal graded sample tested at ΔK=25 MPa$\sqrt{m}$, however, increases gradually from about 4E-6 mm/cycle in the lower laser power region to about 7E-5 mm/cycle in the higher laser power region. The FCGR of the 250 W region of the graded sample at the beginning is lower than its measured value in an NG sample, 2E-5 mm/cycle. However, it reaches this value before the crack propagates to the interface. Although, the FCGR has an increasing trend as the crack grows, it remains below 1.5E-4 mm/cycle which was measured on the NG 950 W specimen. This trend is in agreement with the behaviour observed in the hardness tests (shown in Figure 9). The initially built layers, i.e. the beginning parts of the 250 W region, experienced more thermal cycles which could reduce the presence of the detrimental Laves phases. As a result, those parts have a lower FCGR. As it gets closer to the final passes of deposited material, i.e. the last parts of the 950 W regions, the number of thermal cycles which materials experience reduces resulting in a larger number of Laves phase and consequently higher FCGR values. The differences in FCGR values of G and NG parts can be related to the various compressive residual strength in the NG and G parts. The interface does not influence the constant increase of the FCGR. As was observed in the optical microscopy

images depicted in figure 6, the microstructure of the interface in the vertical graded sample was distinguishable compared with the interface of the horizontal graded sample which has a uniform and smooth transition. These differences explain the FCGR variation in the interface of the vertical G sample compared with the smooth increase of FCGR in the horizontal G specimen.

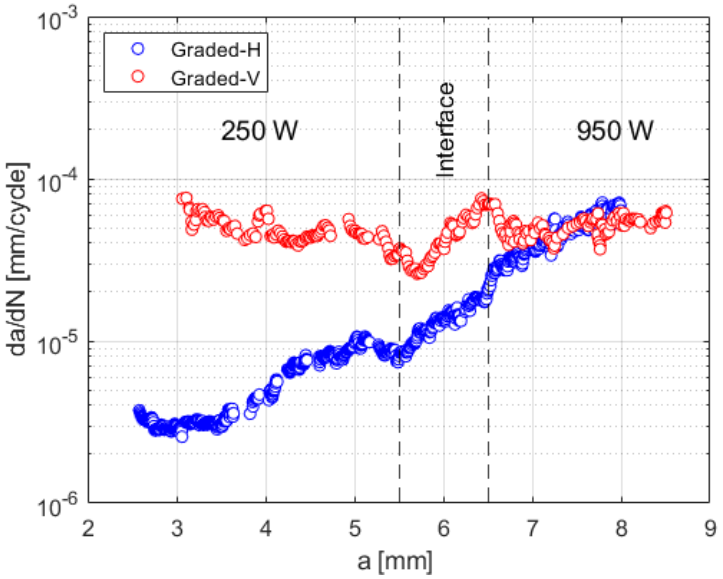

Figure 13. Fatigue crack growth rate of the graded L-PBF samples in constant ΔK experiments.

Table 8. Residual stress values of the L-PBF IN718 samples measured by XRD technique.

Manufacturing condition		Sample direction	Residual stress in BD [MPa]	Residual stress perpendicular to BD [MPa]
L-PBF	250 W	H	-100 ± 23	-151 ± 30
	950 W	H	-368 ± 98	-259 ± 60
	950 W	V	-480 ± 66	-377 ± 44

3.3 Fracture surface and crack path analyses

The fracture surface SEM micrographs of the graded samples are depicted in figure 14, with the interface areas determined by dashed lines. As it was observed in the optical microscopy images of the graded samples shown in figure 6, the vertically built specimen has more defects accumulated in the

boundaries of the interface area compared with the horizontal sample. Those defects could be attributed to the change of the manufacturing parameters in each layer of the V samples around the interface area compared with the H samples in which the laser parameters remain constant in each deposited pass. To find out the type of the defects, the scanning electron microscopy was done in a higher magnification as shown in figure 14-c. The high magnification micrograph along with the subsequent EDS analyses revealed that the present defects are unmelted particles. The presence of these kinds of defects was reported in different additive manufactured alloys [24, 29, 41, 69-71]. The unmelted particles can act as fatigue crack initiation sites and influence crack paths affecting the overall fatigue behaviour of AM materials dramatically [72]. In addition, the coupling of the pores between the unmelted parts with oxides and carbides hinders grain growth [29]. As it can be seen in figure 14 (a), the presence of the unmelted particles is more pronounced on the 250 W laser power side. In addition, the size of the unmelted particles is towards the upper limit of the particle size in the powder, 64 µm. The reason is that the 250 W laser power was not high enough to melt the larger powder particles completely, similar to what was reported in [70].

Figure 15 shows the SEM micrographs of the fractured surface of a graded sample on the 250 W laser power region. No striations were found in the fractured surfaces, however, as seen in Figure 15(a), stair-like features are present, which indicate the local solidification directions. These stairs are revealed after the fracture since the crack propagates through the epitaxial dendrites which were observed to grow along the <001> directions in the columnar grains. Figure 15(b) shows a ridge on the fracture surface that can indicate the grain boundaries with different local orientations in adjacent grains or melt pool boundaries.

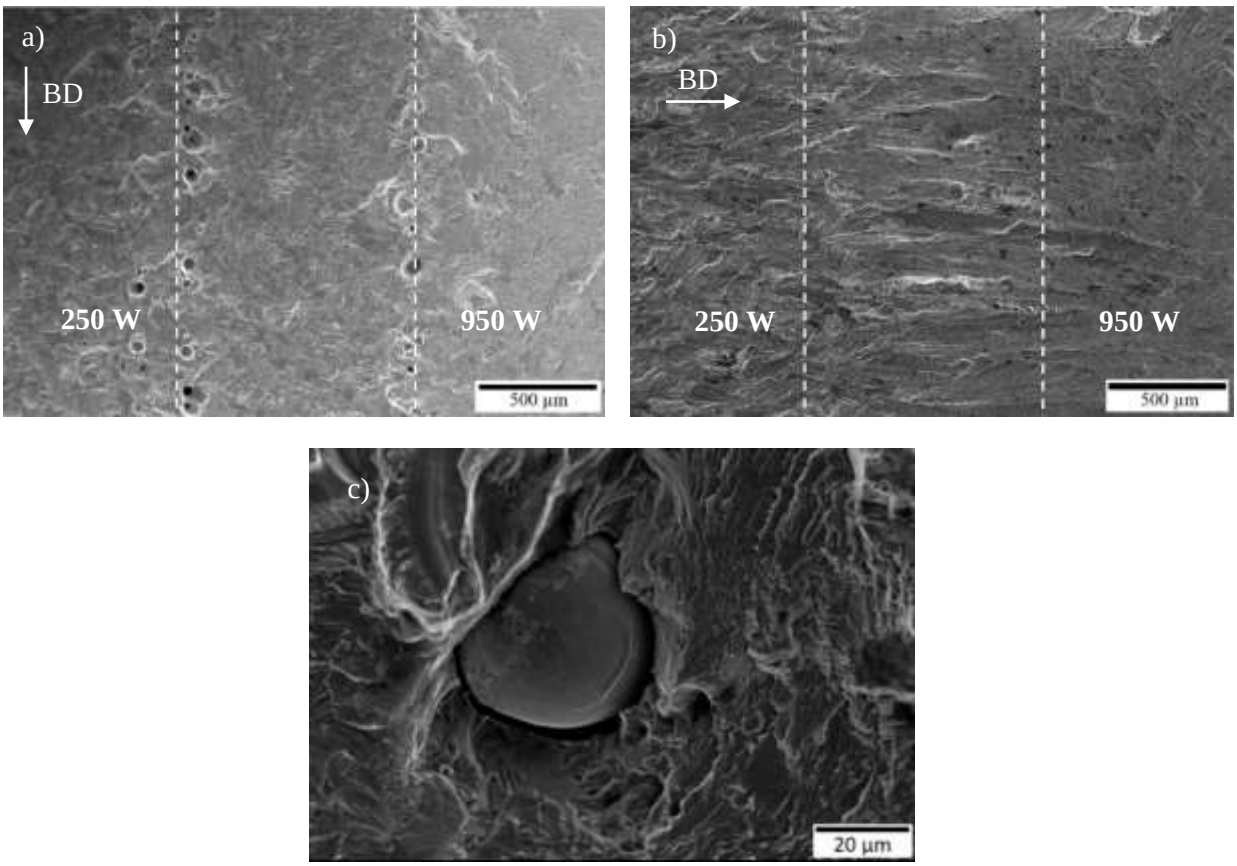

Figure14. SEM micrographs of the graded specimens' fractured surfaces near the interface area on (a) vertical and (b) horizontal orientations. (c) A high magnification micrograph of an un-melted particle in the interface region of the vertical specimen.

The optical micrographs of the crack path of a horizontal graded sample in regions manufactured using different laser powers are given in figures 16 (a) and 16 (b). Note that the macroscopic crack propagation direction is from the bottom (250 W laser power) to the top. Significant deflections are observed when crack encounters the boundaries of melt pools (shown by 1 in figure 16 (a)) and the interface region (shown by 2 in figure 16(a)), resulting in a tortuous crack path. Such deflections are not present at the boundaries of the 950 W region shown in figure 16(b). The crack path of the wrought sample, which has significantly finer grains compared with the graded parts, is shown in 16 (c). The crack path is observed to be relatively straight, featuring a combination of transgranular and intergranular fracture.

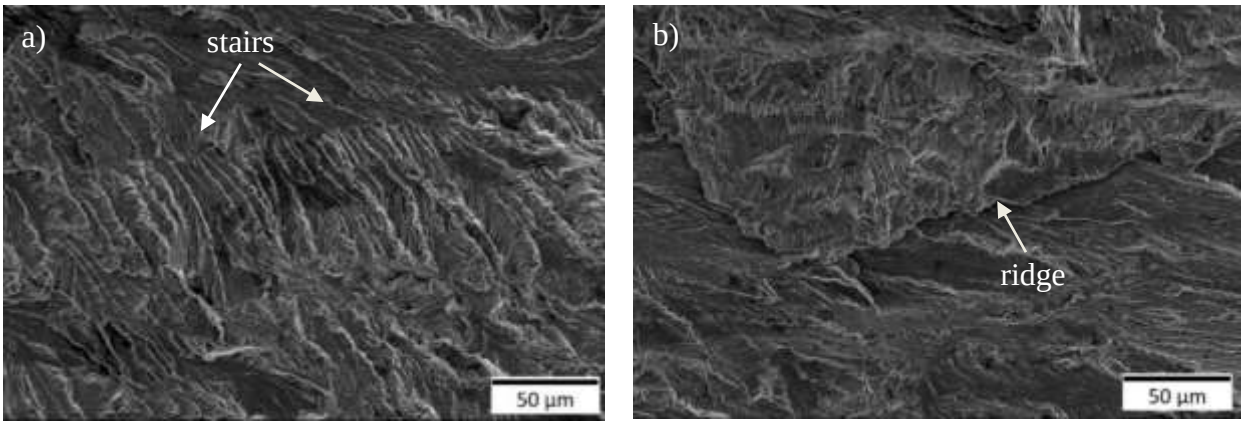

Figure15. SEM micrographs of the fractured surfaces of the graded samples in the regions manufactured using 250 W laser power tested at ΔK=25 MPa$\sqrt{m}$, showing (a) stair like features and (b) ridges revealing two grains.

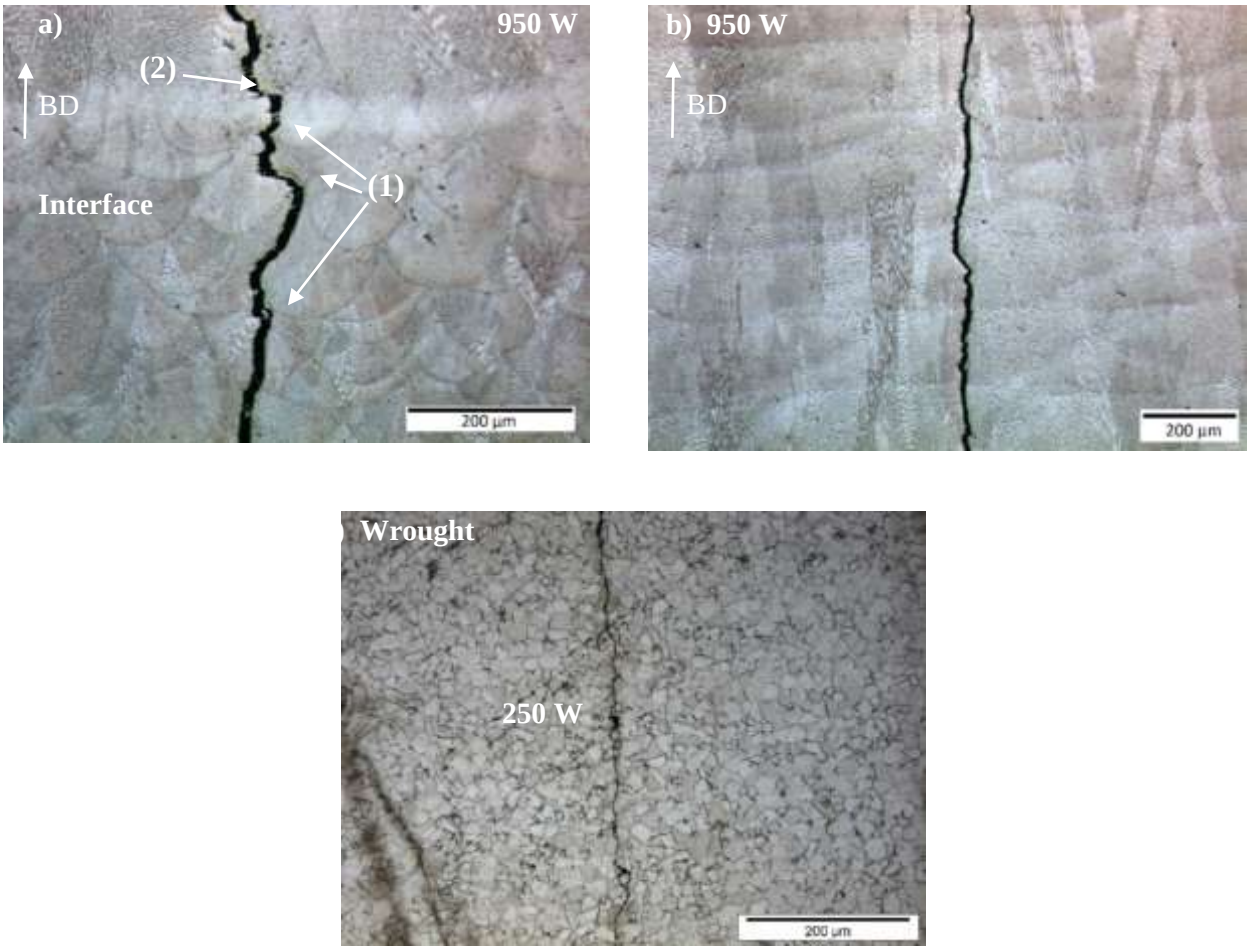

Figure 16. Optical micrographs showing the crack path of a horizontal graded sample in the (a) 250 W laser power side and the interface, (b) 950 W laser power side, and (c) the crack path of the wrought sample. Crack deflections at melt pool boundaries (1) and interface (2) are determined in figure (a).

To analyse the effect of the microstructure and grain orientations on the crack propagation behaviour of the graded and wrought materials, EBSD imaging is performed around the cracks, and the IPF maps are presented in figure 17 (a)- 17(c). The build directions of the graded specimens are indicated on the IPF maps. In all maps, the crack propagates from right to left. The grain sizes manufactured using 250 W laser power were found to be similar in both H and V graded samples and elongated in the build direction. However, similar to what was observed on the NG samples' IPFs shown in figure 10, in the 950 W laser power regions, the build direction influences the grain size. The 950 W side of the H graded sample was observed to have larger grains compared with the V sample. The other difference in the two orientations of the G samples is the interface region. From the optical microscopy images shown in figure 6, the transition from 250 W to 950 W regions in the H samples was found to be smoother compared with the V specimens. This feature is evident in the IPF maps as well. The interface microstructure is not distinguishable in the H sample, while the texture of the interface in the V sample is significantly different from the other parts. The V sample's interface margin on the 250 W side consists of finer grains and defects, which were discussed earlier and shown in the optical micrographs in figure 16. Similarly, on the other side of the interface, where the 950 W laser power is used, grains are finer compared with the remaining area of 950 W. The other noticeable feature of the V sample's interface is the orientations of the grains. The grains located towards the lower laser power are oriented in the <001> direction, while the other parts do not show a preferred texture. In both graded samples, deflections were observed close to the grain boundaries, similar to what was reported in a previous research [73].

From the IPF maps, it can be observed that despite having some intergranular fracture, the transgranular fatigue mechanism is dominant in the fatigue crack growth of the AP graded materials. Similar behaviour was reported in [60, 74]. However, the crack grows as a combination of transgranular and intergranular in the wrought material, as was evident in the optical micrographs in

figure 15. Crack branching (CB), which is known to form at the grain boundary high angle misorientation, was observed in the crack growth path and is determined in the IPFs. Crack branching hinders the fatigue crack growth due to the reduction of effective stress intensity factor at the crack tip [60]. The crack branching phenomenon was observed more in the H sample compared with the V specimen, and it can be related to the lower fatigue crack growth rate of the H sample. The intergranular crack growth mechanism, which was observed in V samples more than H samples, can occur when the crack tip encounters high angle grain boundaries [74].

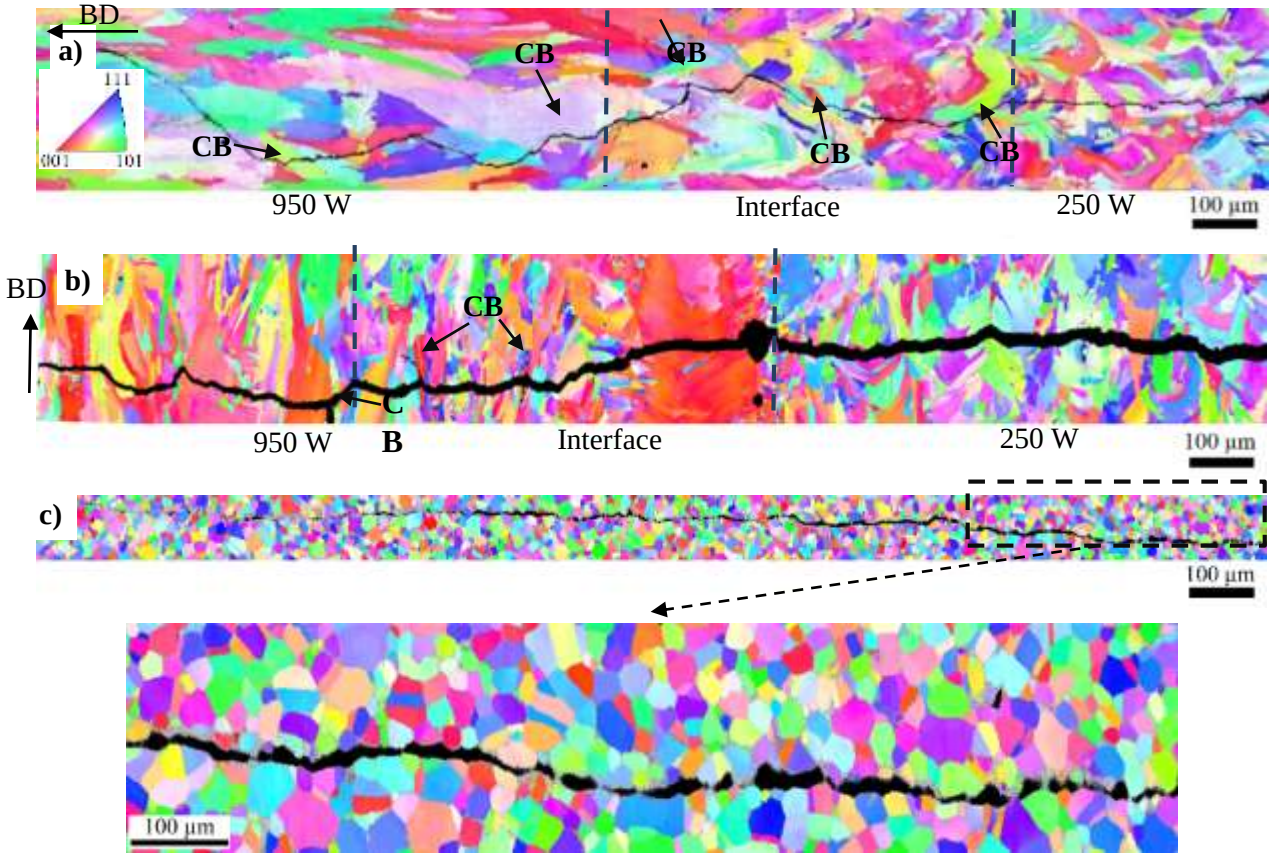

Figure 17. IPF maps showing the crack paths through the interface of the graded samples built in (a) H and (b) V orientations tested at ΔK=22.5 MPa$\sqrt{m}$ and ΔK=25 MPa$\sqrt{m}$ respectively. The orientations of the grains with respect to the local crystal lattice frame in all IPFs are determined based on the IPF triangle presented in (a). A higher magnification IPF of the wrought sample is presented in the insert from the determined area in (c). As it can be seen the crack grows as a combination of intergranular and transgranular mechanisms.

Schematics of the crack path in the H and V samples are provided in figure 18. As it was observed from the optical micrographs given in figure 16 and the IPFs in figure 17, the crack deflections are

larger in H samples which could be resulted from the <001> texture of the grains compared with the V samples, which show deflections around the melt pool boundaries. There are more deflections in the V samples causing a more tortuous crack path. The dominant fracture mechanism in both graded samples was observed to be transgranular due to the encounter of the crack tip to the high angle grain boundaries.

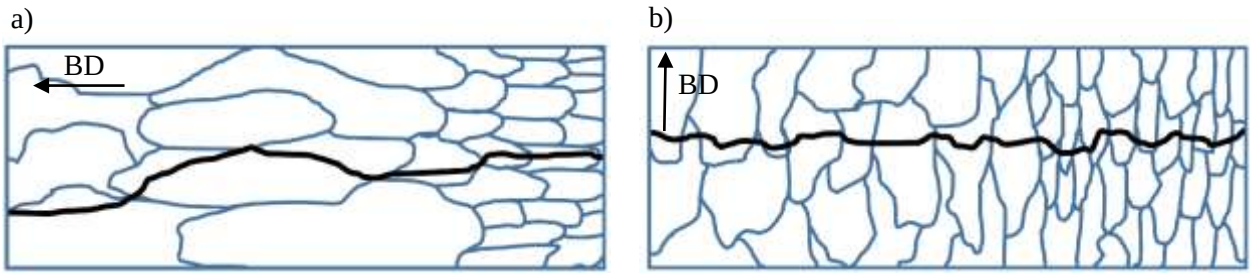

Figure 18. A crack path schematic of (a) horizontal and (b) vertical samples.

4. Conclusions

In this study, we investigated the effect of the different processing parameters in creating various microstructures and resulting hardness and fatigue behaviour of the L-PBF IN718 superalloy. In particular, the correlation of the aforementioned mechanical properties with the microstructure was studied. Three groups of non-graded specimens, along with two categories of the functionally graded samples, in which the processing parameters were used to manipulate the properties, were tested at room temperature. A heat treated wrought IN718 material was also tested as a reference for comparing the performance of the graded and non-graded materials. A finite element model was developed to obtain the accurate K solutions in the interface regions of the graded materials. Several conclusions can be drawn:

Microstructural Anisotropy: The grains' shape and texture were found highly affected by the manufacturing parameters and build directions. The grains are elongated in the build direction and exhibit strong <001> texture, which was found to be the most pronounced in the horizontal build direction of the higher laser power. The wrought material has almost equiaxed fine grains.

Hardness profile: Non-graded L-PBF materials had uniform values of hardness, which were lower than those of the wrought material. The difference was attributed to the finer grains and the presence of the strengthening precipitates in the wrought samples. The hardness profile of the graded material was affected by the processing direction and grading type and was found to reflect well the profile of fatigue crack growth.

Fatigue crack growth behaviour (ΔK_{th} and da/dN) of non-graded material: At a low stress ratio of R=0.1, only 250 W L-BPF material was found to have comparable to wrought heat treated material fatigue crack growth behaviour. The 950 W category was found to exhibit in general worse than the 250 W material fatigue behaviour. This was attributed to the compressive residual stresses, leading to less ΔK_{eff} in the 250 W samples with finer grains. At higher stress ratio of R=0.7, the threshold stress intensity range in AM materials decreases, which is related to the absence of the roughness-induced crack closure mechanisms observed at R=0.1.

Fatigue crack growth behaviour of graded material: A novel approach of using a constant ΔK procedure was employed for graded specimens, which allows investigating the crack growth rate as a function of the crack interaction with the local microstructures. It was observed that the graded microstructures influence the da/dN values. While the values obtained for the low and high laser power zones were different from their ungraded counterparts, the crack growth rates were seen to be reducing as the crack path encounters the interface regions. Fatigue crack path: Melt pool boundaries, graded interface boundaries, and grain orientations close to <001> were found to influence and deflect the crack path. Furthermore, grain boundary misorientation was observed to cause crack branching for horizontal high laser power samples.

Thus, in this study, we have successfully demonstrated the feasibility of using an additive manufacturing process to fabricate functionally graded materials, which could feature tailorable fatigue response based on the location-specific microstructures. Future works will focus on the effects of various heat treatments on fatigue and fracture toughness behaviour of such graded materials.

Acknowledgements

We acknowledge the support from the Russian Science Foundation grant (project No. 19–79-30002).

References

[1] M. Clavel, A. Pineau, Frequency and wave-form effects on the fatigue crack growth behavior of alloy 718 at 298 K and 823 K, Metallurgical Transactions A 9(4) (1978) 471-480.

[2] S. Ghorbanpour, M. Zecevic, A. Kumar, M. Jahedi, J. Bicknell, L. Jorgensen, I.J. Beyerlein, M. Knezevic, A crystal plasticity model incorporating the effects of precipitates in superalloys: Application to tensile, compressive, and cyclic deformation of Inconel 718, International Journal of Plasticity 99 (2017) 162-185.

[3] G. Nicoletto, Smooth and notch fatigue behavior of selectively laser melted Inconel 718 with as-built surfaces, International Journal of Fatigue 128 (2019) 105211.

[4] P.D. Nezhadfar, A.S. Johnson, N. Shamsaei, Fatigue behavior and microstructural evolution of additively manufactured Inconel 718 under cyclic loading at elevated temperature, International Journal of Fatigue 136 (2020) 105598.

[5] S. Ghorbanpour, M.E. Alam, N.C. Ferreri, A. Kumar, B.A. McWilliams, S.C. Vogel, J. Bicknell, I.J. Beyerlein, M. Knezevic, Experimental characterization and crystal plasticity modeling of

anisotropy, tension-compression asymmetry, and texture evolution of additively manufactured Inconel 718 at room and elevated temperatures, International Journal of Plasticity 125 (2020) 63-79.

[6] S. Gribbin, S. Ghorbanpour, N.C. Ferreri, J. Bicknell, I. Tsukrov, M. Knezevic, Role of grain structure, grain boundaries, crystallographic texture, precipitates, and porosity on fatigue behavior of Inconel 718 at room and elevated temperatures, Materials Characterization 149 (2019) 184-197.

[7] E. Hosseini, V.A. Popovich, A review of mechanical properties of additively manufactured Inconel 718, Additive Manufacturing 30 (2019) 100877.

[8] J.M. Oblak, D.F. Paulonis, D.S. Duvall, Coherency strengthening in Ni base alloys hardened by DO22 γ′ precipitates, Metallurgical Transactions 5(1) (1974) 143.

[9] D.F. Paulonis, J.M. Oblak, D.S. Duvall, Precipitation in nickel-base alloy 718, ASM (Amer. Soc. Metals), Trans. Quart. 62 (1969) 611-622.

[10] D.W. Worthem, I.M. Robertson, F.A. Leckie, D.F. Socie, C.J. Altstetter, Inhomogeneous deformation in INCONEL 718 during monotonic and cyclic loadings, Metallurgical transactions. A, Physical metallurgy and materials science 21 A(12) (1990) 3215-3220.

[11] L. Xiao, D.L. Chen, M.C. Chaturvedi, Shearing of γ″ precipitates and formation of planar slip bands in Inconel 718 during cyclic deformation, Scripta Materialia 52(7) (2005) 603-607.

[12] M. Xie, N. Foundoukos, J.C. Chapman, Experimental and numerical investigation on the shear behaviour of friction-welded bar-plate connections embedded in concrete, Journal of Constructional Steel Research 61(5) (2005) 625-649.

[13] C. Wang, R. Li, Effect of double aging treatment on structure in Inconel 718 alloy, Journal of Materials Science 39(7) (2004) 2593-2595.

[14] N.C. Ferreri, S.C. Vogel, M. Knezevic, Determining volume fractions of γ, γ′, γ″, δ, and MC-carbide phases in Inconel 718 as a function of its processing history using an advanced neutron diffraction procedure, Materials Science and Engineering: A 781 (2020) 139228.

[15] A. Strondl, R. Fischer, G. Frommeyer, A. Schneider, Investigations of MX and γ′/γ″ precipitates in the nickel-based superalloy 718 produced by electron beam melting, Materials Science and Engineering: A 480(1–2) (2008) 138-147.

[16] J. Fu, M. Qiu, L. Shen, L. Kong, J. Ma, On processing of Inconel718 through multi-channel discharge ablation, Journal of Manufacturing Processes 57 (2020) 462-468.

[17] T. Connolley, P.A.S. Reed, M.J. Starink, Short crack initiation and growth at 600°C in notched specimens of Inconel718, Materials Science and Engineering: A 340(1) (2003) 139-154.

[18] H. Andersson, C. Persson, In-situ SEM study of fatigue crack growth behaviour in IN718, International Journal of Fatigue 26(3) (2004) 211-219.

[19] H. Andersson, C. Persson, T. Hansson, Crack growth in IN718 at high temperature, International Journal of Fatigue 23(9) (2001) 817-827.

[20] L.A. James, W.J. Mills, Effect of Heat-Treatment Upon the Fatigue-Crack Growth Behavior of Alloy 718 Weldments—Part I: Macroscopic Behavior, Journal of Engineering Materials and Technology 107(1) (1985) 34-40.

[21] G.A. Osinkolu, G. Onofrio, M. Marchionni, Fatigue crack growth in polycrystalline IN 718 superalloy, Materials Science and Engineering: A 356(1) (2003) 425-433.

[22] J.L. Yuen, P. Roy, Effect of grain size on the near threshold fatigue crack propagation of a nickel base precipitation hardened superalloy, Scripta Metallurgica 19(1) (1985) 17-22.

[23] H. Helmer, A. Bauereiß, R.F. Singer, C. Körner, Grain structure evolution in Inconel 718 during selective electron beam melting, Materials Science and Engineering: A 668 (2016) 180-187.

[24] V.A. Popovich, E.V. Borisov, A.A. Popovich, V.S. Sufiiarov, D.V. Masaylo, L. Alzina, Functionally graded Inconel 718 processed by additive manufacturing: Crystallographic texture, anisotropy of microstructure and mechanical properties, Materials & Design 114 (2017) 441-449.

[25] W.A. Tayon, R.N. Shenoy, M.R. Redding, R. Keith Bird, R.A. Hafley, Correlation Between Microstructure and Mechanical Properties in an Inconel 718 Deposit Produced Via Electron Beam Freeform Fabrication, Journal of Manufacturing Science and Engineering 136(6) (2014).

[26] A. Tabei, E. Mirkoohi, H. Garmestani, S. Liang, Modeling of texture development in additive manufacturing of Ni-based superalloys, The International Journal of Advanced Manufacturing Technology 103(1) (2019) 1057-1066.

[27] E. Brandl, U. Heckenberger, V. Holzinger, D. Buchbinder, Additive manufactured AlSi10Mg samples using Selective Laser Melting (SLM): Microstructure, high cycle fatigue, and fracture behavior, Materials & Design 34 (2012) 159-169.

[28] R. Konečná, L. Kunz, G. Nicoletto, A. Bača, Long fatigue crack growth in Inconel 718 produced by selective laser melting, International Journal of Fatigue 92 (2016) 499-506.

[29] C. Pei, D. Shi, H. Yuan, H. Li, Assessment of mechanical properties and fatigue performance of a selective laser melted nickel-base superalloy Inconel 718, Materials Science and Engineering: A 759 (2019) 278-287.

[30] X.F. Ma, H.L. Zhai, L. Zuo, W.J. Zhang, S.S. Rui, Q.N. Han, J.S. Jiang, C.P. Li, G.F. Chen, G.A. Qian, S.J. Zhao, Fatigue short crack propagation behavior of selective laser melted Inconel 718 alloy by in-situ SEM study: Influence of orientation and temperature, International Journal of Fatigue 139 (2020) 105739.

[31] A. Kawasaki, R. Watanabe, Concept and P/M fabrication of functionally gradient materials, Ceramics International 23(1) (1997) 73-83.

[32] W. Meng, W. Zhang, W. Zhang, X. Yin, B. Cui, Fabrication of steel-Inconel functionally graded materials by laser melting deposition integrating with laser synchronous preheating, Optics & Laser Technology 131 (2020) 106451.

[33] W. Liu, J.N. DuPont, Fabrication of functionally graded TiC/Ti composites by Laser Engineered Net Shaping, Scripta Materialia 48(9) (2003) 1337-1342.

[34] V.A. Popovich, E.V. Borisov, V.S. Sufiyarov, A.A. Popovich, Tailoring the Properties in Functionally Graded Alloy Inconel 718 Using Additive Technologies, Metal Science and Heat Treatment 60(11) (2019) 701-709.

[35] V.A. Popovich, E.V. Borisov, V. Heurtebise, T. Riemslag, A.A. Popovich, V.S. Sufiiarov, Creep and Thermomechanical Fatigue of Functionally Graded Inconel 718 Produced by Additive Manufacturing, in: T.M.M. Materials Society (Ed.) TMS 2018 147th Annual Meeting & Exhibition Supplemental Proceedings, Springer International Publishing, Cham, 2018, pp. 85-97.

[36] A. 5383, Nickel Alloy, Corrosion and Heat-Resistant, Investment Castings, 52.5Ni - 19Cr - 3.0Mo - 5.1Cb(Nb) - 0.90Ti - 0.60Al - 18Fe, Vacuum Melted Homogenization and Solution Heat Treated, SAE International, 1966.

[37] J.-N. Zhu, E. Borisov, X. Liang, E. Farber, M.J.M. Hermans, V.A. Popovich, Predictive analytical modelling and experimental validation of processing maps in additive manufacturing of nitinol alloys, Additive Manufacturing 38 (2021) 101802.

[38] M.C. Sow, T. De Terris, O. Castelnau, Z. Hamouche, F. Coste, R. Fabbro, P. Peyre, Influence of beam diameter on Laser Powder Bed Fusion (L-PBF) process, Additive Manufacturing 36 (2020) 101532.

[39] N. Nadammal, S. Cabeza, T. Mishurova, T. Thiede, A. Kromm, C. Seyfert, L. Farahbod, C. Haberland, J.A. Schneider, P.D. Portella, G. Bruno, Effect of hatch length on the development of

microstructure, texture and residual stresses in selective laser melted superalloy Inconel 718, Materials & Design 134 (2017) 139-150.

[40] Standard Test Method for Linear-Elastic Plane-Strain Fracture Toughness of Metallic Materials.

[41] N.C. Ferreri, S. Ghorbanpour, S. Bhowmik, R. Lussier, J. Bicknell, B.M. Patterson, M. Knezevic, Effects of build orientation and heat treatment on the evolution of microstructure and mechanical properties of alloy Mar-M-509 fabricated via laser powder bed fusion, International Journal of Plasticity 121 (2019) 116-133.

[42] ASTM, Standard Test Methods for Vickers Hardness and Knoop Hardness of Metallic Materials.

[43] A. E647, Standard Test Method for Measurement of Fatigue Crack Growth Rates.

[44] H. Tada, P.C. Paris, G.R. Irwin, The Stress Analysis of Cracks Handbook, Third Edition, ASME Press2000.

[45] I. Hacısalihoğlu, F. Yıldiz, A. Çelik, The effects of build orientation and hatch spacing on mechanical properties of medical Ti–6Al–4V alloy manufactured by selective laser melting, Materials Science and Engineering: A 802 (2021) 140649.

[46] M. Balbaa, S. Mekhiel, M. Elbestawi, J. McIsaac, On selective laser melting of Inconel 718: Densification, surface roughness, and residual stresses, Materials & Design 193 (2020) 108818.

[47] A. Keshavarzkermani, M. Sadowski, L. Ladani, Direct metal laser melting of Inconel 718: Process impact on grain formation and orientation, Journal of Alloys and Compounds 736 (2018) 297-305.

[48] S. Raghavan, B. Zhang, P. Wang, C.-N. Sun, M.L.S. Nai, T. Li, J. Wei, Effect of different heat treatments on the microstructure and mechanical properties in selective laser melted INCONEL 718 alloy, Materials and Manufacturing Processes 32(14) (2017) 1588-1595.

[49] E. Chlebus, K. Gruber, B. Kuźnicka, J. Kurzac, T. Kurzynowski, Effect of heat treatment on the microstructure and mechanical properties of Inconel 718 processed by selective laser melting, Materials Science and Engineering: A 639 (2015) 647-655.

[50] K. Sano, N. Oono, S. Ukai, S. Hayashi, T. Inoue, S. Yamashita, T. Yoshitake, γ″-Ni3Nb precipitate in Fe–Ni base alloy, Journal of Nuclear Materials 442(1–3) (2013) 389-393.

[51] Y. Zhang, Z. Li, P. Nie, Y. Wu, Effect of Precipitation on the Microhardness Distribution of Diode Laser Epitaxially Deposited IN718 Alloy Coating, Journal of Materials Science & Technology 29(4) (2013) 349-352.

[52] A. Segerstark, J. Andersson, L.-E. Svensson, O. Ojo, Microstructural characterization of laser metal powder deposited Alloy 718, Materials Characterization 142 (2018) 550-559.

[53] J. Chao, C. Capdevila, The Influence of Texture on the Ductile-to-Brittle Transition Behavior in Fe20Cr4.5Al Oxide Dispersion Strengthened Alloy, Metals 10(1) (2020) 87.

[54] D.H. Smith, J. Bicknell, L. Jorgensen, B.M. Patterson, N.L. Cordes, I. Tsukrov, M. Knezevic, Microstructure and mechanical behavior of direct metal laser sintered Inconel alloy 718, Materials Characterization 113 (2016) 1-9.

[55] H.L. Wei, J. Mazumder, T. DebRoy, Evolution of solidification texture during additive manufacturing, Scientific Reports 5(1) (2015) 16446.

[56] X. Yu, X. Lin, F. Liu, L. Wang, Y. Tang, J. Li, S. Zhang, W. Huang, Influence of post-heat-treatment on the microstructure and fracture toughness properties of Inconel 718 fabricated with laser directed energy deposition additive manufacturing, Materials Science and Engineering: A 798 (2020) 140092.

[57] D. Ma, A.D. Stoica, Z. Wang, A.M. Beese, Crystallographic texture in an additively manufactured nickel-base superalloy, Materials Science and Engineering: A 684 (2017) 47-53.

[58] X.Y. Fang, H.Q. Li, M. Wang, C. Li, Y.B. Guo, Characterization of texture and grain boundary character distributions of selective laser melted Inconel 625 alloy, Materials Characterization 143 (2018) 182-190.

[59] E. Tochigi, A. Nakamura, N. Shibata, Y. Ikuhara, Dislocation Structures in Low-Angle Grain Boundaries of α-Al2O3, Crystals 8(3) (2018) 133.

[60] H. Wu, D. Zhang, B. Yang, C. Chen, Y. Li, K. Zhou, L. Jiang, R. Liu, Microstructural evolution and defect formation in a powder metallurgy nickel-based superalloy processed by selective laser melting, Journal of Materials Science & Technology 36 (2020) 7-17.

[61] X. Yu, X. Lin, H. Tan, Y. Hu, S. Zhang, F. Liu, H. Yang, W. Huang, Microstructure and fatigue crack growth behavior of Inconel 718 superalloy manufactured by laser directed energy deposition, International Journal of Fatigue 143 (2021) 106005.

[62] Y. Gao, Y. Ding, J. Chen, J. Xu, Y. Ma, X. Wang, Effect of twin boundaries on the microstructure and mechanical properties of Inconel 625 alloy, Materials Science and Engineering: A 767 (2019) 138361.

[63] D. Fournier, A. Pineau, Low cycle fatigue behavior of inconel 718 at 298 K and 823 K, Metallurgical Transactions A 8 (1977) 1095.

[64] ISO, Metallic materials — Unified method of test for the determination of quasistatic fracture toughness, 2016, pp. 1-98.

[65] U. Krupp, Crack Propagation: Microstructtural Aspects Fatigue Crack Propagation in Metals and Alloys, John Wiley & Sons2007, pp. 135-206.

[66] H.Y. Li, H.L. Sun, P. Bowen, J.F. Knott, Effects of compressive residual stress on short fatigue crack growth in a nickel-based superalloy, International Journal of Fatigue 108 (2018) 53-61.

[67] Y. Yamada, J.C. Newman, Crack closure under high load-ratio conditions for Inconel-718 near threshold behavior, Engineering Fracture Mechanics 76(2) (2009) 209-220.

[68] X. Hu, Z. Xue, T. Ren, Y. Jiang, C. Dong, F. Liu, On the fatigue crack growth behaviour of selective laser melting fabricated Inconel 625: Effects of build orientation and stress ratio, Fatigue & Fracture of Engineering Materials & Structures 43(4) (2020) 771-787.

[69] J.C. Newman, Y. Yamada, Compression precracking methods to generate near-threshold fatigue-crack-growth-rate data, International Journal of Fatigue 32(6) (2010) 879-885.

[70] P.L. Blackwell, The mechanical and microstructural characteristics of laser-deposited IN718, Journal of Materials Processing Technology 170(1–2) (2005) 240-246.

[71] X.-A. Hu, G.-L. Zhao, Y. Jiang, X.-F. Ma, F.-C. Liu, J. Huang, C.-L. Dong, Experimental Investigation on the LCF Behavior Affected by Manufacturing Defects and Creep Damage of One Selective Laser Melting Nickel-Based Superalloy at 815 °C, Acta Metallurgica Sinica (English Letters) 33(4) (2020) 514-527.

[72] M. Knezevic, S. Ghorbanpour, N.C. Ferreri, I.A. Riyad, A.D. Kudzal, J.D. Paramore, S.C. Vogel, B.A. McWilliams, Thermo-hydrogen refinement of microstructure to improve mechanical properties of Ti–6Al–4V fabricated via laser powder bed fusion, Materials Science and Engineering: A 809 (2021) 140980.

[73] S.R. Daniewicz, N. Shamsaei, An introduction to the fatigue and fracture behavior of additive manufactured parts, International Journal of Fatigue 94 (2017) 167.

[74] P. Peralta, R. Dickerson, N. Dellan , K. Komandur, M.A. Jameel, Effects of Local Grain Orientation on Fatigue Crack Growth in Multicrystalline fcc Metallic Materials, Journal of Engineering Materials and Technology 127(1) (2005) 23-32.

[75] A.R. Balachandramurthi, J. Moverare, T. Hansson, R. Pederson, Anisotropic fatigue properties of Alloy 718 manufactured by Electron Beam Powder Bed Fusion, International Journal of Fatigue 141 (2020) 105898.

Chapter 4: Effects of heat treatment and building orientation on the microstructure and fatigue behaviour of functionally graded Inconel 718 manufactured by laser powder bed fusion

This chapter was published as “Effects of heat treatment and building orientation on the microstructure and fatigue behaviour of functionally graded Inconel 718 manufactured by laser powder bed fusion” in the Materials Characterization journal, 179 (2021). The authors of this paper are Saeede Ghorbanpour, Saswat Sahu, Kaustubh Deshmukh, Evgenii Borisov, Ton Riemslag, Elise Reinton, Virginia Bertolo, Quanxin Jiang, Anatolii Popovich, Aleksey Shamshurin, Marko Knezevic, and Vera Popovich. My contribution to this chapter was analysing the data from the mechanical tests. I also performed EBSD and analysed the microstructures of the materials used in this study. I also wrote the manuscript of this chapter.

Effects of heat treatment and building orientation on the microstructure and fatigue behaviour of functionally graded Inconel 718 manufactured by laser powder bed fusion

Saeede Ghorbanpour[a] , Kaustubh Deshmukh[a], Saswat Sahu[a], Ton Riemslag[a], Elise Reinton[a], Evgenii Borisov[b], Anatolii Popovich[b], Virginia Bertolo[a], Quanxin Jiang[a], María Terol Sanchez[a], Marko Knezevic[c], Vera Popovich[a,b]

a. Department of Materials Science and Engineering, Delft University of Technology, The Netherlands

b. Peter the Great Saint-Petersburg Polytechnic University, Saint Petersburg, Russia

c. Department of Mechanical Engineering, University of New Hampshire, Durham, NH 03824, USA

Abstract

This study addresses the effect of the post process heat treatments on the microstructure and fatigue crack growth behaviour of the functionally graded (FG) laser powder bed fusion (L-PBF) Inconel 718 superalloy. Different samples were additively manufactured (AM) altering the process parameters, namely the laser power, the laser scanning speed, layer thickness, hatch distance, and beam distribution function, resulting in distinctly different microstructures. Two categories of samples underwent heat treatment (HT) and hot isostatic pressing followed by HT (HIP+HT), while one category was kept in the as-processed (AP) condition to reveal the effects of the post-treatments. Also, to study the effect of microstructural anisotropy, samples were printed in horizontal (H) and vertical (V) building directions. To better understand the behaviour of the FG materials, non-graded (NG) L-PBF samples and wrought material were investigated as references. Significant variations in terms of

the grain size and elongation, crystallographic texture, content of the strengthening precipitates or detrimental phases, and the presence of porosity were found in different AM groups. Moreover, the fatigue behaviour of the NG and FG materials was studied by conducting three-point bending tests. After HT, only the threshold for fatigue-crack initiation (ΔK_{th}) of the 950W laser power V samples increased. Although the fatigue crack growth rate (FCGR), $\frac{da}{dN}$, of the HT materials, improved compared with their AP counterparts, it still remained slightly higher than the heat treated wrought IN718. ΔK_{th} of the higher laser power was found to improve by the HIP+HT procedure. Furthermore, the HIP+HT reduced the FCGR of all samples and was found to be the optimum post-treatment for improving fatigue behaviour of the IN718 superalloy. The FCGR of the FG samples after HT and HIP+HT post processing was observed to be close and remain constant throughout the graded sides, regardless of the build orientations. This behaviour was different in the H direction of the AP materials, and it can be related to the different residual stress (RS) levels as a consequence of the post processing procedures. Similar behaviour was found in the hardness of the FG materials. Grain boundaries and annealing twin boundaries, which were present in the HIP+HT materials, deflected the crack path. Also, in the low stress ratio of R=0.1, the effect of the roughness induced crack closure was more pronounced in the H samples compared with the V specimens. The current study demonstrates that heat treatments can enhance the damage tolerance of L-PBF IN718 to the level of wrought material by increasing ΔK_{th} and decreasing FCGR.

1. Introduction

Laser powder bed fusion (L-PBF) is an additive manufacturing (AM) process which allows for producing complex geometries using computer aided design (CAD) models [1]. Despite many advantages of the AM methods, including the capability of producing functionally graded (FG) parts and a significantly lower buy-to-fly ratio (BTF) compared with the conventional manufacturing procedures, tensile residual stresses, detrimental phases and defects might be introduced into the

additive manufactured parts which affect the mechanical properties [2-4]. Post processing heat treatments can be employed to reduce these detrimental effects and enhance the properties.

Inconel 718 (IN718) is a precipitate hardened nickel-based superalloy. The main strengthening precipitates of the A1 γ matrix are coherent ordered γ' (Ni_3Al) with an $L1_2$ lattice structure and γ'' (Ni_3Nb) with a DO_{22} structure [5-8]. γ' precipitates are spherical shaped with diameters ranging between 10 and 40 nm, while γ'' precipitates are disk shaped with diameters of 20-30 nm and thickness of 5-6 nm [9-13]. In addition to the strengthening precipitates, other phases such as hexagonal Laves $(Ni,Fe,Cr)_2(Nb,Mo,Ti)$, orthorhombic δ (Ni_3Nb), and MC carbides could be present in the alloy [6, 14]. Hard and brittle irregular shape micron-sized Laves phase forms at the end of the solidification process due to the micro-segregation of the alloying elements [15, 16]. Due to the low diffusion rate of Nb in the γ matrix, the Laves phases tend to form on the grain boundaries and in interdendritic regions [17]. The intermetallic Laves phase is known to have detrimental effects on mechanical properties, including fatigue properties since they can promote the crack initiation and propagation at high stress amplitudes [15]. The δ phase, in the form of 1-8 μm needle-like incoherent precipitates [5, 18, 19], is known to be detrimental to mechanical properties except the high temperature creep rupture strength [17, 20, 21]. Brittle MC carbides with rough morphologies are also known to form at the grain boundaries, like the δ phase [22].

Post process heat treatments are common procedures to improve the properties of AM parts by minimizing the effects of the non-equilibrium phases and thermal residual stresses [23]. Solutionizing at temperatures around 1000 °C followed by aging is a well-adapted heat treatment used for Inconel superalloys. Solutionizing at 980 °C and double aging (DA) results in precipitation of the δ phase at grain boundaries in addition to preserving some of the Laves phases due to the inefficiency of the temperature to dissolve all those phases [24-26]. Applying the AMS 5663 [27] heat treatment to the L-PBF material increases the δ volume fraction to about 6% [28]. It is also reported that heat treatment results in the disappearance of the dendritic structures formed during the AM process [26, 29].

Similarly, solution treatment at a higher temperature of 1050 °C followed by the double aging procedure results in the dispersion of the δ phase in grain boundaries and vanishing the dendritic structures [30].

The presence of porosity is one of the obstacles deteriorating mechanical properties, particularly in cyclic loading conditions. The hot isostatic pressing (HIP) procedure is a post processing treatment used to decrease internal pores and especially to reduce the size of surface porosity associated with AM process [31]. HIP treatment of the LPBF IN718, at a temperature and pressure of above 1150 °C and 100-150 MPa respectively, with a holding time of 2 hours, was found to reduce the volume fraction of the porosity from 0.3% to 0.07 % [16]. It is worth noting that, due to the entrapped argon gas in the AM parts, the existence of some porosity is inevitable [32].

In several studies [5, 15, 16, 21, 24-26, 29, 30, 33-37], the effect of various post processing treatments on the improvement of mechanical properties, including hardness, tensile strengths, room temperature and high temperature ductility, creep life, high cycle fatigue (HCF) behaviour, and low cyclic fatigue (LCF) properties were investigated. Studying different post-processing treatments on the SLM IN718 revealed that HIP followed by homogenization and double aging results in superior tensile properties due to dissolution of Laves and δ phase, pores closure, and size and density increase of carbides [16]. Yield strength and ultimate tensile strength of an SLM IN718 increased from 889-907 MPa, and 1137-1148 MPa to 1102-1161 MPa and 1280-1358 MPa respectively, when a solution and age hardening post treatment was applied [26]. Furthermore, an increase of about 30% was reported in the microhardness of the SLM material after heat treatment. Comparing different heat treatments of the laser net shape manufactured (LNSM) IN718 revealed that direct age procedure increases the ultimate tensile strength and yield stress of the as-deposited material by about 50% and 100%, respectively [35]. In another study [33], it was found that double aging of an L-PBF IN718 increases the hardness from 310 to 470 HV. However, simulated HIP (without applied pressure) followed by the water quench process (HIPWQ) significantly decreases the hardness of the as processed (AP) material to

about 210 HV. Double aging of the HIPWQ material improves the hardness and it reaches around 440 HV. Examining different heat treatments on an SLM IN718, it turned out that the δ aging at 980 °C followed by a double aging treatment results in the highest hardness of 482 HV compared with the as-processed material, with a microhardness value of 334 HV [34]. This heat treatment improved the tensile strength and elongation of the AM material to be even higher than those values for forged standard AMS 5662 [38] parts. Applying AMS 5662 [38] heat treatment to the L-PBF IN718 parts fabricated by different strategies improved the creep life from 107-188 hours to 320-507 hours which is attributed to the grains recrystallization, δ precipitations at grain boundaries, Laves phase dissolution, and texture reduction [21]. Treating the LPBF IN718 samples by homogenisation followed by solution (at 1093 °C) and ageing (at 718 °C) increased their creep life from 12 hours to about 48 hours but still remained 33% lower than what was reported for the equivalent wrought samples [36]. The high cycle fatigue behaviour of double-aged AM samples was reported to be superior to the heat treated wrought samples at low stress amplitudes (lower than 630 MPa) due to the presence of unbroken Laves phases, which hindered the crack propagation [15]. The high temperature HCF behaviour of heat treated AM IN718 was found to be similar to the wrought samples and outperform the HIP+HT specimens. This behaviour is attributed to the domination of coarse grains in the structure and the high content of incoherent annealing twins in HIP+HT material which affected the cyclic life more than the presence of porosity and δ phase [5]. The room temperature LCF lives of the DMLS-HT samples at strain amplitudes lower than 0.8% were reported to be higher than the wrought-HT materials, while it was the opposite for the higher strain amplitudes, and it was rationalized by the effect of the DMLS manufacturing induced porosity [37]. Similar to the weaker HCF properties of the HIP+HT samples compared with the AM-HT and Wrought-HT materials [5], the LCF behaviours of HIP+HT samples were affected by the incoherent annealing twins, and their lives were shorter than the other counterparts [37].

Moreover, the effect of post processing on the crystallographic texture of the nickel-based superalloys has been explored. One hour annealing at 1080 °C or two hours solution annealing at 1150 °C of the L-PBF Inconel 625 were observed to eliminate the texture, reduce the low angle grain boundaries (LAGB)s, and increase the high angle grain boundaries and twin angle boundaries [39]. The as-built L-PBF IN625 exhibited a relatively strong fibre-like <100> texture, while stress relief annealing and recrystallization annealing treatments make the <100> texture weaker. The same research reports that the solution treatment further weakens the <100> texture and spreads it towards the <110>, and HIP results in a random texture [40]. A similar reduction in the <100> fibre texture of the AM IN718 alloy after applying one-hour solutionizing recrystallization at 1250 °C was reported and was related to the transformation of the columnar grains to equiaxed ones [41]. Homogenization of the SLM IN718 at 1100 °C for one hour caused a reduction in <001> peak while HIP treating at 1160 °C, 100 MPa for 4 hours homogenized material and significantly increased the <001> peak [42]. A moderate <001> fibre texture in the build direction was found in the direct metal laser melted (DMLM) IN718 treated as per AMS 5663 [27], which turned to a weak Goss texture {110}<001> after a four-hour HIPing at 1163°C and 100 MPa due to the recrystallization and presence of the coarse grains [5].

Despite the extensive research on the influence of post process heat treatments on various mechanical properties, the effects of the post treatment and microstructural anisotropy such as grain size, grain orientation, and texture on the fatigue crack growth rate (FCGR) of the functionally graded IN718 has not been investigated yet. In this study, we focused on the influence of the HT (AMS 5383 [43]) and HIP+HT (AMS 5664E [44]) procedures and subsequent different microstructures on the threshold for fatigue-crack initiation (ΔK_{th}) and FCGR of the L-PBF IN718. A variety of specimens with different notch position with respect to the building orientation were fabricated. In addition to the different laser powers used in the non-graded materials, two categories of functionally graded materials (FGM) were produced and post processed. The results of this study were compared to the properties which were found from examining the as-processed (AP) L-PBF materials and wrought samples.

2. Materials and experiments

2.1 IN718 samples manufacturing and post treatment

IN718 alloy powder made by gas atomization, with the chemical composition provided in Table 1 and the distribution of d_{10}=20µm and d_{90}=64µm, was used for L-PBF manufacturing. The IN718 fatigue crack growth rate test specimens were fabricated by an SLM 280^{HL} unit using a laser wavelength of 1070 nm. To accommodate a variety of microstructures, different manufacturing parameters including laser power (P), laser scanning speed (V), layer thickness (t), and hatch distance (h) were selected in a way that their combined effect, which is defined as the volume energy density (VED), E_v, remained around the constant value of 59.5 J/mm^3. In addition to the mentioned parameters, the effect of the Gaussian and flat top beam distribution with different beam diameters were explored. Table 2 gives a summary of the processing parameters used for manufacturing the samples for the current study.

To further investigate the effect of the microstructural anisotropy on the FCGR, two categories of samples were designed and manufactured considering the depositing build direction (BD) and the initial notch direction (the same as the crack direction (CD) during the tests). In all specimens, the crack direction was located on the vertical symmetry axis of the samples. As shown in Figure 1, the directional samples studied in this research were horizontal (H) with parallel BD and CD and vertical (V) with perpendicular BD and CD. Finally, specimens were built in the of non-graded (NG) form with laser specifications remaining the same during sample fabrication, and functionally graded (FG) form with transitions of the laser parameters during the manufacturing process. All samples were designed and made to satisfy the conditions provided in ASTM E399 [45]. NG samples had the size of 70 mm length, 10 mm height, and 5 mm width. The dimensions were slightly larger for the FG samples as 80 mm length, 12 mm height, and 6 mm width. The notch with a total depth of 0.5 mm and a radius of 0.2 mm was made by the electrical discharge machining (EDM) in NG and FG samples. Figure 1 shows the schematics of the NG and FG samples manufactured for this study.

Table 1. Alloy IN718 elemental composition measured by scanning electron microscopy electron dispersive spectroscopy (SEM EDS) [1].

Element	Ni	Cr	Fe	Nb	Mo	Ti	Al	Mn	Co
wt%	51.45	19.38	18.49	5.3	3.4	1.04	0.72	0.12	0.1

Table 2. L-PBF manufacturing parameters.

Sample orientation	Laser power [W]	Laser scanning speed [mm/s]	Layer thickness [mm]	Hatch distance [mm]	Beam distribution function	Beam diameter [µm]
H	250	700	0.05	0.12	Gaussian	80
H	950	320	0.1	0.5	Flat top	100
V	950	320	0.1	0.5	Flat top	100

Manufactured samples were divided into three categories for post-processing purposes. The first group was explored in the as-processed (AP) condition. The detailed characterization and experimental results of this category are reported in our previous study. The second category was heat treated according to AMS 5383 [43], which consists of a homogenisation step at 1080 °C for 1.5 hours followed by the procedure described in AMS 5663 [27], which includes a solutionizing at 980 °C for 1 hour followed by a double-aging procedure at 720 °C and 620 °C each step for 8 hours. In this study, the samples of this category are referred to as the heat treated (HT) ones. The other group of the AM material underwent the hot isostatic pressing (HIP) procedure, followed by an AMS 5664E [44] heat treatment. The HIP procedure was done at 1180 °C and a pressure of 150 MPa for 3 hours. The

heat treatment contained a homogenisation at 1065 °C for 1 hour, followed by a double aging process at 760 °C for 10 hours, and at 650 °C for 8 hours. These samples are referred to as HIP+HT hereon. In addition to the L-PBF specimens, a group of wrought material samples was made and heat treated based on AMS 5663.Table 3 gives a summary of the post treatment procedures of the L-PBF and wrought samples used in this study.

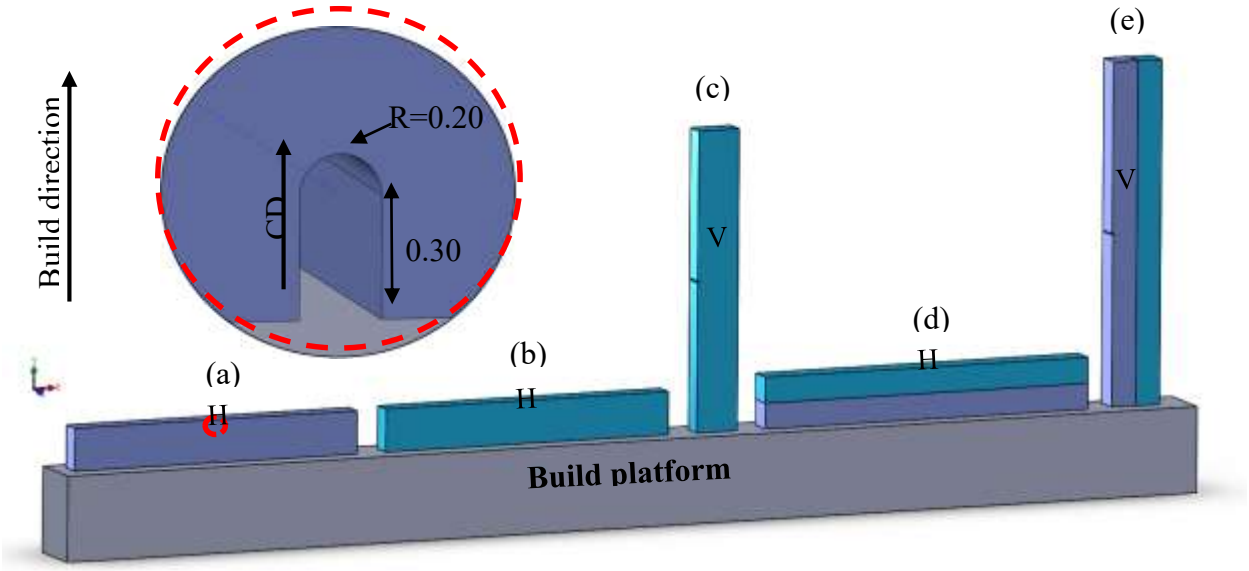

Figure 1. Orientation of the samples with respect to the build (BD) and crack direction (CD) for non-graded: (a) 250W-H, (b) 950W-H, (c) 950W-V, as well as functionally graded specimens: (d) horizontal (H), and (e) vertical (V). The notch dimensions are provided in mm in the insert.

Table 3. A summary of the post processing heat treatments on the samples explored in this study

Group		Post-process heat treatment	Temperature [°C]	Holding time [h]	Cooling specification
L-PBF	AP	-	-	-	-

	HT (AMS 5383)	Homogenisation	1080	1.5	Air cooling (AC)
		Solutionizing	980	1.5	AC
		Double- aging	720	8	Furnace cooling (FC)
			620	8	AC
	HIP+HT (AMS 5664E)	HIP (at 150 MPa)	1180	3	FC
		Homogenisation	1065	1	AC
		Double- aging	760	10	FC
			650	8	AC
Wrought with HT (AMS 5663)		Solutionizing	980	1	AC
		Double- aging	720	8	FC
			620	8	AC

2.2 Microstructural characterization

Grain morphology, the presence and distribution of the precipitates and carbides, and different structures resulted from various manufacturing parameters and post-treatments were investigated utilizing the optical microscopy and scanning electron microscopy (SEM) techniques. The samples were prepared for the optical microscopy and SEM analyses by grinding, polishing, and etching. The final step of the polishing was done using a 1 µm silica suspension. The Glyceregia etchant solution, which consists of 15 ml HCl, 10 ml Glycerol, and 5 ml HNO_3, was used to etch the surfaces for about 3 seconds. Optical microscopy was done using a Leica DMLM optical microscope with analySIS 5.0

by Olympus soft Imaging Solutions GmbH, and a Keyence VHX-5000 device. A JEOL JSM IT-100 SEM equipped with JEOL InTouchScope software was used for exploring the surfaces prior to the tests along with the fracture surface analyses.

X-ray diffraction (XRD) measurements of the AP, HT, and HIP+HT L-PBF materials were carried out using a Bruker D8 advanced diffractometer with a graphite monochromator. The unit was equipped with a Co Kα X-ray beam generator and a Vantec position sensitive detector. The measurements were done using a wavelength of 1.78897 Å and a scanning step size of 0.035 degrees in a 2θ scale between 20 and 140 degrees. To further analyse the XRD data, Bruker software Diffrac was used.

To understand the impact of the post processing procedures on the localized plastic deformation resistance, Vickers hardness tests were performed. A Struers DuraScan G5 testing machine was used to perform the tests at a load of 1000 gf (HV1) and the holding time of 10 seconds. The NG samples' hardness measurements were replicated on ten random spots of the surface to ensure the repeatability and precision of the tests. For the FG samples, however, the measurements were done in lines along the width of the samples to explore the possible influence of the microstructural gradient in the interface zone. In addition, the measurements were carried out on multiple locations to investigate the effect of the build direction and thermal cycles on the hardness.

Grain structures and crystallographic textures of all categories of NG materials before the fatigue tests were acquired using the electron backscattered diffraction (EBSD) technique. Samples were prepared similar to the preparation procedure explained for the optical microscopy and SEM, with an additional polishing step with 0.25 µm colloidal silica suspension. The etching was not necessary, instead, an ultrasonic bath cleaning with isopropanol was added as the final step. An SEM Mira 3 Tescan equipped with channel 5- HKL software, with an accelerating voltage of 20 kV, was used to collect the EBSD data. Moreover, the same technique was used to study the crack growth path of the FG samples. Depending on the optical microscopy and SEM micrographs, the step size was chosen

differently between 0.8 µm and 1.7 µm. The collected EBSD data were post processed using TSL-OIM analysis software version 8. Prior to the tests, for each category of materials, multiple areas were imaged to have a reasonable number of grains detected. Based on the grain size estimates, the EBSD imaging step size varied between 0.5 µm and 1.7 µm. The minimum average confidence index (CI) of all measurements was 0.35. In all measurements, at least 96.6 percent of the collected data, which varied between 1393644 and 6293324 points, were indexed. The data was cleaned up using the Neighbor CI Correlation (NCIC) clean-up procedure with the "minimum confidence index" parameter set to be 0.3. A generalized spherical harmonic expansion smoothing with series rank L=16, a Gaussian half-width of 5 degrees, and triclinic symmetry were used to plot the stereographic pole figures. Multiple EBSD imaging along the crack of the FG specimens and the wrought sample was done to cover a good length of the crack path. To avoid introducing artefacts on the crack path, clean-up procedures were not used.

2.3 Fatigue testing and modelling

To study the fatigue crack growth behaviour of the NG and FG parts, three-point bending fatigue tests with stress intensity factor (SIF) solutions and test configurations in accordance with ASTM E399 [45] were conducted. A hydraulic MTS machine, with a capacity of 25 kN, with the MTS MultiPurpose TestWare and Flextest electronic unit, was used for testing purposes. A direct current potential drop (DCPD) equipment with a measurement resolution of 0.5 mm was used to ascertain the correlation between the visually measured crack length and the output voltage. It should be noted that the visual crack calibration and propagation measurement were done using two Limess digital image correlation (DIC) 5-megapixel cameras.

The NG samples were tested under constant K_{max} condition, which allowed to measure the threshold stress intensity factor range (ΔK_{th}). The frequency of the constant K_{max} tests was 30 Hz. The stress ratio (R), which is defined by equation 1, initially was set to be 0.1 in all constant K_{max} tests and was

increased to values around 0.6-0.7 by the end of the tests. To obtain a sufficient ΔK which allowed for the crack growth, the K_{max} value was calculated from equation 2 and was kept constant during the tests. The value of K_{min} was calculated by the formula given in equation 3.

$$R = \frac{K_{min}}{K_{max}} \quad (1)$$

$$K_{max} = \frac{\Delta K}{1 - R} \quad (2)$$

$$K_{min} = K_0 e^{(C(a-a_0))} \quad (3)$$

Where K_0 is the initial K_{min} value, C is the gradient of the SIF and was set to be -0.4 1/mm, a is the instantaneous crack length measured by DCPD, which was validated by optical and DIC observations, and a_0 is the initial crack length measured by DIC. The value of K_{min} was ramped up during the test to maintain the K_{max}-constant condition. The adjustment of K_{min} was stopped when the crack growth was less than 0.1 mm during 100000 cycles which is equal to a crack growth rate of 10^{-6} mm/cycle or lower. The ΔK reading of this stage is regarded as ΔK_{th}.

The other type of experiment which was done on the NG samples was the constant load amplitude tests. The objective of these tests was to formulate the crack growth rate as a function of the SIF range (ΔK). The experimental procedure was in accordance with ASTM-E647 [46] and the test frequency was set to be 50 Hz. The curves obtained from the constant load amplitude tests in the Paris regime were fit linearly to calculate the Paris constant and Paris exponent values.

To explore the effect of the microstructure of the functionally graded samples on the fatigue crack growth rate, three-point bending tests in the constant SIF range were carried out. It is known that for a given ΔK, and a specific microstructure, the FCGR remains about a constant value. Therefore, the effect of the functionally graded structure on the FCGR should be exposed if K remains constant. The standard K solutions to determine the load levels, which are described based on the crack length and sample width, are developed for homogeneous materials and thus are not applicable for the

functionally graded components. Therefore, to have accurate, customized K solutions for the FGM IN718 parts, an elastic FEA model within ABAQUS was developed. The functionally graded samples were simulated as two main halves of the NG materials, which were joint by the interface layer. For the main halves, Young's moduli of the corresponding NG samples, which were measured from the compliance of the fatigue tests and are provided in

Table 4, were used. The 1 mm interface was divided into five geometrically homologous layers, each of which had its E adjusted linearly. The Poisson's ratio of all parts was set to be 0.3. The model which was used for all three post-treatment categories had the same element types and element numbers. Mesh elements near the crack tip were 0.02 mm. The mesh element size was increased to 0.5 mm in the areas which were not highly influenced by the crack. The types of the elements in the model were CPE6M (6- node modified quadratic plane strain element with hourglass control) and CPE8R (8-node biquadratic plane strain element with reduced integration) and the mesh element numbers were 185 and 4456, respectively.

Figure 2 demonstrates the model which was used in this study. The output of the model was the J-integral value (J), which was employed to calculate the customized K solutions using equation 4.

$$K = \sqrt{J \times \frac{E}{1 - \nu^2}} \quad (4)$$

Where E is Young's modulus at the crack tip, and ν is the Poisson's ratio.

Table 4. Young's moduli measured on the AP, HT, and HIP+HT materials using the three-point bending tests.

Post-processing condition	Sample category	Young's modulus [GPa]
AP	250 W	186 ± 15
	950 W- H	136 ± 10
	950 W- V	139 ± 36
HT	250 W	159 ± 21
	950 W- H	130 ± 9
	950 W- V	132 ± 8
HIP+HT	250 W	188 ± 22
	950 W- H	170 ± 26
	950 W- V	160 ± 21

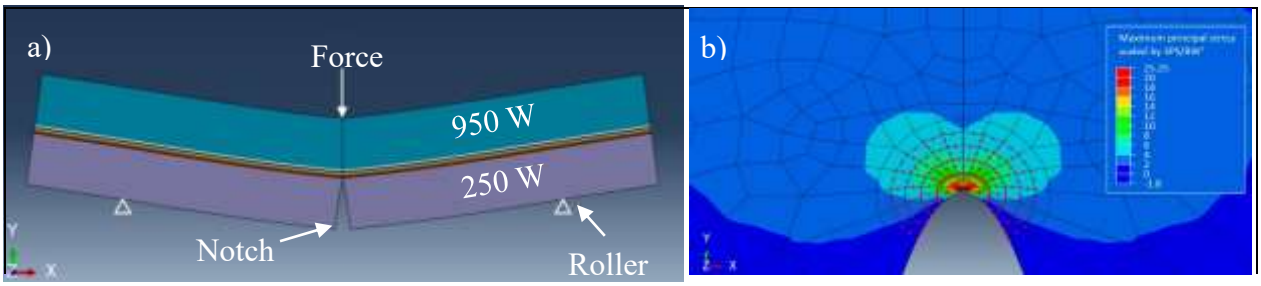

Figure 2. (a) The FEM model used to calculate the customized K-solutions for the graded materials. (b) The node used to calculate the J integral.

3. Results and discussions

3.1 Microstructural analyses

To explore the effect of the post-treatment procedures on the interface zone of the FG samples, optical microscopy images were taken. The optical micrographs over the longitudinal cross sections of the FG samples of AP and post-treated categories are provided in Figure 3. As can be seen in Figure 3 a and b, the melt pools which were introduced by AM are clearly visible with different characteristics in areas of 250 W and 950 W laser powers. The transition from the 250 W region to the 950 W zone was observed to be smooth in the horizontal sample since the laser parameters remained the same in any individual deposited layers. However, the interface area of the AP vertical sample was distinguishable with finer melt pools in the centre and deeper melt pools on the edges, key-hole induced porosities, and unmelted particles, which are the artefacts caused by the change of the laser parameters in the deposition. In both categories of the AP condition, grains were elongated in the building direction. After HT, the grains of both build orientations remained elongated in the BD, which indicates that the homogenisation temperature was not high enough to induce full grain recrystallization. However, the patterns of the deposition layers and melt pools boundaries were faint as compared to AP condition.

As an influence of the HT, the boundaries of the interfaces were not distinct despite what was observed in the AP samples. Nonetheless, the defects and porosities were still present, and similar to the AP samples, were more pronounced in the V specimens. The HIP+HT procedure, however, resulted in a completely different microstructure, as can be seen in Figure 3 e and f. The melt pool tracks of the deposited layers, and columnar grains were not detected. Similar to the HT specimens, the transitions at the interface zone for both sample orientations were smooth. The population of the captured defects was significantly lower compared with the other two categories.

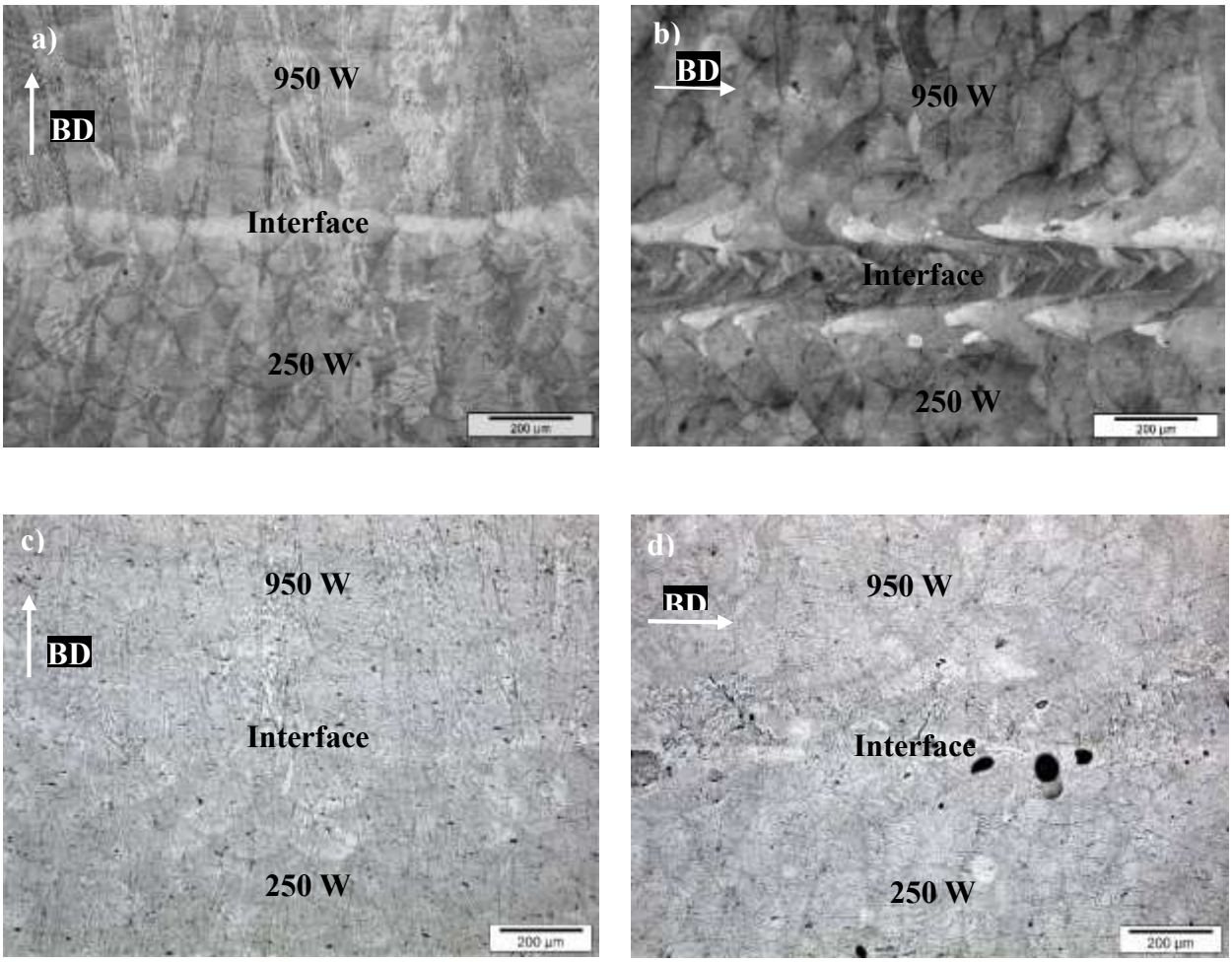

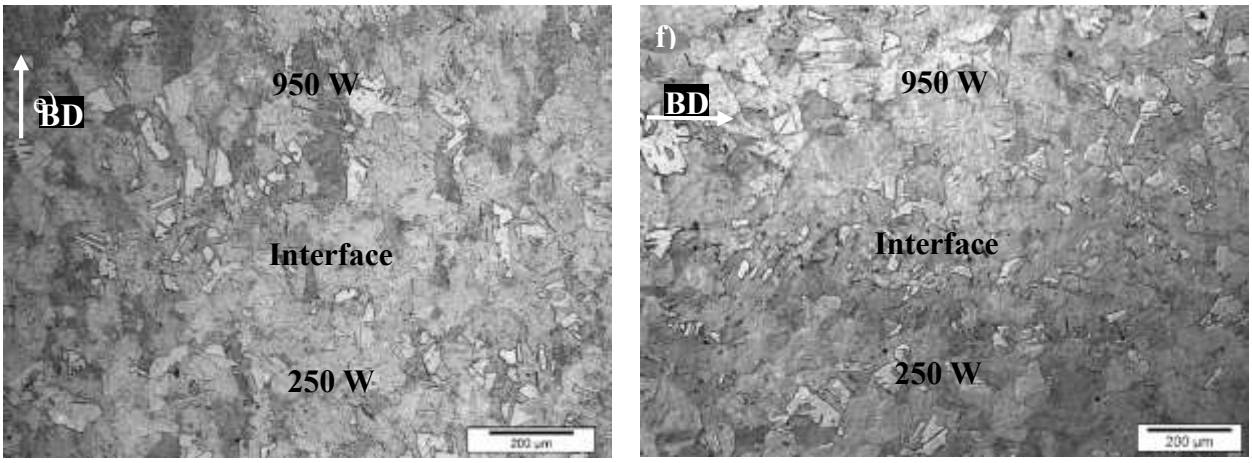

Figure 3. Optical micrographs of the (a) H-AP, (b) V-AP, (c) H- HT, (d) V-HT(e) H-HIP+HT, and (f) V-HIP+HT functionally graded samples at the interface area revealing the effect of the various post processing procedures on the microstructure. The build directions (BD) are indicated in the figures.

To further study the microstructure, SEM images of the NG samples in the AP and post-treated conditions were taken. Figure 4 shows the SEM micrographs of the AP materials along with the samples' build direction. Elongated grains, extended in the build direction, and the melt pool patterns were observed in all SEM images. The major axes of the grains in both 250 W and 950 W laser power groups were found to exceed the deposited layer thickness of those categories, which were 50 µm and 100 µm, respectively. This phenomenon implies the melting of those previously solidified layers and a clear pattern of the epitaxial grain growth through the deposited layers [1].

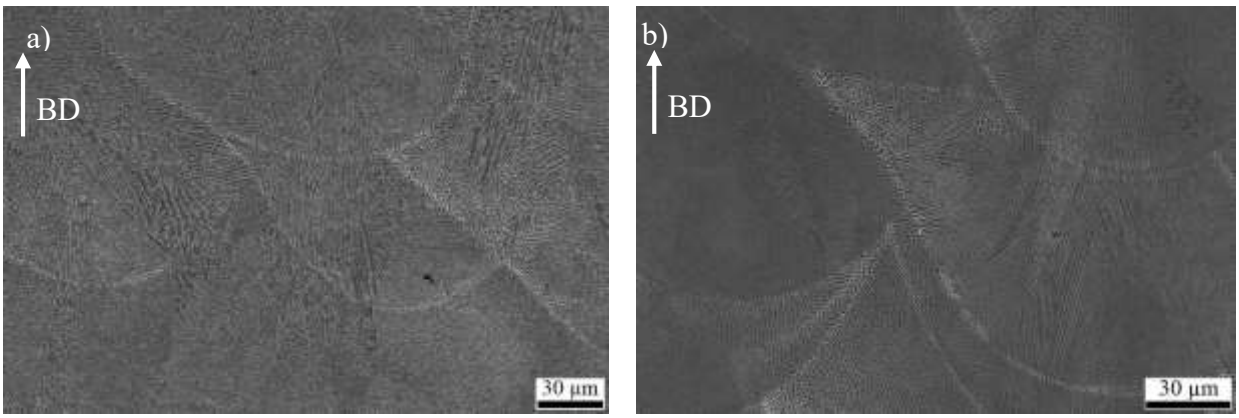

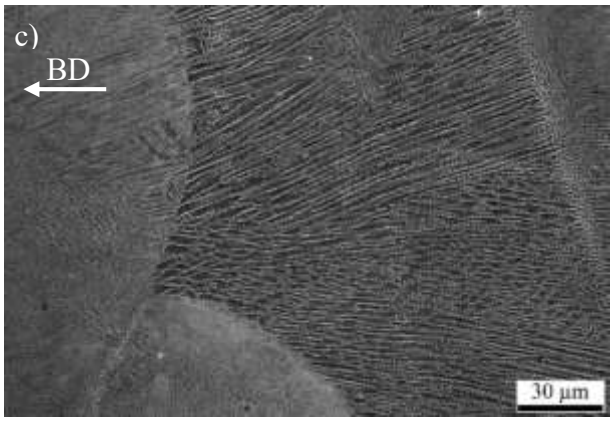

Figure 4. Microstructure of the AP materials in (a) 250W, (b) 950W-H, and (c) 950W-V conditions captured by SEM technique.

The SEM micrographs of the HT IN718 specimens are provided in Figure 5. The micrographs show the growth of the dendritic structure of the γ matrix along the BD. The other feature which was observed in the HT materials' micrographs is the presence of the rod-like and globular δ precipitates, which were not found in the AP material. The volume fraction of the δ phase in the HT L-PBF IN718 was reported to be 5.9 ± 0.4 [28]. In addition to the δ precipitates, carbides were found to exist, which was confirmed by Energy Dispersive X-Ray Spectroscopy (EDS). The content of the MC carbides in a similar material was determined to be 1.9 ± 0.5 vol. % [28]. γ' and γ'' strengthening phases were not detected due to their nanometre scale sizes. Therefore, further studies in this regard were done using the XRD technique and will be discussed later. In addition, several studies [28, 47-50] showed the presence of the strengthening precipitates in the AM nickel-based alloys after the HT procedures. Using neutron diffraction based procedure, the volume fractions of the γ' and γ'' precipitates of the similar material were determined to be 6.5 ± 1.4 and 8.4 ± 0.3, respectively [28].

The SEM micrographs of the HIP+HT IN718 materials, however, captured completely different microstructures, as shown in Figure 6. The grain elongations in the BD, which were observed in the AP and HT categories, did not exist in the HIP+HT material. Grains were found to be significantly larger, and some twin boundaries were detected. Quantitative details on the grain growth and twin

volume fractions will be revealed later in the EBSD part. Comparing the SEM images of the HT and HIP+HT materials, it can be seen that the population of the carbides and δ precipitates is reduced after the HIP+HT procedure. This observation is similar to what was found from the neutron diffraction data on a HIP+HT IN718 superalloy [28]. Similar to the HT category, the existence of the nano-sized γ' and γ'' phases could not be examined using SEM images. Therefore, more analysis using XRD was needed.

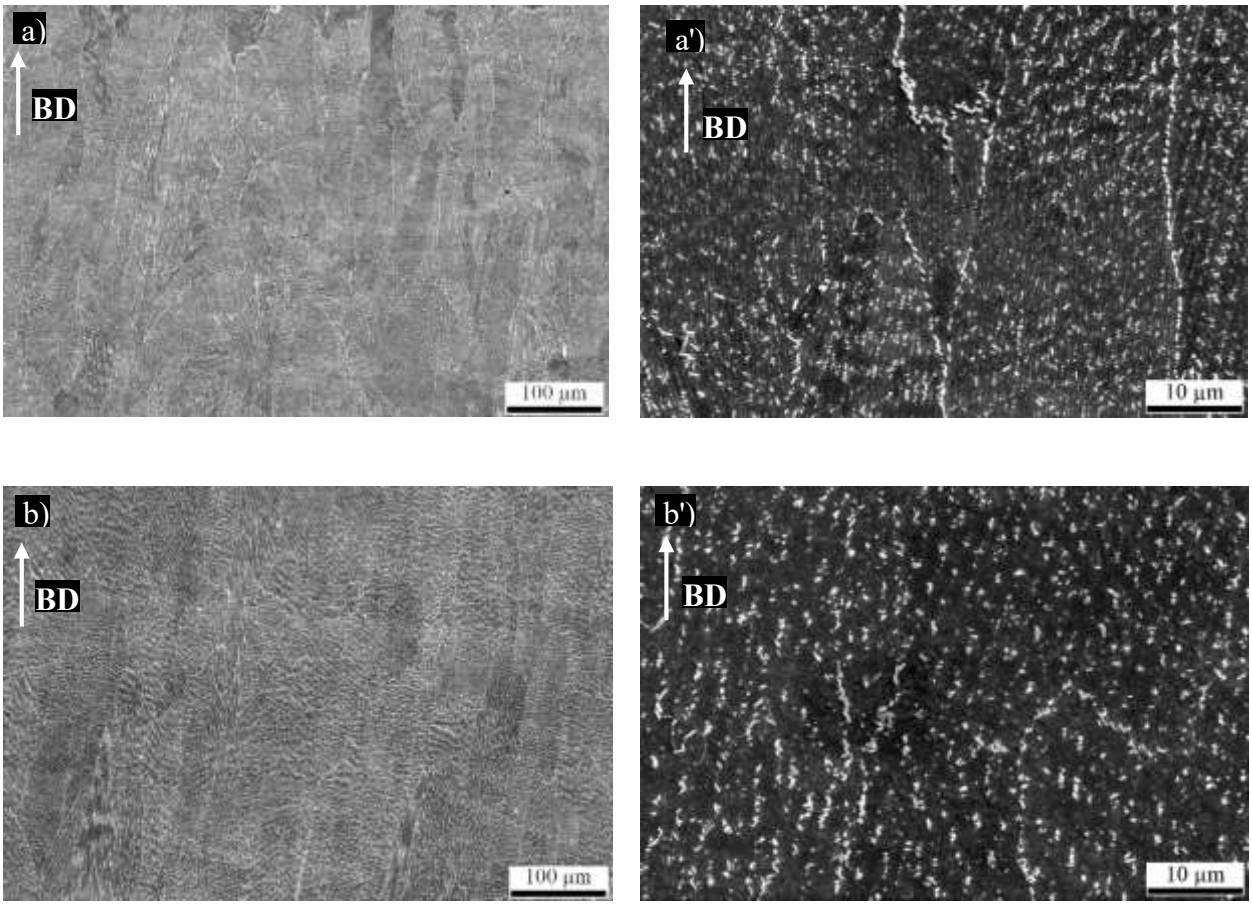

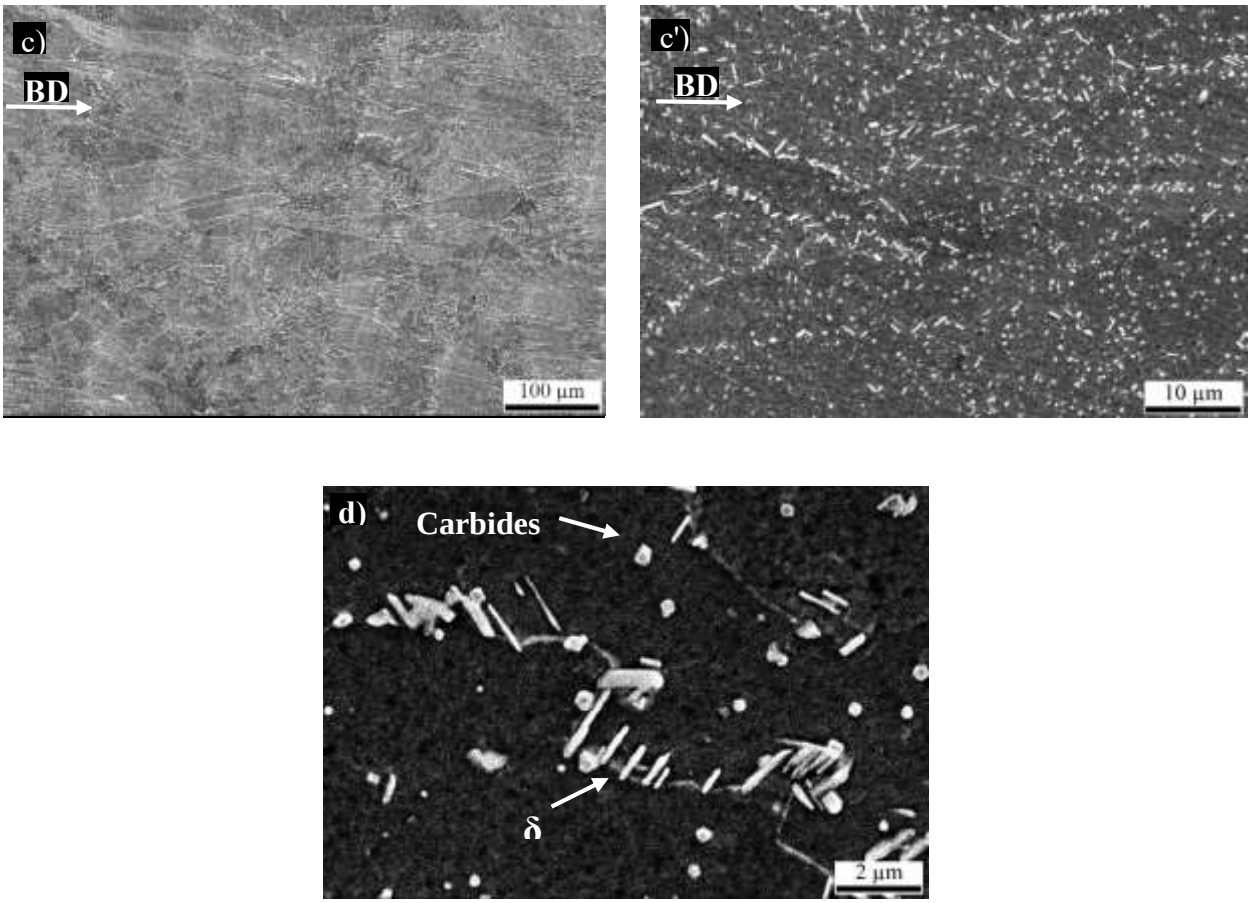

Figure 5. SEM micrographs of (a) 250W, (b) 950W-H, and (c) 950W-V HT samples. The precipitates are captured in the corresponding higher magnification micrographs provided in sub-figures a'-c', respectively. A higher magnification SEM micrograph of the 950W-V HT material is provided in (d). The needle shape and globular δ precipitates, and some carbides were located.

The XRD analyses were carried out on the surfaces along the BD to identify the present phases in the AP and post-processed categories. Figure 7 a and b presents the XRD patterns of the 250 W and 950 W- H samples, respectively, in three categories as far as the post treatment procedure, i.e., AP, HT, HIP+HT. As was expected, the main phase in all categories was the γ phase. In both 250 W and 950 W- H materials, in the AP and HT groups, the relative intensity of the γ(200) was higher than the γ(311) peak. This can be linked to a preference for growth in <001> direction and the existence of a strong thermal gradient in the build orientation [1, 51]. In the HIP+HT category, although the intensity of γ(200) still remained higher than the γ(311) peak, but the preference was not significant. It can be correlated with the grain growth or recrystallization during the HIP procedure [51]. The zoomed-in

views with identified phases are given in Figure 7 a' and b'. As can be seen, the Laves phase peaks were not detected after the HIP+HT procedure. In addition, the MC carbide peaks, which were present in the HT condition, were reduced in the HIP+HT material. These observations are consistent with what was reported from the neutron diffraction analysis of the LPBF IN718 after HIP treatment [28]. Moreover, after the heat treatment, δ phase peaks were present in the XRD spectra of 250 W and 950 W- H materials. This is in agreement with the presence of δ precipitates observed in the SEM micrographs given in Figure 5. The spectra of the HIP+HT samples show a reduction in the precipitates while the carbides are present in the material, as seen in the SEM images in Figure 6.

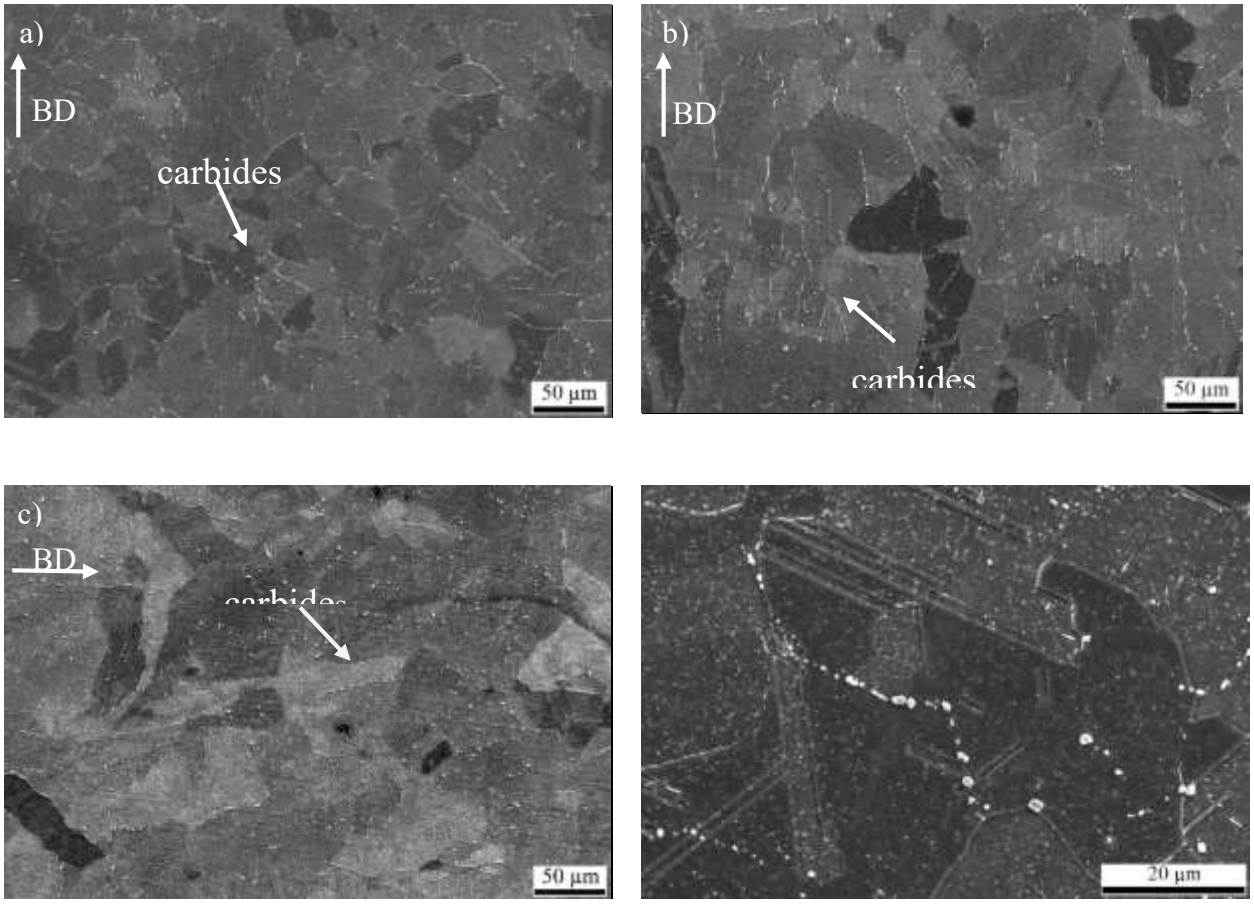

Figure 6. SEM micrographs on the (a) 250W, (b) 950W-H, and (c) 950W-V samples of the HIP+HT category. The MC carbides were captured in all materials and are more visible in a higher magnification SEM micrograph given in (d), which is taken on the 950W-H sample.

To evaluate the effect of the post treatment on the surface hardness of the the LPBF IN718, the Vickers hardness test was performed on the AP, HT, and HIP+HT materials. Figure 8 shows the average hardness of the NG specimens in different post processing conditions. It can be seen that the average hardness of all NG categories increased significantly by the HT and HIP+HT procedures, which is attributed to the precipitation of the γ' and γ" strengthening phases and recrystallization [52].

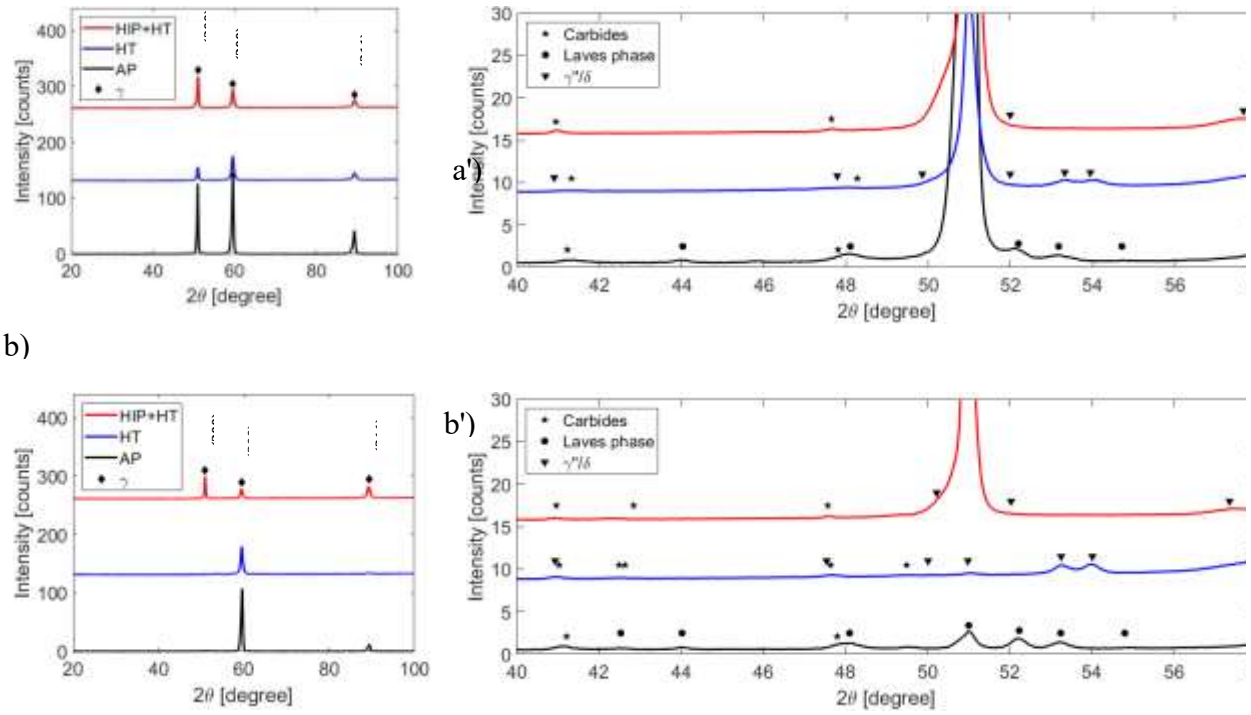

Figure 7. Phase analyses obtained from XRD on (a) 250 W and (b) 950 W- H categories of AM parts. To better reveal the existing phases, corresponding zoomed-in figures of spectra are provided in (a') and (b') respectively.

Different heat treatment procedures, including solution+aging or homogenization+solution+aging, were reported to increase the hardness of the as processed SLM IN718 by about 30% [25]. Similarly, the direct double aging (DA), and solutionizing followed by DA treatments of the laser cladding IN718 coating, were found to increase the hardness significantly due to the precipitation of γ" and reduction of the Laves phase, respectively [53]. The HIP+annealing treatment was found to enhance

the Vickers hardness of the SLM IN718 by 46%, while the increase of the hardness by a 4-hour annealing treatment was just below 20% [48]. It should be noted that the hardness increase by HT was more significant in the 950 W group compared with the 250 W material, where the increase was 51% and 66% for the 950 W- H and 950 W- V, respectively, compared with the 35% rise in the 250 W category. The trend remained the same when the HIP+HT was applied.

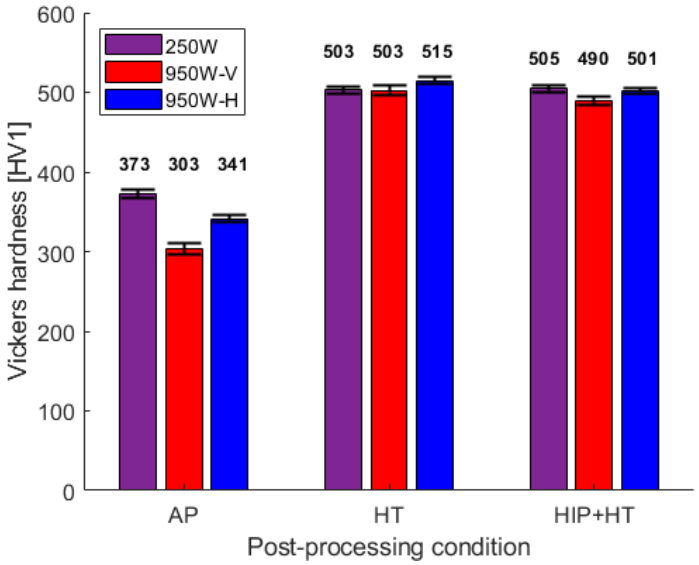

Figure 8. Bar graphs showing the average Vickers hardness values of the non-graded L-PBF materials manufactured using different parameters. The graphs are plotted for as-processed (AP), heat treated (HT), and hot isostatic pressed and heat treated conditions (HIP+HT).

Moreover, the Vickers hardness of the FG materials was measured along the height of the samples, including the interface zone. The measurements were done for both vertical and horizontal samples in all studied categories. The hardness profiles of the FG samples measured on the AP, HT, and HIP+HT conditions are provided in Figure 9. The profiles are averaged over 5 sets of measurements. It can be seen that the hardness values along the samples' height, for H and V orientations, are close in the HT and HIP+HT categories while are significantly higher than the AP materials. This observation is consistent with the hardness behaviour of the NG materials in different post-processed conditions, given in figure 8. In the AP condition, the fit to the hardness profile of the H samples showed a

decreasing trend along the height, i.e., parallel to the BD. While in the V samples, the fit along the height, i.e., perpendicular to the BD, remained fairly constant. The average hardness value of the 250 W side of the H sample, which is closer to the build platform (BP), was 361 ± 6 HV, and it was 340 ± 7 HV for the 950 W side, which is the furthest from the BP. This phenomenon is related to the higher number of thermal cycles that the initially deposited layers, which are closer to the BP, experienced compared with those which are located further from the BP, i.e., the 950 W side. The repetitive local reheating procedures on the initially deposited layers during the solidification of the latter layers decreases the content of the Laves phase in those layers [54, 55]. Moreover, the reheating cycles can precipitate some content of very small size γ' and γ'' on the initially deposited layers [53, 56, 57]. The combination of the mentioned factors resulted in a higher hardness in the 250 W side of the H samples, which was deposited earlier, compared with the other part. On the other hand, the hardness measurements along the height of the V samples were done on the layers which went through the same number of local thermal cycles. As a result, those layers on which the individual sets of hardness measurements were conducted were similar as far as the content of the Laves phase or small strengthening precipitates. Therefore, the hardness value along the height, or the deposition direction, of the V samples remained constant while showed some fluctuations due to the presence of the voids and defects. It should, however, be noted that the hardness values on the AP V samples decreased along the build direction as a consequence of the reduction in the number of the thermal cycles on the previously deposited layers. After post-processing treatments, similar trends were found in the H and V samples, i.e., the hardness of the H samples decreased along the height, and the V samples' hardness was independent of the position along the height. Although, the slope of the hardness decrease in the H samples, lowered which can be related to more homogeneity in the material after post treatment. Another feature which was observed from the hardness profiles of the HIP+HT samples was the reduction in fluctuations compared with the AP and HT samples in both build

orientations. This smoothing in the hardness profiles can be a consequence of fewer defects in the HIP+HT materials.

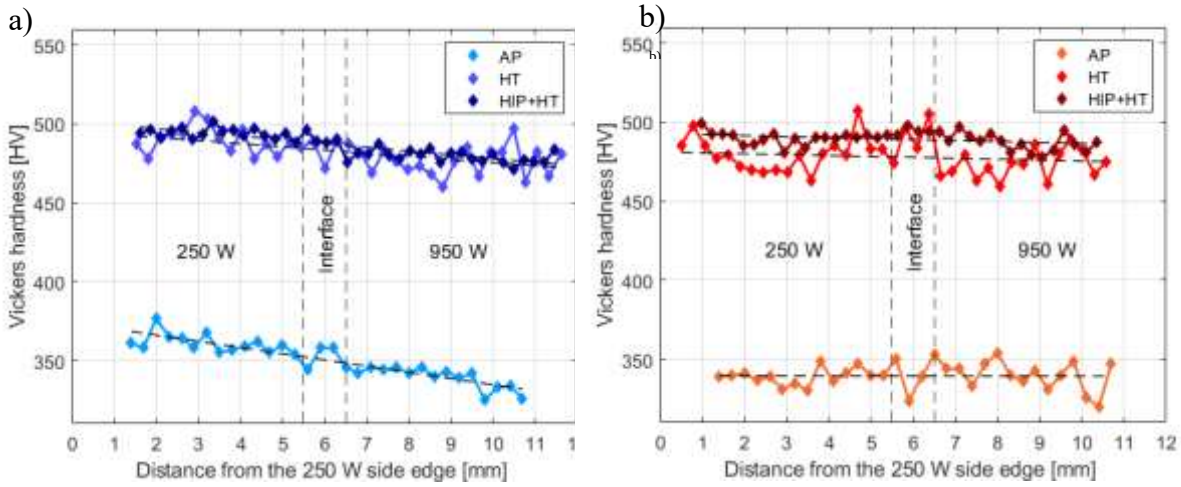

Figure 9. Hardness profiles of (a) horizontal and (b) vertical functionally graded samples in different post-processing conditions.

3.2 Evolution of crystallographic texture and grain size

Comprehensive EBSD analyses were conducted on all categories of NG materials to understand the effect of the post-processing treatments on the microstructure and texture of the L-PBF IN718. Figure 10 and 11 present the inverse pole figure (IPF) maps, pole figures, and the misorientation angle plots for the AP, HT, and HIP+HT materials. From the IPF maps it can be seen that the AP and HT materials have columnar grains extended along the build directions, while the grains of the HIP+HT do not show any preferential orientation. The elongation of the columnar grains of the AP and HT samples was dependent on the laser parameters and build orientations. For easier comparison, the data describing the shapes of the grains are summarized in Table 5. It should be mentioned that the pole figures and the grain shape statistics are calculated from multiple EBSD imaging on the same sample to have a sufficient number of grains representing the material structure. In the AP group, the grain

size and elongation of the 250W and 950W- V materials were close with aspect ratios of 0.27 and 0.25 and the major axis of 135.6 µm and 147.7 µm, respectively.

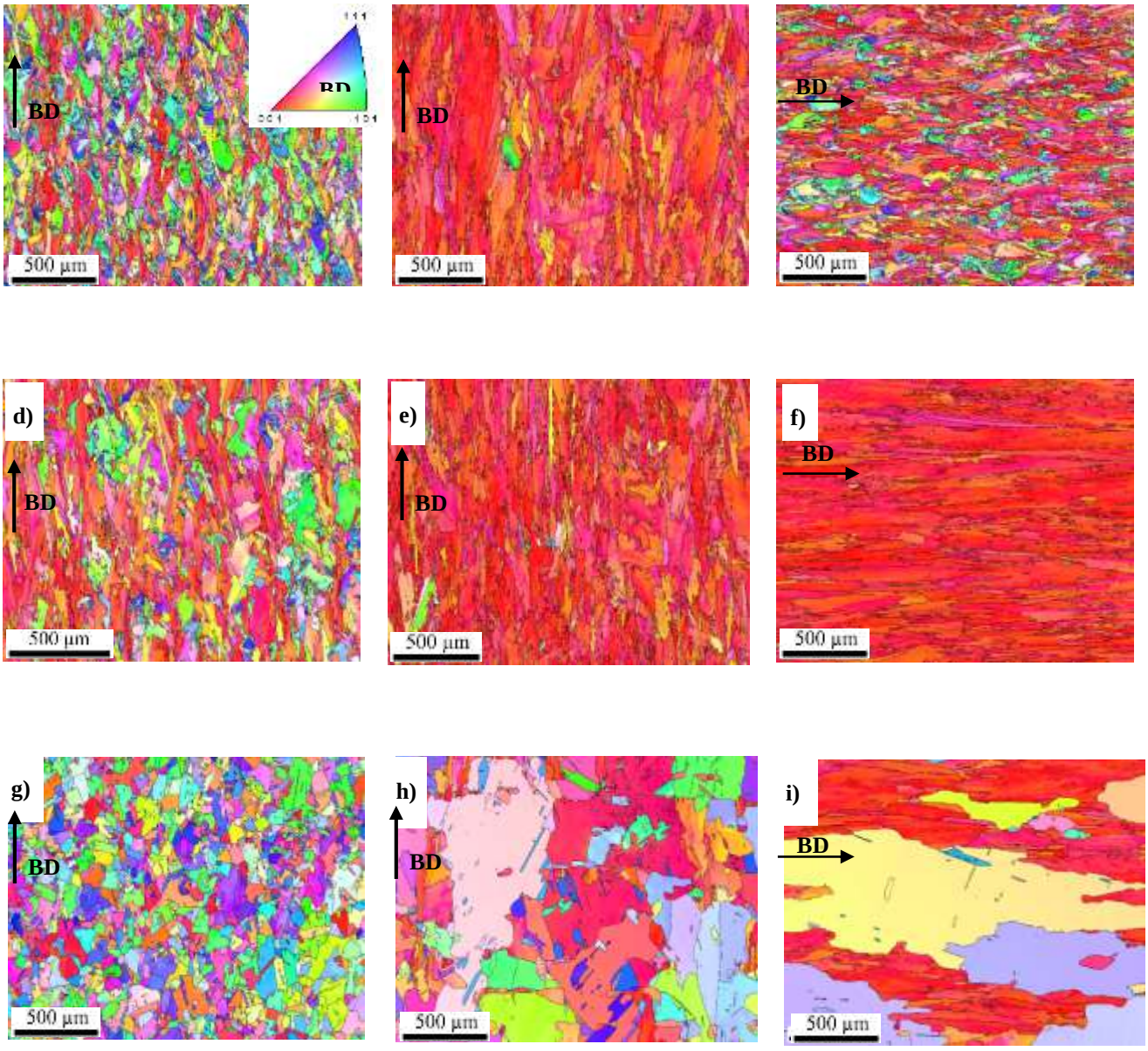

Figure 10. Inverse pole figure maps of different categories of materials explored in this study prior to the fatigue testing. The EBSD imaging was done on large areas of (a) 250 W- AP, (b) 950 W- H- AP, (c) 950 W- V- AP, (d) 250 W- HT, (e) 950 W- H- HT, (f) 950 W- V- HT, (g) 250 W- HIP+HT, (h) 950 W- H- HIP+HT, and (i) 950 W- V- HIP+HT materials.

Although their grains were columnar, the elongation was less compared with the 950W- H sample with an aspect ratio of 0.18 and a major axis of 518.4 µm. These differences can be generated by the heat flow, which is parallel to the build direction and introduces the preferred grain orientation [1, 40, 58, 59]. Observing the IPFs of the HT materials, it is evident that the 250W and 950W- V materials

experienced grain growth and became even more elongated, i.e., a reduction in the aspect ratios. The grain growth caused by HT can be linked to the grain boundary migration caused by atoms diffusion [60, 61]. The 950W- H material, which had the largest and most elongated grains in the AP condition, however, showed a reduction in the grain size and a tendency to become more equiaxed, where the aspect ratio increased from 0.18 to 0.2. Similar behaviour of the reduction in grain size after stress relief annealing treatment of an L-PBF IN625 [40] and 2-h and 6-h heat treatment of L-PBF MAR-M-509 [62] were reported. Moreover, as it will be discussed in the following parts, the residual stress of the 950W- H samples was found to be higher than the 950W- V specimens. The residual stresses caused by the thermal cycles are considered as the driving forces of recrystallization in IN718 [63]. This can influence the grain size evolution after the HT process. Grains had a totally different microstructure after the HIP+HT procedure. As the IPFs in Figure 10 g-i demonstrate, the grains were not as extended along the BD as the AP and HT categories and were oriented randomly. The IPFs and grains' statistics listed in Table 5 show that all categories had grain growth and recrystallization after HIP+HT. The 250W and the 950W-H microstructures show more equiaxed grains while still, some extent of elongation is present in the 950W-V sample. Another feature of the IPFs is the presence of the annealing twin boundaries in the HIP+HT materials. The Σ3 twins are defined as boundaries with 60° misorientations along the <111> orientation [64]. Equiaxed grains with annealing twin boundaries define a low stacking fault energy matrix. Blank IPFs highlighting the grain boundaries and Σ3 twin boundaries are provided in figure 12. While the HIP+HT samples, especially the 250W and 950W-H groups, contained significant amounts of twin boundaries, considerable annealing twin boundaries were not found in the AP and HT samples. This is in agreement with the misorientation angle plots given in figure 11, where the annealing twins have the 60° misorientation angle. The formation of incoherent annealing twins after HIP treatment on the LPBF nickel-based superalloys was reported in other research [5, 40]. The low angle grain boundaries (angles $<15°$ [65]) were present in the AP material. They are formed by arrays of dislocations as consequences of rapid solidification and the

fact that during solidification, sub-grains grow along the proffered crystallographic direction, i.e., <100> for the FCC materials [39, 66, 67]. The presence of LAGB, which can be an indication of the extent of local deformation or residual stresses, was reported in the LPBF nickel-based superalloys [39-41, 60, 68, 69]. Their fractions after HIP+HT were found to be less than those in the AP condition. The reduction in LAGB content was more pronounced for the 250W and 950W-H, which had more annealing twins after the HIP+HT process (see figure 12 g-i). It is related to the recrystallization and formation of the Σ3 twin boundaries and high angle grain boundaries. Similar behaviour was reported after post-processing of the AM nickel-based superalloys [39-41, 58].

The stereographic pole figures with triclinic symmetry of NG materials in AP, HT, and HIP+HT conditions are plotted in figure 11. Pole figures were constructed employing an orientation distribution function. Additively manufactured nickel-based superalloys are expected to possess either a Goss texture component ($\{110\}\langle 100\rangle$) or a cubic texture component $\{001\}\langle 100\rangle$ which originate from the solidification of $\langle 100\rangle$-oriented grains or dendrites and is affected by the processing parameters [70]. Figure 11 a-c provides the crystallographic textures of the AP materials. The 250 W IN718 showed a weak Goss texture with a maximum multiples of random distribution (m.r.d.) of 3.4. The texture derived for the 950W- H sample, however, was a strong cubic texture with a maximum m.r.d. intensity of 17.2. The 950W- V material had a moderate texture. The formation of Goss, cubic, and fibre textures in AM nickel-based alloys were reported [41, 69-74]. Strong $\langle 001\rangle$ fibre textures in the AM IN718 built with the higher laser power of 950 W, compared with a near random texture in the lower laser power builds, i.e., 250 W, was observed. Applying the heat treatment, the 250 W material's texture evolved to $\langle 001\rangle$ fibre, and the intensity showed a slight increase but remained moderate. Similarly, the 950 W- V material had a fibre texture after HT, but the increase in the intensity was significant, and the maximum value of m.r.d. was about 27, which was the strongest in all HT parts. The formation of $\langle 001\rangle$ fibre texture after HT was observed in other research [5, 40, 58].

The crystallographic texture of the 950W- H material remained similar to the AP condition with slight spreads. The intensity showed a modest decrease but remained strong with a value just below 16.

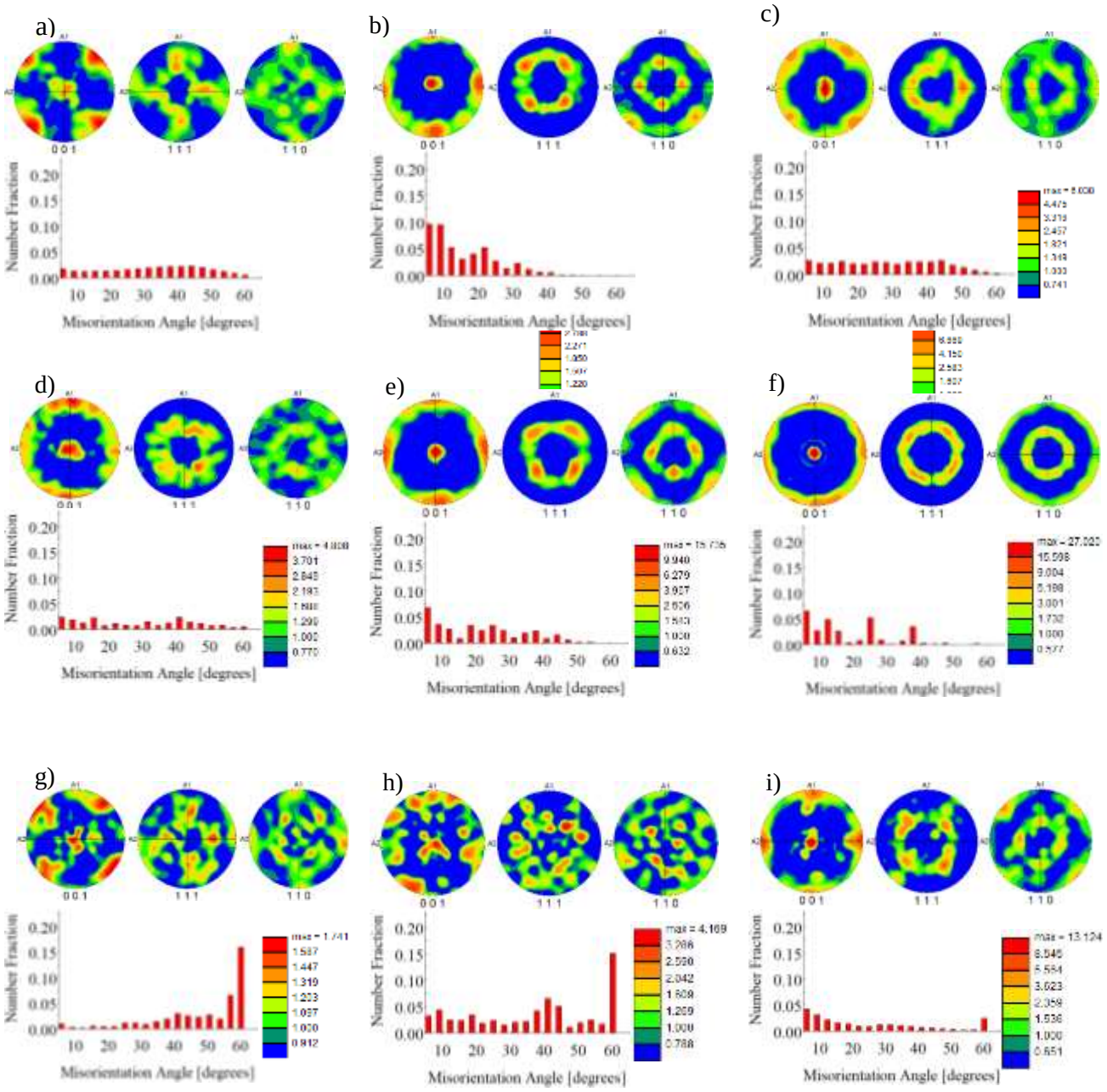

Figure 11. Pole figures and misorientation angle plots corresponding to the IPFs provided in **Figure 10** as (a) 250 W- AP, (b) 950 W- H- AP, (c) 950 W- V- AP, (d) 250 W- HT, (e) 950 W- H- HT, (f) 950 W- V- HT, (g) 250 W- HIP+HT, (h) 950 W- H- HIP+HT, and (i) 950 W- V- HIP+HT materials In all pole figures the build direction is parallel to the A3 (the out of the plane direction). Note that the misorientation angles lower than 5° are not included in the misorientation plots.

In the HT materials, the intensity of the ⟨001⟩ was found to be high, especially for 950 W materials compared with the 250 W. This behaviour is in line with what was detected by XRD, where the intensity of γ(200) remained higher than γ(311). The HIP+HT procedure changed the microstructure of the horizontal samples significantly. Both 250 W and 950 W-H materials exhibited random textures with weak intensities. The decrease in the maximum intensity of the H samples is consistent with the less difference in the γ(311) and γ(311) peaks of the XRD spectra. The 950 W- V sample, however, behaved differently after the HIP+HT. The texture was cubic-like, and the maximum intensity increased to about 13.

Table 5. Grain shape statistics of different NG materials obtained from multiple EBSD imaging

Material category	250 W			950 W- H			950 W- V		
	AP	HT	HIP+HT	AP	HT	HIP+HT	AP	HT	HIP+HT
Minor axis [μm]	28.9	35.9	55.1	79.9	58	181.3	27.3	103	113.5
Major axis [μm]	135.6	203.9	141.7	518.4	335.5	582.3	147.7	938.9	719.2
Aspect ratio	0.27	0.24	0.41	0.18	0.2	0.36	0.25	0.12	0.18

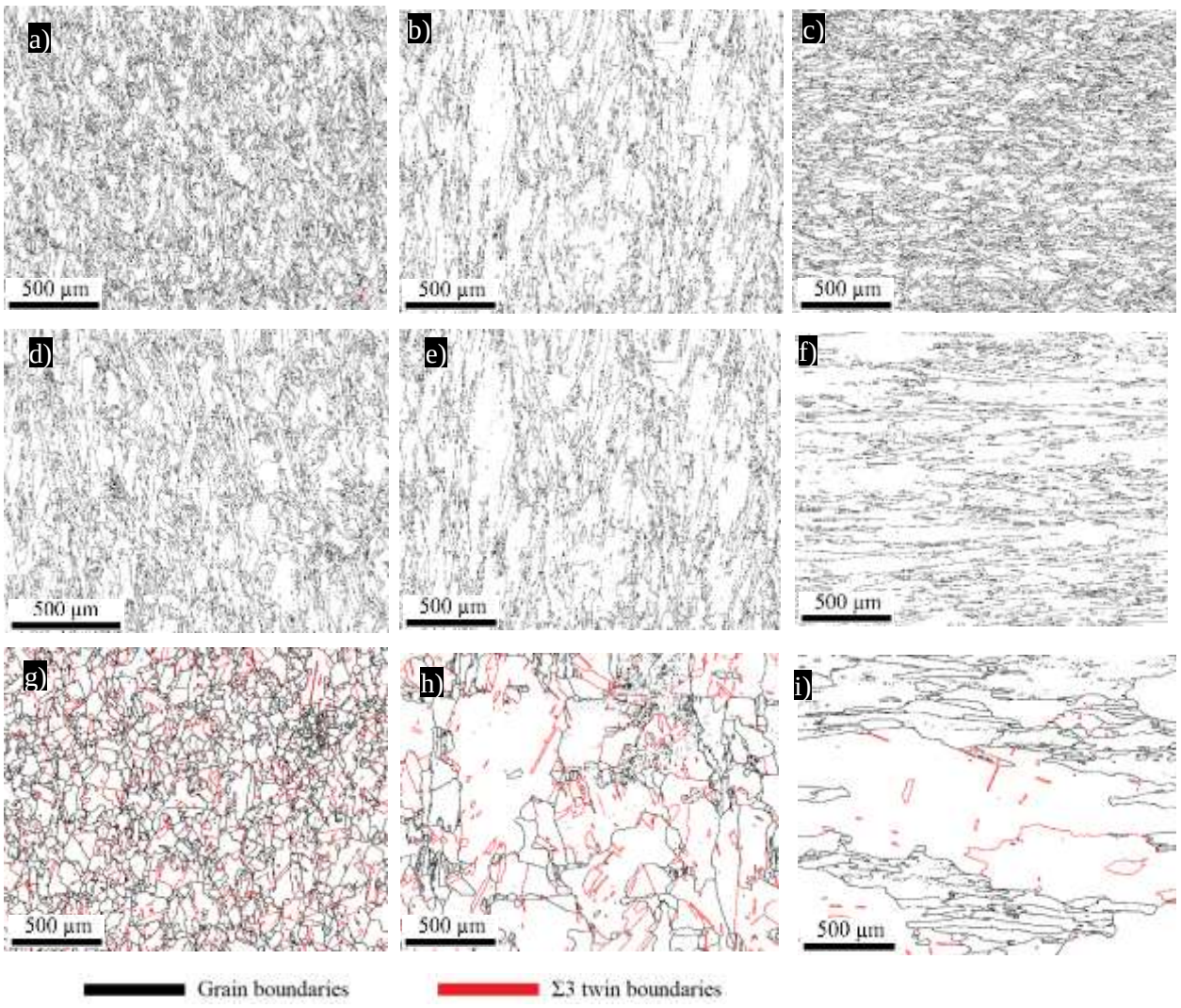

Figure 12. Blank maps identifying the grain boundaries in black, and annealing twin boundaries, in red. The blank maps a-i correspond to the IPFs provided in Figure 10.

Lastly, using the measured EBSD data, the grain orientation spread (GOS) maps were plotted for all categories of materials. Figure 13 shows the GOS maps of the 250W, 290W- H, and 290W-V materials in AP, HT, and HIP+HT conditions. The average GOS and the maximum GOS values of each plot are also provided. The GOS plots give an indication intragranular distortions and also of the residual stress in the material where higher GOS values imply higher misorientations and residual stress [75-78].

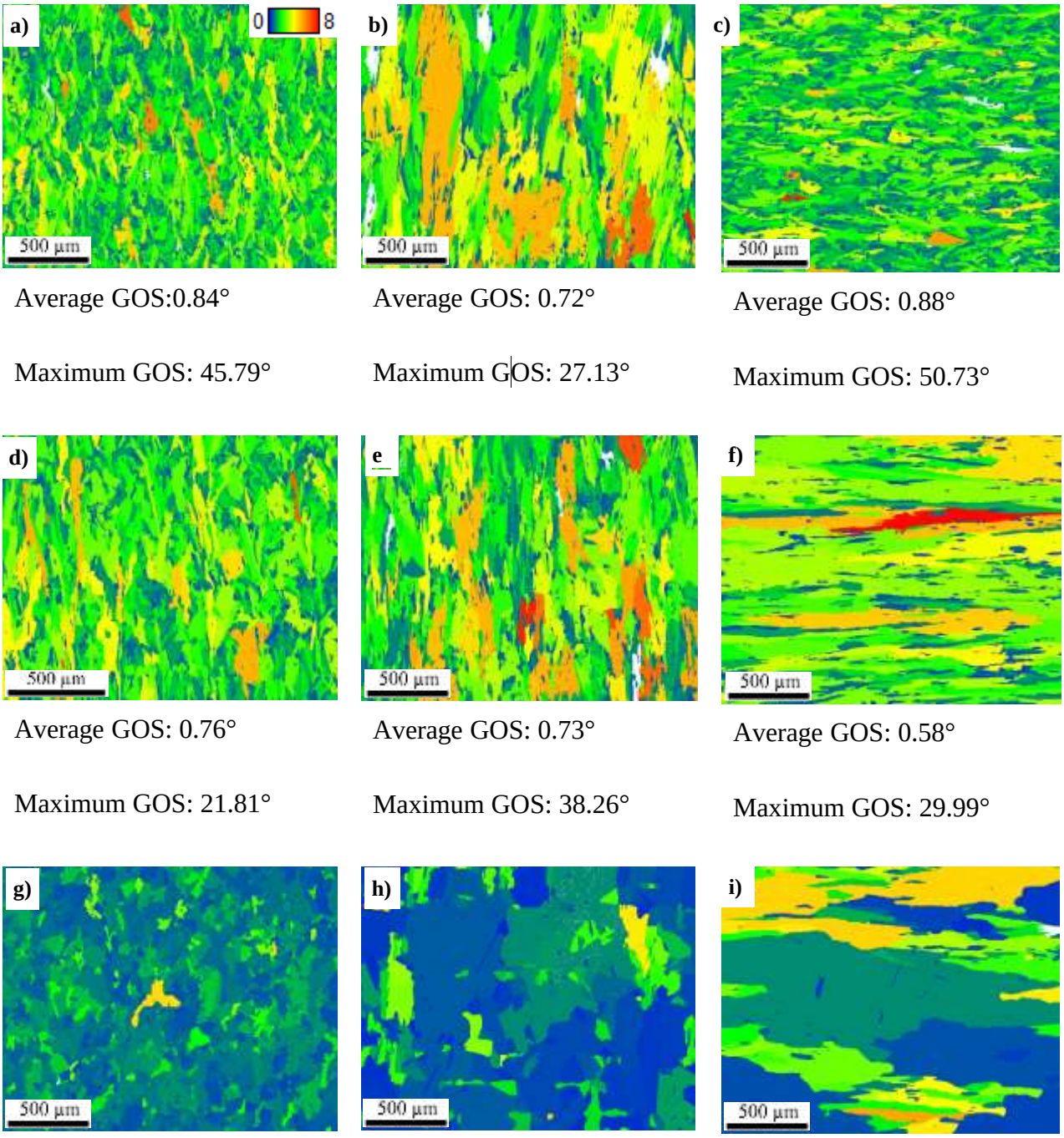

Figure 13. Grain orientation spread (GOS) of (a) 250 W- AP, (b) 950 W- H- AP, (c) 950 W- V- AP, (d) 250 W- HT, (e) 950 W- H- HT, (f) 950 W- V- HT, (g) 250 W- HIP+H, (h) 950 W- H- HIP+H, and (i) 950 W- V- HIP+H samples. The values of average GOS and maximum GOS of each plot are provided. The colour-bar provided in (a) applies to all plots.

Comparing the GOS plots of the 250W materials, the average values reduced after both HT and HIP+HT, which means the residual stresses decreased after post-processing. The trends were different for the higher laser power samples. It should be noted that the residual stress of the 950W samples varied depending on the build orientation. It can be a consequence of more free surfaces or free edges of the vertical compared with the horizontal specimens. In addition, the distance from the build platform on the V and H samples were different. These factors can end up in different thermal profiles in different build directions, which influences the residual stress values. While the average GOS of the 950W- H material remained almost the same after post-processing treatments, the maximum GOS increased after HT and decreased significantly from 27.13° in AP to 4.83° in the HIP+HT condition. The average GOS of the 950W- V samples was measured to be 0.88° in the AP condition, and it decreased to 0.58° after the HT procedure. While the maximum GOS of the HIP+HT material decreased to 10.26°, compared with the 50.73° in the AP condition, its average GOS increased to 1.14°, which shows a higher residual stress value.

3.3 Mechanical properties

3.3.1 Fatigue behaviour of non-graded (NG) material

The effects of the different post processing procedures on the microstructure were explored in the previous section. The results of two types of fatigue crack growth parameters, namely the stress intensity range threshold (ΔK_{th}) and the Paris law crack growth, are discussed in this part. To find out the influence of the microstructure on the crack propagation behaviour, constant K_{max} experiments were conducted on the NG and wrought-HT parts. The starting stress ratios were set to 0.1, and the final stress ratios were about 0.6-0.7. ΔK_{th} values obtained for different categories of tested materials are listed in [74]. It should be noted that the K_{max} value for all tests was 25 MPa$\sqrt{m}$. In the AP category, the ΔK_{th} values were close, while the 250W material had the highest threshold stress

intensity factor (SIF) range followed closely by the 950W- V samples. This behaviour can be a consequence of the different grain sizes in the tested materials. It is known that more grain boundaries or finer grains hinder crack growth [79]. On the other hand, large grains are capable of accommodating more slip damage due to their fewer constraint to slip compared with the small grains, which can result in a higher ΔK_{th} value [80]. So, as suggested in the literature, the relationship between the grain size and the threshold SIF range is influenced by different competing parameters [79, 81].

Table 6. A summary of constant K_{max} tests performed on the NG-HT, NG-HIP+HT, and wrought-HT samples to obtain the ΔK_{th} values.

Processing condition	Sample category	Final stress ratio	ΔK_{th} [MPa$\sqrt{m}$]
L-PBF- AP	250 W	0.7	7.2 ± 0.3
	950 W- H	0.7	6.0 ± 0.2
	950 W- V	0.7	7.0 ± 0.3
L-PBF- HT	250 W	0.7	9.5 ± 0.2
	950 W- H	0.7	7.9 ± 0.2
	950 W- V	0.7	7.5 ± 0.3
L-PBF- HIP+HT	250 W	0.7	7.7 ± 0.3
	950 W- H	0.6	10.2 ± 0.2
	950 W- V	0.7	8.8 ± 0.2
Wrought-HT	-	0.6	13.1 ± 0.9

In addition, at low stress ratios, roughness-induced crack closure in the coarse grains can induce an overall better near threshold crack growth behaviour [82, 83]. Finer-grained microstructure on the other hand can lead to a straighter crack with lower surface roughness, which reduces the effects of crack tortuosity and roughness-induced crack closure and hence lessens the fatigue overload retardation effects. From the microstructural analysis, AP-250W material had the finest grains, followed by the 950W- V category. Moreover, the orientations of the grains in the 950W- V parts created more grain boundaries in front of the crack path.

For the HT materials category, the ΔK_{th} values increased compared with the AP materials. This improvement in the threshold SIF range is associated with the presence of the strengthening phases, which precipitated after the HT process. Similar to the AP category, the 250W samples showed the highest ΔK_{th} due to possessing the finest grains in their microstructure, which adds up the grain boundaries in front of the crack path. The ΔK_{th} of a laser directed energy deposited (LDED) IN718 after a similar HT to this study was reported to be 10.8 ± 0.1 MPa$\sqrt{m}$ [84]. Comparing the wrought-HT and L-PBF- HT materials, it turned out that the ΔK_{th} of the wrought samples were higher, which can be associated with their equiaxed fine grains with major axes of less than 20 µm. The threshold SIF range of a solutionized and double-aged extruded Inconel 706, at R= 0.8, was reported to be in the range of 5.7-13.9 MPa$\sqrt{m}$ in different directions [85]. In the HIP+HT category, the grain size increased, which could affect the ΔK_{th}. Also, the strengthening precipitates were present in the materials compared with the AP condition. Additionally, the content of the porosity in the HIP+HT material was found to be less than the AP and HT samples [16], which can increase the ΔK_{th} value. As a result, after HIP+HT, all materials showed an increase in the threshold SIF range, with the 950W- H samples having the highest ΔK_{th} values. The high threshold SIF range value of these categories can be

a consequence of the formation of annealing twins as the annealing twin boundaries can act as dislocation barriers in the early stages of the crack growth [80].

Furthermore, the K_{max} constant tests of the NG and wrought-HT materials were conducted at a constant stress ratio of R=0.1, i.e., compared with the increasing R ratio in the previous section. Figure 14 gives the fatigue crack growth rate, *da/dN*, versus SIF range, *ΔK*, curves plotted for AP, HT, and HIP+HT samples. In addition to the curves based on the collected data points, the fits to the measured curves are provided. Equation 5 [86], Which has two empirical constants, namely Paris exponent, *m*, and Paris constant, *C*, was used for fitting purposes.

$$\frac{da}{dN} = C(\Delta K)^m \tag{5}$$

[73] lists the empirical constants of the Paris curves and the threshold SIF range values of all curves, plotted in figure 14. It should be mentioned that the ΔK_{th} values from the Paris curves are slightly different from those which are provided in [78]. The differences are related to the different stress ratios (R) in the tests, which alter the crack closure phenomenon. In the coarse grains, the roughness induced crack closure is supposed to improve the fatigue crack growth behaviour. However, in the HT materials, which still remained directional, the orientations of the grains and their elongation direction with respect to the crack direction played an important role. For instance, in the 950 W- H samples, the large axes of the grains, i.e., 336 µm, faced the crack path while it was the short axes, i.e., 103 µm, in the 950 W- V samples. Even in the lower laser power samples, the axes of the grains facing the crack were about two times the 950 W- V specimens. Therefore, a higher roughness induced crack closure effect in the H samples was expected.

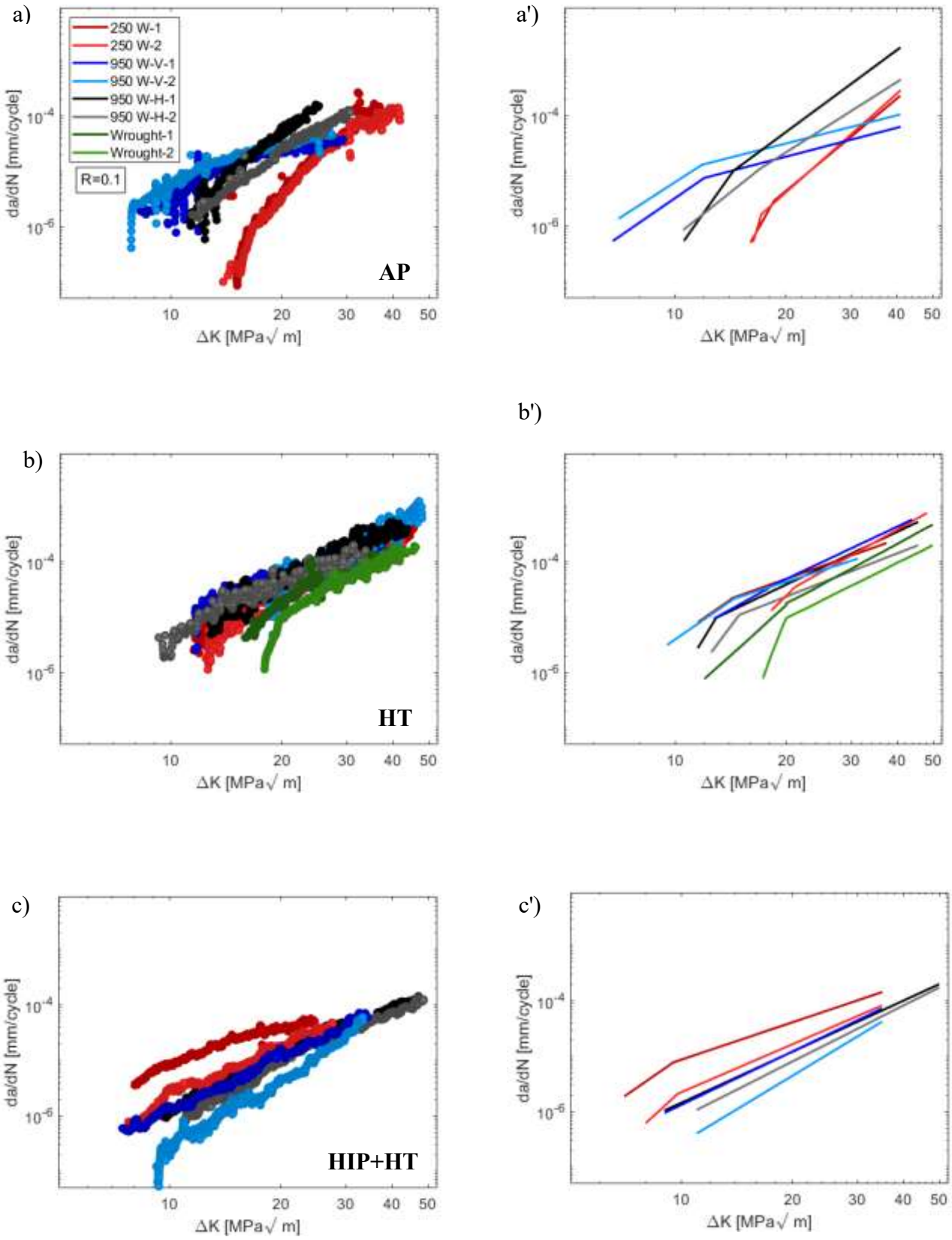

Figure 14. Fatigue crack growth curves of non-graded samples measured in (a) AP, (b) HT and (c) HIP+HT conditions at a stress ratio of R= 0.1. The corresponding Paris law fits are provided in (a'), (b'), and (c'), respectively. The legend given in (a) applies to all plots.

Changes in the threshold SIF range values depending on the stress ratios were observed in the nickel-based alloys [82, 87-89]. Increasing the stress ratio from 0.1 to 0.7 in a wrought IN718, which was solutionized at 1050°C for 1 hour and double aged analogous to the double-aging procedure of the wrought material in this study, decreased the ΔK_{th} from 10.2 to 5.8 MPa$\sqrt{m}$ [90].

Table 7. A summary of Paris law constants for L-PBF non-graded AP, HT, HIP+HT, and wrought-HT samples tested at R=0.1. The ΔK_{th} values are calculated at FCGR of 10-6 mm/cycles.

Processing condition		ΔK_{th} [MPa$\sqrt{m}$]	Paris exponent (m_1)	Paris exponent (m_2)	Paris constant (C_1)	Paris constant (C_2)
AP	250 W	16.5 ± 0.1	5.7 ± 0.1	-	(1.6 ± 0.5) E-13	-
	950 W- H	9.2 ± 0.2	4.6 ± 0.8	-	(1.2 ± 1.1) E-10	-
	950 W- V	6.0 ± 0.5	3.0 ± 0.1	1.1 ± 0.2	(6.0 ± 2.3) E-9	(9.4 ± 4.3) E-7
HT	250 W	10.9 ± 0.5	9.9 ± 1.0	2.9 ± 0.3	(2.0 ± 1.95) E-16	(6.5 ± 3.5) E-9
	950 W- H	7.2 ± 0.2	4.2 ± 0.4	2.6 ± 0.5	(4.2 ± 3.2) E-10	(7.4 ±0.4) E-8
	950 W- V	9.9 ± 2.5	5.6 ± 1.0	3.1 ± 0.7	(5.0 ±4.9) E-11	(2.0 ±1.9) E-8
HIP+HT	250 W	9.8 ± 0.9	3.2 ± 0.2	-	(8.0 ± 4.6) E-10	-
	950 W- H	11.5 ± 2.3	3.6 ± 0.4	-	(4.4 ± 4.2) E-10	-
	950 W- V	7.4 ± 1.3	5.4 ± 0.7	2.6 ± 0.3	(1.2 ± 1.1) E-10	(2.7 ± 2.4) E-8
Wrought- HT		15.1 ± 2.4	11.3 ± 5.7	6.1 ± 0.1	(4.5 ± 4.5) E-13	(3.5 ± 1.1) E-10

Based on the previous research, the fatigue crack growth resistance of the AM IN718 is remarkably lower than the conventional materials, which can be caused by the higher residual stress and the microstructural specifications of the AM parts [87]. However, proper post-processing treatments can improve the FCG behaviour of the AM parts and make it comparable with the wrought material. Comparing the HT curves, it can be seen that the fatigue crack growth rate (FCGR) of the HT L-PBF parts is still higher than the wrought material. Moreover, the ΔK_{th} of the wrought samples, 15.1 ± 2.4 MPa$\sqrt{m}$, are significantly higher than the L-PBF specimens ranging around 7-11 MPa$\sqrt{m}$. The ΔK_{th} of a laser directed energy deposited (LDED) IN718 with similar HT as the current study, found to be 10.8 ± 0.1 MPa$\sqrt{m}$ [84], which is in good agreement with the findings of this study. However, in the mentioned study [84], the FCGR of the HT LDED material was found to be consistent with the wrought ones, which was relatively weaker compared with the wrought samples in the current research. Figure 14 b and b' give the HIP+HT samples' curves. Putting them up against their HT counterparts, it is evident that the FCGR decreased significantly, resulting in a better performance than the wrought-HT samples. The improvement in the fatigue behaviour can be related to the crack tip blunting caused by the carbides present at the grain boundary, shown in figure 6, similar to what was reported in HT Inconel 690 [91]. The ΔK_{th} of both 950 W categories increased after HIP+HT compared with the AP materials. However, they still did not reach the ΔK_{th} of the wrought-HT samples explored in our research. The increase in the threshold SIF range values after HIP+HT can be related to the decrease in the residual stress and defects such as porosities which were induced during the manufacturing process. Furthermore, after the HIP+HT procedure, the texture in all categories became more isotropic, and grain growth was observed, which is known to hinder fatigue crack propagation [91, 92]. It should also be noted that ΔK_{th} of the HIP+HT samples was not affected by the crack-closure. In figure 14, it can be seen that the FCGR decreased after post processing and it was more pronounced in the HIP+HT category. The 0.2% yield strength of the 250W and 950W laser power categories were measured to be 668 $\pm$ 16 and 531 $\pm$ 9 MPa, respectively [16]. The values

increased to 1145 ± 16 and 1065 ± 20 MPa after HIP+HT [16]. The lower FCGR in the parts with higher yield strength after heat treatment procedures is consistent with an earlier report [93].

3.3.2 Fatigue behaviour of functionally graded (FG) materials

One of the main purposes of the current study was to explore the fatigue behaviour of the FG materials which was possible by conducting the ΔK-constant tests. Prior to performing the ΔK-constant tests on the FG parts, customized K solutions were obtained using an FEM model. The K values were calculated for different crack lengths between 1.5 mm and 7.5 mm, along the width of the samples. The calculations were done with crack length interval of 0.5 mm when the potential crack was far enough from the interface and 0.2 mm in zones closer to the interface. Figure 15-a shows the calculated SIF values for AP and post-processed FG materials, along with the K values calculated according to ISO 12135 [94] for the NG materials. To make an easier comparison, the values of the SIF of the FGMs are normalized by the K values calculated based on the standard. The normalized plots are provided in Figure 15-b. From the plots, it can be seen that due to the presence of the interface zone, the K values of the graded parts are higher than that of the non-graded materials. The largest difference in the K values of the FG parts and the NG material calculated from the standard was observed in the AP group, while the HIP+HT category showed the least deviation. When the crack tip was about to reach the interface, all FG curves showed the most noticeable variance from the standard curve calculated for the NG material. After crack enters the interface, the effect of the interface on K starts to reduce in all samples. Quickly after the crack passes to the other region, the K values of the FG and NG parts converge.

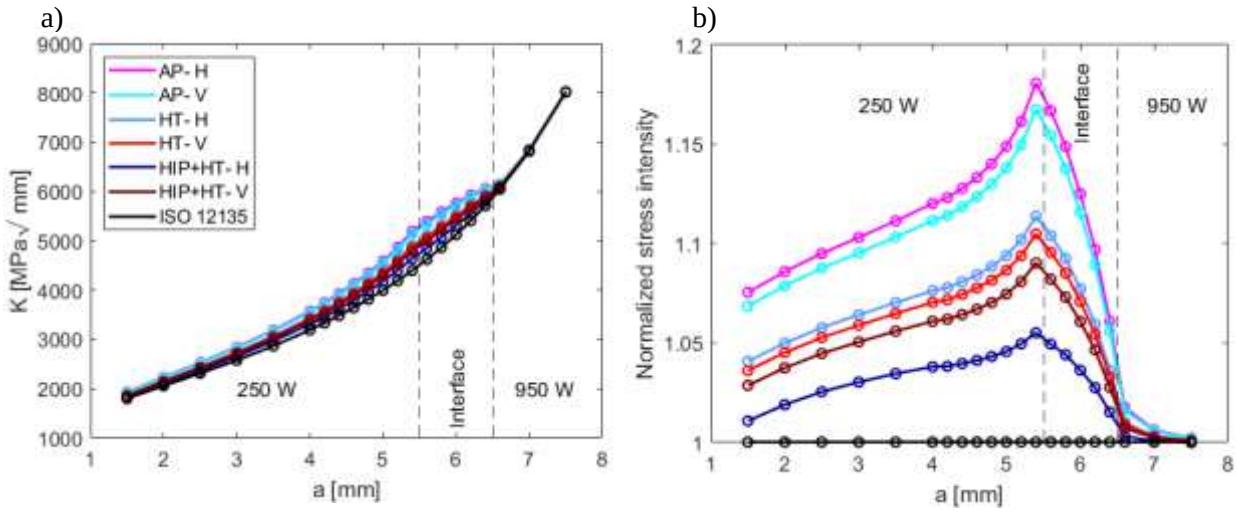

Figure 15. (a) Stress intensity factor values against the crack length calculated by the FEM model showing the variation of K in the functionally graded specimens for a constant load of 10 kN and (b) the normalized values of the stress intensity against the crack length over the width of the samples. In both plots, the ISO 12135 [94] values are plotted for comparison purposes. The legend given in (a) applies to both figures.

Having the customized K solutions calculated, ΔK-constant tests were carried out on the FG materials. Figure 16 provides the FCGR, *da/dN*, against the crack length, *a*, for different sample orientations in HT and HIP+HT conditions. Also, the dashed lines represent the fits to the AP curves, which are discussed in more details in our previous research. It should be noted that all samples were tested at ΔK=22.5 MPa$\sqrt{m}$.

The FCGR of HT and HIP+HT samples in both directions found to be approximately constant along the width of the samples as the crack propagated. The FCGR fluctuated between 2E-5 and 5.5E-5 mm/cycle in the HT and 2.3E-5-6.9E-5 mm/cycle in the HIP+HT conditions, which are considered as close ranges. This observation in the FCGR of the FG samples after HT and HIP+HT is similar to their hardness behaviour. The horizontal direction samples exhibited a slightly lower *da/dN*, which could be related to their relatively moderate texture.

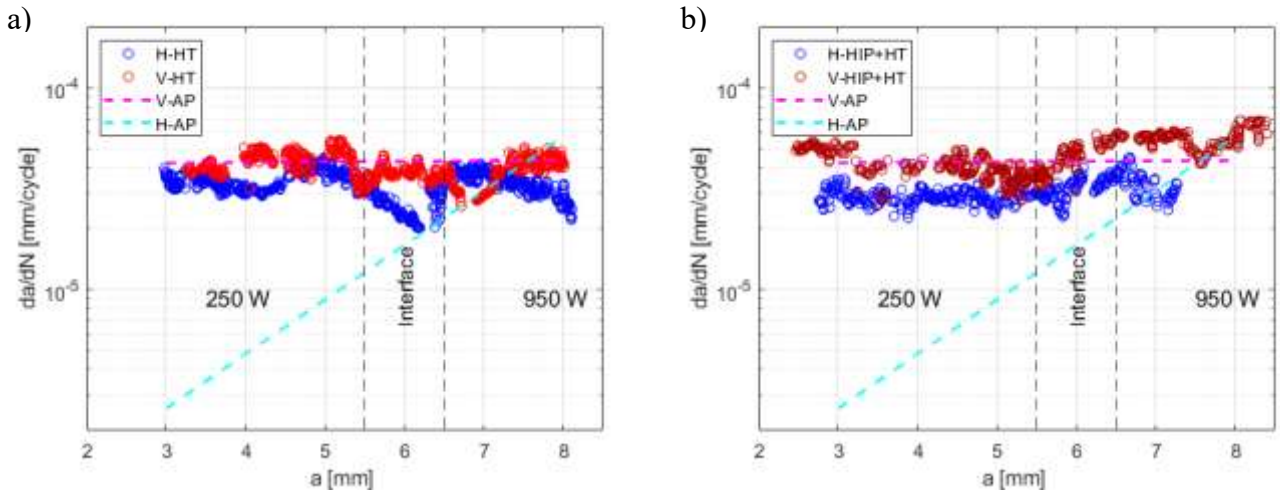

Figure 16. Fatigue crack growth rate curves of the horizontal and vertical functionally graded samples obtained on the (a) HT and (b) HIP+HT categories in constant ΔK tests. The dashed lines are fits to the data obtained from the tests on the AP materials.

The AP- H samples showed a different fatigue behaviour, with FCGR starting from 4E-6 mm/cycle, which was lower than the other samples and gradually increasing to about 7.2E-5 mm/cycle. This gradual increase in the FCGR arises from the different number of thermal cycles and consequently various fractions of the Laves phases and possible strengthening precipitates in the deposited layers closer to the build platform, i.e., the 250W side, and those layers which are further from the build platform, i.e., the 950W side. This behaviour is consistent with the hardness of the graded H samples. After post processing, the microstructure becomes more uniform with a more homogenous distribution of the precipitates so the gradual change in FCGR was not observed. The minimum FCGR of the AP- H material, 4E-6 mm/cycle, was lower than the post processed samples. This can be related to differences in compressive RS as they are known to act as extrinsic crack closure factors [90]. The average GOS of the 250W samples found to be lower after HT and HIP+HT compared with the AP materials (see figure 13). This is an indication of the reduction in the RS values after post-processing treatments. To confirm this quantitatively, the residual stress measurements using the XRD technique were done on the 250W materials in the different conditions. As it was expected from the GOS plots, the compressive residual stress, which was measured to be -483 ± 74 MPa, decreased to -

311 ± 38 MPa after HT and -186 ± 36 MPa after HIP+HT. Similar to the findings in the current study, the level of the compressive RS in the post-processed AM materials was reported to be lower as the heat treatment procedures at 650-870 °C can release them [40, 95].

3.3.3 Fracture surface and crack path

Fracture surface analyses were performed on the functionally graded materials. The SEM micrographs around the interface zones of the AP, HT, and HIP+HT conditions are shown in figure 17. It should be noted that the presented micrographs are from the V samples, which showed more defects in the interface area compared with the H specimens. The defects were accumulated in the interface boundaries where the manufacturing parameters changed. As can be seen, the defects are more pronounced on the 250W side of the interface. In addition, they are visible in the AP and HT condition materials, while their presence is not significant in the HIP+HT material.

To investigate the type of the defects, higher magnification SEM micrographs, as shown in figure 17-d, as well as EDS analyses were performed. It was concluded that the observed defects were unmelted particles which is a common defect in the AM parts [1, 62, 96, 97]. The unmelted or partially melted particles remained in the microstructure since the laser power was not high enough to (fully) melt the larger particles of the powder [96]. The unmelted or partially melted particles were still present in the material after the HT process, while their content was significantly reduced after HIP+HT. Also, it should be noted that the materials in AP and HT conditions contain porosity while the HIP+HT post processing reduces the porosity content noticeably, as was reported in different AM alloys [37, 97, 98].

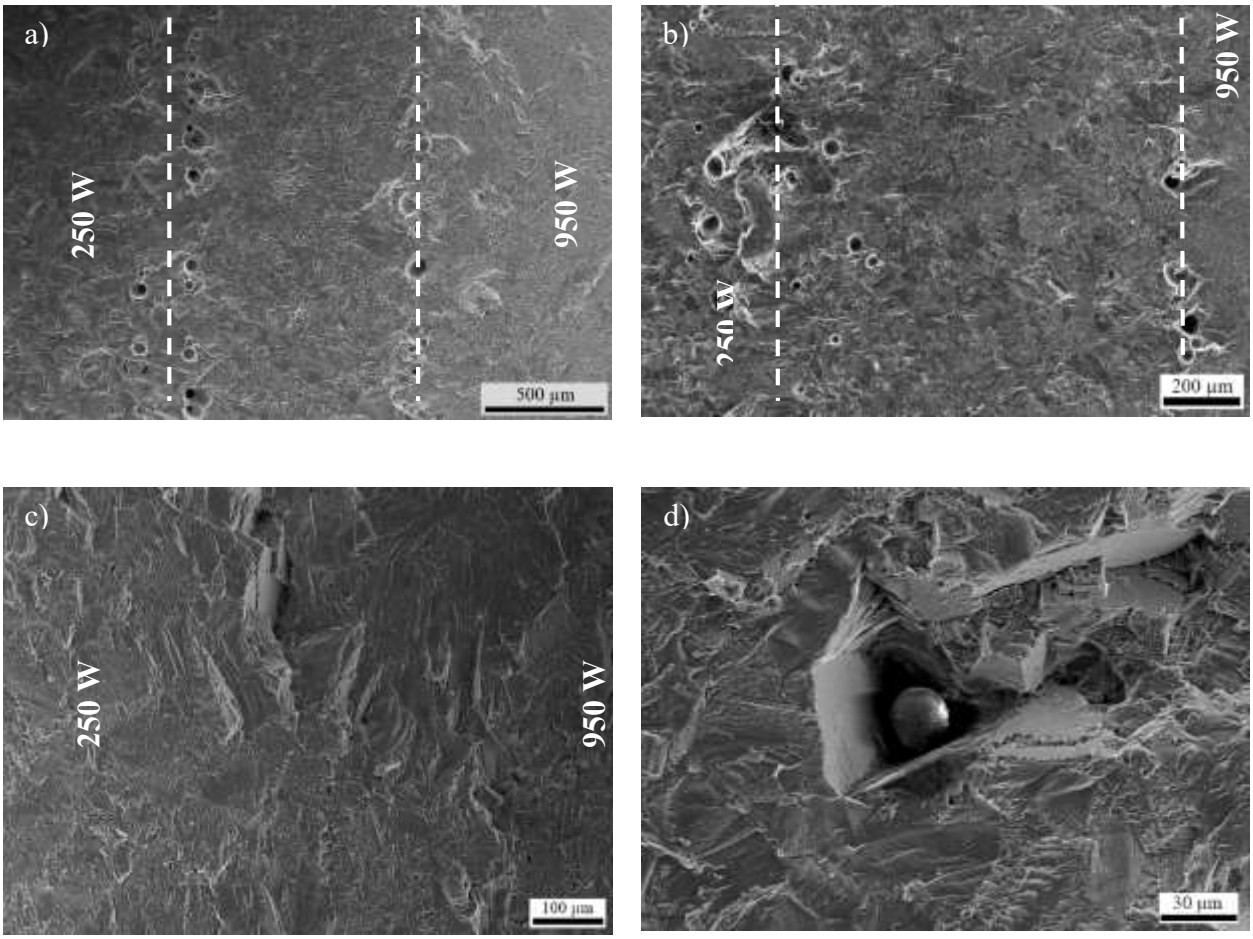

Figure 17. SEM micrographs of the functionally graded vertical samples around the interface region on the (a) AP, (b) HT, and (c) HIP+HT samples. (d) A high magnification micrograph of an un-melted particle close to the interface zone.

Higher magnification SEM micrographs of the fractured surfaces in the 250W region of the FG samples in AP, HT, HIP+HT conditions are depicted in figure 18.In the fracture surface of the AP material, stair-like features were observed, which can be indications of the local solidification direction. Crack propagation through the epitaxial dendrites revealed those stairs. The stair-like features were also observed in the micrograph of the HT material. In comparison to the AP specimen, however, the stairs seemed to be sharper, featuring lamellae. Those lamellae were accompanied by the secondary microcracks. Such microcracks could be promoted by the strengthening phases to diffuse the stress build-ups. The microcracks are believed to hinder the short crack growth. The formation of

the microcracks in this study is consistent with the other research on the AM IN718 superalloy [99]. The stair-like features were not dominant on the HIP+HT material's fracture surface. Unlike the other two groups, intergranular facets were observed on the micrographs of the HIP+HT samples. The facets originate from the annealing twin boundaries, which were formed after HIP+HT. Extended crystallographic facets develop in the large grains of the HIP+HT microstructure like what was observed in the HIP IN718 in the high cyclic fatigue tests [5].

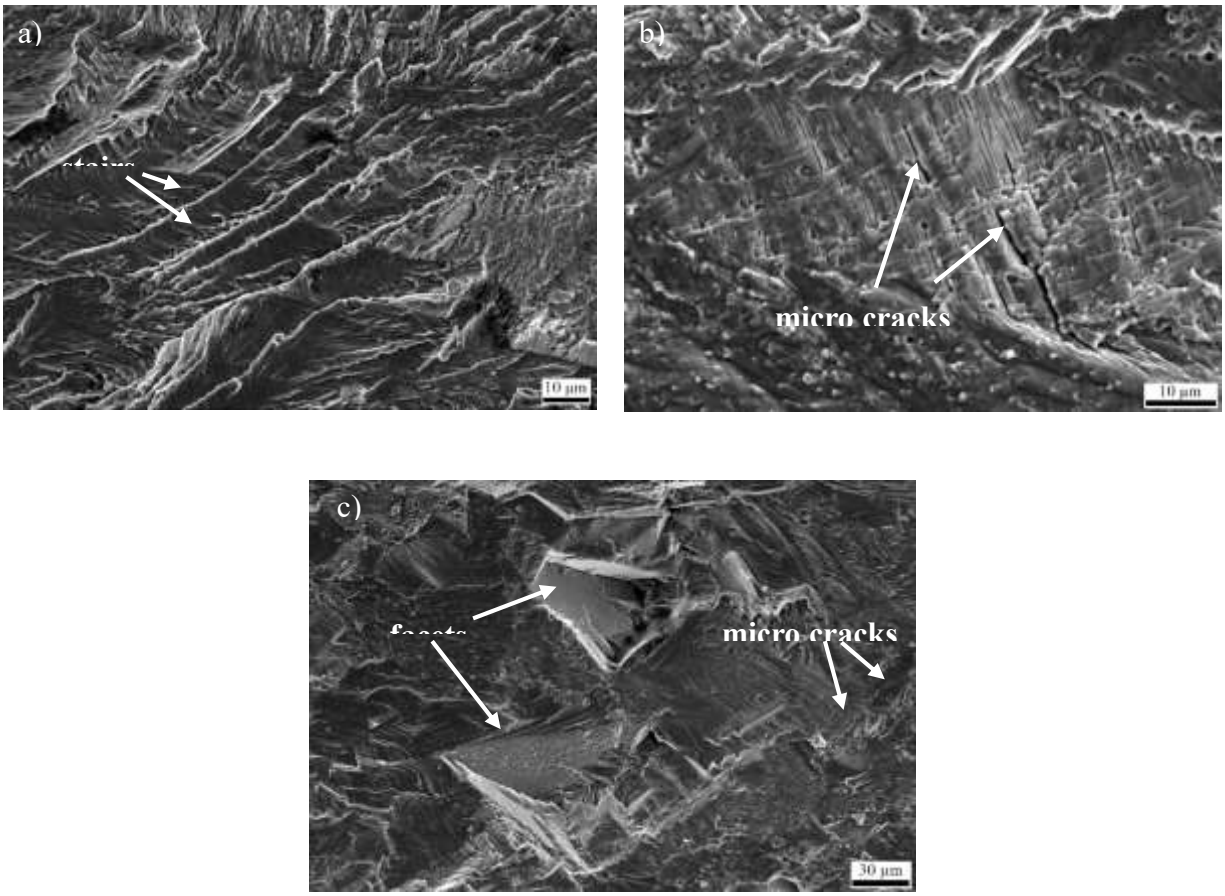

Figure 18. SEM micrographs of the fractured surfaces in the regions manufactured using 250 W laser power on the (a) AP, (b) HT, and (c) HIP+HT materials. Note that all the images are taken on the H category samples.

Figure 19 gives the IPF maps of the HT and HIP+HT functionally graded samples as well as the wrought-HT sample in the areas close to the crack. As it was observed for the NG materials shown in figure 10, the AM samples kept their directional microstructure in the HT condition while the grains

were more equiaxed with random textures in the HIP+HT condition. Clean-ups were not applied to the EBSD data close to the cracks to avoid inducing artefacts. In all maps, as the insert indicates, the crack propagates from right to left.

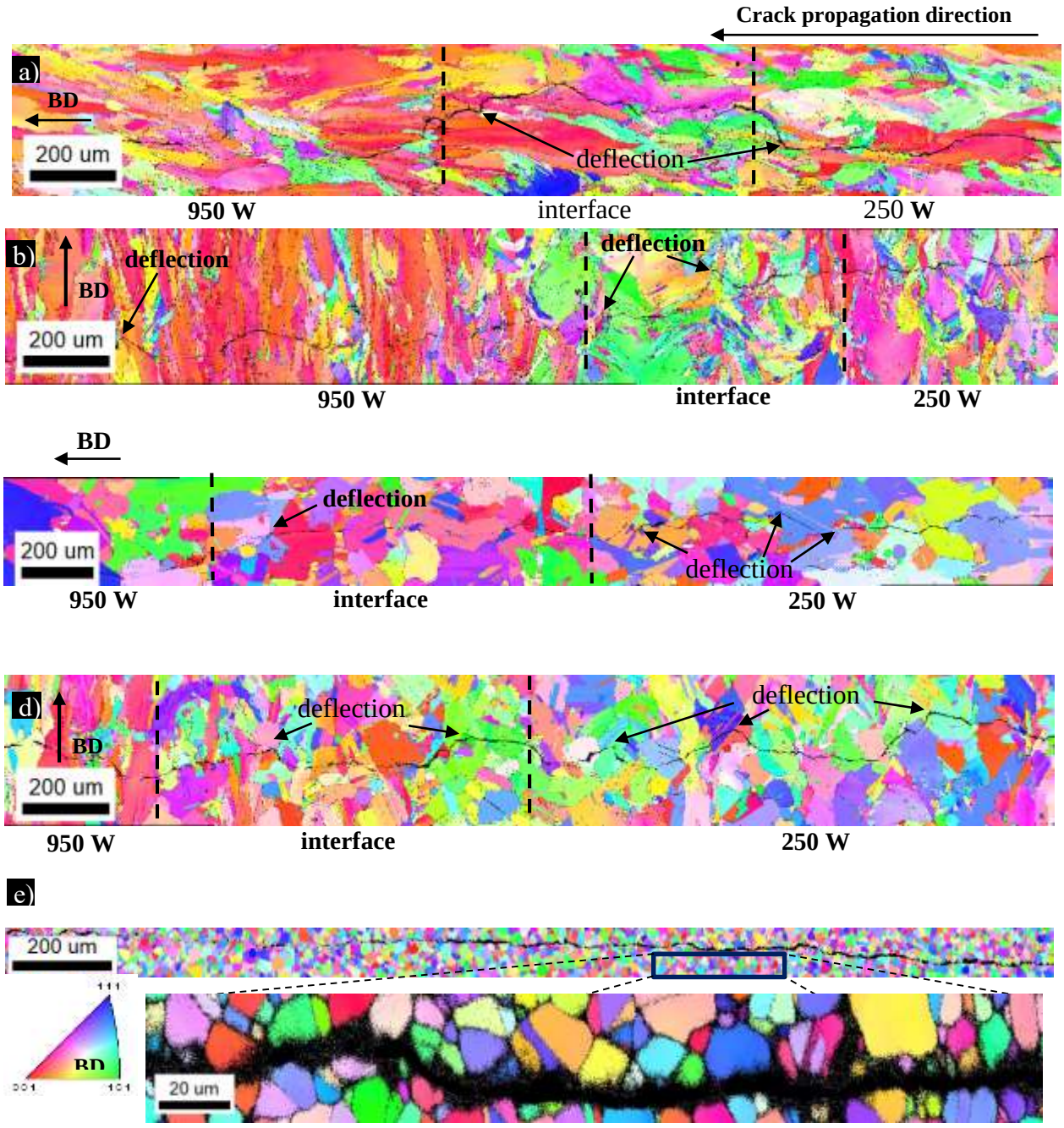

Figure 19. Inverse pole figure maps of (a) H-HT, (b) V-HT, (c) H-HIP+HT, (d) V-HIP+HT, and (e) wrought-HT samples along the crack path. The IPFs of the L-PBF specimens include the interface region. All samples were tested at a constant ΔK of 22.5 MPa$\sqrt{m}$. Note that the micron bars of the L-PBF and wrought IPFs are different. To visualize the crack path of the wrought-HT sample, a higher magnification IPF map is provided in the insert.

The regions manufactured with different laser powers, and the interface zones are determined in the maps. The characteristics of those zones, i.e., 250 W or 950 W side, remained similar to what was observed in the NG parts. For instance, the grains were finer in the 250W sides and coarser in the 950W regions. The texture of the 250 W sides of the HT samples was weaker, while the <001> preferential direction in the 950 W regions of the HT samples were observed. This behaviour is consistent with the dominant <001> orientation, which was discussed in the NG EBSD maps. Likewise, the texture of the HIP+HT samples in different zones was similar to their NG counterparts being random in 250 W and 950 W-H, while moderate in 950 W- V.

The crack paths of the L-PBF samples show the domination of the transgranular fracture mechanism while intergranular fracture happened at some points. This trend was observed for both post-processed conditions and was reported in other research as well [84, 88]. The fracture mechanism in the wrought material, however, was found to be a combination of intergranular and transgranular fractures. Some deflections were observed on the fracture surfaces of the AM parts. The tortuous crack path on the HT samples' fracture surface can be related to the effect of the melt pools, which have not completely disappeared after the heat treatment (see figure 3). In addition, the pinning effect of the rod shape δ precipitates which formed after HT (see figure 5), are the in favour of crack deflection [93]. In the HIP+HT samples, the deflections were mostly located close to the annealing twin boundaries. Such deflections can hinder crack propagation [84]. This is consistent with the lower FCGR observed for the HIP+HT samples in this study.

4. Conclusions

In the current research, the effects of the manufacturing parameters and post-processing procedures on the microstructural and fatigue behaviour of the L-PBF IN718 were explored. Three categories of samples using different laser parameters and build orientations were manufactured, which were

regarded as non-graded. Using the same parameters, two groups of functionally graded samples were fabricated. All aforementioned specimens were divided into three groups as far as the post-treatment, namely, as-processed (AP), heat treated (HT), and hot isostatic pressing followed by heat treatment (HIP+HT). Three-point bending tests at room temperature were conducted to evaluate the fatigue crack growth behaviour of the materials. The study resulted in the following conclusions:

The grains in the AP condition were found elongated in the build direction. The horizontal 950 W material had the largest grains. In all non-graded materials, as far as the post-processing, the <001> orientation was dominant. However, the intensity of the 001 pole was significantly higher in the 950W- H samples, 17.2, compared with the 250W and 950W- V, which were found to be 3.4 and 6.0, respectively. The HT reduced the grains elongation in the 950W- H group, while the other two materials showed an increase in their grain sizes. It should be noted that while the <001> remained the dominant orientation and its intensity did not change significantly for the 250W and 950W- H specimens, it increased to 27 for the 950W- V material. HIP+HT changed the grains of the 250W and 950W- H materials to equiaxed-like with random textures, while the elongation of the 950W- V material's grains was preserved to some extent.

Vickers hardness of all non-graded materials increased after post heat treatments, with close values for HT and HIP+HT. The same trends were found for the graded materials. The AP graded material showed a direction dependency with a decreasing hardness value pattern along the width for the H samples and near to constant hardness values along the width for the V samples. A similar trend was observed after HT and HIP+HT while the slope of the fit in the H samples was reduced. This can be related to the higher level of homogeneity in the alloy after post-treatment.

In the HT samples, at a low stress ratio of R= 0.1, the effect of the roughness induced crack closure was found to be higher in the H samples compared with the V specimens, which is related to the elongation of the grains in front of the crack path. After heat treatment, the L-PBF non-graded

materials exhibited slightly higher FCGR compared with the wrought-HT samples. However, after HIP+HT, the FCGR improved significantly and reached a lower level than the wrought samples. This behaviour can be a consequence of more isotropic textures and defects reduction. It was found that when the stress ratio increased to about 0.6-0.7, materials with finer grains had higher threshold stress intensity range which can be caused by the larger number of grain boundaries hindering the crack growth. After post-processing treatments, the ΔK_{th} values in all categories increased which was related to the presence of the strengthening phases and the reduction of defects and porosity. In addition, post processing treatments, increased the yield strength, which consequently resulted in a lower FCGR as was observed more pronounced in the HIP+HT category.

To study the fatigue crack growth behaviour of the FG materials, an FEM model was employed to calculate the customized K-solutions in order to perform the ΔK-constant tests. The FCGR of both build orientations after HT and HIP+HT remained constant as the crack grew. This behaviour was observed in the AP-V samples while the trend was different in the AP-H samples, having the $\frac{da}{dN}$ increasing with the increase in the crack length. It was suggested that the increasing FCGR trend in the AP-H samples is related to the different number of thermal cycles and consequently the different content of the Laves phases or strengthening precipitates in different deposited layers. In addition, the constant FCGR of the HT and HIP+HT H samples on the 250W side was higher than the AP materials. This can be related to the lower amount of the residual stress after the post processing in the 250W material, as was experimentally confirmed by the EBSD measurements (GOS) and XRD.

The crack path of the L-PBF samples in both post-processed conditions identified as the transgranular fracture mechanism, while intergranular fracture was also sometimes present. In the wrought-HT material, the fracture was a combination of the intergranular and transgranular fracture. In the L-PBF samples' crack path, deflections were located. Those deflections mostly happened near the grain boundaries in the HT materials and near the twin boundaries formed during the HIP+HT procedure.

This study comprehensively investigated the effect of the post-processing treatments on anisotropy and improving the fatigue crack growth behaviour of the laser powder bed fusion IN718. It was demonstrated that by applying the proper post-processing procedure, the fatigue behaviour can be enhanced to a level even higher than the wrought material.

Acknowledgements: We acknowledge the support from the Russian Science Foundation grant (project No. 19–79-30002).

References

[1] V.A. Popovich, E.V. Borisov, A.A. Popovich, V.S. Sufiiarov, D.V. Masaylo, L. Alzina, Functionally graded Inconel 718 processed by additive manufacturing: Crystallographic texture, anisotropy of microstructure and mechanical properties, Materials & Design, 114 (2017) 441-449.

[2] M. Knezevic, S. Ghorbanpour, N.C. Ferreri, I.A. Riyad, A.D. Kudzal, J.D. Paramore, S.C. Vogel, B.A. McWilliams, Thermo-hydrogen refinement of microstructure to improve mechanical properties of Ti–6Al–4V fabricated via laser powder bed fusion, Materials Science and Engineering: A, 809 (2021) 140980.

[3] J. Hönnige, C.E. Seow, S. Ganguly, X. Xu, S. Cabeza, H. Coules, S. Williams, Study of residual stress and microstructural evolution in as-deposited and inter-pass rolled wire plus arc additively manufactured Inconel 718 alloy after ageing treatment, Materials Science and Engineering: A, 801 (2021) 140368.

[4] X. Wang, K. Chou, The effects of stress relieving heat treatment on the microstructure and residual stress of Inconel 718 fabricated by laser metal powder bed fusion additive manufacturing process, Journal of Manufacturing Processes, 48 (2019) 154-163.

[5] S. Gribbin, S. Ghorbanpour, N.C. Ferreri, J. Bicknell, I. Tsukrov, M. Knezevic, Role of grain structure, grain boundaries, crystallographic texture, precipitates, and porosity on fatigue behavior of Inconel 718 at room and elevated temperatures, Materials Characterization, 149 (2019) 184-197.

[6] E. Hosseini, V.A. Popovich, A review of mechanical properties of additively manufactured Inconel 718, Additive Manufacturing, 30 (2019) 100877.

[7] J.M. Oblak, D.F. Paulonis, D.S. Duvall, Coherency strengthening in Ni base alloys hardened by DO22 γ″ precipitates, Metallurgical Transactions, 5 (1974) 143-153.

[8] M. Clavel, A. Pineau, Frequency and wave-form effects on the fatigue crack growth behavior of alloy 718 at 298 K and 823 K, Metallurgical Transactions A, 9 (1978) 471-480.

[9] S. Ghorbanpour, M. Zecevic, A. Kumar, M. Jahedi, J. Bicknell, L. Jorgensen, I.J. Beyerlein, M. Knezevic, A crystal plasticity model incorporating the effects of precipitates in superalloys: Application to tensile, compressive, and cyclic deformation of Inconel 718, International Journal of Plasticity, 99 (2017) 162-185.

[10] D.F. Paulonis, J.M. Oblak, D.S. Duvall, Precipitation in nickel-base alloy 718, ASM (Amer. Soc. Metals), Trans. Quart., 62 (1969) 611-622.

[11] D.W. Worthem, I.M. Robertson, F.A. Leckie, D.F. Socie, C.J. Altstetter, Inhomogeneous deformation in INCONEL 718 during monotonic and cyclic loadings, Metallurgical transactions. A, Physical metallurgy and materials science, 21 A (1990) 3215-3220.

[12] L. Xiao, D.L. Chen, M.C. Chaturvedi, Shearing of γ″ precipitates and formation of planar slip bands in Inconel 718 during cyclic deformation, Scripta Materialia, 52 (2005) 603-607.

[13] M. Xie, N. Foundoukos, J.C. Chapman, Experimental and numerical investigation on the shear behaviour of friction-welded bar-plate connections embedded in concrete, Journal of Constructional Steel Research, 61 (2005) 625-649.

[14] A. Strondl, R. Fischer, G. Frommeyer, A. Schneider, Investigations of MX and γ′/γ″ precipitates in the nickel-based superalloy 718 produced by electron beam melting, Materials Science and Engineering: A, 480 (2008) 138-147.

[15] S. Sui, J. Chen, E. Fan, H. Yang, X. Lin, W. Huang, The influence of Laves phases on the high-cycle fatigue behavior of laser additive manufactured Inconel 718, Materials Science and Engineering: A, 695 (2017) 6-13.

[16] V.A. Popovich, E.V. Borisov, A.A. Popovich, V.S. Sufiiarov, D.V. Masaylo, L. Alzina, Impact of heat treatment on mechanical behaviour of Inconel 718 processed with tailored microstructure by selective laser melting, Materials & Design, 131 (2017) 12-22.

[17] P.D. Nezhadfar, A.S. Johnson, N. Shamsaei, Fatigue behavior and microstructural evolution of additively manufactured Inconel 718 under cyclic loading at elevated temperature, International Journal of Fatigue, 136 (2020) 105598.

[18] C. Wang, R. Li, Effect of double aging treatment on structure in Inconel 718 alloy, Journal of Materials Science, 39 (2004) 2593-2595.

[19] M. Burke, M. Miller, Precipitation in alloy 718: a combined Al3M and apfim investigation, in: E.A. Loria (Ed.) Superalloys 718, 625 and Various Derivatives, The Minerals, Metals & Materials Society, 1991.

[20] S. Ghosh, S. Yadav, G. Das, Study of standard heat treatment on mechanical properties of Inconel 718 using ball indentation technique, Materials Letters, 62 (2008) 2619-2622.

[21] S. Sanchez, G. Gaspard, C.J. Hyde, I.A. Ashcroft, G.A. Ravi, A.T. Clare, The creep behaviour of nickel alloy 718 manufactured by laser powder bed fusion, Materials & Design, (2021) 109647.

[22] A. Mostafa, I. Picazo Rubio, V. Brailovski, M. Jahazi, M. Medraj, Structure, Texture and Phases in 3D Printed IN718 Alloy Subjected to Homogenization and HIP Treatments, Metals, 7 (2017) 196.

[23] E. Chlebus, K. Gruber, B. Kuźnicka, J. Kurzac, T. Kurzynowski, Effect of heat treatment on the microstructure and mechanical properties of Inconel 718 processed by selective laser melting, Materials Science and Engineering: A, 639 (2015) 647-655.

[24] Y. Zhao, K. Guan, Z. Yang, Z. Hu, Z. Qian, H. Wang, Z. Ma, The effect of subsequent heat treatment on the evolution behavior of second phase particles and mechanical properties of the Inconel

718 superalloy manufactured by selective laser melting, Materials Science and Engineering: A, 794 (2020) 139931.

[25] D. Zhang, W. Niu, X. Cao, Z. Liu, Effect of standard heat treatment on the microstructure and mechanical properties of selective laser melting manufactured Inconel 718 superalloy, Materials Science and Engineering: A, 644 (2015) 32-40.

[26] Z. Wang, K. Guan, M. Gao, X. Li, X. Chen, X. Zeng, The microstructure and mechanical properties of deposited-IN718 by selective laser melting, Journal of Alloys and Compounds, 513 (2012) 518-523.

[27] A. 5663, Nickel Alloy, Corrosion and Heat Resistant, Bars, Forgings, and Rings 52.5Ni 19Cr 3.0Mo 5.1Cb 0.90Ti 0.50Al 19Fe, Consumable Electrode or Vacuum Induction Melted 1775°F (968°C) Solution and Precipitation Heat Treated, in: AMS 5663, SAE International, 1965.

[28] N.C. Ferreri, S.C. Vogel, M. Knezevic, Determining volume fractions of γ, γ′, γ″, δ, and MC-carbide phases in Inconel 718 as a function of its processing history using an advanced neutron diffraction procedure, Materials Science and Engineering: A, 781 (2020) 139228.

[29] K. Moussaoui, W. Rubio, M. Mousseigne, T. Sultan, F. Rezai, Effects of Selective Laser Melting additive manufacturing parameters of Inconel 718 on porosity, microstructure and mechanical properties, Materials Science and Engineering: A, 735 (2018) 182-190.

[30] K.-y. Feng, P. Liu, H.-x. Li, S.-y. Sun, S.-b. Xu, J.-n. Li, Microstructure and phase transformation on the surface of Inconel 718 alloys fabricated by SLM under 1050°C solid solution + double ageing, Vacuum, 145 (2017) 112-115.

[31] K. Karami, A. Blok, L. Weber, S.M. Ahmadi, R. Petrov, K. Nikolic, E.V. Borisov, S. Leeflang, C. Ayas, A.A. Zadpoor, M. Mehdipour, E. Reinton, V.A. Popovich, Continuous and pulsed selective laser melting of Ti6Al4V lattice structures: Effect of post-processing on microstructural anisotropy and fatigue behaviour, Additive Manufacturing, 36 (2020) 101433.

[32] W. Tillmann, C. Schaak, J. Nellesen, M. Schaper, M.E. Aydinöz, K.P. Hoyer, Hot isostatic pressing of IN718 components manufactured by selective laser melting, Additive Manufacturing, 13 (2017) 93-102.

[33] R. Jiang, A. Mostafaei, Z. Wu, A. Choi, P.-W. Guan, M. Chmielus, A.D. Rollett, Effect of heat treatment on microstructural evolution and hardness homogeneity in laser powder bed fusion of alloy 718, Additive Manufacturing, 35 (2020) 101282.

[34] L. Huang, Y. Cao, J. Zhang, X. Gao, G. Li, Y. Wang, Effect of heat treatment on the microstructure evolution and mechanical behaviour of a selective laser melted Inconel 718 alloy, Journal of Alloys and Compounds, 865 (2021) 158613.

[35] H. Qi, M. Azer, A. Ritter, Studies of Standard Heat Treatment Effects on Microstructure and Mechanical Properties of Laser Net Shape Manufactured INCONEL 718, Metallurgical and Materials Transactions A, 40 (2009) 2410-2422.

[36] Z. Xu, C.J. Hyde, C. Tuck, A.T. Clare, Creep behaviour of inconel 718 processed by laser powder bed fusion, Journal of Materials Processing Technology, 256 (2018) 13-24.

[37] S. Gribbin, J. Bicknell, L. Jorgensen, I. Tsukrov, M. Knezevic, Low cycle fatigue behavior of direct metal laser sintered Inconel alloy 718, International Journal of Fatigue, 93 (2016) 156-167.

[38] A. 5662, Nickel Alloy, Corrosion and Heat Resistant, Bars, Forgings, and Rings 52.5Ni 19Cr 3.0Mo 5.1Cb 0.90Ti 0.50Al 18Fe, Consumable Electrode or Vacuum Induction Melted 1775°F (968°C) Solution Heat Treated, Precipitation Hardenable, in, SAE International, 1965.

[39] G. Marchese, S. Parizia, M. Rashidi, A. Saboori, D. Manfredi, D. Ugues, M. Lombardi, E. Hryha, S. Biamino, The role of texturing and microstructure evolution on the tensile behavior of heat-treated Inconel 625 produced via laser powder bed fusion, Materials Science and Engineering: A, 769 (2020) 138500.

[40] A. Kreitcberg, V. Brailovski, S. Turenne, Effect of heat treatment and hot isostatic pressing on the microstructure and mechanical properties of Inconel 625 alloy processed by laser powder bed fusion, Materials Science and Engineering: A, 689 (2017) 1-10.

[41] N. Kouraytem, J. Varga, B. Amin-Ahmadi, H. Mirmohammad, R.A. Chanut, A.D. Spear, O.T. Kingstedt, A recrystallization heat-treatment to reduce deformation anisotropy of additively manufactured Inconel 718, Materials & Design, 198 (2021) 109228.

[42] R. Seede, A. Mostafa, V. Brailovski, M. Jahazi, M. Medraj, Microstructural and Microhardness Evolution from Homogenization and Hot Isostatic Pressing on Selective Laser Melted Inconel 718: Structure, Texture, and Phases, Journal of Manufacturing and Materials Processing, 2 (2018).

[43] A. 5383, Nickel Alloy, Corrosion and Heat-Resistant, Investment Castings, 52.5Ni - 19Cr - 3.0Mo - 5.1Cb(Nb) - 0.90Ti - 0.60Al - 18Fe, Vacuum Melted Homogenization and Solution Heat Treated, in, SAE International, 1966.

[44] A. 5664E, Nickel Alloy, Corrosion and Heat Resistant, Bars, Forgings, and Rings, 52.5Ni - 19Cr - 3.0Mo - 5.1Cb - 0.90Ti - 0.50Al - 18Fe, Consumable Electrode or Vacuum Induction Melted, 1950 °F (1066 °C) Solution Heat Treated, Precipitation Hardenable, in, SAE International, 1965.

[45] Standard Test Method for Linear-Elastic Plane-Strain Fracture Toughness of Metallic Materials, in.

[46] A. E647, Standard Test Method for Measurement of Fatigue Crack Growth Rates, in.

[47] L.E. Murr, E. Martinez, S.M. Gaytan, D.A. Ramirez, B.I. Machado, P.W. Shindo, J.L. Martinez, F. Medina, J. Wooten, D. Ciscel, U. Ackelid, R.B. Wicker, Microstructural Architecture, Microstructures, and Mechanical Properties for a Nickel-Base Superalloy Fabricated by Electron Beam Melting, Metallurgical and Materials Transactions A, 42 (2011) 3491-3508.

[48] K. Amato, S. Gaytan, L. Murr, E. Martinez, P. Shindo, J. Hernandez, S. Collins, F. Medina, Microstructures and mechanical behavior of Inconel 718 fabricated by selective laser melting, Acta Materialia, 60 (2012) 2229-2239.

[49] J. Ding, S. Xue, Z. Shang, J. Li, Y. Zhang, R. Su, T. Niu, H. Wang, X. Zhang, Characterization of precipitation in gradient Inconel 718 superalloy, Materials Science and Engineering: A, 804 (2021) 140718.

[50] J. Schneider, B. Lund, M. Fullen, Effect of heat treatment variations on the mechanical properties of Inconel 718 selective laser melted specimens, Additive Manufacturing, 21 (2018) 248-254.

[51] L. Zhou, A. Mehta, B. McWilliams, K. Cho, Y. Sohn, Microstructure, precipitates and mechanical properties of powder bed fused inconel 718 before and after heat treatment, Journal of Materials Science & Technology, 35 (2019) 1153-1164.

[52] M. Komarasamy, S. Shukla, S. Williams, K. Kandasamy, S. Kelly, R.S. Mishra, Microstructure, fatigue, and impact toughness properties of additively manufactured nickel alloy 718, Additive Manufacturing, 28 (2019) 661-675.

[53] Y. Zhang, Z. Li, P. Nie, Y. Wu, Effect of Heat Treatment on Niobium Segregation of Laser-Cladded IN718 Alloy Coating, Metallurgical and Materials Transactions A, 44 (2013) 708-716.

[54] Y. Zhang, Z. Li, P. Nie, Y. Wu, Effect of Precipitation on the Microhardness Distribution of Diode Laser Epitaxially Deposited IN718 Alloy Coating, Journal of Materials Science & Technology, 29 (2013) 349-352.

[55] A. Segerstark, J. Andersson, L.-E. Svensson, O. Ojo, Microstructural characterization of laser metal powder deposited Alloy 718, Materials Characterization, 142 (2018) 550-559.

[56] W.M. Tucho, P. Cuvillier, A. Sjolyst-Kverneland, V. Hansen, Microstructure and hardness studies of Inconel 718 manufactured by selective laser melting before and after solution heat treatment, Materials Science and Engineering: A, 689 (2017) 220-232.

[57] Y. Tian, D. McAllister, H. Colijn, M. Mills, D. Farson, M. Nordin, S. Babu, Rationalization of Microstructure Heterogeneity in INCONEL 718 Builds Made by the Direct Laser Additive Manufacturing Process, Metallurgical and Materials Transactions A, 45 (2014) 4470-4483.

[58] D.H. Smith, J. Bicknell, L. Jorgensen, B.M. Patterson, N.L. Cordes, I. Tsukrov, M. Knezevic, Microstructure and mechanical behavior of direct metal laser sintered Inconel alloy 718, Materials Characterization, 113 (2016) 1-9.

[59] H.L. Wei, J. Mazumder, T. DebRoy, Evolution of solidification texture during additive manufacturing, Scientific Reports, 5 (2015) 16446.

[60] S. Holland, X. Wang, X.Y. Fang, Y.B. Guo, F. Yan, L. Li, Grain boundary network evolution in Inconel 718 from selective laser melting to heat treatment, Materials Science and Engineering: A, 725 (2018) 406-418.

[61] R.W. Balluffi, J.W. Cahn, Mechanism for diffusion induced grain boundary migration, Acta Metallurgica, 29 (1981) 493-500.

[62] N.C. Ferreri, S. Ghorbanpour, S. Bhowmik, R. Lussier, J. Bicknell, B.M. Patterson, M. Knezevic, Effects of build orientation and heat treatment on the evolution of microstructure and mechanical properties of alloy Mar-M-509 fabricated via laser powder bed fusion, International Journal of Plasticity, 121 (2019) 116-133.

[63] F. Liu, X. Lin, G. Yang, M. Song, J. Chen, W. Huang, Microstructure and residual stress of laser rapid formed Inconel 718 nickel-base superalloy, Optics & Laser Technology, 43 (2011) 208-213.

[64] C. Blochwitz, W. Tirschler, Twin boundaries as crack nucleation sites, Crystal Research and Technology, 40 (2005) 32-41.

[65] E. Tochigi, A. Nakamura, N. Shibata, Y. Ikuhara, Dislocation Structures in Low-Angle Grain Boundaries of α-Al2O3, Crystals, 8 (2018) 133.

[66] J.N. DuPont, J.C. Lippold, S.D. Kiser, Solid-Solution Strengthened Ni-base Alloys, in: Welding Metallurgy and Weldability of Nickel-Base Alloys, 2009, pp. 47-156.

[67] T. DebRoy, H.L. Wei, J.S. Zuback, T. Mukherjee, J.W. Elmer, J.O. Milewski, A.M. Beese, A. Wilson-Heid, A. De, W. Zhang, Additive manufacturing of metallic components – Process, structure and properties, Progress in Materials Science, 92 (2018) 112-224.

[68] P. Kanagarajah, F. Brenne, T. Niendorf, H.J. Maier, Inconel 939 processed by selective laser melting: Effect of microstructure and temperature on the mechanical properties under static and cyclic loading, Materials Science and Engineering: A, 588 (2013) 188-195.

[69] X.Y. Fang, H.Q. Li, M. Wang, C. Li, Y.B. Guo, Characterization of texture and grain boundary character distributions of selective laser melted Inconel 625 alloy, Materials Characterization, 143 (2018) 182-190.

[70] D. Ma, A.D. Stoica, Z. Wang, A.M. Beese, Crystallographic texture in an additively manufactured nickel-base superalloy, Materials Science and Engineering: A, 684 (2017) 47-53.

[71] R. Muñoz-Moreno, V.D. Divya, S.L. Driver, O.M.D.M. Messé, T. Illston, S. Baker, M.A. Carpenter, H.J. Stone, Effect of heat treatment on the microstructure, texture and elastic anisotropy of the nickel-based superalloy CM247LC processed by selective laser melting, Materials Science and Engineering: A, 674 (2016) 529-539.

[72] S. Li, Q. Wei, Y. Shi, Z. Zhu, D. Zhang, Microstructure Characteristics of Inconel 625 Superalloy Manufactured by Selective Laser Melting, Journal of Materials Science & Technology, 31 (2015) 946-952.

[73] G.P. Dinda, A.K. Dasgupta, J. Mazumder, Texture control during laser deposition of nickel-based superalloy, Scripta Materialia, 67 (2012) 503-506.

[74] E. Cakmak, M.M. Kirka, T.R. Watkins, R.C. Cooper, K. An, H. Choo, W. Wu, R.R. Dehoff, S.S. Babu, Microstructural and micromechanical characterization of IN718 theta shaped specimens built with electron beam melting, Acta Materialia, 108 (2016) 161-175.

[75] Y. Zhao, K. Li, M. Gargani, W. Xiong, A comparative analysis of Inconel 718 made by additive manufacturing and suction casting: Microstructure evolution in homogenization, Additive Manufacturing, 36 (2020) 101404.

[76] D. Kumar, S. Idapalapati, W. Wang, D.J. Child, T. Haubold, C.C. Wong, Microstructure-mechanical property correlation in shot peened and vibro-peened Ni-based superalloy, Journal of Materials Processing Technology, 267 (2019) 215-229.

[77] S.J. Lainé, K.M. Knowles, P.J. Doorbar, R.D. Cutts, D. Rugg, Microstructural characterisation of metallic shot peened and laser shock peened Ti–6Al–4V, Acta Materialia, 123 (2017) 350-361.

[78] D.J. Child, G.D. West, R.C. Thomson, Assessment of surface hardening effects from shot peening on a Ni-based alloy using electron backscatter diffraction techniques, Acta Materialia, 59 (2011) 4825-4834.

[79] E. Hornbogen, K.-H.Z. Gahr, Microstructure and fatigue crack growth in a γ-Fe-Ni-Al alloy, Acta Metallurgica, 24 (1976) 581-592.

[80] S.F. Toh, W.M. Rainforth, Fatigue of a nickel base superalloy with bimodal grain size, Materials Science and Technology, 12 (1996) 1007-1014.

[81] J.E. King, Effects of grain size and microstructure on threshold values and near threshold crack growth in powder-formed Ni-base superalloy, Metal Science, 16 (1982) 345-355.

[82] Y. Yamada, J.C. Newman, Crack closure under high load-ratio conditions for Inconel-718 near threshold behavior, Engineering Fracture Mechanics, 76 (2009) 209-220.

[83] G.T. Gray, J.C. Williams, A.W. Thompson, Roughness-Induced Crack Closure: An Explanation for Microstructurally Sensitive Fatigue Crack Growth, Metallurgical Transactions A, 14 (1983) 421-433.

[84] X. Yu, X. Lin, H. Tan, Y. Hu, S. Zhang, F. Liu, H. Yang, W. Huang, Microstructure and fatigue crack growth behavior of Inconel 718 superalloy manufactured by laser directed energy deposition, International Journal of Fatigue, 143 (2021) 106005.

[85] P.K. Liaw, W.A. Logsdon, Fatigue crack growth behavior in inconel 706 at 297 K and 4.2 K, Acta Metallurgica, 36 (1988) 1731-1744.

[86] P. Paris, F. Erdogan, A Critical Analysis of Crack Propagation Laws, Journal of Basic Engineering, 85 (1963) 528-533.

[87] R. Konečná, L. Kunz, G. Nicoletto, A. Bača, Long fatigue crack growth in Inconel 718 produced by selective laser melting, International Journal of Fatigue, 92 (2016) 499-506.

[88] X. Hu, Z. Xue, T. Ren, Y. Jiang, C. Dong, F. Liu, On the fatigue crack growth behaviour of selective laser melting fabricated Inconel 625: Effects of build orientation and stress ratio, Fatigue & Fracture of Engineering Materials & Structures, 43 (2020) 771-787.

[89] J.C. Newman, Y. Yamada, Compression precracking methods to generate near-threshold fatigue-crack-growth-rate data, International Journal of Fatigue, 32 (2010) 879-885.

[90] H.Y. Li, H.L. Sun, P. Bowen, J.F. Knott, Effects of compressive residual stress on short fatigue crack growth in a nickel-based superalloy, International Journal of Fatigue, 108 (2018) 53-61.

[91] H.-B. Park, Y.-H. Kim, B.-W. Lee, K.-S. Rheem, Effect of heat treatment on fatigue crack growth rate of Inconel 690 and Inconel 600, Journal of Nuclear Materials, 231 (1996) 204-212.

[92] Y. Hu, X. Lin, Y. Li, Y. Ou, X. Gao, Q. Zhang, W. Li, W. Huang, Microstructural evolution and anisotropic mechanical properties of Inconel 625 superalloy fabricated by directed energy deposition, Journal of Alloys and Compounds, 870 (2021) 159426.

[93] X. Yu, X. Lin, F. Liu, Y. Hu, S. Zhang, Y. Zhan, H. Yang, W. Huang, Microstructure and Fatigue Crack Growth Behavior of Inconel 718 Superalloy Fabricated Via Laser Directed Energy Deposition Additive Manufacturing., SSRN, (2020).

[94] ISO, ISO 12135:2016(E), in: Metallic materials — Unified method of test for the determination of quasistatic fracture toughness, 2016, pp. 1-98.

[95] T. Mishurova, K. Artzt, B. Rehmer, J. Haubrich, L. Ávila, F. Schoenstein, I. Serrano-Munoz, G. Requena, G. Bruno, Separation of the impact of residual stress and microstructure on the fatigue performance of LPBF Ti-6Al-4V at elevated temperature, International Journal of Fatigue, 148 (2021) 106239.

[96] X.-A. Hu, G.-L. Zhao, Y. Jiang, X.-F. Ma, F.-C. Liu, J. Huang, C.-L. Dong, Experimental Investigation on the LCF Behavior Affected by Manufacturing Defects and Creep Damage of One Selective Laser Melting Nickel-Based Superalloy at 815 °C, Acta Metallurgica Sinica (English Letters), 33 (2020) 514-527.

[97] R. Molaei, A. Fatemi, N. Phan, Multiaxial fatigue of LB-PBF additive manufactured 17–4 PH stainless steel including the effects of surface roughness and HIP treatment and comparisons with the wrought alloy, International Journal of Fatigue, 137 (2020) 105646.

[98] R. Cunningham, S.P. Narra, T. Ozturk, J. Beuth, A.D. Rollett, Evaluating the Effect of Processing Parameters on Porosity in Electron Beam Melted Ti-6Al-4V via Synchrotron X-ray Microtomography, JOM, 68 (2016) 765-771.

[99] C. Pei, D. Shi, H. Yuan, H. Li, Assessment of mechanical properties and fatigue performance of a selective laser melted nickel-base superalloy Inconel 718, Materials Science and Engineering: A, 759 (2019) 278-287.

Chapter 5: Summary and future work

This thesis investigated the effects of the additive manufacturing parameters on the microstructure and consequently mechanical behaviors of L-PBF Inconel 718 superalloy. To study the effect of the microstructures caused by the AM process on the mechanical properties, specimens were built and tested in different orientations. Mechanical properties such as monotonic tension and compression strength, in addition to the large strain cyclic behaviour ,also known as pre-strained cyclic performance, in different build orientations were measured at room temperature. Moreover, since the material is used in high temperature applications, the monotonic strength of the material was investigated at high temperatures of 450°C and 550°C. Initial texture of the AM materials as well as the deformed textures were measured using electron backscattered diffraction (EBSD) technique. To simulate the mechanical responses of the material incorporating the microstructure, an elastoplastic self-consistent (EPSC) model was developed. The model was capable of accurately simulating monotonic behaviors including tension-compression asymmetry and directional anisotropy not only in room temperature but also in high temperatures using one set of parameters. In addition, the Bauschinger effect, the non-linearities in cyclic unloading steps, and the permanent softening associated with cyclic loadings were accurately captured by the EPSC model. Also, the simulated deformed textures were in good agreements with the measured deformed textures.

In the second part of this work, the fatigue behavior of functionally graded (FG) IN718 was studied. FG IN718 samples were manufactured altering AM parameters such as laser power, hatch distance, scanning speed, layer thickness and beam diameter. Non-graded (NG) samples were also fabricated using the same parameters to compare the results of the FG parts. A variety of post processing procedures were applied to the FG and NG samples to find the optimum post treatment. It turned out that at the stress ratio of R= 0.1, the HIP+HT process results in the lowest fatigue crack growth rate (FCGR) in the AM parts. The effect of the HT and HIP+HT procedures on the FG materials were found to be similar.

Although, a good number of mechanical properties of the L-PBF IN718 were studied in this research, still some properties such as fracture toughness, high temperature pre-strained cyclic behavior, and creep behavior were not studied in details. In addition, the effect of more build orientations , both for NG and FG materials, can be investigated in the future. Lastly, the data obtained in the second part of the study is comprehensive and can be used for modeling purposes.